SANDIA REPORT

SAND2016-9961
Unlimited Release
Printed October, 2016

Reinvestigation into Closure Predictions of Room D at the Waste Isolation Pilot Plant

Benjamin Reedlunn

Prepared by
Sandia National Laboratories
Albuquerque, New Mexico 87185 and Livermore, California 94550

Sandia National Laboratories

Issued by Sandia National Laboratories, operated for the United States Department of Energy by Sandia Corporation.

Available to DOE and DOE contractors from
U.S. Department of Energy
Office of Scientific and Technical Information
P.O. Box 62
Oak Ridge, TN 37831

Telephone: (865) 576-8401
Facsimile: (865) 576-5728
E-Mail: reports@adonis.osti.gov
Online ordering: http://www.osti.gov/bridge

Available to the public from
U.S. Department of Commerce
National Technical Information Service
5285 Port Royal Rd
Springfield, VA 22161

Telephone: (800) 553-6847
Facsimile: (703) 605-6900
E-Mail: orders@ntis.fedworld.gov
Online ordering: http://www.ntis.gov/help/ordermethods.asp?loc=7-4-0#online

SAND2016-9961
Unlimited Release
Printed October, 2016

Reinvestigation into Closure Predictions of Room D at the Waste Isolation Pilot Plant

Benjamin Reedlunn
Sandia National Laboratories
P.O. Box 5800
Albuquerque, NM 87185-0840

Abstract

Room D was an *in-situ*, isothermal, underground experiment conducted at the Waste Isolation Pilot Plant between 1984 and 1991. The room was carefully instrumented to measure the horizontal and vertical closure immediately upon excavation and for several years thereafter. Early finite element simulations of salt creep around Room D under predicted the vertical closure by 4.5×, causing investigators to explore a series of changes to the way Room D was modeled. Discrepancies between simulations and measurements were resolved through a series of adjustments to model parameters, which were openly acknowledged in published reports.

Interest in Room D has been rekindled recently by the U.S./German Joint Project III and Project WEIMOS, which seek to improve the predictions of rock salt constitutive models. Joint Project participants calibrate their models solely against laboratory tests, and benchmark the models against underground experiments, such as room D. This report describes updating legacy Room D simulations to today's computational standards by rectifying several numerical issues. Subsequently, the constitutive model used in previous modeling is recalibrated two different ways against a suite of new laboratory creep experiments on salt extracted from the repository horizon of the Waste Isolation Pilot Plant. Simulations with the new, laboratory-based, calibrations under predict Room D vertical closure by 3.1×. A list of potential improvements is discussed.

Acknowledgment

I am indebted to a number of people for ushering me into the world of rock salt mechanics. J. Guadalupe Argüello invited me take his place on Joint Project III, and was incredibly patient with all of my questions during the transition period. Frank Hansen has been an invaluable resource for the science behind the modeling, for the history of WIPP, and for promoting the Joint Project activities. James Bean helped me understand the Munson-Dawson material model, and continues to give me suggestions on how to make simulations run efficiently. Courtney Herrick and Michael Schuhen have provided many crucial bits of information from their first-hand knowledge of WIPP. Christi Leigh saw the importance of this work and found funding to support it. John Holland and Frank Hansen reviewed this report and provided useful feedback. Kirby Mellegard, Kerry DeVries, Stuart Buchholz, and Leo Van Sambeek at RESPEC also informally reviewed the work and gave thoughtful suggestions. Last, but not least, I would like to acknowledge my collaborators in Germany: Andreas Hampel, Klaus Salzer, Ralf-Michael Gunther, Christoph Lüdeling, Karl-Heinz Lux, Kai Herchen, Joachim Stahlmann, Andreas Gährken, Christian Missal, Savas Yildirim, Kurt Staudtmeister, and Alexandra Pudewillis. They have generously shared their knowledge, and graciously hosted me on my trips to Germany.

Contents

Appendix

List of Figures

List of Tables

Chapter 1

Introduction

1.1 Motivation

Thermo-mechanical simulations are an essential component of salt repository science. An excavated drift filled with nuclear waste (or other hazardous waste) will creep closed over the course of a few decades. Simulations play an important role in predicting the waste isolation process. Simulations also provide short-term predictions that are valuable to the operation and design of salt repositories. For example, operations personnel need to know how long they can operate in an area before it becomes unsafe. Simulations that include the disturbed rock zone can help predict when a slab of salt might detach from the roof and fall to the floor. As another example, repository operators may wish to backfill a large area with crushed salt or seal off a section of the repository. Many seal designs rely on drift closure to compress the seal, so simulations can help predict the seal maturation time. As one further example, engineers must consider operational efficiency, worker safety, environmental impact, costs, and many other factors when they lay out a repository design. Simulations of the underground evolution can be quite helpful to select between various design concepts. For these reasons and others, it is important to invest in geomechanical modeling tools.

This report documents Sandia's participation in Joint Project III and Joint Project WEIMOS. The Joint Projects are a collaboration between salt researchers in the United States and Germany. The participants calibrate their constitutive models for rock salt against laboratory tests, and benchmark the models against underground experiments. This process helps identify deficiencies in both the constitutive model and the methods used to simulate the underground experiments. Further research hopefully reduces existing discrepancies, and eventually leads to improved constitutive models and simulation techniques.

To date, the Joint Projects have primarily focused on predicting underground experiments in domal salt, rather than bedded salt. Each type of salt formation has advantages and disadvantages, so the Joint Project partners decided they wanted to exercise their models against *in -situ* experiments in bedded salt. Rooms B and D at the Waste Isolation Pilot Plant (WIPP) in south eastern New Mexico were a natural choice.

1.2 The Room B and Room D Experiments

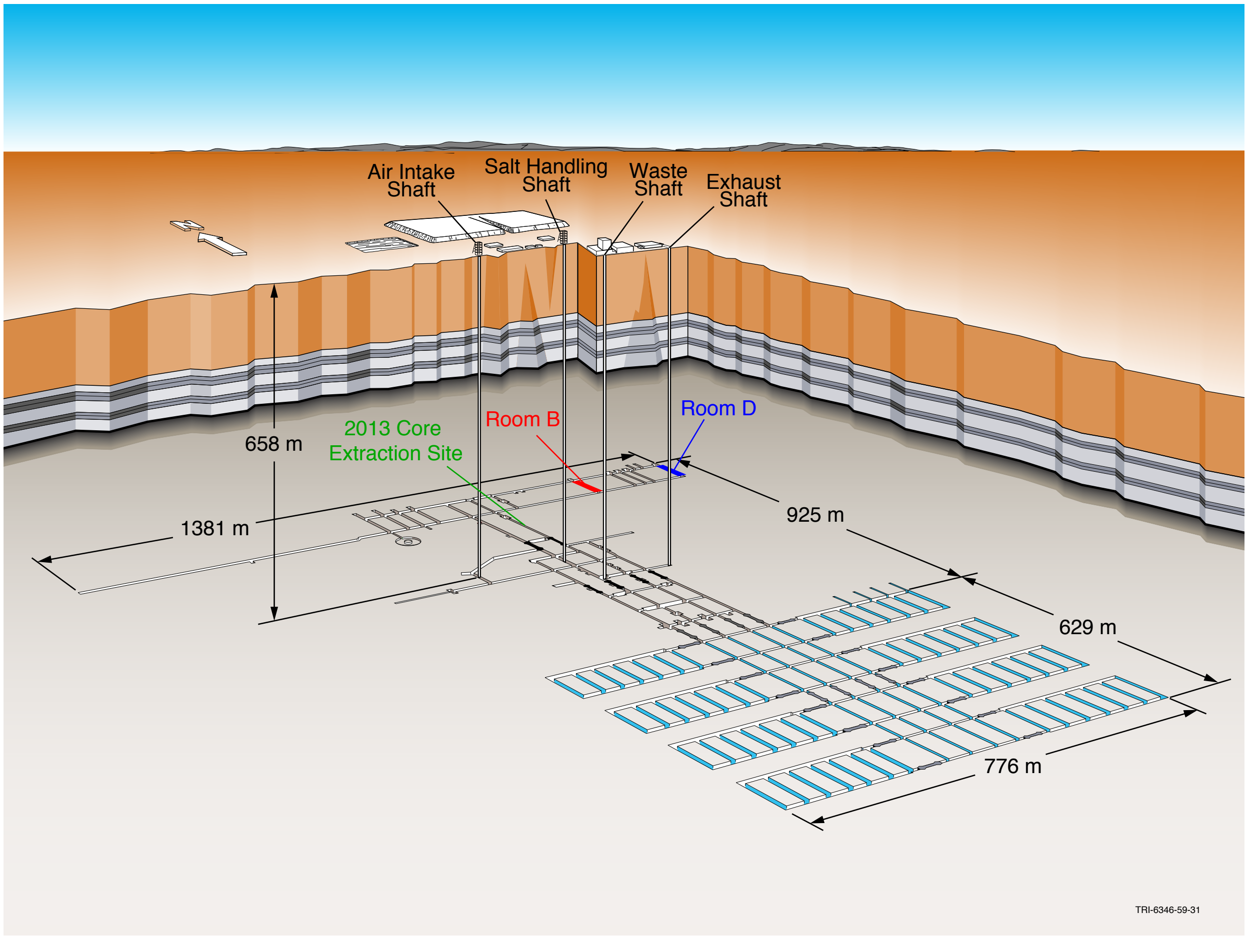

Figure 1.1: Locations of Room B and Room D at WIPP.

Rooms B and D are two drifts located in the northern experimental area at WIPP (see Fig. 1.1). The closure measurements from both rooms were used to validate the M-D model (*Munson et al.*, 1989, 1990a). Although the focus of this report is on Room D, the two were virtually identical for the first 354 days after excavation. At that point, Room B was heated to measure the closure at elevated temperatures, while Room D was left unheated.

As shown in Fig. 1.2, both rooms were designed to be long and slender. They were mined with a nominal width of 5.5 m, a height of 5.5 m, and a length of 93.3 m. This configuration was chosen so analysts could assume that a cross-section midway along the length of the room ($Y = 0$) deforms only in the X-Z plane (a plane strain analysis). After the excavation, an extensive effort confirmed that the actual, as-mined, dimensions of the room met the design tolerances (*Munson et al.*, 1987a). (A photo of a geotechnical team measuring the "as-built" cross section of Room D is shown in Fig. 1.3b.) Despite the thorough nature of this effort, the radius at the four corners of the room cross-section does not seem to be documented, even though the corners are clearly rounded in Fig. 1.3a. In lieu of such information, a 0.46 m radius was selected based on the 18 inch radius cutting head of the

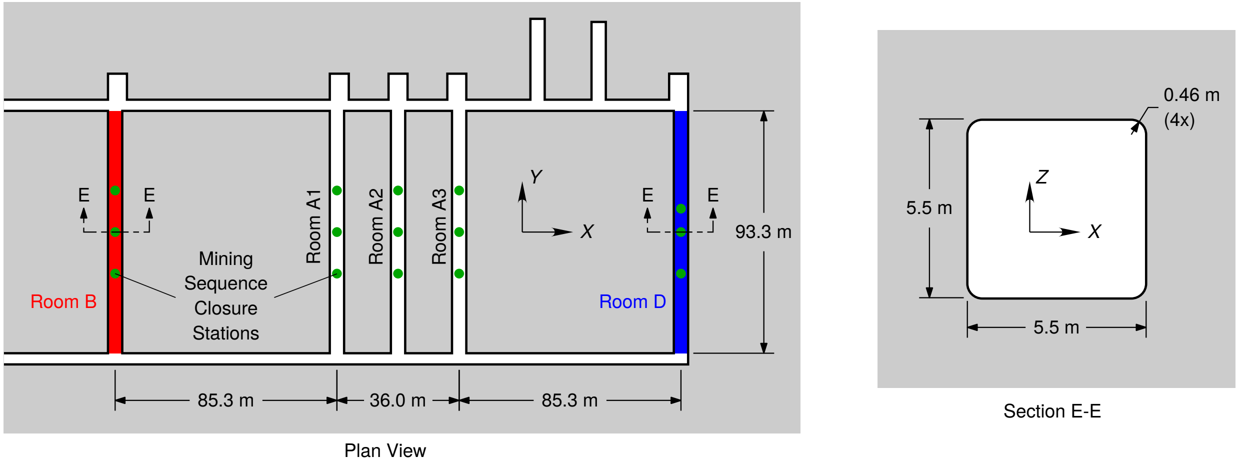

Figure 1.2: Room B and Room D dimensions

(a) Room B

(b) Room D

Figure 1.3: Photos of Room B being instrumented (*Munson et al.*, 1990b) and Room D being surveyed (*Munson et al.*, 1988).

Dosco roadheader miner used to finish the corners (*Carrasco*, 2015). *Herrick* (2015) verified this value by fitting circles to the measured profiles in *Munson et al.* (1987a).

Rooms B and D were carefully instrumented to capture the closure immediately after excavation and for years afterward. (See Fig. 1.3a for an image of instruments being installed in Room B.) The horizontal and vertical closure was measured at three closure stations along the rooms (see Fig. 1.2 for their approximate locations). The closure rate is always highest directly after a drift is excavated, so the mining sequence measurements of room closure were started within 30 minutes after the mining face passed a closure station. Typically, the mining face was still within 1 m of the closure station (*Munson et al.*, 1989). Details of the mining sequence data, as well as the data analysis, are reported in *Munson et al.* (1992). After Room D was excavated the mining sequence gages were replaced by temporary manual gages, then by permanent manual gages, and finally by remote gages. Details of the temporary, permanent, and remote gage data for Room D can be found in *Munson et al.* (1988).

The raw closure data for Room B and Room D was analyzed, resulting in the plots in Fig. 1.4. The experimental data was measured directly from an image of Fig. 3-5 in *Munson et al.* (1989) and an image of Fig. 2 in *Munson et al.* (1990a). The horizontal and vertical closure predictions are respectively normalized by the width L_h and height of the room L_v to give a sense of the closure relative to the room dimensions. Room B and Room D were both unheated for the first 354 days, so it is encouraging to see that they both have almost the same horizontal and vertical closure during this time. After 354 days, the heaters were turned on in Room B, causing the horizontal and vertical closure measurements to accelerate and deviate from Room D.

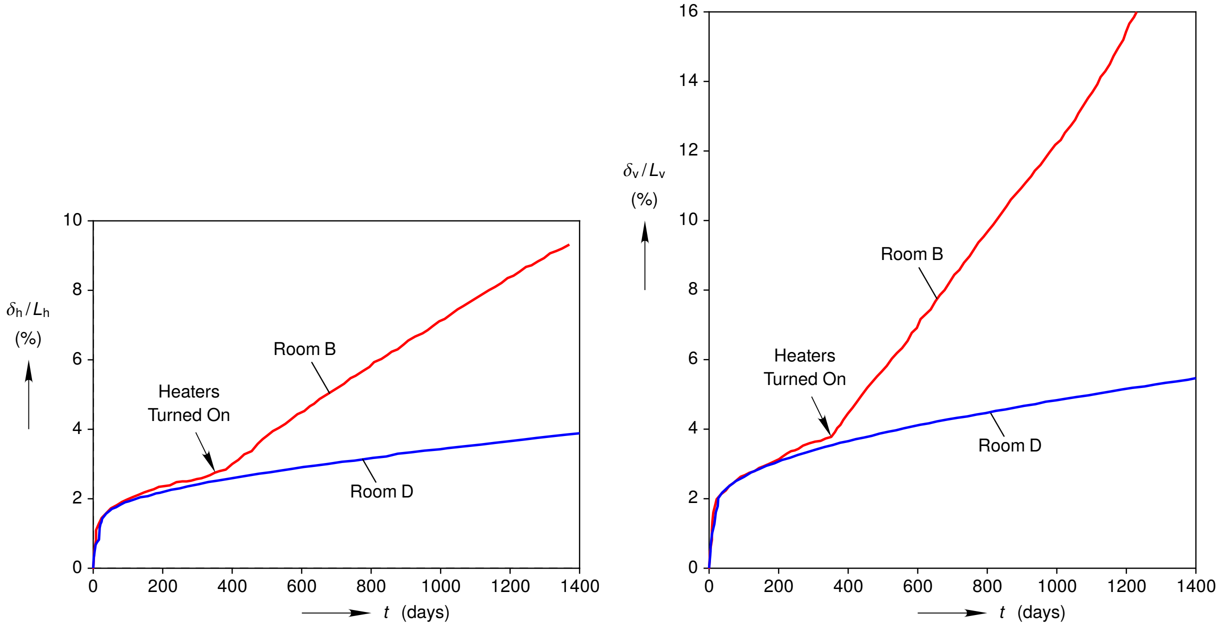

(a) Horizontal closure

(b) Vertical closure

Figure 1.4: Closure measurements of Room B and D. (Recreated from Figure 3-5 in *Munson et al.* (1989) and Figure 2 in *Munson et al.* (1990a))

1.3 Munson-Dawson Model

The Munson-Dawson (M-D) constitutive model for rock salt has been described in several reports over the last three decades (see *Munson et al.* (1989); *Munson* (1997); *Rath and Argüello* (2012), for example). The model is reviewed here because it is essential to the rest of this report, and a slightly different notation is used than in previous presentations.

The M-D model is an isotropic, hypoelastic, viscoplastic material model. The model additively decomposes the total strain rate $\dot{\boldsymbol{\varepsilon}}$ into an elastic strain rate $\dot{\boldsymbol{\varepsilon}}^{\mathrm{e}}$, a thermal strain rate $\dot{\boldsymbol{\varepsilon}}^{\mathrm{th}}$, and a viscoplastic strain rate $\dot{\boldsymbol{\varepsilon}}^{\mathrm{vp}}$:

$$\dot{\boldsymbol{\varepsilon}} = \dot{\boldsymbol{\varepsilon}}^{\mathrm{e}} + \dot{\boldsymbol{\varepsilon}}^{\mathrm{th}} + \dot{\boldsymbol{\varepsilon}}^{\mathrm{vp}}. \tag{1.1}$$

The hypoelastic portion of the M-D model utilizes the following simple linear relationship between the elastic strain rate $\dot{\boldsymbol{\varepsilon}}^{\mathrm{e}}$ and the stress rate $\dot{\boldsymbol{\sigma}}$,

$$\dot{\boldsymbol{\sigma}} = \boldsymbol{\mathcal{C}} : \dot{\boldsymbol{\varepsilon}}^{\mathrm{e}} \tag{1.2}$$

$$\boldsymbol{\mathcal{C}} = (B - 2/3\,\mu)\,\boldsymbol{I} \otimes \boldsymbol{I} + 2\,\mu\,\boldsymbol{\mathcal{I}}, \tag{1.3}$$

where $\boldsymbol{\mathcal{C}}$ is the fourth-order elastic stiffness tensor composed of the bulk modulus B, the shear modulus μ, the second-order identity tensor $\boldsymbol{I}$, and the forth-order symmetric identity tensor $\boldsymbol{\mathcal{I}}$. (As is common in the geomechanics literature, compressive stresses and strains are treated as positive.) The thermal strain portion of the model is simply

$$\dot{\boldsymbol{\varepsilon}}^{\mathrm{th}} = \alpha\,\dot{T}\,\boldsymbol{I} \tag{1.4}$$

where α is the coefficient of thermal expansion, and T is the temperature. The viscoplastic portion of the model captures the stress, time, and temperature dependence of plastic deformation. Plastic deformation of intact salt is isochoric and only occurs in the presence of shear stress. The M-D model's measure of shear stress is the Tresca equivalent stress

$$\bar{\sigma} = \max\left(|\sigma_1 - \sigma_2|,\ |\sigma_2 - \sigma_3|,\ |\sigma_3 - \sigma_1|\right), \tag{1.5}$$

where σ_i are the principal stresses. The viscoplastic strain evolves according to an associated flow rule

$$\dot{\boldsymbol{\varepsilon}}^{\mathrm{vp}} = \dot{\bar{\varepsilon}}^{\mathrm{vp}} \frac{\partial \bar{\sigma}}{\partial \boldsymbol{\sigma}}, \tag{1.6}$$

where $\dot{\bar{\varepsilon}}^{\mathrm{vp}}$ is the equivalent viscoplastic strain rate. It can be decomposed into two components

$$\dot{\bar{\varepsilon}}^{\mathrm{vp}} = \dot{\bar{\varepsilon}}^{\mathrm{tr}} + \dot{\bar{\varepsilon}}^{\mathrm{ss}}, \tag{1.7}$$

where $\dot{\bar{\varepsilon}}^{\mathrm{tr}}$ is the transient equivalent viscoplastic strain rate and $\dot{\bar{\varepsilon}}^{\mathrm{ss}}$ is the steady state equivalent viscoplastic strain rate.

The steady state behavior is modeled as a sum of three mechanisms, each of which vary with stress and temperarture:

$$\dot{\bar{\varepsilon}}^{\mathrm{ss}} = \sum_{i=0}^{3} \dot{\bar{\varepsilon}}_i^{\mathrm{ss}}, \tag{1.8}$$

where

$$\dot{\bar{\varepsilon}}_1^{\mathrm{ss}} = A_1 \exp\left(-\frac{Q_1}{RT}\right) \left(\frac{\bar{\sigma}}{\mu}\right)^{n_1}, \tag{1.9}$$

$$\dot{\bar{\varepsilon}}_2^{\mathrm{ss}} = A_2 \exp\left(-\frac{Q_2}{RT}\right) \left(\frac{\bar{\sigma}}{\mu}\right)^{n_2}, \tag{1.10}$$

$$\dot{\bar{\varepsilon}}_3^{\mathrm{ss}} = H(\bar{\sigma} - \bar{\sigma}_0) \left[B_1 \exp\left(-\frac{Q_1}{RT}\right) + B_2 \exp\left(-\frac{Q_2}{RT}\right)\right] \sinh\left(q \frac{(\bar{\sigma} - \bar{\sigma}_0)}{\mu}\right). \tag{1.11}$$

The variables A_i, B_i, Q_i, n_i, $\bar{\sigma}_0$, and q are all model parameters. All three mechanisms have an Arrhenius temperature dependence, where Q_i is an activation energy and $R = 8.314$ J/(K mol) is the universal gas constant. The first mechanism Eq. (1.9) is meant to capture dislocation climb, which dominates at high temperatures and low equivalent stresses. The second mechanism Eq. (1.10) dominates at low temperatures and low equivalent stresses. The micro-mechanical cause for the second mechanism is unknown, but cross-slip has been recently suggested (*Hansen*, 2014). Regardless, the macroscopic behavior corresponding to the second mechanism has been well characterized. The third mechanism Eq. (1.11) models dislocation glide, which is only activated when $\bar{\sigma}$ exceeds $\bar{\sigma}_0$, as reflected in the heaviside function $H(\bar{\sigma} - \bar{\sigma}_0)$.

The transient behavior is somewhat more complex than the steady-state because it involves an ordinary differential equation rather than the simple functional forms in Eqs. (1.9) to (1.11). During work hardening, $\bar{\varepsilon}^{\mathrm{tr}}$ approaches the transient strain limit $\bar{\varepsilon}^{\mathrm{tr}*}$ from below, and the creep strain rate slows down over time. (See Fig. 1.5b for an example.) During recovery, $\bar{\varepsilon}^{\mathrm{tr}}$ approaches $\bar{\varepsilon}^{\mathrm{tr}*}$ from above, and the creep strain rate speeds up over time. The value of $\bar{\varepsilon}^{\mathrm{tr}*}$ varies with temperature and stress as,

$$\bar{\varepsilon}^{\mathrm{tr}*} = K_0 \, \exp(c\,T) \left(\frac{\bar{\sigma}}{\mu}\right)^m, \tag{1.12}$$

where K_0, c, and m are parameters to be calibrated against experiments. The rate that $\bar{\varepsilon}^{\mathrm{tr}}$ approaches $\bar{\varepsilon}^{\mathrm{tr}*}$ is governed by

$$\dot{\bar{\varepsilon}}^{\mathrm{tr}} = (F - 1)\, \dot{\bar{\varepsilon}}^{\mathrm{ss}}, \tag{1.13}$$

where the proportionality $(F - 1)$ depends on whether the material is work hardening or recovering. These two behaviors are captured in the following equations

$$F = \begin{cases} \exp\left[\kappa_{\mathrm{h}} \left(1 - \frac{\bar{\varepsilon}^{\mathrm{tr}}}{\bar{\varepsilon}^{\mathrm{tr}*}}\right)^2\right] & \bar{\varepsilon}^{\mathrm{tr}} \leq \bar{\varepsilon}^{\mathrm{tr}*} \\ \exp\left[-\kappa_{\mathrm{r}} \left(1 - \frac{\bar{\varepsilon}^{\mathrm{tr}}}{\bar{\varepsilon}^{\mathrm{tr}*}}\right)^2\right] & \bar{\varepsilon}^{\mathrm{tr}} > \bar{\varepsilon}^{\mathrm{tr}*}. \end{cases} \tag{1.14}$$

The quantities κ_{h} and κ_{r} control how quickly the transient equivalent viscoplastic strain approaches the transient limit, for a given $\dot{\bar{\varepsilon}}^{\mathrm{ss}}$. These quantities vary with equivalent stress as,

$$\kappa_{\mathrm{h}} = \alpha_{\mathrm{h}} + \beta_{\mathrm{h}} \, \log_{10}\left(\frac{\bar{\sigma}}{\mu}\right), \tag{1.15}$$

$$\kappa_{\mathrm{r}} = \alpha_{\mathrm{r}} + \beta_{\mathrm{r}} \, \log_{10}\left(\frac{\bar{\sigma}}{\mu}\right), \tag{1.16}$$

where α_j and β_j are model parameters.

1.3.1 A Simple Analysis of a Triaxial Creep Test

A triaxial creep test is analyzed to make $\dot{\bar{\varepsilon}}^{\mathrm{ss}}$ and $\bar{\varepsilon}^{\mathrm{tr}}$ more concrete. The purpose of a triaxial creep test is to apply a known stress difference (a shear stress upon coordinate

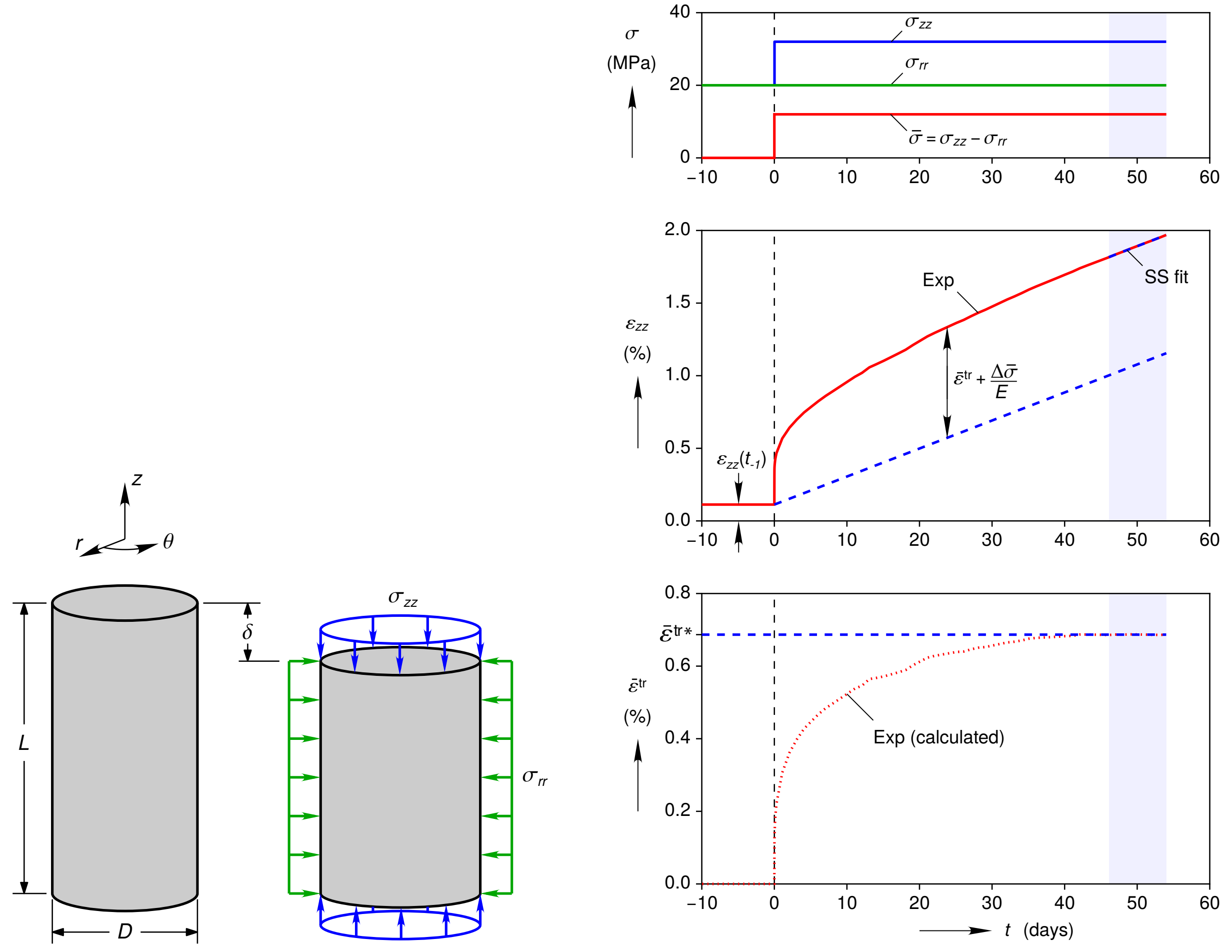

(a) Triaxial compression schematic

(b) Analysis of triaxial compression results

Figure 1.5: A simple triaxial creep experiment

transformation) and monitor the amount of creep strain. Fig. 1.5 depicts a triaxial creep specimen with a length to diameter ratio of $L/D = 2$ and results from a creep experiment. Specimens are placed in a triaxial cell in a specially outfitted load frame that allows the test operator to independently control the test temperature T, the axial Cauchy stress σ_{zz}, and the radial Cauchy stress σ_{rr}, while monitoring the axial strain. ε_{zz}. Usually, the axial log strain (positive in compression) is calculated from the axial compressive displacement of the platens δ as $\varepsilon_{zz} = \ln(1 + \delta/L)$. Although triaxial creep specimens can barrel outwards due to friction at the top and bottom platens, here the deformation and stresses are assumed to be spatially uniform. First, the temperature is raised to the test temperature and the hydrostatic pressure is raised to $\sigma_{rr} = \sigma_{zz} = 20$ MPa, causing a strain $\varepsilon_{zz}(t_{-1})$. At $t = t_0 = 0$, the axial stress is quickly raised to $\sigma_{zz} = 32$ MPa, changing $\bar{\sigma}$ from 0 to 12 MPa. This causes a rapid increase in the axial strain ε_{zz}. As the stress difference $\bar{\sigma}$ is held fixed for the next 53 days, the axial strain rate $\dot{\varepsilon}_{zz}$ slows down and eventually reaches a steady state rate.

The quantities $\dot{\bar{\varepsilon}}^{\mathrm{ss}}$ and $\bar{\varepsilon}^{\mathrm{tr}}$ can now be identified. The equation

$$\dot{\varepsilon}_{zz} = \dot{\varepsilon}^{\mathrm{e}}_{zz} + \dot{\varepsilon}^{\mathrm{th}}_{zz} + \dot{\bar{\varepsilon}}^{\mathrm{tr}} + \dot{\bar{\varepsilon}}^{\mathrm{ss}}. \tag{1.17}$$

results from combining Eqs. (1.1) and (1.5) to (1.7) and isolating the axial direction. For $t > t_0$ the thermal and elastic strain rates are zero ($\dot{\varepsilon}^{\mathrm{th}}_{zz} = \dot{\varepsilon}^{\mathrm{e}}_{zz} = 0$), which simplifies Eq. (1.17) further to

$$\dot{\varepsilon}_{zz} = \dot{\bar{\varepsilon}}^{\mathrm{tr}} + \dot{\bar{\varepsilon}}^{\mathrm{ss}}. \tag{1.18}$$

By the end of the experiment, Eq. (1.18) becomes $\dot{\varepsilon}_{zz} = \dot{\bar{\varepsilon}}^{\mathrm{ss}}$, because the transient strain rate is zero. In other words, $\dot{\bar{\varepsilon}}^{\mathrm{ss}}$ is the slope of the "SS fit" line in Fig. 1.5b. Let t_i^- be the instant in time immediately before t_i, and t_i^+ be the instant in time immediately after t_i. To find $\bar{\varepsilon}^{\mathrm{tr}}(t)$, integrate Eq. (1.18) from the initial time t_0^+ to the current time t, and rearrange to obtain

$$\bar{\varepsilon}^{\mathrm{tr}}(t) - \bar{\varepsilon}^{\mathrm{tr}}(t_0^+) = \left[\varepsilon_{zz}(t) - \varepsilon_{zz}(t_0^+)\right] - \left[\bar{\varepsilon}^{\mathrm{ss}}(t) - \bar{\varepsilon}^{\mathrm{ss}}(t_0^+)\right]. \tag{1.19}$$

The initial total strain at t_0^+ can be related back to the total strain at t_0^- as

$$\varepsilon_{zz}(t_0^+) = \varepsilon_{zz}(t_0^-) + \frac{\Delta\bar{\sigma}(t_0)}{E}, \tag{1.20}$$

where $\Delta\bar{\sigma}(t_0)$ is the change in equivalent stress at t_0 and $E = 9\,B\,\mu/(3\,B + \mu)$ is Young's modulus. The total strain $\varepsilon_{zz}(t_0^-)$ is simply $\varepsilon_{zz}(t_{-1})$, the thermal strain and elastic strain due to hydrostatic compression. The viscoplastic strain cannot immediately respond to a jump in stress, so $\bar{\varepsilon}^{\mathrm{tr}}(t_0^+) = \bar{\varepsilon}^{\mathrm{tr}}(t_0^-)$. The change in steady-state equivalent viscoplastic strain is

$$\bar{\varepsilon}^{\mathrm{ss}}(t) - \bar{\varepsilon}^{\mathrm{ss}}(t_0^+) = \dot{\bar{\varepsilon}}^{\mathrm{ss}}\,t, \tag{1.21}$$

because $\bar{\sigma}$ and T remain constant for $t > t_0$. Plugging these into Eq. (1.19) gives,

$$\bar{\varepsilon}^{\mathrm{tr}}(t) - \bar{\varepsilon}^{\mathrm{tr}}(t_0^-) = \left[\varepsilon_{zz}(t) - \varepsilon_{zz}(t_0^-)\right] - \frac{\Delta\bar{\sigma}(t_0)}{E} - \dot{\bar{\varepsilon}}^{\mathrm{ss}}\,t. \tag{1.22}$$

Typically, the specimen is *assumed* to be virgin, such that $\bar{\varepsilon}^{\mathrm{tr}}(t_0^-) = 0$. Equation Eq. (1.22) with $\bar{\varepsilon}^{\mathrm{tr}}(t_0^-) = 0$ is shown schematically in the ε_{zz} vs. t plot in Fig. 1.5b. The resulting $\bar{\varepsilon}^{\mathrm{tr}}(t)$ curve is shown in the plot below. As one might expect, the transient strain reaches a limiting value, labeled $\bar{\varepsilon}^{\mathrm{tr}*}$, once the creep curve reaches steady state.

The example in Fig. 1.5 only includes one step in $\bar{\sigma}$, but experimentalists often shift $\bar{\sigma}$ during a triaxial experiment. (See Fig. 3.3 for examples.) Measuring $\dot{\bar{\varepsilon}}^{\mathrm{ss}}$ after changing $\bar{\sigma}$ at an arbitrary time t_i is still just the slope of the ε_{zz} curve after the transient response has completed. Calculating $\bar{\varepsilon}^{\mathrm{tr}}(t)$ simply requires replacing t_0 with t_i in Eq. (1.22):

$$\bar{\varepsilon}^{\mathrm{tr}}(t) - \bar{\varepsilon}^{\mathrm{tr}}(t_i^-) = \left[\varepsilon_{zz}(t) - \varepsilon_{zz}(t_i^-)\right] - \frac{\Delta\bar{\sigma}(t_i)}{E} - \dot{\bar{\varepsilon}}^{\mathrm{ss}}\,t. \tag{1.23}$$

Of course, $\bar{\varepsilon}^{\mathrm{tr}}(t_i^-)$ is typically non-zero when $t_i \neq 0$.

1.3.2 Temperature and Stress Dependence

In an effort to make the equations that govern the steady-state strain rate and transient strain limit more familiar, they have been plotted in Figs. 1.6 and 1.7 for the (legacy) clean salt calibration in *Munson et al.* (1989).

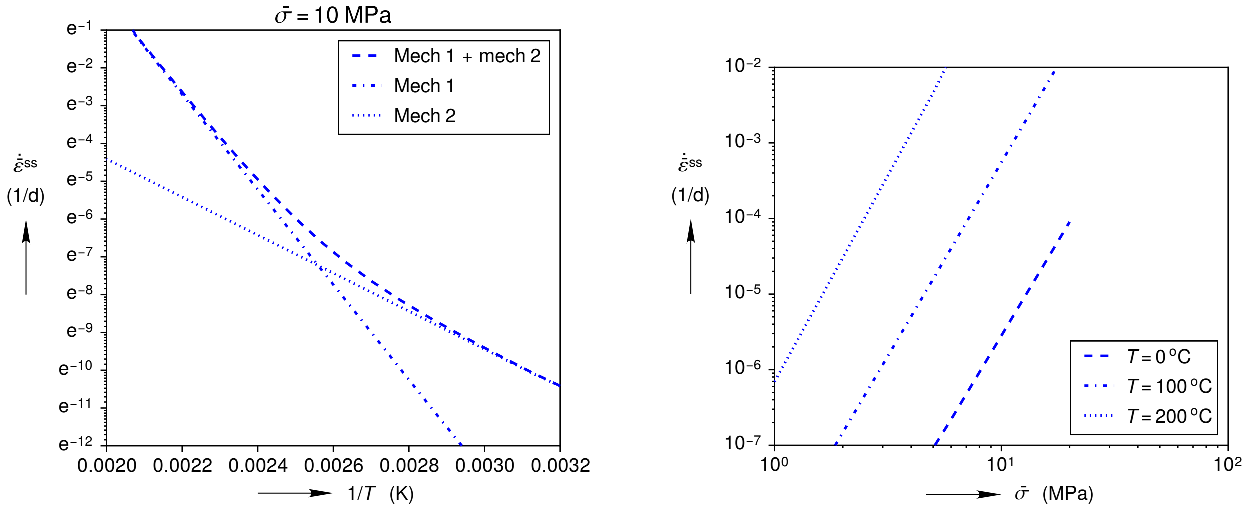

(a) Temperature Dependence

(b) Stress Dependence

Figure 1.6: Temperature and stress dependence of the steady-state strain rate for the (legacy) clean salt calibration in *Munson et al.* (1989).

Recall that the steady-state creep rate in the M-D model is a sum of three mechanisms. Dislocation climb (mechanism 1) dominates at high temperatures and low stresses, while the undefined mechanism (mechanism 2) dominates at low temperatures and low stresses. The third mechanism will be ignored for simplicity in this section. Taking the natural logarithm of both sides of Eq. (1.8) results in

$$\ln \dot{\bar{\varepsilon}}^{\mathrm{ss}} = \sum_{i=1}^{2} \left\{ \ln \left[A_i \left(\frac{\bar{\sigma}}{\mu} \right)^{n_i} \right] - \frac{Q_i}{RT} \right\} . \tag{1.24}$$

In Fig. 1.6a the steady state strain rate has been plotted with the individual mechanisms. In this plot, Eq. (1.24) is a straight line with slope Q_1/R at high temperatures, a straight line with slope Q_2/R at low temperatures, and a smooth curve connecting the lines in-between. One can also take the base 10 logarithm of Eq. (1.8) to obtain

$$\log_{10} \dot{\bar{\varepsilon}}^{\mathrm{ss}} = \sum_{i=1}^{2} \left\{ \log_{10} \left[\frac{A_i}{\mu^{n_i}} \exp \left(-\frac{Q_i}{RT} \right) \right] + n_i \log_{10} \bar{\sigma} \right\} . \tag{1.25}$$

In Fig. 1.6b, Eq. (1.25) is a straight line at a given temperature. Decreasing the temperature from 200 °C to 0 °C causes the slope to change from n_1 to n_2, but it also significantly reduces the height of the straight line. In summary, the Q_i control the temperature dependence, the n_i control the stress dependence, and the A_i shift the height of the lines.

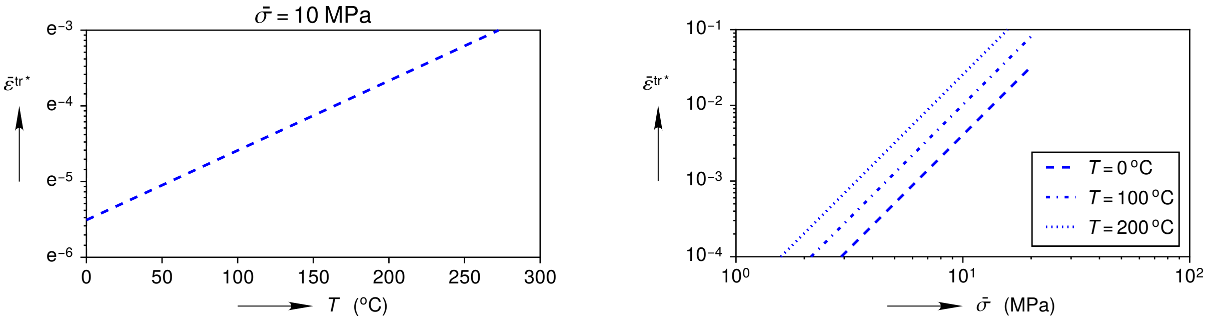

(a) Temperature Dependence

(b) Stress Dependence

Figure 1.7: Temperature and stress dependence of the transient strain limit for the (legacy) clean salt calibration in *Munson et al.* (1989).

The transient strain limit is more straightforward and will be included just for completeness. Applying a natural logarithm to Eq. (1.12) results in

$$\ln \bar{\varepsilon}^{\mathrm{tr}*} = \ln \left[K_0 \left(\frac{\bar{\sigma}}{\mu} \right)^m \right] + c\,T, \tag{1.26}$$

which produces a single straight line with slope c in Fig. 1.7a. Take the base 10 logarithm to Eq. (1.12) to obtain

$$\log_{10} \bar{\varepsilon}^{\mathrm{tr}*} = \log_{10} \left[\frac{K_0}{\mu^m} \exp\left[c\,T\right] \right] + m\,\bar{\sigma}. \tag{1.27}$$

Equation (1.27) produces the straight lines with slope m in Fig. 1.7b. Lowering the temperature still lowers the height of the lines, but less so than in Fig. 1.6b for this particular calibration. To summarize, c controls the temperature dependence, m controls the stress dependence, and K_0 controls the height of the lines.

1.4 Legacy Simulations

This section reviews the legacy closure simulations of Room D. The initial attempt to simulate the closure of Room D is discussed first, followed by the changes that improved the agreement between the simulations and the experiments.

1.4.1 Initial Room D Simulation

Early on in the WIPP project, thermal and structural analysts would each build their own model. Between 1979 and 1983, a series of meetings was held between the Department of Energy, Bechtel, TSC/D'Appolonia, and Sandia to establish a stratigraphy and a set of material models to use. This culminated in the 1983 reference (*Krieg*, 1984), which

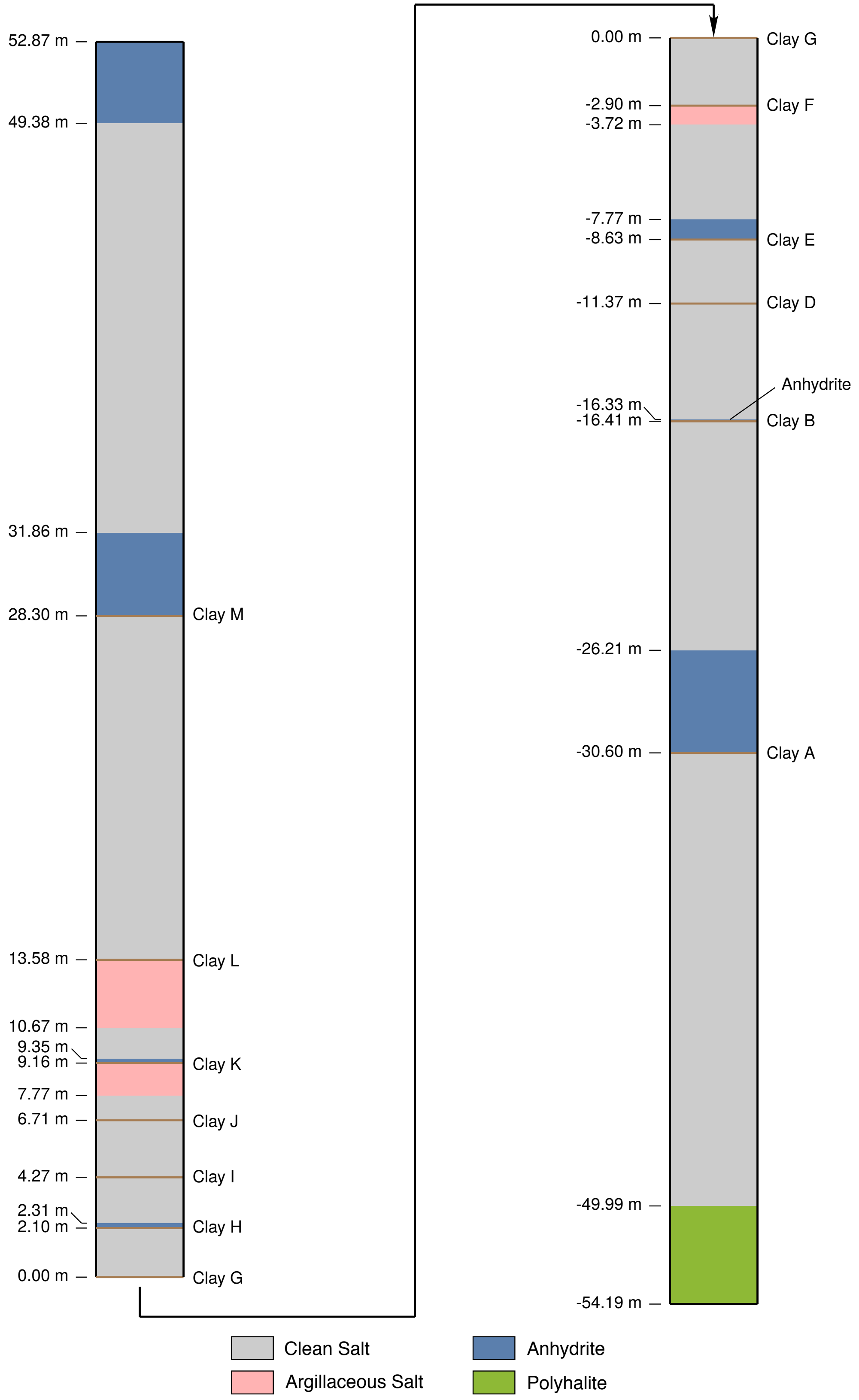

Figure 1.8: 1983 reference stratigraphy. (Recreated from Figure 5 in *Krieg* (1984))

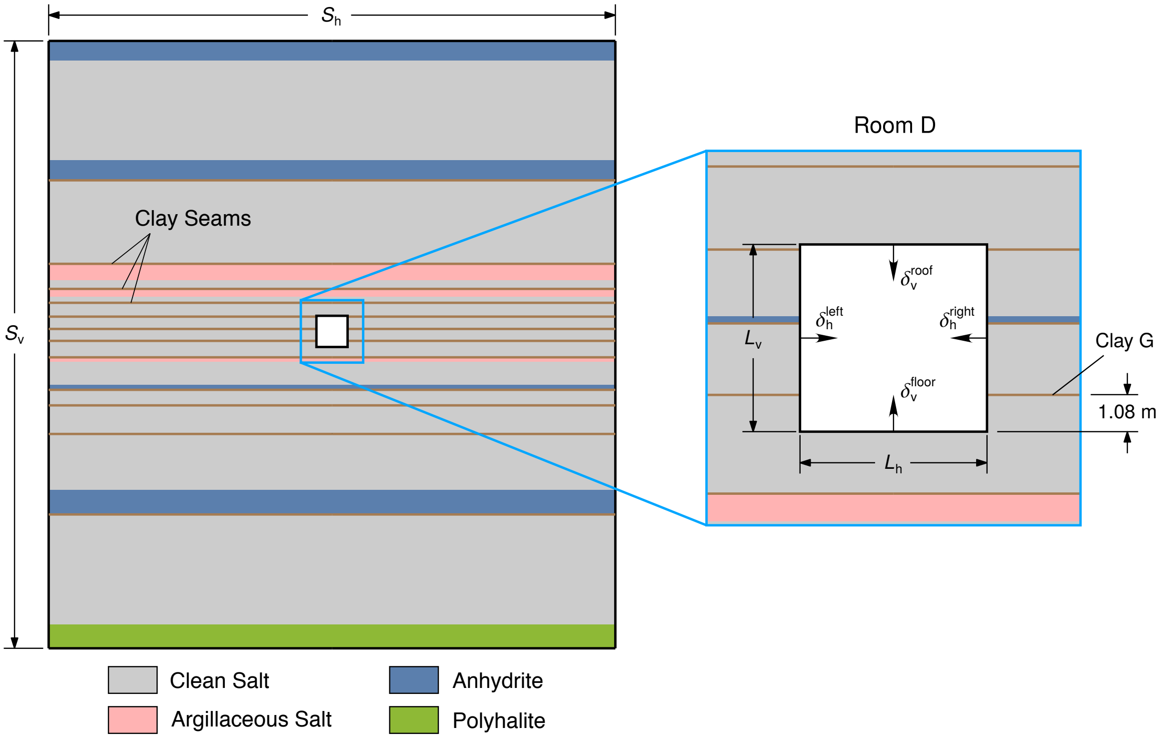

Figure 1.9: Model dimensions. (Recreated from Figure 9 in *Munson et al.* (1986).)

specified a reference stratigraphy, and a group of reference material models. The agreed-upon idealization of the actual stratigraphy at WIPP is shown in Fig. 1.8. Layers are color coded as to whether they are clean salt, argillaceous salt, anhydrite, or polyhalite. Some layers have clay seams between them, marked with brown lines. All elevations are referenced off of clay seam G, which is about 648 m beneath the surface (*Munson et al.*, 1988). The material models and material parameters in the 1983 reference were not expected to be the final values, but analysts were expected to provide justifications for changing them. For instance, soon after the 1983 reference was established, a memo (*Morgan and Krieg*, 1984) updated the Drucker-Prager constants for the anhydrite and polyhalite based on a collection of experimental data.

The first published simulation of Room D (*Munson et al.*, 1986) was faithful to the 1983 reference. The calculations were performed using SANCHO (*Stone*, 1997b), a two-dimensional, large deformation, finite element code. A schematic of Room D in relation to the 1983 reference stratigraphy is shown in Fig. 1.9. The configuration was assumed to be sufficiently long in the Y-direction (into the page) to be approximated by the plane strain condition. The overall width and height of the simulated area were $S_\mathrm{h} = 100$ m, and $S_\mathrm{v} = 107$ m. The width and height of Room D were $L_\mathrm{h} = 5.5$ m and $L_\mathrm{v} = 5.5$ m, respectively, and the floor of Room D was 1.08 m beneath clay seam G. The horizontal displacement of the left wall $\delta_\mathrm{h}^\mathrm{left}$ and the the right wall $\delta_\mathrm{h}^\mathrm{right}$, as well as the vertical displacement of the floor $\delta_\mathrm{v}^\mathrm{floor}$ and the roof $\delta_\mathrm{v}^\mathrm{roof}$ are shown in Fig. 1.9. These are used to define the horizontal and

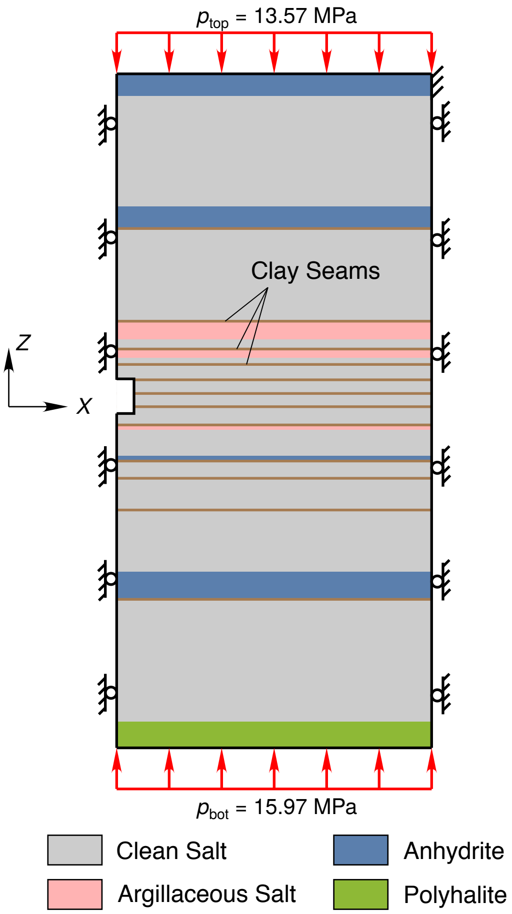

Figure 1.10: Legacy model boundary conditions (Recreated from Figure 9 in *Munson et al.* (1986)).

vertical closure of the room as

$$\delta_{\mathrm{h}} = \delta_{\mathrm{h}}^{\mathrm{left}} + \delta_{\mathrm{h}}^{\mathrm{right}}, \tag{1.28}$$

$$\delta_{\mathrm{v}} = \delta_{\mathrm{v}}^{\mathrm{floor}} + \delta_{\mathrm{v}}^{\mathrm{roof}}. \tag{1.29}$$

The room corners were sharp in Fig. 1.9 instead of the rounded corners shown in Fig. 1.2. The density of the clean salt, argillaceous salt, anhydrite, and polyhalite was taken as $\rho = 2,300\ \mathrm{kg/m^3}$, and the acceleration due to gravity was taken as $g = 9.79\ \mathrm{m/s^2}$. The boundary conditions are shown in Fig. 1.10. A mirror boundary condition was assumed on the left side, reducing the width of the finite element model to $S_{\mathrm{h}}/2$. The right side of the model was deemed far enough away from Room D to place rollers on the right boundary. The pressure applied to the top surface was $p_{\mathrm{top}} = 13.57$ MPa. The pressure applied to the bottom surface $p_{\mathrm{bot}} = 15.97$ MPa represented the overburden minus the missing rock from Room D. All material points were initialized with a hydrostatic stress state that varied linearly from p_{top} at the top of the model to p_{bot} at the bottom of the model. The room was assumed to appear instantaneously as a void at time $t = 0$, rather than modeling the excavation process. For simplicity, the rock mass temperature was assumed to be spatially constant at

300 K. The lateral sliding of the layers on either side of a clay seam were modeled using Coulomb friction, with a friction coefficient of $\eta = 0.4$. The salt was modeled using the secondary creep law and parameter set specified in the 1983 reference. Both the argillaceous and clean salt used the same set of parameters. The anhydrite and polyhalite were modeled with a hypoelastic, perfectly plastic, Drucker-Prager model with a non-associated flow rule (see Appendix A.1 for further details).

This first simulation of the Room D closure compared quite poorly against the experimental measurements. In Fig. 1.11, the vertical closure prediction is labeled as "Reference Law" and the measured vertical closure at the central station for Room D is labeled as "Manual Data" and "Remote Data". On the whole, the lack of agreement appears to due to an under-prediction of the transient strain. After only 50 days, the simulation under-predicts the vertical closure by 8.4×. After 500 days, as the salt creep transitions toward steady state behavior, the discrepancy reduces to 4.6×.

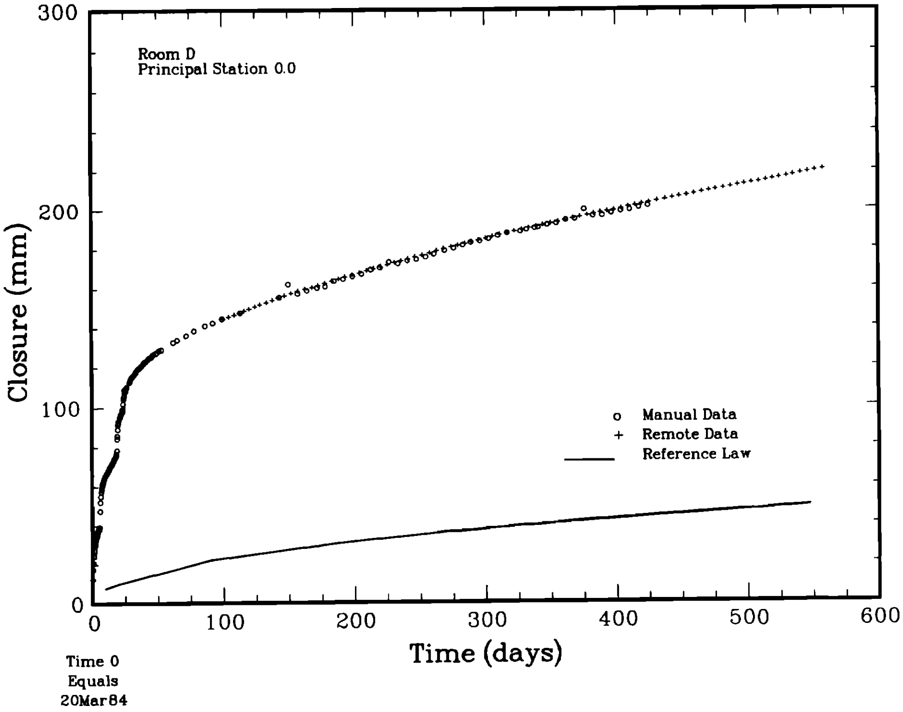

Figure 1.11: Initial predictions of Room D vertical closure (solid line) compared against closure measurements (markers) (*Munson et al.*, 1986).

1.4.2 Changes made by *Munson et al.* (1989)

The inability to predict *in-situ* test results, such as those in Fig. 1.11, caused much consternation in the WIPP Thermal/Structural Interactions program. Similar disparities were found when comparing the South Drift closure measurements against simulations using the 1983 reference salt model (*Morgan et al.*, 1985, 1986) and the M-D model (*Munson and*

Fossum, 1986). *Morgan et al.* (1985, 1986) showed through a parametric study that the discrepancy could not be due to known uncertainties in the salt material parameters, the anhydrite material parameters, the clay seam friction value, and several other items. *Munson et al.* (1987b) investigated reducing the, laboratory measured, elastic moduli, because reductions of μ in Eqs. (1.9) to (1.12) increase $\dot{\bar{\varepsilon}}^{\mathrm{ss}}$ and $\bar{\varepsilon}^{\mathrm{tr}}$. They first decreased the moduli by a factor of 12.5 to match the horizontal closure of the South Drift. Using the decreased moduli, they then calculated closures of Room D that were in reasonable agreement with the measurements. This approach, however, was deemed "not acceptable from the standpoint of obtaining a predictive capability since the reduced moduli values cannot be substantiated by laboratory tests" (*Munson et al.*, 1989).

In an attempt to put the modeling on a stronger physical foundation, *Munson et al.* (1989) elected to make six significant changes to improve the match between the simulations and the measured closures of Room D.

1. *Munson et al.* (1989) switched from the von Mises equivalent stress to the Tresca equivalent stress shown in Eq. (1.5). As shown in the π-plane plot in Fig. 1.12a, the maximum difference between these two equivalent stress measures is only 15.5 %, so one might not expect a large impact on the room closure. This difference, however, gets amplified by the exponents in Eqs. (1.9) to (1.12). For example, typically $n_2 \approx 5$, so a 15.5 % increase in $\bar{\sigma}$ causes a 2.05× increase in $\dot{\bar{\varepsilon}}_2^{\mathrm{ss}}$. *Munson et al.* (1989) justified the switch to the Tresca equivalent stress by inspecting measurements on hollow cylinders of Avery Island rock salt subjected to axial compression, internal pressurization, and external pressurization

2. *Munson et al.* (1989) reduced the coefficient of friction at the clay seams from 0.4 to 0.2 (see Fig. 1.12b), based on engineering judgement. They candidly stated that the coefficient of friction was "a free parameter" of the model.

3. *Munson et al.* (1989) altered the room temperature portion of the clean salt M-D model calibration. They justified altering the original clean salt calibration (*Munson and Dawson*, 1979, 1982) based on new creep tests in *Senseny* (1986) and new, unpublished, creep tests that were later documented in *Senseny* (1990)[1]. The new triaxial creep tests were preferred over the old tests because Senseny was careful to retain the "loading strains" due to applying triaxial stresses at the start of the experiments. Three ERDA-9-D specimens from *Senseny* (1990) were thought to be close approximations to virgin salt because they came from borehole cores rather than drift cores. The drift core specimens in *Senseny* (1986) were extracted months, if not years, after the drifts were excavated. The salt surrounding the drift experienced a significant amount of deformation between drift excavation and core extraction. This "excavation hardening" was thought to cause the $\bar{\varepsilon}^{\mathrm{tr}*}$ values measured on drift core specimens to be lower than

---

[1] *Munson et al.* (1989) cites "Private Communication" with Paul Senseny for creep tests on specimens from the ERDA-9 core at the horizon of Room D. The three ERDA-9-D $\bar{\varepsilon}^{\mathrm{tr}*}$ values in Figure 2-11 of *Munson et al.* (1989) match the three ERDA-9 $\bar{\varepsilon}^{\mathrm{tr}*}$ values for specimen ID 2127, 2124, and 2126 in Table 4-1 of *Senseny* (1990).

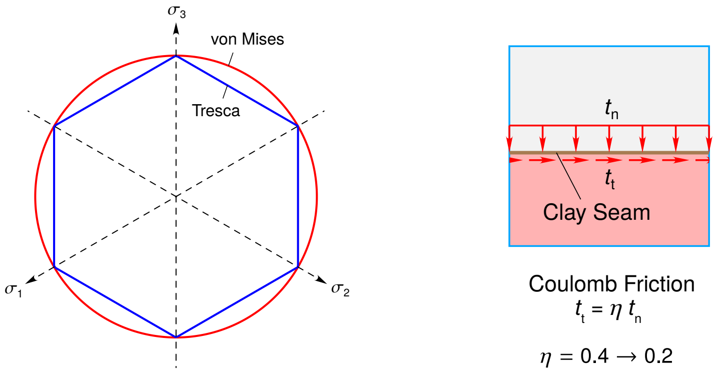

(a) Equivalent stress measure change

(b) Friction coefficient change

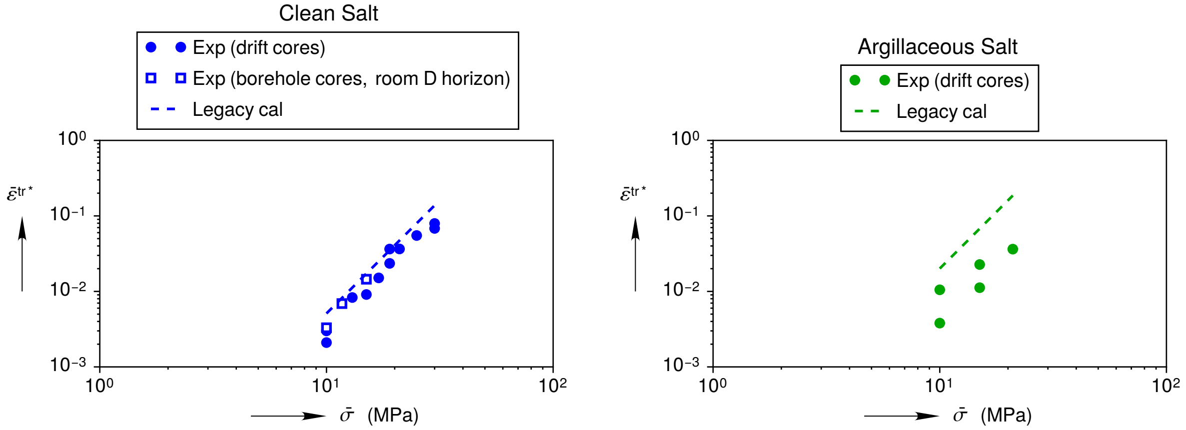

(c) Material model calibration change

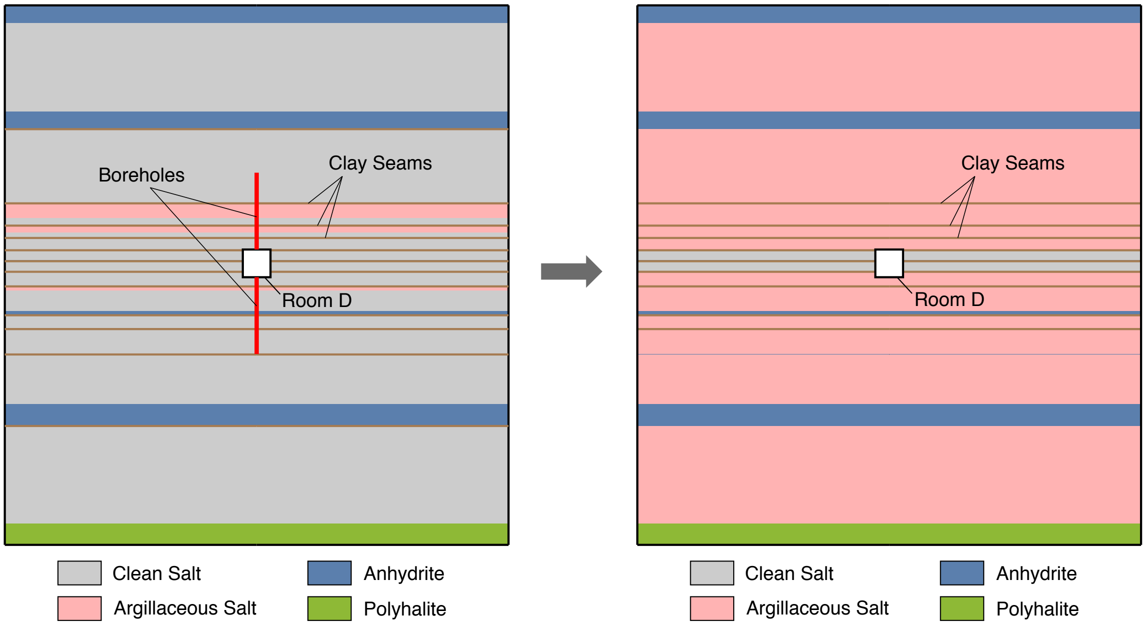

(d) Stratigraphy change

Figure 1.12: Summary of five out of the six modifications made in *Munson et al.* (1989).

virgin values. Thus, *Munson et al.* (1989) chose $K_0 = 6.275 \times 10^5$ for the clean salt, which placed the dashed line at the upper edge of the clean salt experimental data in Fig. 1.12c.

4. *Munson et al.* (1989) created a new argillaceous salt M-D model calibration, because *Senseny* (1986) also found that the argillaceous salt specimens crept more than the clean salt specimens. For the argillaceous salt, they chose $K_0 = 2.470 \times 10^6$, which placed the dashed line above the five data points in Fig. 1.12c. To justify the argillaceous K_0, *Munson et al.* (1989) state that they did not have any fresh, argillaceous, borehole specimens from the Room D horizon to limit the value of K_0. In other words, the argillaceous K_0 was treated as another "free parameter" of the model.

5. *Munson et al.* (1989) changed nearly all the clean salt in the 1983 reference stratigraphy to argillaceous salt, as demonstrated in Fig. 1.12d. Only the salt between clay I and clay G was left as clean salt. To justify the change, they state that boreholes were drilled 15.2 m into the roof of Room D and 15.2 m into the floor of Room D, and both cores appeared to be argillaceous to the eye. No composition measurements or creep tests were made to confirm this assertion. Furthermore, they simply assumed that all salt beyond the aforementioned 15.2 m boreholes was argillaceous.

6. *Munson et al.* (1989) chose not to model the anhydrite or polyhalite layers "[b]ecause these layers are either sufficiently thin to be insignificant in the calculational response or are sufficiently removed from the room being simulated to be quite uninfluential in the calculational response". It is not clear whether they modeled the anhydrite layers as clean salt or argillaceous salt.

Besides the six changes, a few other details are worth mentioning. First, in addition to switching to the Tresca equivalent stress, *Munson et al.* (1989) also added an exponent of 2 to $(1 - \bar{\varepsilon}^{\text{tr}}/\bar{\varepsilon}^{\text{tr}*})^2$ in Eq. (1.14). Second, of the twelve clay seams labeled in Fig. 1.8, only the nine nearest the room, labeled D through L, were allowed to slide. (Presumably, preliminary studies found that seams A, B, and M did not slide enough to be worth the computational expense.) Third, *Munson et al.* (1989) did not show the finite element mesh they used, but it was probably similar to the Room B pretest simulations (see Figure 7 in *Morgan and Stone* (1985)). Finally, the simulations were run in SPECTROM-32 (*Callahan et al.*, 1986), a two-dimensional, small-strain finite element code.

The new predictions are shown in Fig. 1.13, and the results were described as follows: "In view of the complexity of this calculation, the agreement between calculation and measurement is, we believe, exceptional. These results simulate the measured data much more exactly than any previous reference calculation. The agreement between calculated and measured vertical closure is so close, about 2%, in magnitude and form that little can be said. However, there remains enough uncertainty in the exact values of the argillaceous transient strain limit and the clay seam coefficient of friction that the closeness of the calculation to the measured closure is better than could be expected." Note that the underline of the last sentence was not added by the current author. It was copied verbatim from *Munson et al.* (1989). The report ends with, "In summary, the results of this work suggest a relatively large

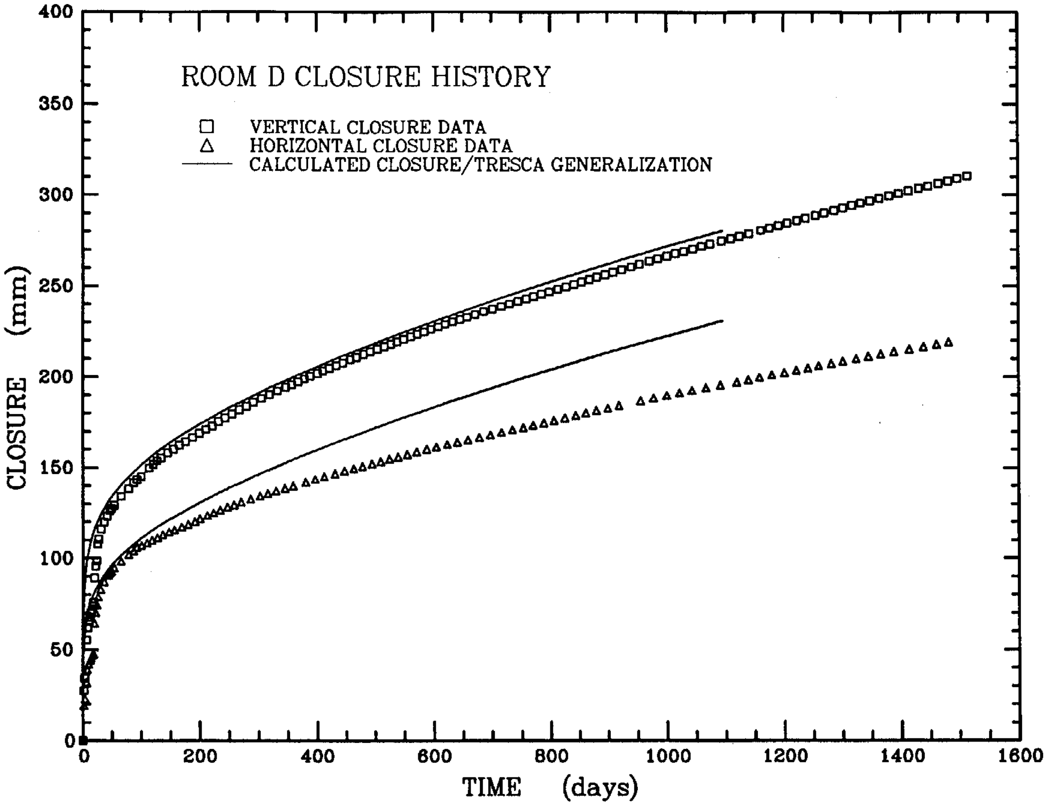

Figure 1.13: Predictions of Room D horizontal and vertical closure after the modifications in summarized in Fig. 1.12, (*Munson et al.*, 1989).

stride has been taken in the development of the predictive technology for the structural response of salt." Thus, they felt relatively certain they were moving in the right direction, but willing to admit that further work needed to be done to reduce uncertainties.

In the end, the changes proposed by *Munson et al.* (1989) were accepted. A series of simulations used the *Munson et al.* (1989) changes to predict the closure in the Room A series, Room B, Room G, Room Q, the air intake shaft, and an intermediate scale borehole test. As summarized in *Munson* (1997), these simulations agree remarkably well with the measured closures. The M-D model calibrations and a simplified version of the stratigraphy were used in the final simulations of the waste disposal rooms at WIPP (*Stone*, 1997a) and listed in a summary of the input parameter values for WIPP calculations (*Butcher*, 1997). Note that from here forward, the mesh, boundary conditions, material model calibrations, etc. used in *Munson et al.* (1989) will be referred to as the legacy mesh, legacy boundary conditions, legacy calibrations, etc.

Chapter 2

Revisiting the Legacy Simulations

2.1 Recent Simulations of Room D

Study of Room D (and Room B) has been reignited in recent years by Joint Project III and Joint Project WEIMOS. As a first step, *Rath and Argüello* (2012); *Argüello and Rath* (2013); *Argüello and Holland* (2015); *Argüello* (2015) attempted to recreate the simulations in *Munson et al.* (1989) using Sierra/Solid Mechanics, a large deformation, finite element code. The results of those simulations can be found in the aforementioned reports, but the relevant simulations from *Argüello and Holland* (2015); *Argüello* (2015) were reran using the latest version of Sierra/Solid Mechanics (*Sierra/Solid Mechanics*, 2016), in order to have the results available for post-processing. Besides increasing the simulation time to 1,354 days, the exact same input files were used.

Although the simulation inputs followed *Munson et al.* (1989) as faithfully as possible, the model of Room D will be quickly reviewed for completeness. The stratigraphy, boundary conditions, and meshes are shown in Fig. 2.1. Only clay seams D through L were active. *Munson et al.* (1989) did not show their finite element mesh, so the mesh in Fig. 2.1b was made to match the mesh in Fig. 7 of *Morgan and Stone* (1985), with six elements across the half-width of the room. The mesh is a single layer of hexahedral elements because Sierra/Solid Mechanics does not have two-dimensional plane strain elements. As such, the Y displacements of the front and back surfaces of the single layer were held to zero. The simulations used the mean quadrature hexahedral element with hourglass scaling after rotations and midpoint strain incrementation (*Sierra/Solid Mechanics*, 2016). As before, $\rho = 2,300$ kg/m^3, $g = 9.79$ m/s^2, and $T = 300$ K over the whole model. All material points were initialized with a hydrostatic stress state that varied linearly from p_{top} to p_{bot}. The room was treated as a void that appeared instantaneously at time $t = 0$. The clean and argillaceous salt were both simulated using the Crushed Salt model (*Callahan*, 1999) specialized to be intact salt, which reduces to the M-D model. The material parameters for both salt types are provided as the legacy calibrations in Table 3.1 of Chapter 3, and the Sierra input syntax is listed in Appendices A.2.2 and A.2.3. Anhydrite and polyhalite were both simulated using the Soil and Crushable Foam model (*Sierra/Solid Mechanics*, 2016) specialized to be an elastic, perfectly plastic, Drucker-Prager model. See Appendix A.1 for further details on the model formulation, and see Appendices A.2.4 and A.2.5 for the Sierra input syntax. The clay seam friction coefficient was $\eta = 0.2$.

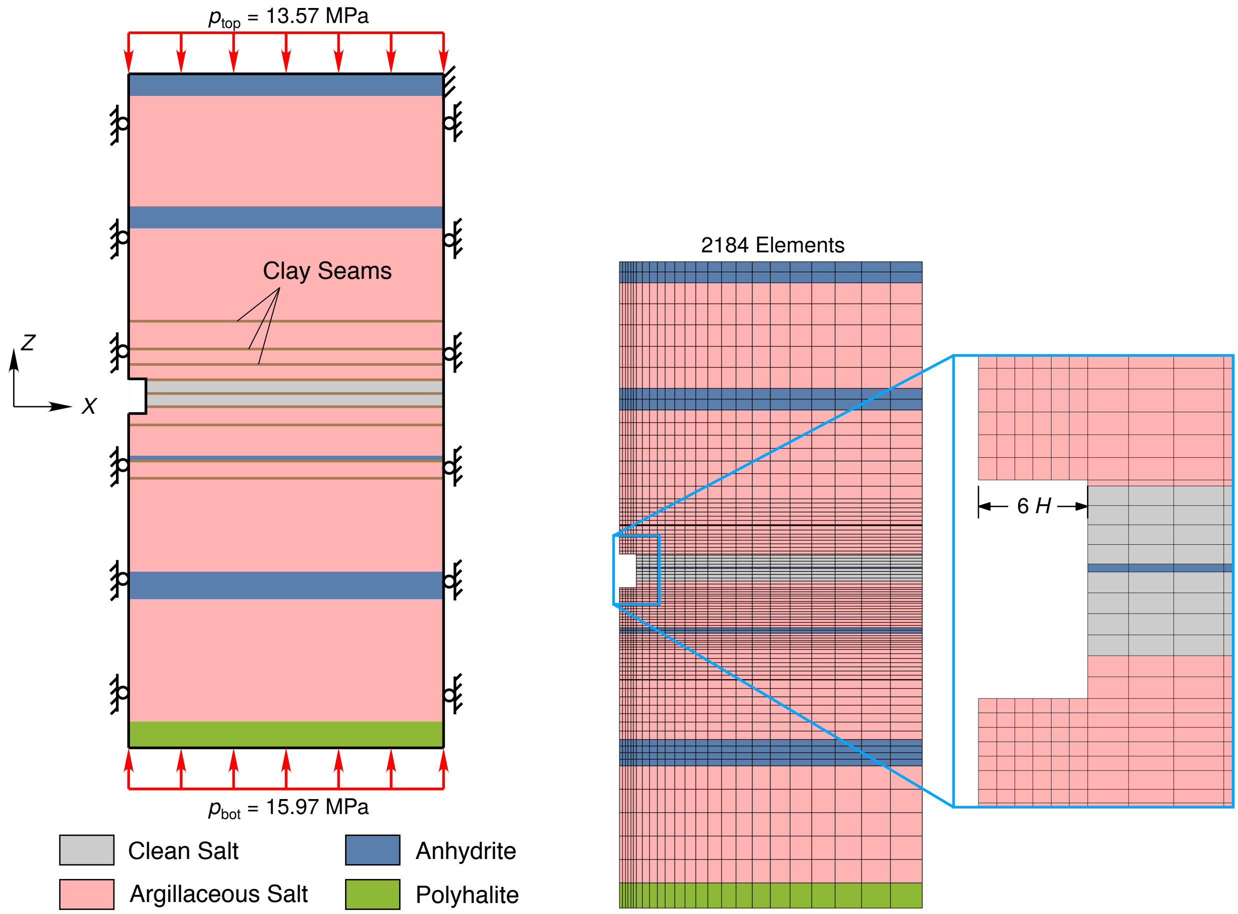

(a) Legacy stratigraphy and legacy boundary conditions

(b) Legacy mesh

Figure 2.1: Stratigraphy, boundary conditions, and mesh used to recreate the legacy simulations.

An implicit multi-level solver (*Sierra/Solid Mechanics*, 2016) was used to solve the discretized equilibrium equations. The inner loop utilized a conjugate gradient solver for the equilibrium equations, with the contact interactions held fixed. The outer loop utilized the Kinematic algorithm to resolve the contact interactions, with the nodal displacements outside of the contact zone held fixed. The tolerance on the outer loop relative residual norm was $R_{\text{tol}} = 10^{-3}$. The relative residual norm was defined as the L_2 norm of the total residual divided by the L_2 norm of the externally applied traction boundary conditions. The initial time step was 10^{-6} s, but this was allowed to grow as much as 5 % per time step.

Closure predictions from these simulations are compared against experimental data and legacy predictions in Fig. 2.2. Recall that legacy simulations of Room D did not include anhydrite or polyhalite, so the legacy recreated, all salt, simulation should be compared against the legacy results. *Munson et al.* (1989) did not state whether they treated the anhydrite and polyhalite as clean salt or argillaceous salt, so *Argüello and Holland* (2015); *Argüello* (2015) chose to treat those layers as clean salt. The recreated horizontal closure prediction

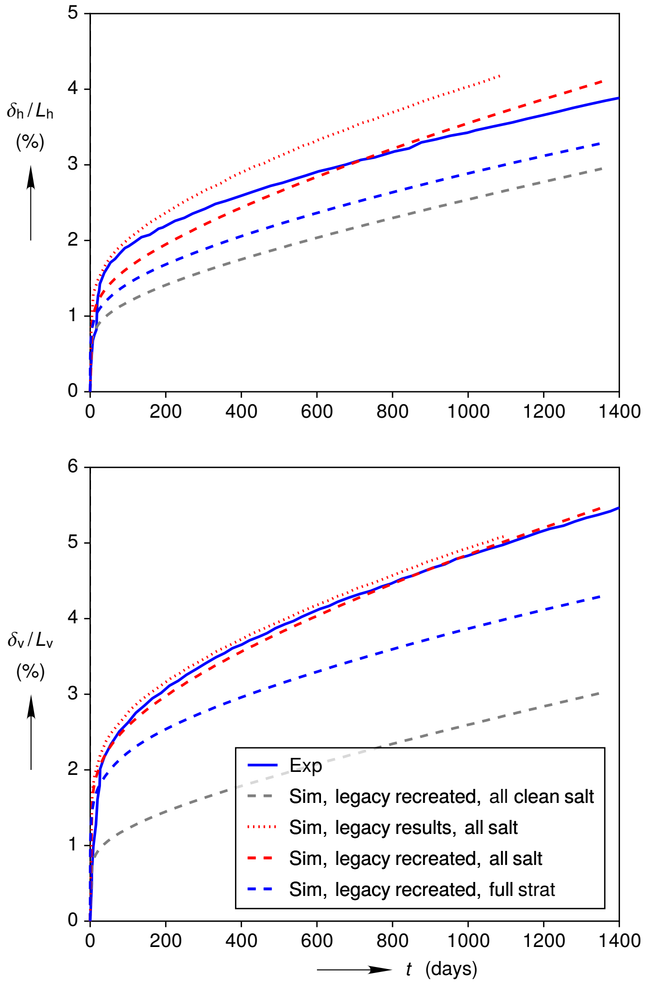

Figure 2.2: Predictions and experimental measurements of Room D horizontal and vertical closure. The legacy closure prediction (*Munson et al.*, 1989), which treated all geomaterials as salt, is compared against a recreation of the legacy prediction, as well as predictions from two other stratigraphies.

is low compared to the legacy, but the vertical closure prediction is quite close to the legacy. This difference may be due to the way that SPECTROM-32 and Sierra/Solid Mechanics handle sliding at the clay seams, because the horizontal closure should be more sensitive to the clay seams than the vertical. *Morgan et al.* (1987) performed a benchmarking exercise between different finite element codes, and traced back discrepancies between SANCHO and SPECTROM-32 to the sliding algorithms. Regardless, the agreement between the legacy predictions and the legacy recreated, all salt, predictions is fairly repeatable considering that about 25 years separates the two finite element simulations.

The legacy recreated closure predictions in Fig. 2.2 show a significant sensitivity to the stratigraphy being modeled. Comparing the all clean salt and all salt closure predictions shows the large impact of the separate argillaceous salt calibration created in *Munson et al.* (1989). The horizontal closure increases by 39 % and the vertical closure increases by 81 %

at $t = 1,354$ days. Comparing the all salt and full stratigraphy closure prediction displays the impact of the anhydrite and polyhalite layers. The anhydrite and polyhalite decrease both the horizontal and vertical closures by about 20 % at $t = 1,354$ days. As noted in *Argüello and Holland* (2015); *Argüello* (2015), this result refutes the assumption in *Munson et al.* (1989) that the anhydrite and polyhalite layers are negligible.

The mesh in Fig. 2.1b was chosen to match the mesh that *Munson et al.* (1989) most likely used, but it is quite coarse, so *Argüello* (2015) ran a preliminary study to assess sensitivity to element size. He ran full stratigraphy simulations using meshes with 2184, 17298, 29748, and 81042 elements, but he did not observe mesh convergence. The vertical room closure predictions continued to be appreciably more compliant as the mesh was refined, causing *Argüello* (2015) to recommend a formal mesh convergence study.

2.2 Resolving the Numerics

Several numerical modeling choices in *Argüello* (2015) were refined in preparation for the formal mesh convergence study described here.

1. The relative residual tolerance was tightened from $R_{\mathrm{tol}} = 10^{-3}$ to 10^{-5}. This value was chosen based on a previous study (*Reedlunn*, 2013) of the Mindlin problem, a canonical contact and sliding boundary value problem.
2. The element formulation was changed from the mean quadrature (MQ) element to the selective deviatoric (SD) element, with the deviatoric parameter set to 1 and strongly objective strain incrementation. The MQ element is faster because it under-integrates the element response, similar to a single integration point element. The SD element is more accurate because it fully integrates the deviatoric response, while still under-integrating the volumetric response to avoid pressure locking, similar to a Q1P0 element. Typically, the SD element is not much slower for implicitly solved problems because integrating the element response is relatively quick compared to solving the linearized equilibrium equations.
3. The mesh was completely rebuilt using Cubit's Python scripting environment (*CUBIT Team*, 2015). An example of the script is in Appendix A.2.1, and a comparison of the legacy mesh and the new mesh is shown in Fig. 2.3. Both meshes have the same number of elements across the half width of the room, but the new mesh has more elements in the vicinity of the room and less elements far away from the room. For comparison, the total element count dropped from 2184 to 1139.
4. The contact enforcement algorithm was changed from the Kinematic algorithm to the Augmented Lagrange (AL) algorithm in Sierra/Solid Mechanics. The Kinematic algorithm guarantees that bodies do not interpenetrate, and iterates on the position of the interface to balance the forces until R_{tol} has been met. The AL algorithm guarantees force equilibrium across the contact interface and iterates on the force

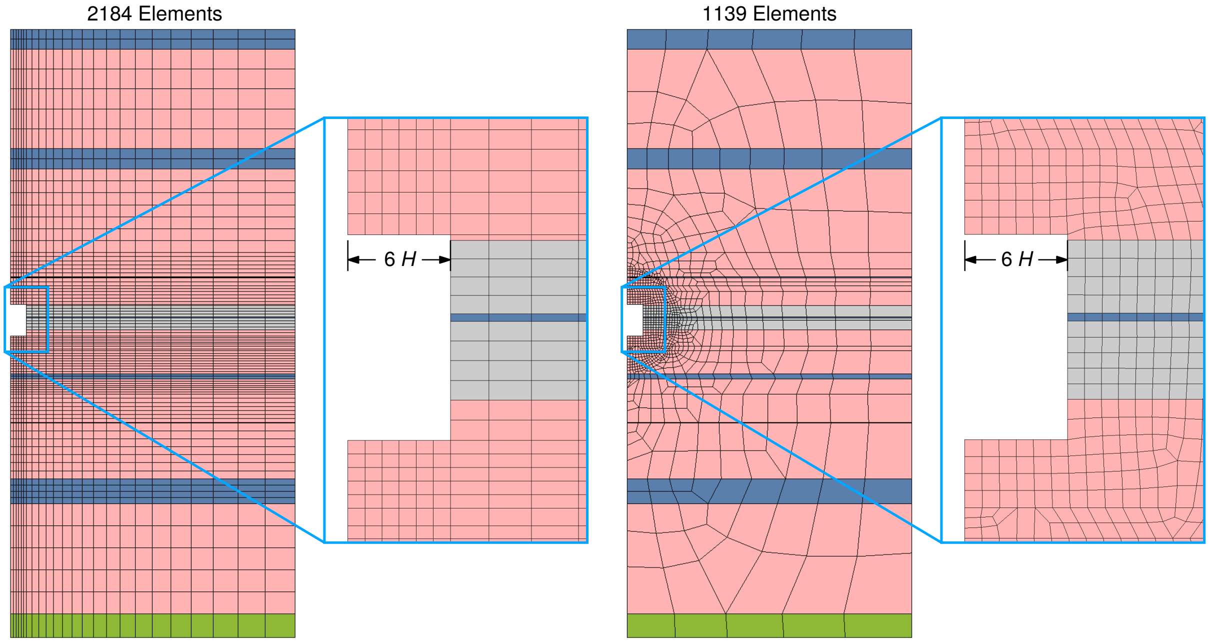

(a) Legacy mesh (b) New mesh

Figure 2.3: Updated mesh with the same number of elements across the room width

magnitudes to reduce the interpenetration until R_{tol} has been met. The AL algorithm is currently the default contact enforcement algorithm in Sierra/Solid Mechanics because it is typically more robust. It may also be more accurate for problems involving friction, since it balances the forces *a-priori*.

5. *Argüello and Holland* (2015); *Argüello* (2015) instantaneously excavated the room as a void at $t = 0$, which causes the stress surrounding the room to jump from hydrostatic to highly deviatoric in a single time step. When this approach was tried here, the conjugate gradient solver sometimes would not converge, especially on the finest meshes. (If the salt responded as an elastic material, the solver would likely never be able to converge.) To avoid this issue, the instantaneous excavation was spread out over multiple time steps by applying a time-varying fluid pressure to the surfaces of the room. At $t = -10$ ms, the fluid pressure varied linearly from the top to the bottom of the room according to the lithostatic pressure that existed prior to excavating the room. Then the fluid density was ramped down to zero between $t = -10$ ms and $t = 0$. For $t > 0$, the fluid pressure was held to zero. A small time step of 10^{-6} s was required during the fluid pressure ramp down, but it was reset to 10^{-2} s at $t = 0$.

The impact of modifying the numerical approach was investigated for an all clean salt simulation. The total effect of these changes can be seen in Fig. 2.4a, where the vertical closure is 26 % larger by the end of the simulation. Individual contributions of the five changes were also investigated. The changes were added sequentially, which gives an idea of their first-order effects, but it does not allow one to investigate interactions between the changes. That said, it appears that tightening the relative residual to $R_{\text{tol}} = 10^{-5}$

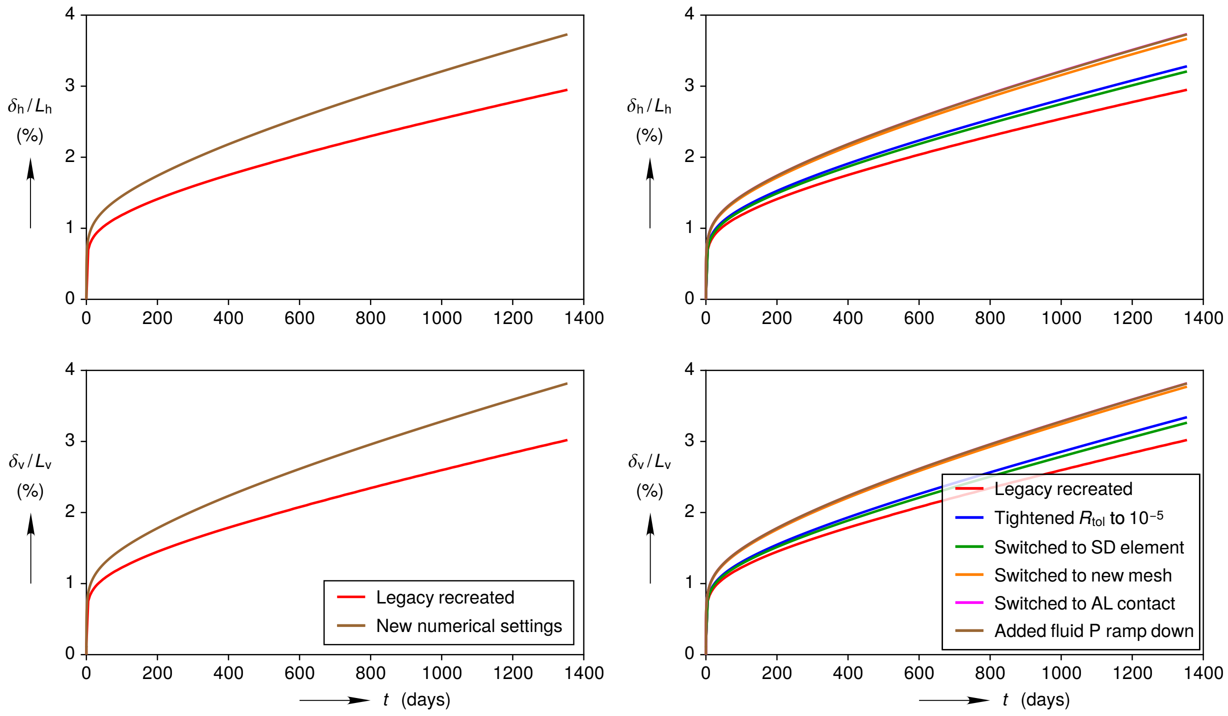

(a) Total effect

(b) Individual accumulated effects

Figure 2.4: Effects of various numerical choices on a all clean salt simulation. The legacy mesh and the new mesh used in the study are shown in Fig. 2.3.

and switching from the legacy mesh to the new mesh in Fig. 2.3 had the biggest impacts. Adding the pressure ramp down, by contrast, had no effect (the pink and brown curves overlap perfectly).

Next, the attention shifted to the full stratigraphy, which turned out to be much more difficult than anticipated. Adding the anhydrite caused the conjugate gradient solver to fail to converge during the fluid pressure ramp down. Solver settings were adjusted, the time step was reduced, the clay seams were eliminated, the finite element mesh was refined, and hardening was added to the Soil and Crushable Foam model, but the simulation repeatedly failed to converge at $t \approx -3.5$ ms. The Kayenta material model (*Brannon et al.*, 2015) was even reduced to the Soil and Crushable Foam model, but it exhibited the exact same behavior. Eventually, the problem was traced back to the von Mises flow potential in the Soil and Crushable Foam model.

Fig. 2.5 depicts the issue with the von Mises flow potential and the result of switching to an associated flow potential. The discussion will focus first on the results from the von Mises flow potential. The fluid pressure at the center of the room is plotted against time in Fig. 2.5a, and the red circled number instances correspond to the ε_{xx} fields near Room D in Fig. 2.5c. The faint yellow layer in Fig. 2.5c is the problematic anhydrite. From the beginning of the fluid pressure ramp down to ②, the anhydrite behaves as expected. Between ② and ③, however, the strain in the anhydrite localizes into two nearly vertical bands in a

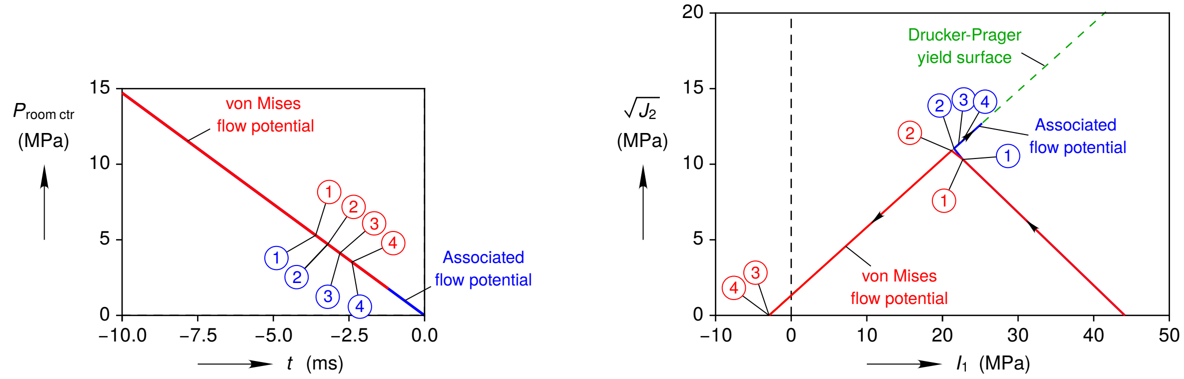

(a) Pressure history at room center

(b) Stress paths at element 369

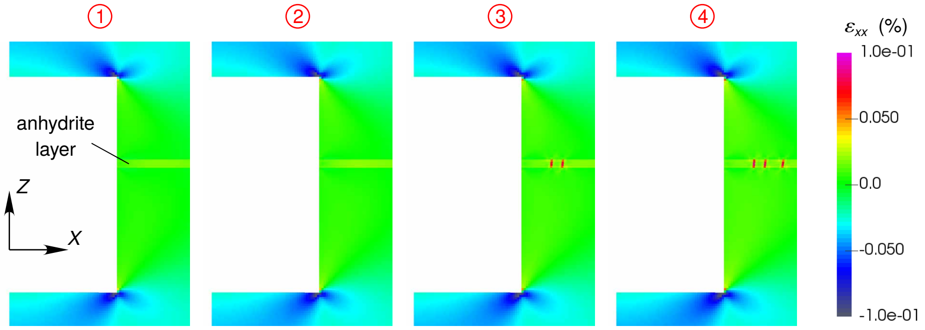

(c) Horizontal strain fields near the room when the anhydrite model uses a von Mises flow potential

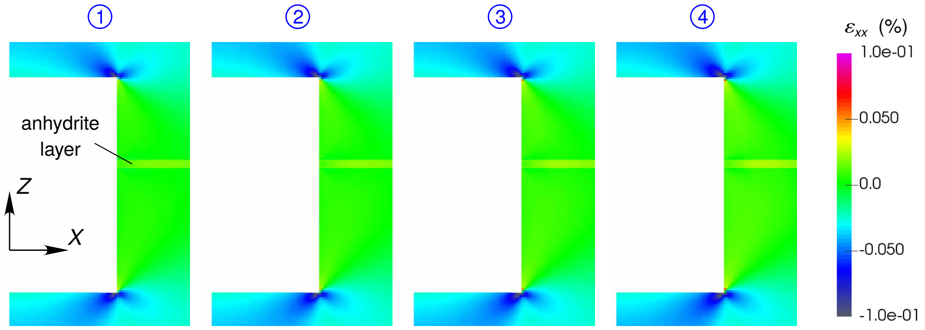

(d) Horizontal strain fields near the room when the anhydrite model uses an associated flow potential

Figure 2.5: Strain localization occurs during the fluid pressure ramp down if the anhydrite model uses a von Mises flow potential. Switching to an associated flow potential eliminates the issue.

single time step. Another time step produces another localization band to the right of the first two in ④. More localization bands appeared after ④, and the conjugate gradient solver was eventually unable to converge at $t = -1.7$ ms. In order to understand this behavior further, the stress averaged over element 369, which is at the center of the second localization band from the left in ②, was examined. The average stress in this element is plotted in the Rendulic plane in Fig. 2.5b. The axes of this plot are the square root of the the second invariant of the deviatoric stress $\sqrt{J_2}$ and the first invariant of the total stress I_1. Between $t = -10$ ms and ②, element 369 slowly moves from 44.1 MPa on the I_1 axis to the Drucker-Prager yield surface. From ② to ③, the strain localizes in element 369 and the stress state jumps down to the tip of the Drucker-Prager cone in a single time step. Element 369 remains at the tip of the cone for the rest of the simulation.

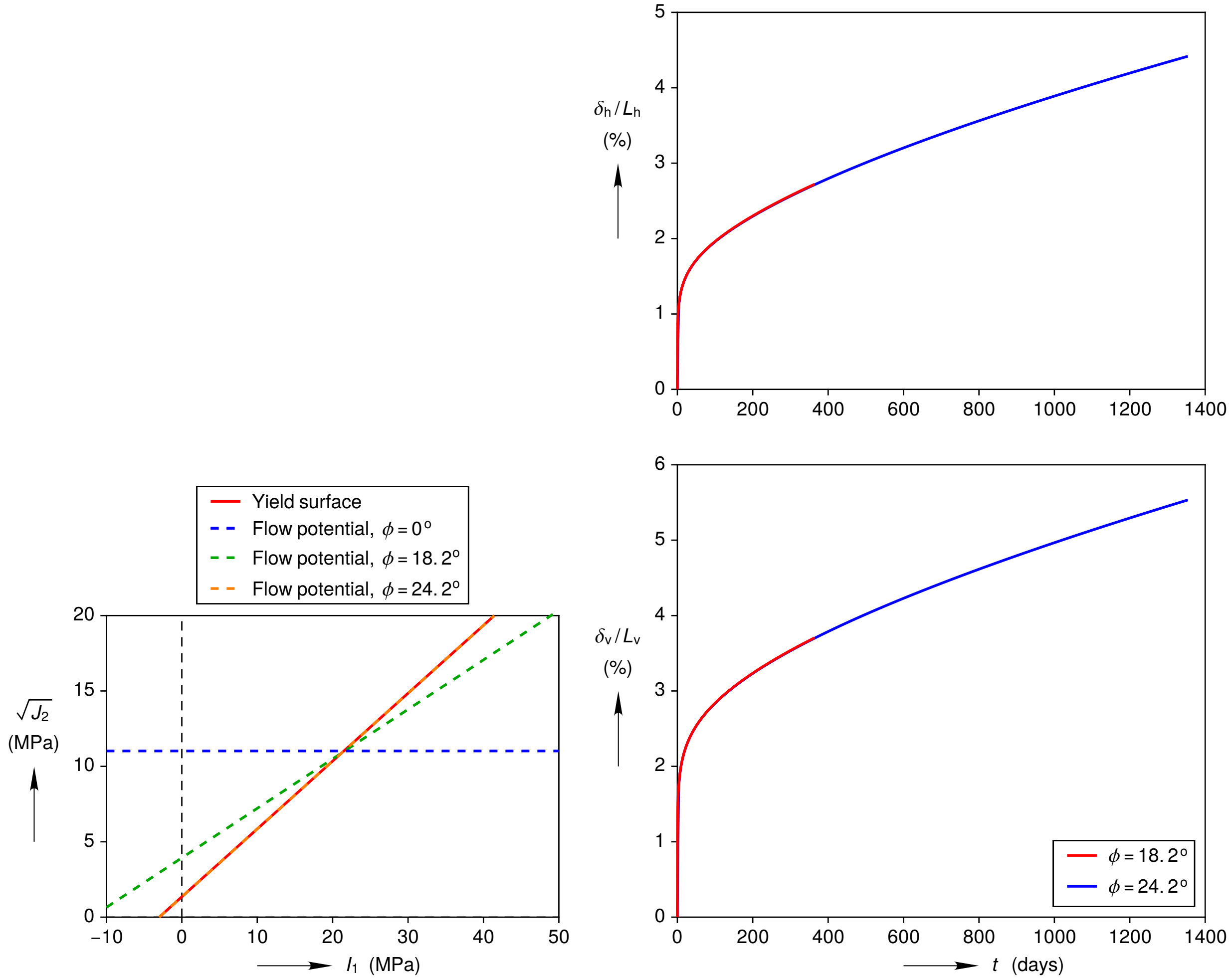

(a) Anhydrite dilatation angles

(b) Room closure predictions

Figure 2.6: Room closure prediction sensitivity to the anhydrite dilatation angle

Anhydrite is a brittle material, so the strain localization shown in Fig. 2.5c may appear to be fractures, but that is not the case. Intact anhydrite responds elastically to deformation. Once its strength is exceeded, microcracks develop in real anhydrite and it cannot carry further load. Instead of modeling these micro-cracks explicitly, they are smeared out and modeled as a continuum. Once material points reach the Drucker-Prager yield surface, they are considered failed. The microcracks and inability to carry further load is captured by the perfect plasticity.

Instead of fractures, it is far more likely that the strain localizations in Fig. 2.5c were due to a material instability. *Rudnicki and Rice* (1975) (and others) showed that non-associated flow rules cause material instabilities, so an associated flow rule was utilized instead. The dilatation angle ϕ is defined as the counterclockwise angle from the I_1 axis in the $\sqrt{J_2}$ vs. I_1 plane. The Soil and Crushable Foam model can only use a dilatation angle of $\phi = 0°$ (a von Mises flow potential). The Kayenta material model, on the other hand, can be reduced to the Soil and Crushable Foam model and allows the adjustment of the dilation angle ϕ. The Sierra/Solid Mechanics input syntax to reduce Kayenta to the Soil and Crushable Foam model with an associated flow potential ($\phi = 24.2°$) is shown in the anhydrite material block in Appendix A.2.6. With the associated flow rule, the strain localizations did not appear (see Fig. 2.5d) and the conjugate gradient solver had no trouble converging. In addition, the average stress at element 369 reached the Drucker-Prager yield surface at ② (see Fig. 2.5b) and slowly moved up the surface between ② and ④, instead of jumping down to the tip of the Drucker-Prager cone.

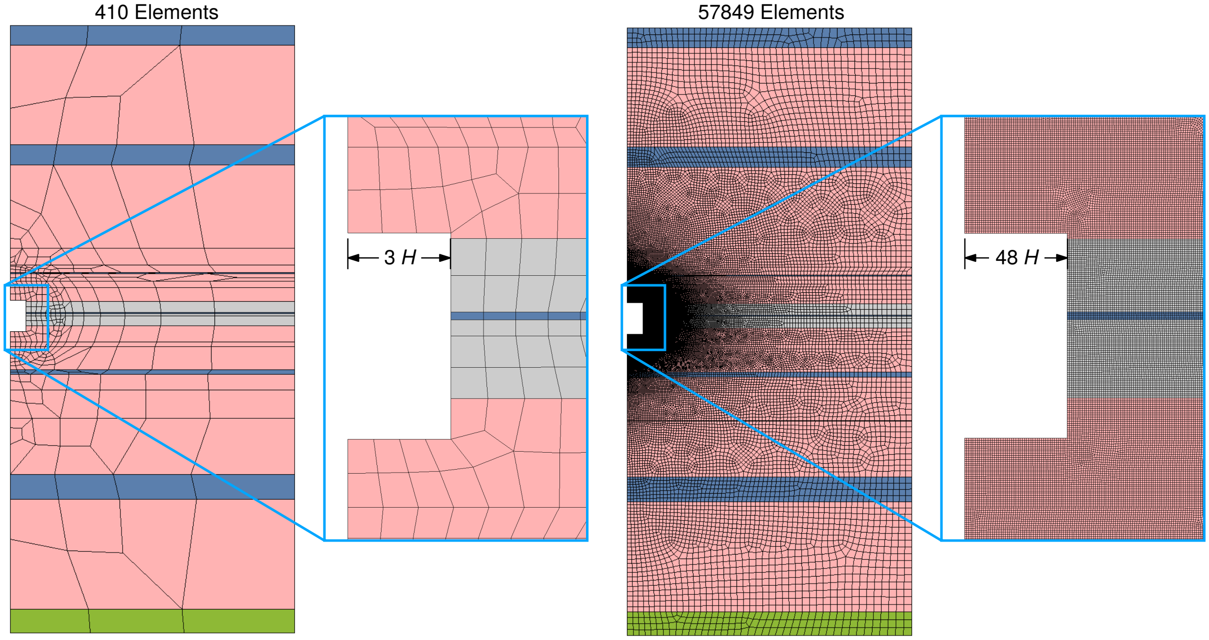

(a) Coarsest mesh (b) Finest mesh

Figure 2.7: Meshes used in the mesh convergence study.

The room closure sensitivity to the anhydrite dilatation angle is displayed in Fig. 2.6. Using the mesh in Fig. 2.7b, dilatation angles of $\phi = 6.1°$, 12.1°, 18.2°, and 24.2° were all attempted, but only $\phi = 18.2°$ and 24.2° did not exhibit strain localizations. The simulation with $\phi = 18.2°$ ran extremely slowly, so it was terminated early. For at least the first 365 days, the room closure appears to be insensitive to ϕ. Consequently, the anhydrite model used an associated flow rule for all further simulations.

One might ask how did this strain localization issue only appear now? Prior to *Argüello and Holland* (2015), simulations of Room D only used coarse meshes, which tend to restrain strain localizations. In addition, the full stratigraphy, fine mesh, simulations in *Argüello and Holland* (2015); *Argüello* (2015) were inspected, and they also exhibited strain localizations in the anhydrite layers. The localizations did not stop the simulations presumably because the relative residual was 10^{-3} instead of 10^{-5}. Therefore, the localizations were probably suppressed by coarse meshes or simply went undetected until now.

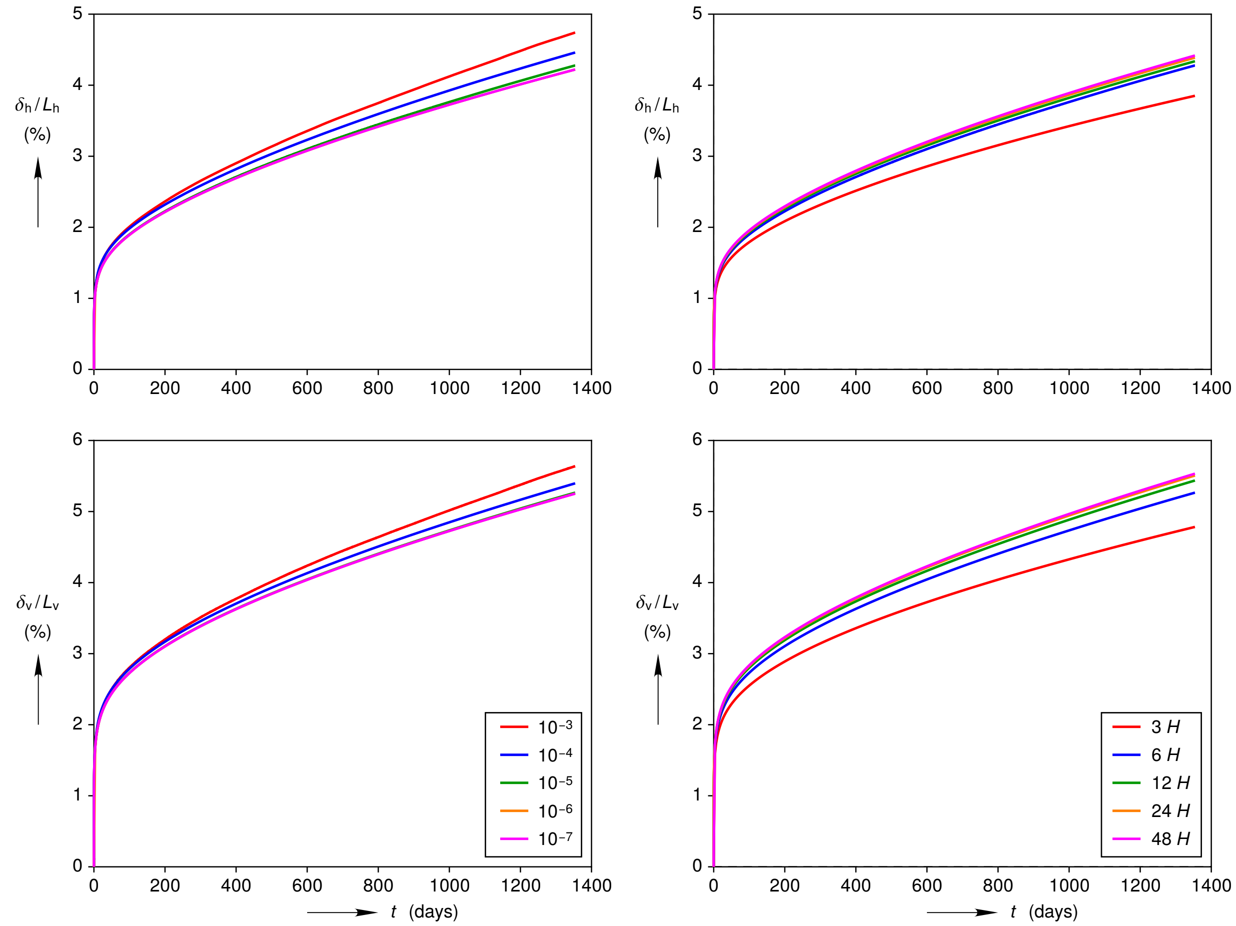

(a) Residual Sensitivity

(b) Mesh Sensitivity

Figure 2.8: Sensitivity of the closure predictions to the relative residual tolerance and the mesh density.

Next, the sensitivity to the relative residual tolerance is assessed. The mesh in Fig. 2.3b was used in simulations with $R_{\text{tol}} = 10^{-3}$ to 10^{-7}. As shown in Fig. 2.8a, significant differences were found between 10^{-3} and 10^{-5}, with diminishing returns beyond 10^{-5}. For that reason, $R_{\text{tol}} = 10^{-5}$ was considered sufficient.

Mesh convergence can now be demonstrated. Six meshes were used, ranging from 3 elements across the half width of the room to 48 elements across the half width. The coarsest mesh and the finest mesh are displayed in Fig. 2.7, and the results of the study are shown in Fig. 2.8b. It appears that 24 elements (or maybe even 12 elements) across the half width of the room is likely sufficient for many applications, but 48 elements was chosen here to be consistent with the mesh used by the Joint Project III partners.

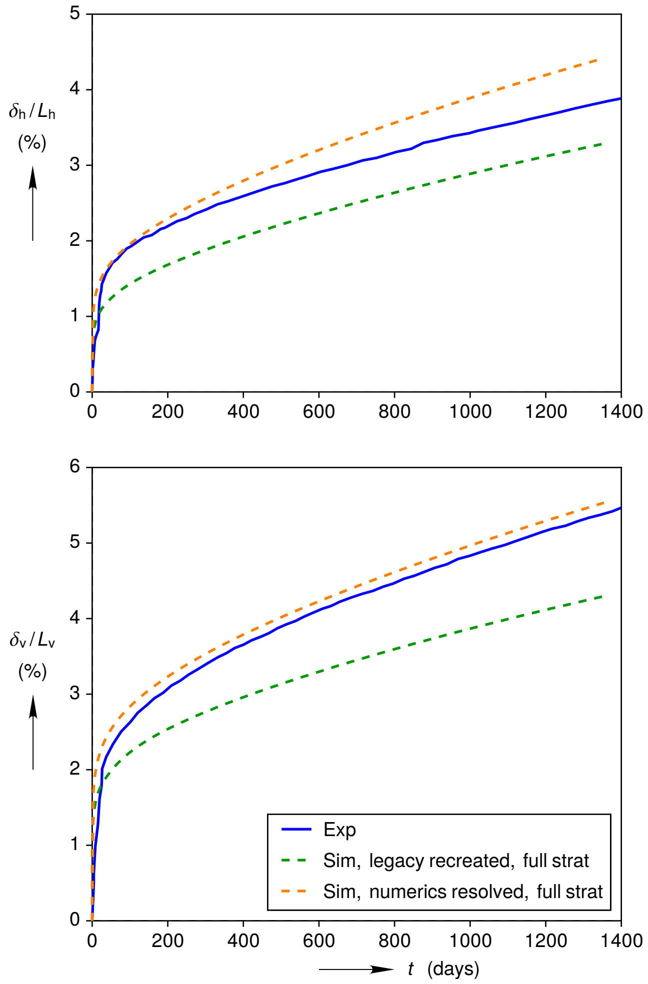

Figure 2.9: Impact of resolving the numerics.

All the changes up until now were aimed at resolving the numerics, so it is useful to quantify their impact. As depicted in Fig. 2.9, the horizontal and vertical closure increased by 34 % and 29 %, respectively, at $t = 1,354$ days. Thus, resolving the numerics more than made up for the decrease in room closure due to adding the anhydrite and polyhalite layers.

2.3 Two Minor Changes

Two minor modifications bear mentioning before proceeding to recalibrating the Munson-Dawson model. First, the corners of the room were rounded to a radius of 0.46 m (see Fig. 2.10a). The sharp corners in Fig. 1.9 were probably chosen for ease of meshing. The actual room corners, however, were rounded (see Section 1.2), and current meshing technology can easily handle such corners. Rounding the corners reduced the stress concentrations there, resulting in 4.1 % and 2.6 % less room closure in the horizontal and vertical directions at $t = 1,354$ days (see Fig. 2.11). Second, the right boundary of the top anhydrite layer was

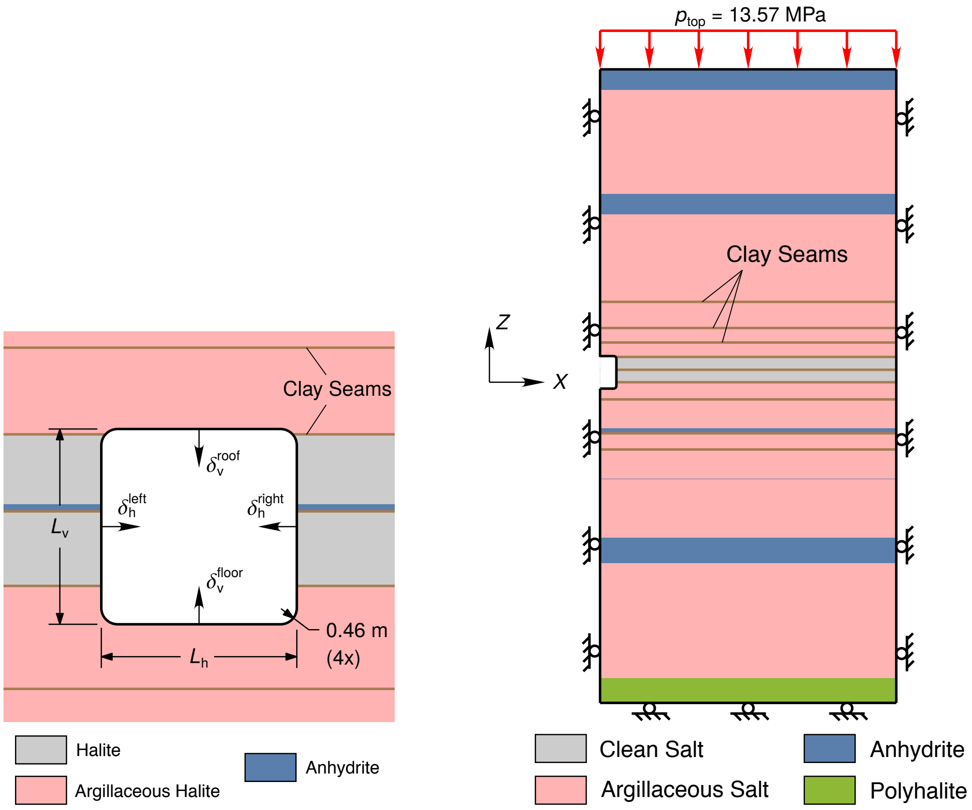

(a) Rounded corners (b) New boundary conditions

Figure 2.10: Minor changes to the room geometry and the boundary conditions

allowed to move in the Z direction, and the traction boundary condition at the bottom was replaced with rollers (compare Fig. 2.1a to Fig. 2.10b). This change was made to simplify the boundary conditions, and to be consistent with the Joint Project III partners. Changing the boundary conditions had an even smaller effect than rounding the room corners. At $t = 1,354$ days, the horizontal and vertical room closure was reduced by only 2.1 % and 1.1 %.

As discussed in Appendix A.9, the simulation with the new boundary conditions was subsequently converted to the Joint Project III setup for the comparison of salt constitutive models.

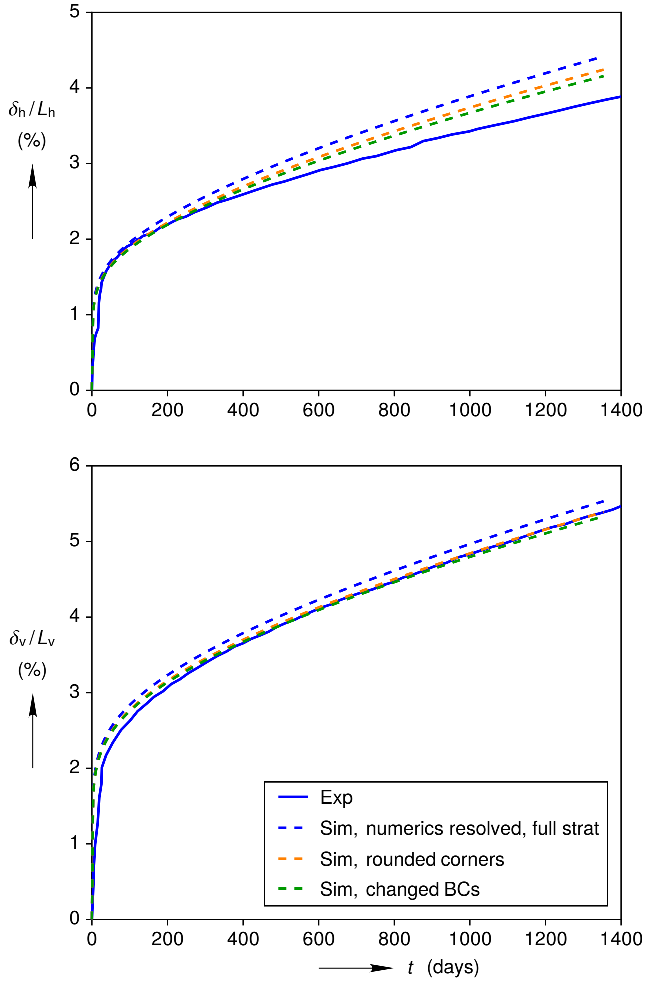

Figure 2.11: Effect of rounding the corners of the room and changing the boundary conditions.

Chapter 3

Recalibration of the Munson-Dawson model

3.1 Extraction of 2013 Cores

Early on in Joint Project III, the partners wished to know whether they could accurately calibrate their models against the existing laboratory geomechanical tests on WIPP salt. These experiments were conducted by Sandia and RE/SPEC in the 1980s and 1990s (see *Mellegard and Munson* (1997) for a summary). Measurement and control technologies have obviously improved since then, but so have experimental procedures for accurately determining model parameters. Furthermore, careful measurements of the dilatancy during strength tests are required to calibrate the damage and healing processes in the German models. Such dilatancy measurements were not included in the 1980s and 1990s tests. Therefore, the partners decided a new systematic series of creep and strength tests were needed, and they generously offered to perform the experiments themselves.

To accommodate the new experiments, Sandia commissioned the drilling of new cores from December 2012 through May 2013 (*Schuhen*, 2016a). The cores were extracted from the north rib of the N780 Drift, within about 30 m of the intersection with the E140 drift, and along the east rib of the E140 drift, between the N780 and N1100 drifts. This general location is marked as the “2013 Core Extraction Site” in Fig. 1.1. The vertical locations of the drill holes on the wall were selected consistent with the stratigraphy in Fig. 2-2 and Fig. 2-3 of *Deal et al.* (1989). As shown in Fig. 3.1a, the clean salt cores came from above the orange band (Mapping Unit 3 in *Deal et al.* (1989)), and the argillaceous cores came from below the orange band (Mapping Unit 0 in *Deal et al.* (1989)). A photo of the drilling process is shown in Fig. 3.1b. The shallowest point on any core came from 0.7 m into the rib, and the deepest came from 4.9 m into the rib. The cores were 300 mm in diameter and 600 mm long, on average.

Unfortunately, the *Deal et al.* (1989) stratigraphy does not match the 1983 reference stratigraphy (*Krieg*, 1984) or the *Munson et al.* (1989) stratigraphy. According to the 1983 reference stratigraphy, the salt above and below the orange band is clean. According to the *Munson et al.* (1989) stratigraphy, the salt above and below the orange band is argillaceous. Nevertheless, further study indicates that the salt above and below the orange band is

(a) Core extraction sites with respect to the *Deal et al.* (1989) stratigraphy

(b) Photo of core extraction

Figure 3.1: New cores were extracted from the WIPP in 2013.

visually distinct, even if the differences are small. Dennis Powers, a consulting geologist, was contracted by Sandia to inspect the cores (*Powers*, 2016) and reported, "The cores from "clean" halite consist of mainly light orange halite up to ≈ 3 cm (≈ 1 inch) diameter, lesser gray halite, and local very coarse (up to 10 cm; 4 inches) clear halite. There is little to no discernible clay in the orange halite, and sulfate is estimated to be less than 0.5 % by volume. Gray halite locally includes up to 2-3 % sulfate with minor clay. . . . Cores from "argillaceous" halite consist of zones or intervals of a) relatively fine (< 5 mm; 0.4 inch) light brown or slightly orange halite and b) coarser (up to 2.5 cm; 1 inch) halite that is more translucent and lighter in color than the fine halite. Overall, the non-halite components in the "argillaceous" halite appear to average ≈ 1 % but are higher in coarser halite." In addition, the Institut für Gebirgsmechanik in Germany found the argillaceous salt had, on average, roughly twice the water content of the clean salt by measuring the weight change after flue-curing specimens at 105 °C for 24 hours (see Fig. 7 in *Salzer et al.* (2015)). They presumed the extra water in the argillaceous salt was bound to the clay minerals. Finally, the 1983 reference stratigraphy is most similar to the *Deal et al.* (1989) stratigraphy, except the 1983 reference is missing the argillaceous salt beneath the orange band. Most likely, the argillaceous salt beneath the orange band was omitted from the 1983 reference to simplify modeling.

To prepare the cores for shipping, they were placed in wax coated cardboard tubes while still in the underground. As shown in Fig. 3.2a, the core fit tightly into the tubes, with very little dead air space around the core annulus. The tube ends were filled with foam packing material, a fitted plastic end cap and plywood disks to hold the plastic end cap in place. This packaging occurred generally within a week of core extraction and the tubes were wrapped in plastic when shipped. Hence, although the core was not sealed, it was not exposed to a

(a) Core packaging

(b) Sub-coring to create specimens

Figure 3.2: Cores were sent to the IfG and the TUC, where they were sub-cored for rock mechanics testing.

large volume of dry air.

The cores were sent to the Institut für Gebirgsmechanik (IfG) and the Technical University of Clausthal (TUC) in Germany, where the shipment arrived in excellent condition. *Salzer et al.* (2015) and *Düsterloh et al.* (2015) give the details on the petro-physical tests, creep tests, strength tests, and permeability tests they performed. This report will focus on the creep tests, because the M-D model cannot incorporate the other results.

3.2 Details of the Triaxial Creep Tests

The IfG and TUC identified their creep specimens as TCC1, TCC3, TCC5, etc. in *Salzer et al.* (2015) and *Düsterloh et al.* (2015). Both labs used the same naming scheme as the other, and each lab used the same naming scheme on both types of salt. Unique names were created by prepending A_ or C_ and IfG_ or TUC_ to the original names. For example, the clean salt specimen TCC6 tested at the IfG became C_IfG_TCC6, and the argillaceous salt specimen TCC9 tested at the TUC became A_TUC_TCC9.

The majority of the triaxial creep tests on the 2013 cores were performed at the IfG. The TUC also conducted creep tests on older cores drilled in 2001 (see Appendix A.5) and two tests on 2013 cores (see Appendix A.6), but the TUC tests were eventually discarded for the reasons discussed in Appendix A.7. Only the IfG creep tests were used to recalibrate the M-D model, so they are the focus of the remainder of this work.

The IfG triaxial creep tests were similar to the simple example test described in Section 1.3.1. The IfG cut the cores into two halves lengthwise on the "Clipper rock saw", and then drilled out cylindrical test specimens (see Fig. 3.2b). The original, undeformed, specimen dimensions were $D = 40$ mm and $L = 80$ mm. The radial Cauchy stress σ_{rr} was controlled by simply pressurizing the triaxial cell with oil (probably silicone). The axial

Cauchy stress σ_{zz} was held fixed by adjusting the axial force W based on the axial compressive displacement of the platens δ. To relate W and δ, they assumed the specimen underwent isochoric, affine, deformations such that $\sigma_{zz} = W\,(1 - \delta/L)/A$, where $A = \pi\, D^2/4$. The IfG simply stated the nominal values of σ_{rr} and σ_{zz} for each test, so the idealized stress histories are plotted in Figs. 3.3 and 3.4 and Appendix A.4. They calculated the axial log strain from the platen displacement as $\varepsilon_{zz} = \ln(1 + \delta/L)$. The specimen temperature was set by controlling the silicone oil temperature. The oil temperature was raised to the test temperature T before applying deviatoric stresses to the specimen, and T was held fixed for the duration of the experiment.

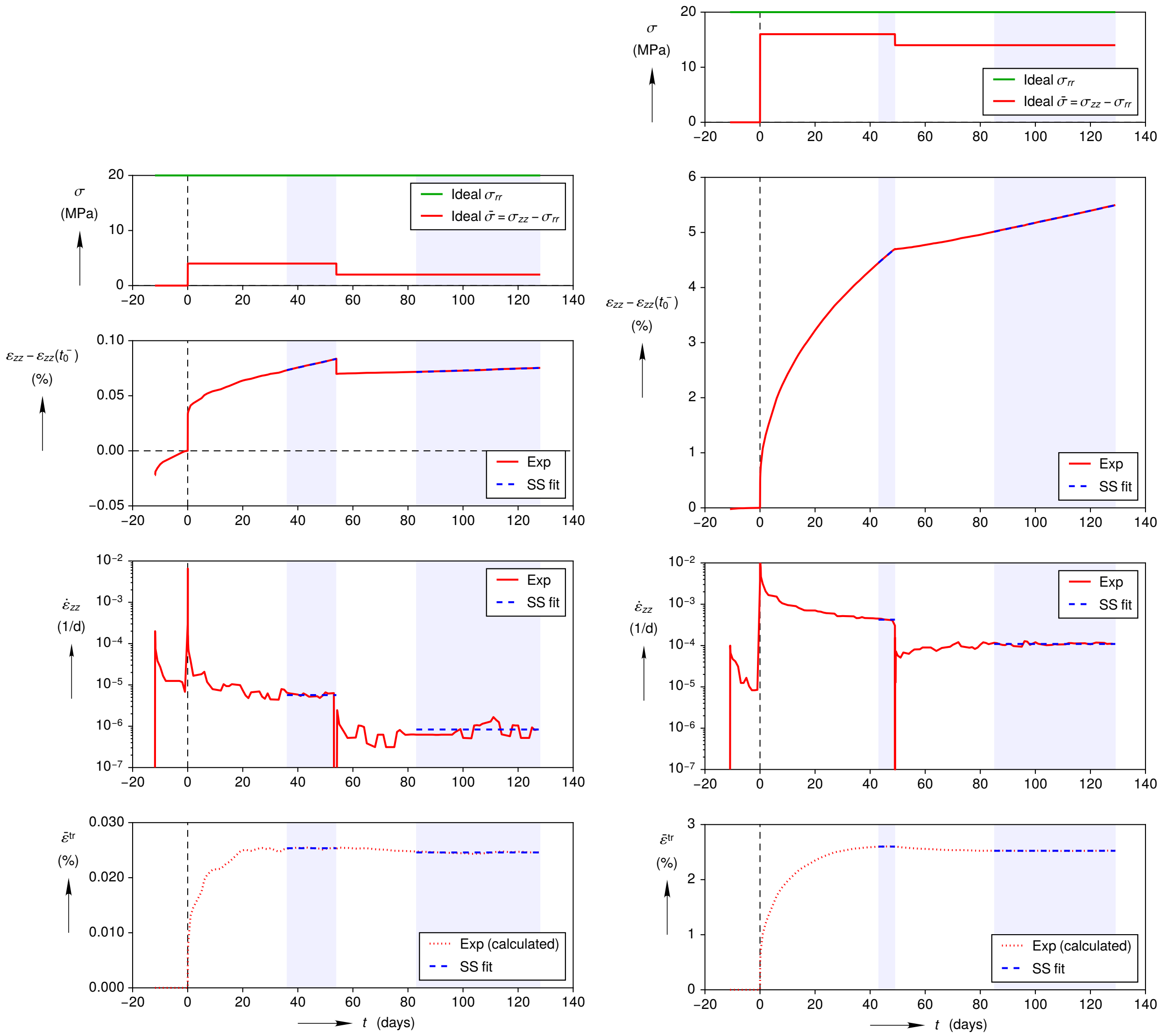

(a) Low equivalent stress (C_IfG_TCC15) (b) High equivalent stress (C_IfG_TCC11)

Figure 3.3: Creep experiments at low and a high equivalent stresses.

The IfG tests began with applying hydrostatic pressure to the specimen for a length of time before applying a non-zero equivalent stress at t_0. Hydrostatic pressure causes consolidation, which should return the specimen to a more virgin state by healing microcracks. Although the practice is becoming standard, it was not performed during the legacy experiments on WIPP salt, and the application time varies from lab to lab. For example, the TUC applied hydrostatic pressure for one day and did not record data during this time, while the IfG applied hydrostatic pressure for at least 10 days before every test. The hydrostatic response during $t < t_0$ can be seen for a low equivalent stress experiment and a high equivalent stress experiment in Fig. 3.3. It appears the sample in the low equivalent stress test would have continued consolidating had the hydrostatic pressure been applied for longer. In future experiments, the IfG plans to wait until $\dot{\varepsilon}_{zz} \approx 0$ before applying deviatoric stress. Fortunately, the hydrostatic deformation does stabilize prior to t_0 in many of the experiments in Appendix A.4. Also, the hydrostatic deformation is a negligible percentage of the total deformation in the medium to high equivalent stress tests (see Fig. 3.3b, for example).

At the end of the hydrostatic consolidation period, the IfG (and TUC) did not unload or return to room temperature to find the new stress free length. Hence, the elastic strain due to the hydrostatic stress at t_0^- or the thermal strain due to raising the temperature are not precisely known. This uncertainty is not important because $\varepsilon_{zz}(t_0^-)$ gets subtracted from $\varepsilon_{zz}(t)$ to calculate $\bar{\varepsilon}^{\mathrm{tr}}(t)$ in Eq. (1.22). For consistency, $\varepsilon_{zz}(t_0^-)$ was subtracted from $\varepsilon_{zz}(t)$ before plotting the axial strain in all the IfG (and TUC) experiments.

The IfG changed $\bar{\sigma}$ at multiple points during their creep testing. At $t_1 \approx 50$ days, the axial stress was changed by $\Delta\sigma_{zz}(t_1) = \Delta\bar{\sigma}(t_1) = -2$ MPa, which leads elastic unloading followed by some recovery and a new steady-state strain rate. This 2 MPa drop was part of a scheme developed to measure the steady-state strain rate $\dot{\bar{\varepsilon}}^{\mathrm{ss}}$ more accurately by approaching from "above" and from "below" (see *Günther et al.* (2014) for further details).

The change in axial strain $\Delta\varepsilon_{zz}(t_1)$ due to the change in axial stress $\Delta\sigma_{zz}(t_1)$ revealed an issue that affects the calculation of $\bar{\varepsilon}^{\mathrm{tr}*}$ in the low equivalent stress tests. The prediction of the $\Delta\varepsilon_{zz}(t_1)$ drop was too small in all the low equivalent stress tests. This discrepancy is probably due to a combination of the axial compliance of the load frame, the triaxial cell, and the specimen-to-specimen variation in E. As described in detail in Appendix A.3, the issue was likely corrected by analyzing the experiments using E^{eff} instead of E.

3.3 Analysis of the Triaxial Creep Tests

The typical procedure to calibrate the thermo-viscoplastic portion of the M-D model involves two steps. First, one extracts $\dot{\bar{\varepsilon}}^{\mathrm{ss}}$, $\bar{\varepsilon}^{\mathrm{tr}*}$, κ_{h}, and κ_{r} from creep tests at a variety of stresses $\bar{\sigma}$ and temperatures T. Second, one fits model parameters, such as Q_1 and m, in Eqs. (1.9) to (1.12), (1.15) and (1.16) to the collection of $\dot{\bar{\varepsilon}}^{\mathrm{ss}}$, $\bar{\varepsilon}^{\mathrm{tr}*}$, κ_{h}, and κ_{r} values. This section is concerned with the first step.

One method to extract $\dot{\bar{\varepsilon}}^{\mathrm{ss}}$, $\bar{\varepsilon}^{\mathrm{tr}*}$, κ_{h}, and κ_{r} is to fit the M-D model to individual experiments. In order to do so, the M-D model was specialized to triaxial creep and implemented in the Python programming language. Although triaxial creep specimens can barrel outwards due to friction at the top and bottom platens, the specialized model adopted the usual assumption that the deformation and stresses are spatially uniform so that the test could be simulated as a material point. The ordinary differential equation that describes the transient behavior (Eqs. (1.12) to (1.16)) was numerically integrated using LSODA from ODEPACK (*Hindmarsh*, 1983). The Python implementation of the M-D model was verified by simulating the two experiments in Fig. 3.3 using Python and Sierra/Solid Mechanics. The two codes gave identical results for both experiments. Having a Python version of the M-D model avoided passing data back and forth between Python and Sierra/Solid Mechanics during the fitting process. It also permitted adjusting the elastic moduli in Eq. (1.3) to account for the axial compliance issue detailed in Appendix A.3, while still leaving μ untouched in Eqs. (1.9) to (1.12).

Two methods were used to extract $\dot{\bar{\varepsilon}}^{\mathrm{ss}}$, $\bar{\varepsilon}^{\mathrm{tr}*}$, and κ_{h} from each experiment. Both methods are shown for two examples in Figs. 3.3 and 3.4, which should help make the following description of the methods more concrete.

- Method A:
    1. The axial strain rate $\dot{\varepsilon}_{zz}$ was calculated using centered differences and plotted against t in a semi-log plot.
    2. The steady state region was selected by visually detecting where $\ddot{\varepsilon}_{zz} \approx 0$ on the $\dot{\varepsilon}_{zz}$ versus t plot. (The steady state region is marked with a light blue stripe in the background of every plot.)
    3. A straight line was least squares fit to the ε_{zz} versus t plot in the steady state region, and the slope was taken as $\dot{\bar{\varepsilon}}^{\mathrm{ss}}$.
    4. The transient equivalent viscoplastic strain $\bar{\varepsilon}^{\mathrm{tr}}$ was calculated using Eq. (A.7).
    5. The average value of $\bar{\varepsilon}^{\mathrm{tr}}$ in the steady state region was taken as $\bar{\varepsilon}^{\mathrm{tr}*}$.
    6. The hardening parameter κ_{h} was iteratively optimized. The directly measured values of $\dot{\bar{\varepsilon}}^{\mathrm{ss}}$ and $\bar{\varepsilon}^{\mathrm{tr}*}$ were input into the M-D model, and the axial strain $\varepsilon_{zz}^{\mathrm{sim}}$ due to triaxial creep was simulated. The simulated axial strain was compared against the measured $\varepsilon_{zz}^{\mathrm{exp}}$ using a trapezoidal rule integrated version of $r = \int_{t_0}^{t_1} (\varepsilon_{zz}^{\mathrm{exp}} - \varepsilon_{zz}^{\mathrm{sim}})^2 \,\mathrm{d}t$ during the work hardening portion of the test. This objective function was input into the Nelder-Mead algorithm *Nelder and Mead* (1965) to iteratively optimize κ_{h}.
    7. The recovery portion of the tests did not have enough curvature to uniquely determine κ_{r}, so only $\dot{\bar{\varepsilon}}^{\mathrm{ss}}$ and $\bar{\varepsilon}^{\mathrm{tr}*}$ were measured during recovery.
- Method B:
    1. All three parameters that control the transient hardening response ($\dot{\bar{\varepsilon}}^{\mathrm{ss}}$, $\bar{\varepsilon}^{\mathrm{tr}*}$, and κ_{h}) were fit at the same time by comparing $\varepsilon_{zz}^{\mathrm{sim}}$ from the M-D model to the measured $\varepsilon_{zz}^{\mathrm{exp}}$ during the work hardening portion of the test. The optimization algorithm, objective function, and numerical integration scheme used to fit κ_{h} in method A were used again to fit $\dot{\bar{\varepsilon}}^{\mathrm{ss}}$, $\bar{\varepsilon}^{\mathrm{tr}*}$, and κ_{h} together.

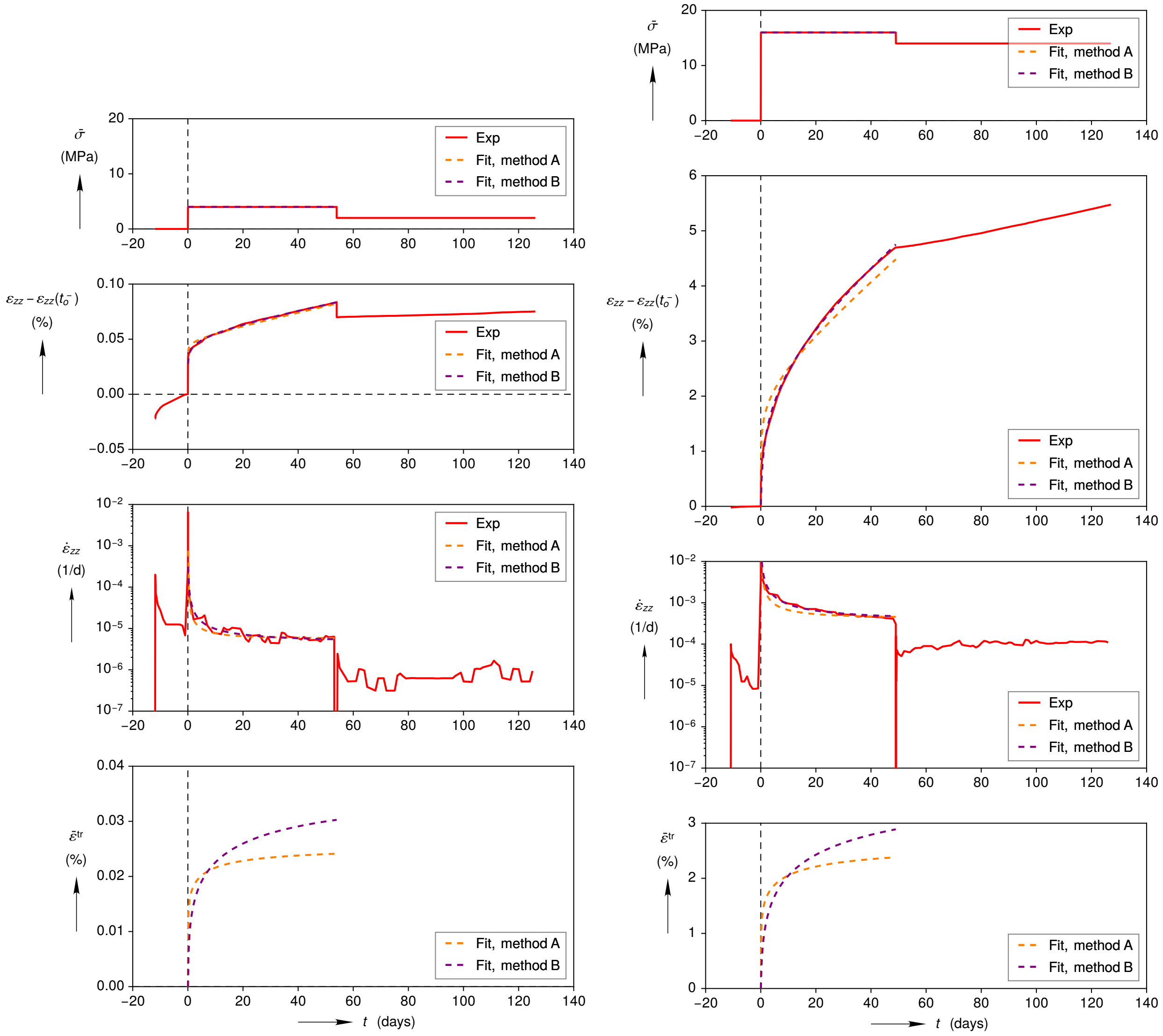

(a) C_IfG_TCC15 (b) C_IfG_TCC11

Figure 3.4: Fits to the creep experiments in Fig. 3.3.

2. The recovery portion of the tests again did not have enough curvature to uniquely determine $\dot{\bar{\varepsilon}}^{\mathrm{ss}}$, $\bar{\varepsilon}^{\mathrm{tr}*}$, and κ_{r}, so the measured $\dot{\bar{\varepsilon}}^{\mathrm{ss}}$ and $\bar{\varepsilon}^{\mathrm{tr}*}$ values from method A were utilized instead and κ_{r} was left undetermined.

These two methods were applied to every experiment, as shown in Appendices A.4 to A.6. The resulting values of $\dot{\bar{\varepsilon}}^{\mathrm{ss}}$, $\bar{\varepsilon}^{\mathrm{tr}*}$, and κ_h are shown in Tables A.2 to A.4. Tables A.2 to A.4 also include weighting factors w between 0 and 1 for each experiment. The w values were selected by judging the quality of the ε_{zz} versus t curve. Smooth, classical looking, creep curves that appear close to the steady-state region were assigned values of 1, while irregular curves that appear far from the steady-state region were assigned lower values. The weighting factors in Table A.2 were used in the recalibrations of the M-D model in Section 3.4 and Appendix A.8.

The two fitting methods each have their advantages and disadvantages. The primary advantage of method A is it can measure $\dot{\bar{\varepsilon}}^{\mathrm{ss}}$ and $\bar{\varepsilon}^{\mathrm{tr}*}$ with the minimal set of assumptions that went into analyzing the triaxial creep test in Section 1.3.1. This advantage makes method A useful for comparing experiments to experiments. One disadvantage is the analyst must assume that sufficient strain has accumulated that the specimen has reached stead-state creep. Salt only asymptotes to steady-state creep, so one must wait several months to approach the true steady-state value. This issue is mitigated by the IfG's scheme to approach the steady-state region from "above" and "below", but it does not eliminate the problem. A second disadvantage is one still must select a value for κ_{h}. *Munson et al.* (1989) used the relation

$$\kappa_{\mathrm{h}} = \ln\left(\frac{\dot{\varepsilon}_{zz}(t_0^+)}{\dot{\bar{\varepsilon}}^{\mathrm{ss}}}\right) \tag{3.1}$$

to calculate κ_{h}, but that relies on an accurate measurement of the slope at a single experimentally measured data point. Taking derivatives of experimental data amplifies noise, and is especially problematic if the slope is changing rapidly, as it is at t_0^+. Instead, method A fits κ_{h} by comparing the predicted ε_{zz} against the whole measured ε_{zz} during hardening. The fit can sometimes be quite good (see Fig. 3.4a), but other times it is not (see Fig. 3.4b) because $\dot{\bar{\varepsilon}}^{\mathrm{ss}}$ and $\bar{\varepsilon}^{\mathrm{tr}*}$ were constrained to be their measured values. Method B, on the other hand, varies $\dot{\bar{\varepsilon}}^{\mathrm{ss}}$, $\bar{\varepsilon}^{\mathrm{tr}*}$, and κ_{h} together to get the best possible fit of the ε_{zz} during hardening. As shown in Fig. 3.4 (and Appendices A.4 to A.6), the method B fits match nearly all of the experiments very well, despite varying only three values in the M-D model. Besides better fits, method B also avoids assuming that steady-state creep was reached in the experiment. The result is Method B typically selects smaller values of $\dot{\bar{\varepsilon}}^{\mathrm{ss}}$ and larger values of $\bar{\varepsilon}^{\mathrm{tr}*}$ than method A. Of course, the analyst must be cautious with Method B. With insufficient curvature in the ε_{zz} curve, the fit selected by the optimizer may not be unique. To be prudent, the results from Method A and Method B are compared below to verify that method B did not pick unreasonable values of $\dot{\bar{\varepsilon}}^{\mathrm{ss}}$, $\bar{\varepsilon}^{\mathrm{tr}*}$, and κ_{h}. This potential for non-uniqueness is also why $\dot{\bar{\varepsilon}}^{\mathrm{ss}}$, $\bar{\varepsilon}^{\mathrm{tr}*}$, and κ_{r} were not fit to the recovery portion of the creep tests, and use the $\dot{\bar{\varepsilon}}^{\mathrm{ss}}$ and $\bar{\varepsilon}^{\mathrm{tr}*}$ values from method A. Fortunately, the IfG found that approaching the steady-state rate from from below tends to be better than from above (*Günther et al.*, 2014), so the $\dot{\bar{\varepsilon}}^{\mathrm{ss}}$ and $\bar{\varepsilon}^{\mathrm{tr}*}$ values selected by method A during recovery should be reasonably accurate.

Despite attention to detail, fitting methods A and B were unable to produce satisfactory values of $\bar{\varepsilon}^{\mathrm{tr}*}$ and κ_{h} in some IfG experiments. As discussed in Appendix A.4, only the $\dot{\bar{\varepsilon}}^{\mathrm{ss}}$ values were utilized from C_IfG_TCC16 and A_IfG_TCC11 because of doubts about the transient behavior.

The log-log plots in Fig. 3.5 show that there is almost no difference in the creep behaviors of clean and argillaceous specimens. Fitting method A was utilized here to avoid convolving the creep measurements with the specific form of the M-D model. The majority of the experiments were performed at $T = 60$ °C, but two experiments were performed at $T = 24$ °C, and two experiments were performed at $T = 80$ °C. (Recall that each IfG experiment applied two values of $\bar{\sigma}$, so two experiments become eight markers in Fig. 3.5) A statistical analysis might be able to detect a very slight difference between the clean and argillaceous creep behavior, but it is not large enough to bother distinguishing between the two. Note

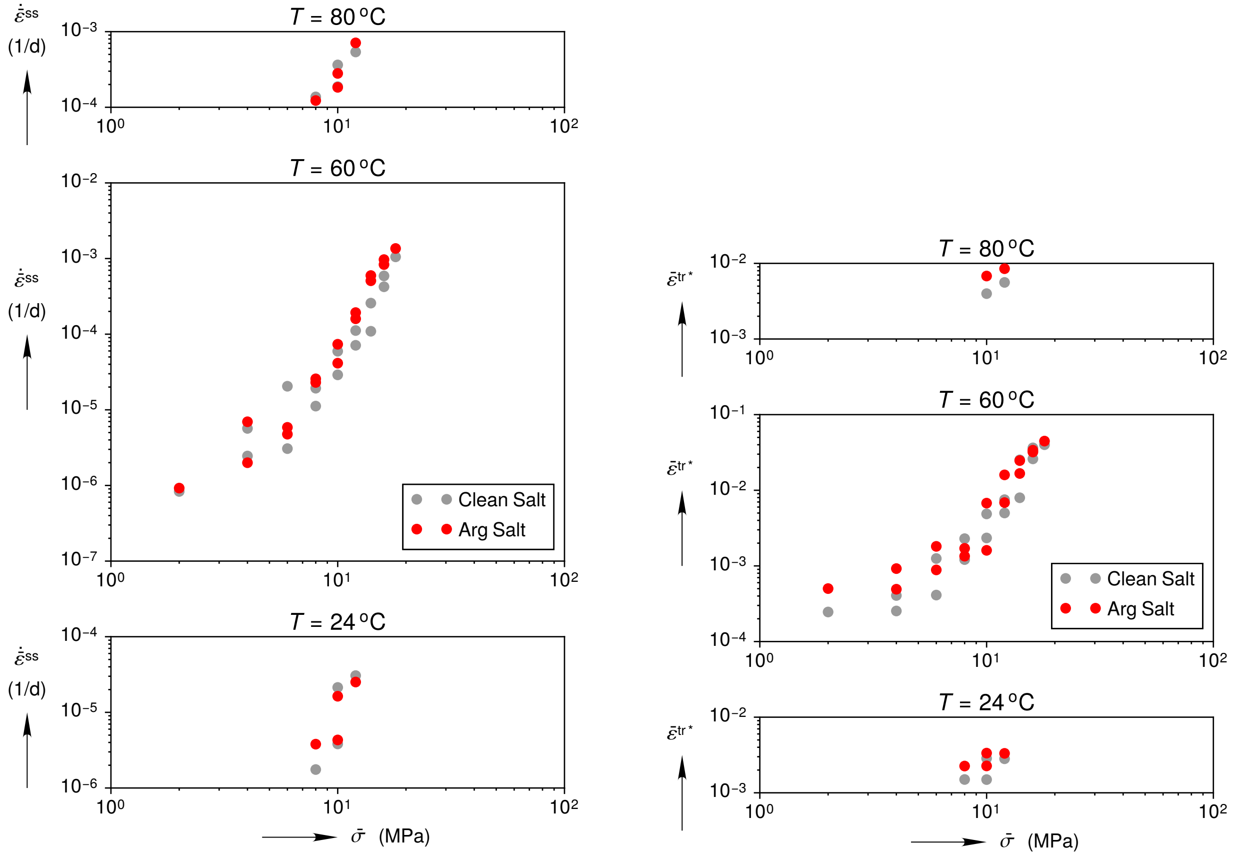

(a) Steady State Rate

(b) Transient Limit

Figure 3.5: Clean salt creep and argillaceous salt creep compared. All data points were obtained from the IfG experiments using fitting method A.

that *Düsterloh et al.* (2015) performed an independent analysis of the same creep experiments and also concluded that the argillaceous and clean creep responses are virtually the same.

Fig. 3.6 compares the results of fitting method A to fitting method B. Half the $\dot{\bar{\varepsilon}}^{\mathrm{ss}}$ and $\bar{\varepsilon}^{\mathrm{tr}*}$ points are identical because method B uses method A's $\dot{\bar{\varepsilon}}^{\mathrm{ss}}$ and $\bar{\varepsilon}^{\mathrm{tr}*}$ values during recovery. During hardening, Method B's $\dot{\bar{\varepsilon}}^{\mathrm{ss}}$ values are generally a little lower than method A's values, and method B's $\bar{\varepsilon}^{\mathrm{tr}*}$ values are generally a little higher, as expected. The κ_{h} values for method B, however, are significantly lower than those of method A. This difference in κ_{h} is probably connected to method A's primary assumption that $\dot{\bar{\varepsilon}}^{\mathrm{ss}}$ and $\bar{\varepsilon}^{\mathrm{tr}*}$ were measured in the steady-state region. When the optimization algorithm selected κ_{h} in Fig. 3.4b, for example, it was unable to vary $\dot{\bar{\varepsilon}}^{\mathrm{ss}}$ and $\bar{\varepsilon}^{\mathrm{tr}*}$ to get the best possible match with ε_{zz}. To compensate, the algorithm chose a large value of κ_{h} to make the primary assumption almost true and make the M-D model reach steady-state more quickly than the corresponding method B fit.

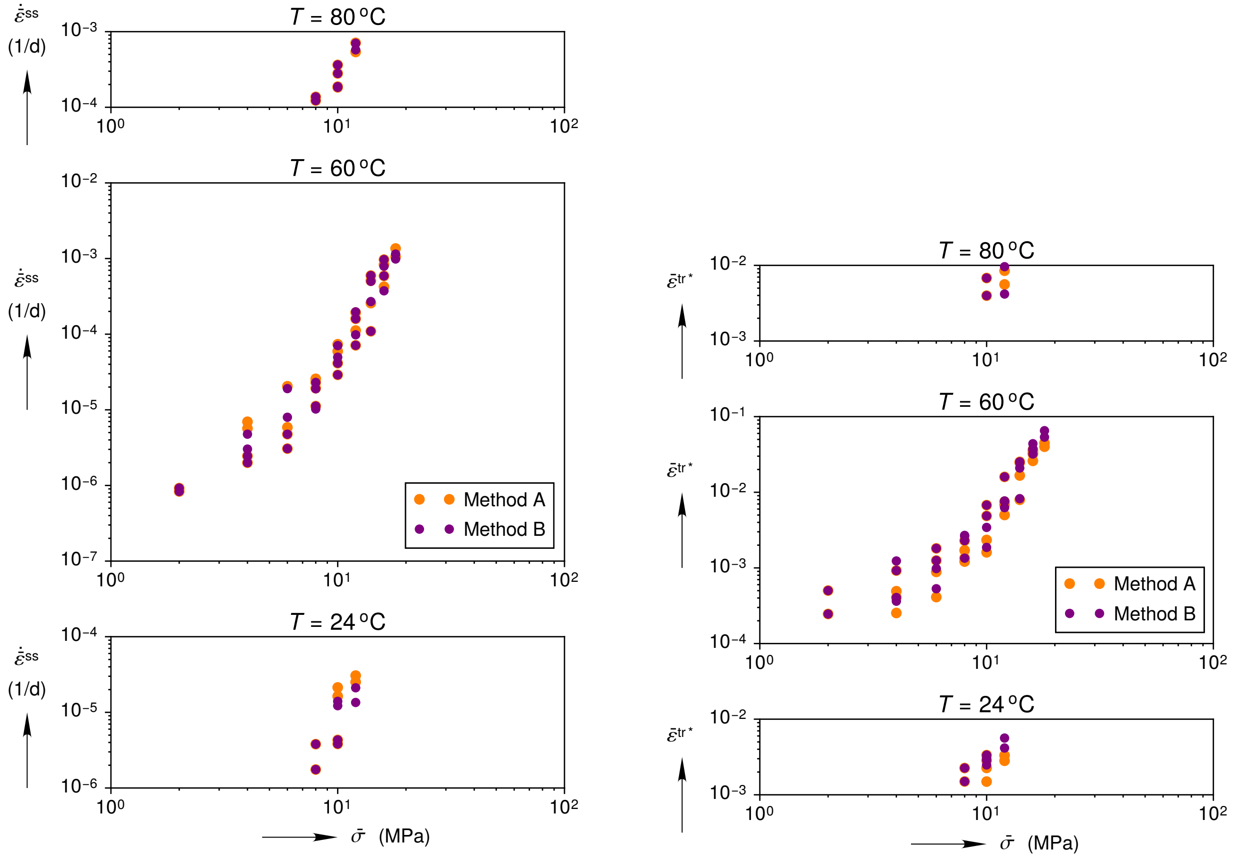

(a) Steady state rate

(b) Transient limit

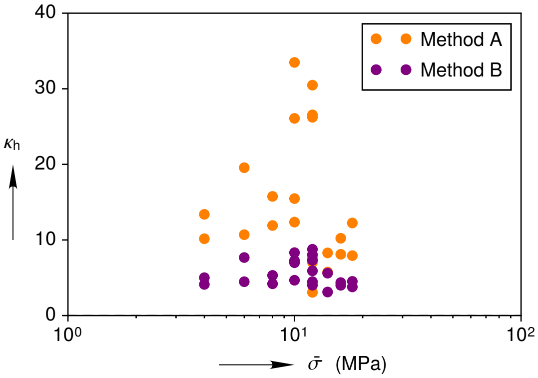

(c) Hardening rate variable

Figure 3.6: Creep experiment fitting methods compared. All data points were obtained from the IfG experiments.

3.4 Munson-Dawson Calibration 1B

This section covers the second part of calibrating the thermo-viscoplastic portion of the M-D model. Several of the model parameters that control the temperature and equivalent stress dependence are recalibrated to the collection of $\dot{\bar{\varepsilon}}^{ss}$, $\bar{\varepsilon}^{tr*}$, and κ_h values from the previous section. The values extracted using method A are used to create M-D model calibration 1A, while the values from method B are used to create M-D model calibration 1B. This section will focus on calibration 1B, but the same plots for calibration 1A are included in Appendix A.8. Both new calibrations started with the legacy calibration and then modified parameters, as necessary, to fit the IfG experiments.

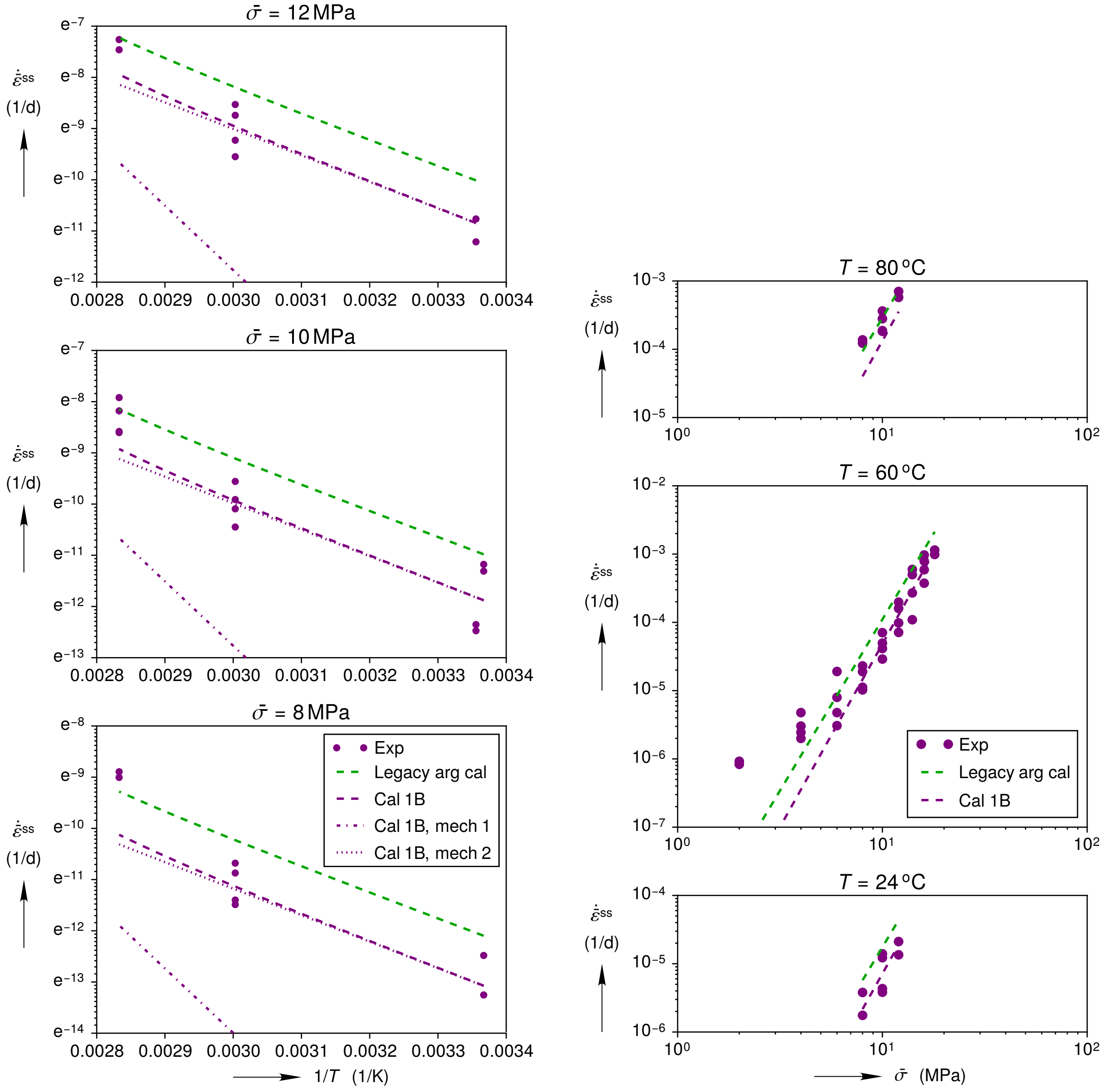

(a) Temperature dependence

(b) Stress dependence

Figure 3.7: Calibration 1B steady-state creep strain rate compared against experiments. Experimental data points were obtained from the IfG tests using fitting method B.

Room D was not heated, so this report only concerns the room temperature viscoplastic response of salt. The IfG, however, performed most of their tests at 60 °C, meaning the temperature dependence must still be calibrated to properly capture the room temperature behavior. As discussed in Section 1.3, the steady-state strain rate's temperature and stress dependences are controlled by three mechanisms. The third mechanism is inactive here because *Munson et al.* (1989)'s stress limit for dislocation slip $\bar{\sigma}_0 = 20.57$ MPa is above $\bar{\sigma}$ for all the IfG tests. The second mechanism dominates at room temperature, but the first mechanism begins to play a role at moderately higher temperatures. The IfG performed creep tests at 25, 60, and 80 °C, which is enough to detect a non-linear dependence in the $\ln \dot{\bar{\varepsilon}}^{\mathrm{ss}}$ versus $1/T$ plots in Fig. 3.7a, but not enough to precisely locate where mechanism 2 starts to get activated. The curved region in the clean salt legacy calibration is between roughly 80 °C and 150 °C in Fig. 1.6a. Thus, it should be safe to assume that only mechanism 2 dominates between 25 °C and 60 °C.

Mechanism 2's stress dependence is linear on a log-log plot, yet the experimental measurements in Fig. 3.7b at $T = 60$ °C exhibit what appears to be bi-linear behavior. Higher than expected $\dot{\bar{\varepsilon}}^{\mathrm{ss}}$ values at low equivalent stresses have been previously observed (*Bérest et al.*, 2005, 2015). Notably, the $\bar{\varepsilon}^{\mathrm{tr}*}$ values also exhibit a change in slope at about $\bar{\sigma} = 8$ MPa in Fig. 3.8b. Probably a new micro-mechanical mechanism for creep is activated at these low equivalent stresses. Unfortunately, the M-D model in its present form is incapable of capturing this bi-linear behavior. One could use mechanism 1 to model the low equivalent stress regime instead of modeling dislocation climb at high temperatures, but the transient strain limit relation (Eq. (1.12)) cannot capture both low and high equivalent stresses. Therefore, only the medium to high equivalent stress regime will be modeled, until the M-D model can be modified.

Mechanism 2 was calibrated against experimental data in Fig. 3.7 for which $T \leq 60$ °C, and $\bar{\sigma} \geq 8$ MPa. The Nelder-Mead algorithm was again used to select new values of A_2, Q_2, and n_2 by minimizing the following objective function

$$r = \sum_{j=1}^{J} \left[w^{(j)} \left(\ln \dot{\bar{\varepsilon}}_{\mathrm{exp}}^{\mathrm{ss}(j)} - \ln \dot{\bar{\varepsilon}}_{\mathrm{sim}}^{\mathrm{ss}(j)} \right) + w^{(j)} \left(\log_{10} \dot{\bar{\varepsilon}}_{\mathrm{exp}}^{\mathrm{ss}(j)} - \log_{10} \dot{\bar{\varepsilon}}_{\mathrm{sim}}^{\mathrm{ss}(j)} \right) \right]^2, \tag{3.2}$$

where $\dot{\bar{\varepsilon}}_{\mathrm{exp}}^{\mathrm{ss}(j)}$ is the experimental measurement of $\dot{\bar{\varepsilon}}^{\mathrm{ss}}$ in test segment j, $\dot{\bar{\varepsilon}}_{\mathrm{sim}}^{\mathrm{ss}(j)}$ is the simulated value for the same T and $\bar{\sigma}$ as test segment j, and $w^{(j)}$ is the weighting factor for test segment j (see Section 3.3).

The resulting fit is shown in Fig. 3.7, and compared against the legacy argillaceous salt calibration. As expected, calibration 1B does not represent the data where $T > 60$ °C or $\bar{\sigma} < 8$ MPa, but it does represent the rest of the data well. The slope $n_2 = 5.353$ is slightly steeper than the legacy $n_2 = 5.0$ and the height of the line is lower. At $\bar{\sigma} = 10$ MPa and $T = 24$ °C, calibration 1B predicts a 2.4× smaller steady-state creep rate. The fit was also decomposed into mechanism 1 and mechanism 2 in order to verify that mechanism 1 has a negligible contribution for $T \leq 60$ °C.

The transient strain limit parameters K_0, c, and m were calibrated in the same manner as the steady-state mechanism 2 parameters, and resulting fit is shown in Fig. 3.8. As before, calibration 1B represents the medium to high equivalent stress, $T \leq 60$ °C, data well. Most striking, though, is the large difference between calibration 1B and the legacy argillaceous salt calibration. The slope $m = 4.041$ is steeper than the legacy $m = 3$ slope, and the height of the dashed line is much lower. At $\bar{\sigma} = 10$ MPa and $T = 24$ °C, calibration 1B predicts a 6.2× smaller transient strain limit.

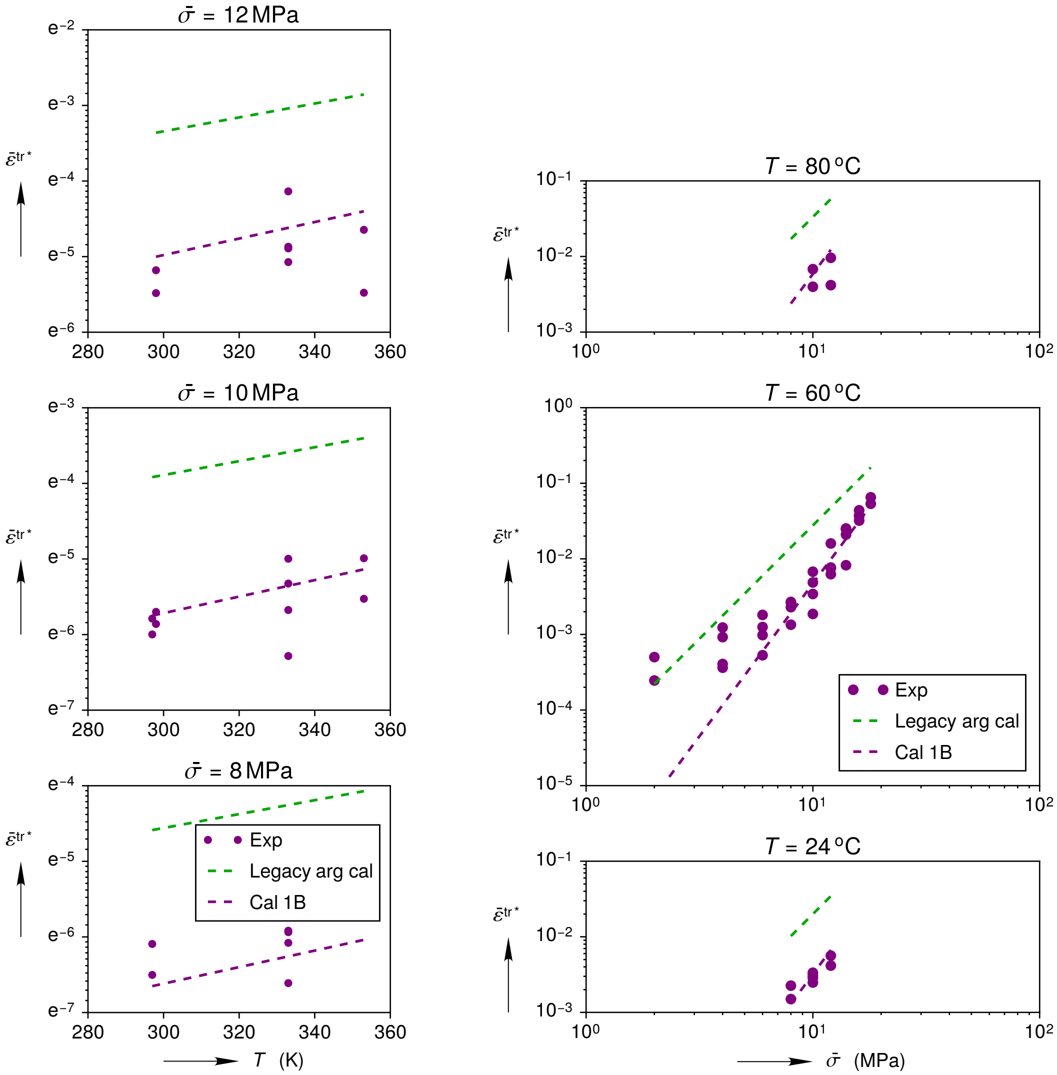

(a) Temperature dependence

(b) Stress dependence

Figure 3.8: Calibration 1B equivalent creep strain transient limit compared against experiments. Experimental data points were obtained from the IfG tests using fitting method B.

The parameters α_{h} and β_{h} that control κ_{h} were calibrated a little differently. The transient rate κ_{h} does not depend on temperature, and the experimental values in Fig. 3.9 do not exhibit a discernible kink at low equivalent stresses. Consequently, all the IfG tests were used to select α_{h} and β_{h}. The objective function used to optimize the parameters was

$$r = \sum_{j=1}^{J} \left[w^{(j)} \left(\kappa_{\text{h}_{\text{exp}}}^{(j)} - \kappa_{\text{h}_{\text{sim}}}^{(j)} \right) \right]^2 , \tag{3.3}$$

where $\kappa_{\mathrm{h_{exp}}}^{(j)}$ is the experimental measurement of κ_{h} in test segment j, $\kappa_{\mathrm{h_{sim}}}^{(j)}$ is the simulated value for the same $\bar{\sigma}$ as test segment j, and $w^{(j)}$ is the weighting factor for test j.

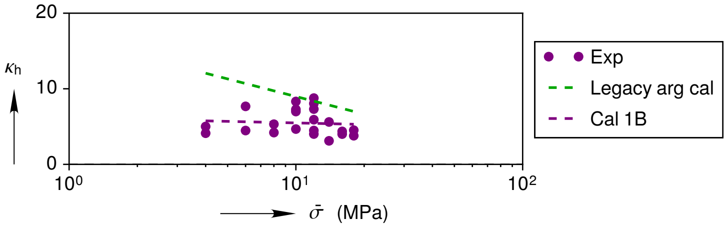

Figure 3.9: Calibration 1B hardening rate variable compared against experiments. Experimental data points were obtained from the IfG tests using fitting method B.

The new calibration 1B κ_{h} line is compared with the legacy argillaceous calibration in Fig. 3.9. The slope of the the calibration 1B is considerably less than the legacy, and line height is again lower than the legacy line.

To end this section, the legacy clean salt and legacy argillaceous salt calibrations are listed next to the two new calibrations in Table 3.1. The legacy calibrations are the same as those listed in *Munson et al.* (1989); *Butcher* (1997), and the colored parameters indicate deviations from the legacy clean salt calibration.

One important clarification should be made. Table 1 in *Munson* (1997) lists $K_0 = 1.783 \times 10^6$ for the argillaceous salt, but all other references before 1997 found by the current author have $K_0 = 2.470 \times 10^6$. The $K_0 = 1.783 \times 10^6$ was probably just a typographical error. Unfortunately, the error seems to have propagated into *Argüello and Holland* (2015); *Argüello* (2015), where they also claim they used $K_0 = 1.783 \times 10^6$. The input file, however, for the "all salt" simulation in *Argüello and Holland* (2015) had $K_0 = 2.470 \times 10^6$. To verify further, the simulation was rerun with $K_0 = 2.470 \times 10^6$ and $K_0 = 1.783 \times 10^6$. The simulation with $K_0 = 2.470 \times 10^6$ returned the exact same result as Figure 3 in *Argüello and Holland* (2015), while the simulation with $K_0 = 1.783 \times 10^6$ gave significantly smaller closures.

Table 3.1: Munson-Dawson Calibrations. (Colors highlight deviations from the legacy clean salt calibration.)

Parameter	Units	Legacy Clean Salt	Legacy Argillaceous Salt	Cal 1A	Cal 1B
μ	GPa	12.4	12.4	12.4	12.4
K	GPa	20.7	20.7	20.7	20.7
A_1	s^{-1}	8.386×10^{22}	1.407×10^{23}	8.386×10^{22}	8.386×10^{22}
Q_1/R	K	12580.5	12580.5	12580.5	12580.5
n_1	–	5.5	5.5	5.5	5.5
A_2	s^{-1}	9.672×10^{12}	1.314×10^{13}	3.273×10^{13}	1.074×10^{14}
Q_2/R	K	5032.2	5032.2	4995	5177
n_2	–	5.0	5.0	5.249	5.353
$\bar{\sigma}_0$	MPa	20.57	20.57	20.57	20.57
B_1	s^{-1}	6.086×10^{6}	8.998×10^{6}	6.086×10^{6}	6.086×10^{6}
B_2	s^{-1}	3.034×10^{-2}	4.289×10^{-2}	3.034×10^{-2}	3.034×10^{-2}
q	–	5335	5335	5335	5335
K_0	–	6.275×10^{5}	2.470×10^{6}	4.607×10^{8}	3.918×10^{8}
c	K^{-1}	9.198×10^{-3}	9.198×10^{-3}	1.085×10^{-2}	1.093×10^{-2}
m	–	3.0	3.0	4.083	4.041
α_h	–	-17.37	-14.96	-3.661	3.367
β_h	–	-7.738	-7.738	-5.797	-0.6838
α_r	–	0.58	0.58	0.58	0.58
β_r	–	0.0	0.0	0.0	0.0
α	K^{-1}	45.0×10^{-6}	45.0×10^{-6}	45×10^{-6}	45×10^{-6}
ρ	kg/m^3	2300	2300	2300	2300

Chapter 4

Closure Predictions Using the New Calibrations

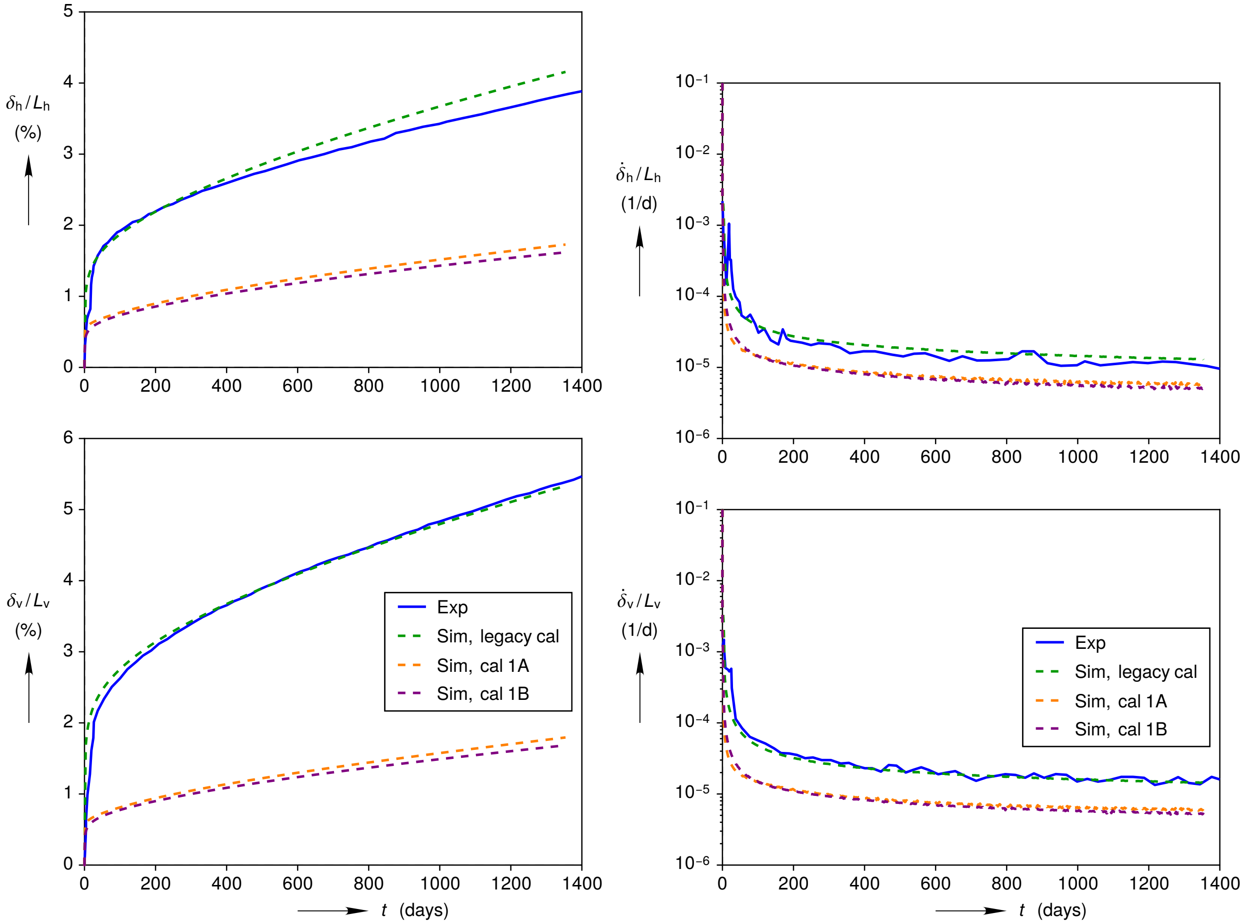

(a) Closure

(b) Closure Rates

Figure 4.1: Predictions of the two new M-D model calibrations compared against the experimental measurements of Room D horizontal and vertical closure.

To assess the impact of calibration 1A and calibration 1B, the new M-D model parameter sets were input into two simulations of Room D. All the changes used to resolve the the numerics in Section 2.2 were utilized, the room corners were rounded, and the boundary conditions were those shown in Fig. 2.10b. The new M-D model calibrations both considerably reduce the predicted room closure (see Fig. 4.1a). At $t = 50$ days, the new calibrations under-predict the horizontal closure measurements by about 2.5× and the vertical closure measurements by about 3.2×. By $t = 1,354$ days, these have reduced only slightly to 2.3× and 3.1×, respectively. Thus, the bulk of the discrepancy between the predictions and the measurements originates in the first 50 days. Fig. 4.1b also compares the closure rates, since the rates are far more important than the initial transient jump for long term waste isolation. The horizontal and vertical closure rates are under-predicted by about 2.1× and 2.8×, respectively, at $t = 1,354$ days.

As discussed in Appendix A.9, the calibration 1B simulation was subsequently converted to the Joint Project III setup for the comparison of salt constitutive models.

4.1 Open Questions

The causes for the poor match between the calibration 1A / 1B predictions and the measurements in Fig. 4.1 are not immediately apparent. This section will chronicle the issues that are currently being considered. It is by no means exhaustive, and some issues have been investigated more than others.

4.1.1 Creep behavior at low equivalent stresses

The new M-D model calibrations both significantly under predict creep at low equivalent stresses. As displayed in Figs. 3.7b and 3.8b, the steady-state strain rate and the transient strain limit exhibit bi-linear behavior, while calibration 1B (and 1A) can only capture the behavior for $\bar{\sigma} \geq 8$ MPa. Increasing the creep at low equivalent stresses would clearly increase the amount of room closure, but would it be significant? The equivalent stress contours in Fig. 4.2 suggest it would be. The strains might be small, but the vast majority of salt within 50 m of room D has low equivalent stress. Integrating small strains over the simulation volume may add up to a significant displacement.

4.1.2 Extent of the Simulation Area

A question related to the creep at low equivalent stresses is, "How far away should the simulation boundaries be from the room?" According to *Munson et al.* (1986), "The right boundary distance (50 m) was chosen so that room response would not be affected by boundary conditions." A distance of 50 m may have been far enough with the old 1983 reference law used to create the prediction in Fig. 1.11, but it does not appear to be far enough when the model comes closer to predicting the closure measurements. The traction on the right boundary is plotted in Fig. 4.3 for a clean salt simulation without any clay seams, and an all

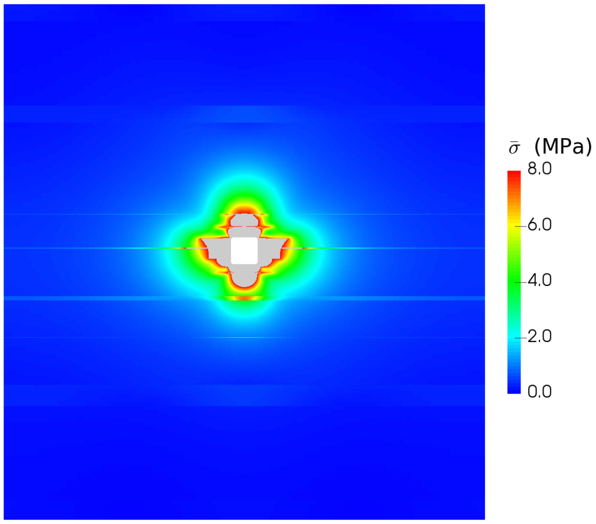

Figure 4.2: Distribution of equivalent stresses below 8 MPa at $t = 0$. (Equivalent stresses above 8 MPa are colored gray.)

clean salt simulation with sliding at the clay seams. Both simulations use the legacy clean salt calibration and are compared at $t = 1,354$ days. The traction distribution is non-linear, less than the lithostatic pressure, and quite erratic if the clay seams are included. If the right boundary was far enough away from the disturbance created by the void of Room D, then the traction distribution would be lithostatic. To the left of Room D, the distance to the next closest room (room A3) is 85.3 m (see Fig. 1.2). This is not close, but it is not far enough away to completely rule out interactions between the rooms. Future simulations should reassess how far away the top, bottom, left and right boundaries need to be such that increasing the distance further has no impact on the room closure.

4.1.3 1983 reference stratigraphy versus Munson 1989 stratigraphy

The 1983 reference stratigraphy was agreed upon by analysts, geologists, geophysicists, and mining engineers from the Department of Energy, TSC/D'Appolonia, and Sandia. *Munson et al.* (1989) changed the idealized stratigraphy from mostly clean salt to mostly argillaceous salt, purely based on the visual appearance of cores drilled 15.2 m above and below Room D. More recently, Dennis Powers, a consulting geologist, was contracted by Sandia to inspect cores from the Salt Disposal Investigations (SDI) area (*Powers*, 2016). The cores (SDI-BH-00004 and SDI-BH-00005) came from 15.5 m boreholes above and below the intersection of N780 and E1310. He concluded, "This study does not sustain the assessment of *Munson et al.* (1989) that all of the halite within the reference stratigraphy, with the exception of halite above and below anhydrite a, could or should be treated as argillaceous halite." He, on the other hand, stopped short of endorsing the 1983 reference stratigraphy, presumably because "[t]here appears to be sparse data in which the weight % of clay can be compared to

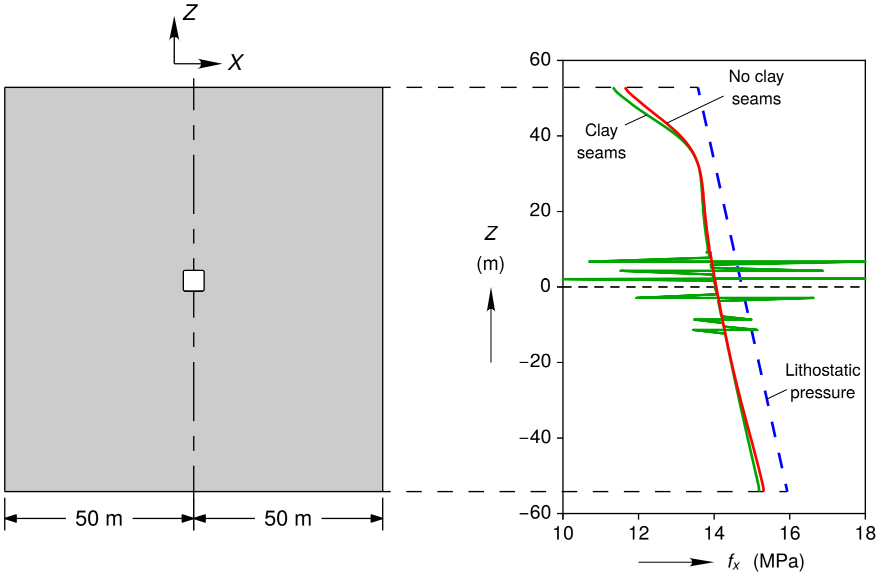

Figure 4.3: Horizontal traction (in the X-direction) along the right boundary of two all clean salt simulations at $t = 1,354$ days. Both simulations used the legacy clean salt calibration.

mechanical behavior." Without a correlation between non-halite components and mechanical behavior, it is difficult to decide where to draw the line between clean and argillaceous salt. Dennis Powers's evaluation of the various stratigraphies is expected to continue. In the end, the WIPP community needs to reach a consensus on an official stratigraphy for geomechanical modeling.

4.1.4 Creep Behavior of Clean Salt and Argillaceous Salt

Munson et al. (1989) chose to distinguish between clean and argillaceous salt based on the experiments in *Senseny* (1986). Similar differences between clean and argillaceous salt were later found in *Mellegard and Pfeifle* (1993). Fig. 4.4 compares the legacy clean and argillaceous values of $\dot{\bar{\varepsilon}}^{\mathrm{ss}}$ and $\bar{\varepsilon}^{\mathrm{tr}*}$. These values were copied verbatim from Table 4-1 and 4-2 in *Mellegard and Pfeifle* (1993)[1] [2]. Despite scatter in the measurements, legacy argillaceous salt creeps more than clean salt at all temperatures and stresses.

This result is inconsistent with the IfG measurements on the 2013 cores in Fig. 3.5, so the legacy and IfG measurements are directly compared in Fig. 4.5. The IfG only performed four room temperature tests, so the 60 °C tests were shifted down to 25 °C according to the temperature dependence in Eq. (1.10) and Eq. (1.12). The steady-state strain rates were

---

[1] Although *Munson et al.* (1989) pointed out that the legacy measurements prior to *Senseny* (1986) did not include the inelastic loading strains, *Mellegard and Pfeifle* (1993) state, "The transient strain limits reported in Tables 4-1 and 4-2 are sometimes larger than those reported in the original references because the inelastic loading strains have been included here."

[2] *Mellegard and Pfeifle* (1993) has a typo in Table 4-1. Specimen 9-2655 should be specimen 9-2625.

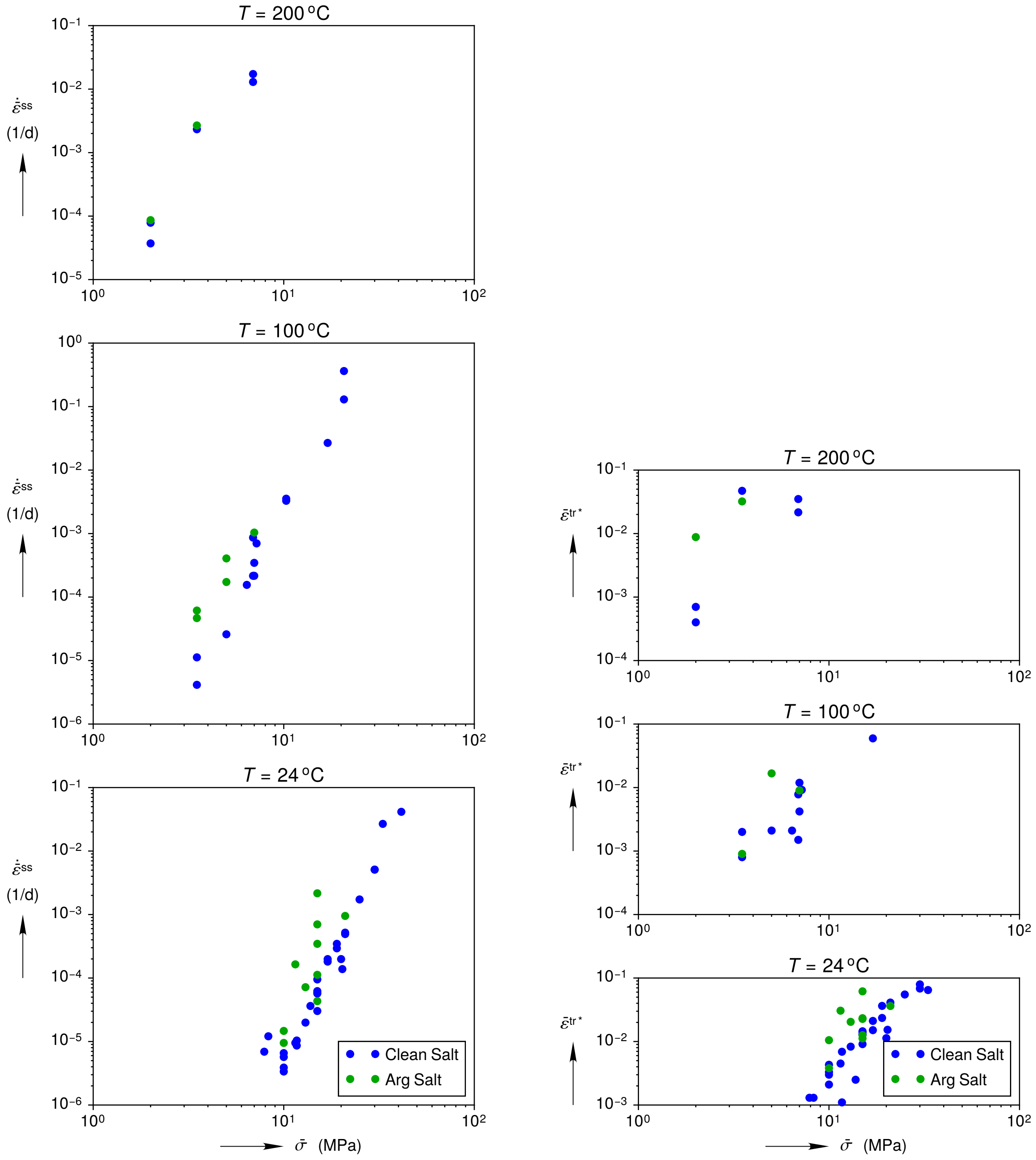

(a) Steady State Rate

(b) Transient Limit

Figure 4.4: Legacy clean and argillaceous salt creep experiments compared All experimental data points were were copied verbatim from Table 4-1 and 4-2 in *Mellegard and Pfeifle* (1993)

multiplied by $\exp\left[-Q_2/R\left(1/T^{(1)} - 1/T^{(2)}\right)\right]$, and the transient strain limits were multiplied by $\exp\left[c\left(T^{(1)} - T^{(2)}\right)\right]$, where $T^{(1)} = 298$ K, $T^{(2)} = 333$ K, $Q_2/R = 4995$ K, and $c = 1.085 \times 10^{-2}$ K^{-1}. (The values for Q_2/R and c came from calibration 1A.) In addition, the legacy and IfG experimental procedures were not identical. Keeping these caveats in mind, the legacy and IfG measurements in Fig. 4.5 agree reasonably well for the clean salt, but not for the argillaceous salt. The legacy argillaceous salt seems to creep more than the 2013 argillaceous salt.

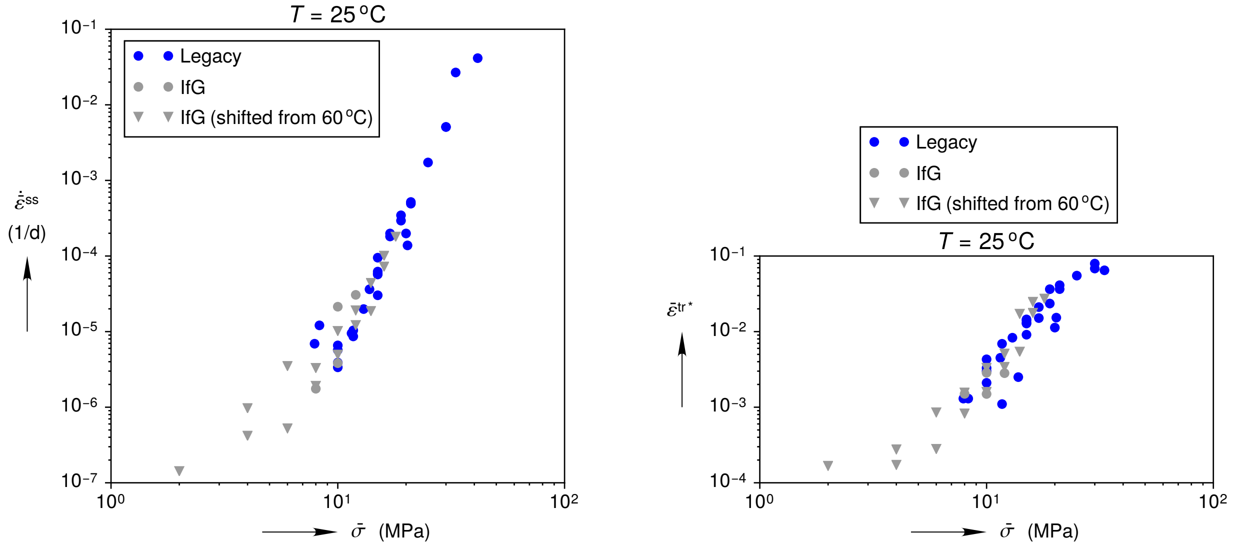

(a) Clean salt, steady-state rate

(b) Clean salt, transient limit

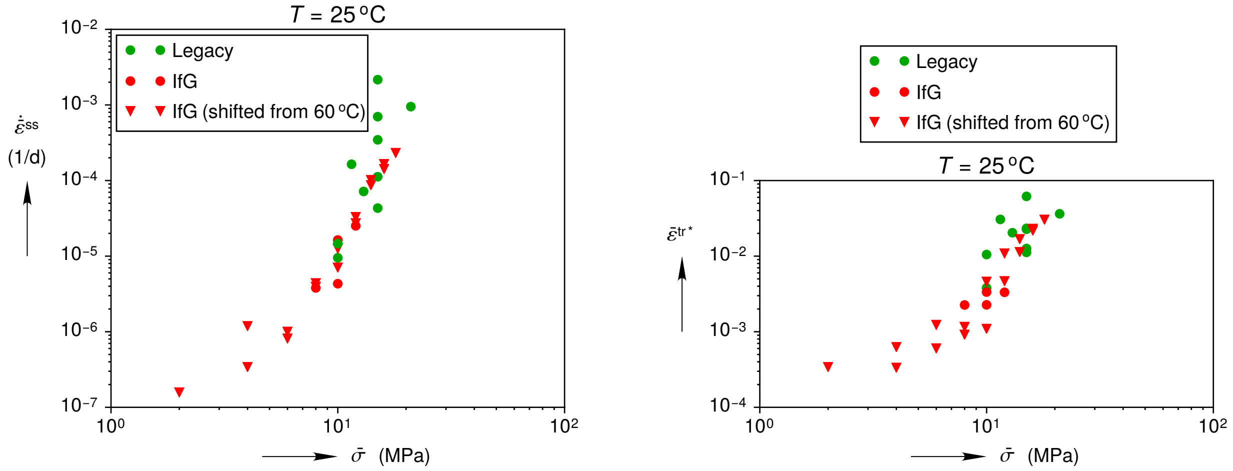

(c) Argillaceous salt, steady-state rate

(d) Argillaceous salt, transient limit

Figure 4.5: IfG and legacy creep experiments compared. IfG data points were obtained using method A. Legacy data points were copied verbatim from Table 4-1 and 4-2 in *Mellegard and Pfeifle* (1993).

The root of the discrepancy between the legacy argillaceous salt and 2013 core argillaceous salt is unknown. The report by *Senseny* (1986) is perhaps the only study to measure the composition of clean and argillaceous WIPP salt specimens before creep testing. He found that, "[t]he average water and EDTA insoluble content of the argillaceous salt was 1.5 to 0.75 %, respectively." Yet, "... the small amount of insolubles [in] the argillaceous specimens correspond to systematic increases in the creep deformation over that of clean specimens. The differences obtained are usually small, as less than an order of magnitude difference in the steady-state strain rate is generally observed. This result is in contrast to that obtained by *Hansen et al.* (1988b). In their study using salt from the Palo Duro Basin, no influence of clay impurities on creep deformation was detected for impurity contents up to 25 percent."

Salt creep's sensitivity to moisture may be one potential reason for the difference between the *Senseny* (1986) and *Hansen et al.* (1988b) results. According to *Senseny* (1986), "[t]he argillaceous salt was sealed after drilling, but the clean salt was not." Once the cores arrived at RE/SPEC and the specimens were prepared, the "[a]rgillaceous specimens were immediately sealed by wrapping in aluminum foil and dipping in plastic coating. They remained sealed until they were jacketed for testing. Clean specimens were not sealed." Similar statements can be found in *Mellegard and Pfeifle* (1993). All the 2013 cores, on the other hand, were treated the same way. They were packaged to avoid exposure to large volumes of air (see Section 3.1), and the creep specimens were drilled out of the larger 300 mm×600 mm cores. Presuming the 2013 core preparation was equivalent to sealing, then one would expect the 2013 cores to creep similar to the legacy argillaceous cores. The data in Fig. 4.5, however, shows that the 2013 cores creep similar to the legacy clean cores. Thus, the selective sealing the legacy argillaceous cores does not fully explain things. To further complicate matters, the 2013 cores were drilled decades after the drifts were excavated. The constant flow of air through the drift may have desiccated the salt surrounding the drifts. *Salzer et al.* (2015) found the clean and argillaceous salt contained roughly 0.15 % and 0.35 % water content, respectively, but moisture content was not measured on the legacy creep specimens, so a direct comparison is not possible.

Another potential reason for the increased creep in the legacy argillaceous salt is cores from one location at WIPP may behave differently than cores from another location. *Senseny* (1986) and *Mellegard and Pfeifle* (1993) say the specimens were cored from the ribs of the experiment rooms at the WIPP. No further information is given, so the drill sites cannot be pinpointed as was done for the 2013 cores in Section 3.1.

This discussion underscores the need to (1) always document where cores came from at WIPP, (2) seal all specimens immediately after drilling, and (3) measure the composition and moisture content before mechanical testing. In the event that composition plays a role, it may be necessary to also investigate the spatial distribution of the impurities in the halite microstructure. Finely dispersed particles may impact the mechanical behavior very differently than large inclusions at the grain boundaries, for example.

4.1.5 Lost Transient Strains

All the 2013 cores were extracted from drifts, but recall that *Munson et al.* (1989) trusted creep specimens that came from boreholes, such as ERDA-9, more than specimens that came from drifts for $\bar{\varepsilon}^{\mathrm{tr}*}$ measurements. They argued that the salt surrounding a drift experiences a significant amount of transient strain after the drift is excavated. A specimen extracted from near that drift will have undergone a degree of deformation. Some of the transient strain is not accounted for and is often referred to as "lost" transient strain. For this reason, *Munson et al.* (1989) placed the transient strain limit at the upper edge of the clean salt experimental data in Fig. 1.12c.

Two studies of dislocation density in salt crystals support the assertion that drift cores should not be considered virgin. *Hansen* (1988) compared the dislocation density of specimens extracted from the ribs of drifts at WIPP against that of ERDA-9 specimens at the Room D horizon. Dislocation density increases as salt work hardens, and *Hansen* (1988) found that the dislocation density of the drift specimens was two to three times higher than those of the ERDA-9 salt specimens. In a follow-up study, *Hansen et al.* (1988a) found, "dislocation density varies monotonically as a function of horizontal depth into the rib, ranging from 5.4 to 2.4×10^{7} cm^{-2} between 0.3 and 14.3 m depth, respectively. Density of the laterally equivalent ERDA-9 salt is 1.7×10^{7} cm^{-2}." As mentioned in Section 3.1, the horizontal depth of the 2013 cores ranged from 0.7 m to 4.9 m.

To quantify the amount of lost transient strain, *Senseny* (1990) performed three creep tests on ERDA-9 cores from the Room D horizon and three annealed drift core specimens. *Senseny* (1990) heated drift cores to 200 °C for 65 hours to anneal them. He compared his ERDA-9 results to existing results on drift core on a log $\bar{\varepsilon}^{\mathrm{tr}}$ vs. log $\bar{\sigma}$ plot, but he did not include his annealed drift core results, or results from ERDA-9 cores from other elevations. Fig. 4.6 gives a more holistic picture, with solid markers for drift core specimens, and hollow markers for borehole core specimens or annealed drift core specimens. This plot includes all but two of the legacy clean salt creep experiments (the two performed at $T = 70$ °C).

A first glance at the values of $\bar{\varepsilon}^{\mathrm{tr}*}$ in Fig. 4.6c suggests that there might not be a systematic difference between drift cores and borehole cores. On the other hand, the approximate elevation of the borehole cores relative to room D have been delineated, based on the specimen IDs and depths listed in *Hansen and Mellegard* (1977); *Wawersik and Hannum* (1979); *Senseny* (1990)[3]. If one focuses on the drift cores and the borehole cores at Room D (ignore the triangle markers), the annealed cores and the borehole cores do have higher $\bar{\varepsilon}^{\mathrm{tr}*}$ values than the drift cores at room temperature. Presumably, the borehole cores from other elevations (triangle markers) do not agree with the borehole and annealed cores from Room D due to creep property variations with respect to elevation. (This is probably why *Munson et al.* (1989) only used the $\bar{\varepsilon}^{\mathrm{tr}*}$ measurements that came from cores at the elevation of Room D to select K_0.) The annealed drift cores and the borehole cores at the elevation of Room D have roughly 2× the transient strain of drift cores (*Senseny*, 1990), which is not large on the log scale of Fig. 4.6c. That being said, the comparison was done at medium to high equivalent stresses. The difference between borehole / annealed core versus work hardened

---

[3] The four specimens from 11.8 ± 0.8 m above Room D are listed in *Mellegard and Pfeifle* (1993) and *Mellegard and Munson* (1997) as clean salt specimens, even though they would be classified as argillaceous salt specimens according to the Munson 1989 stratigraphy. Herein, they remain designated as clean salt for simplicity.

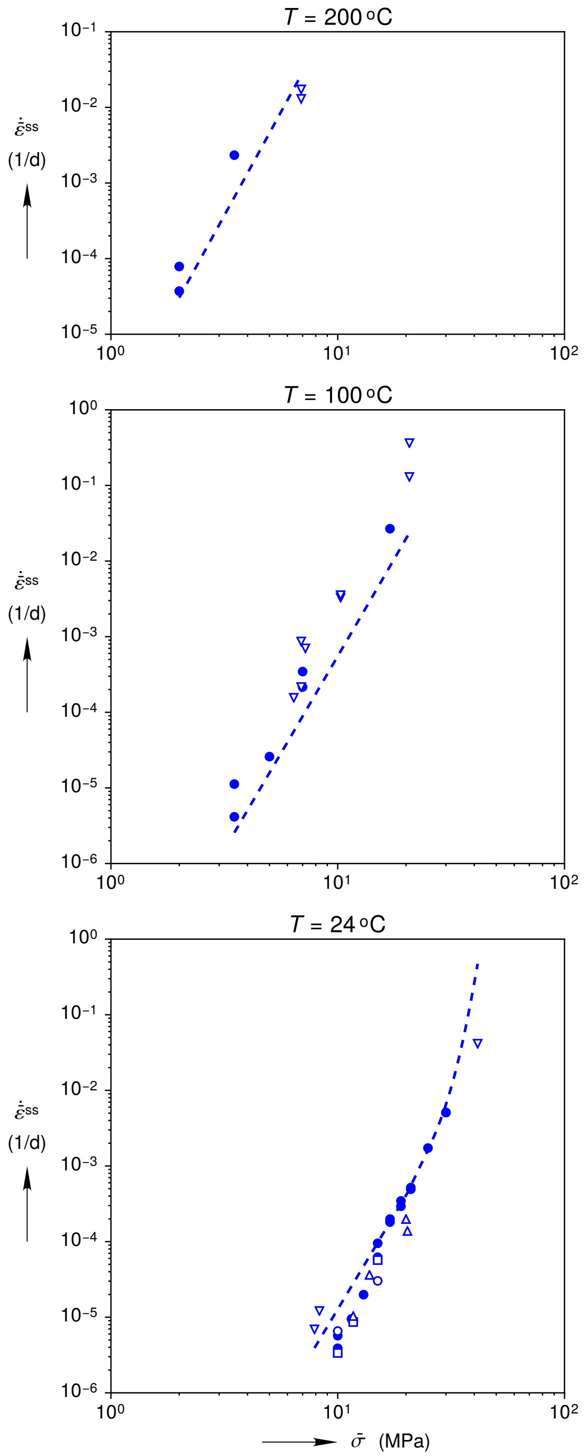

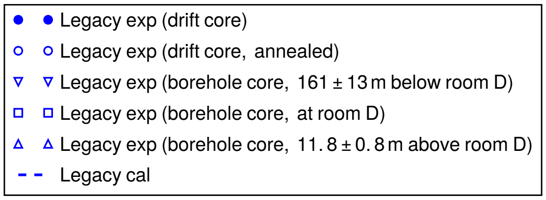

(b) Legend

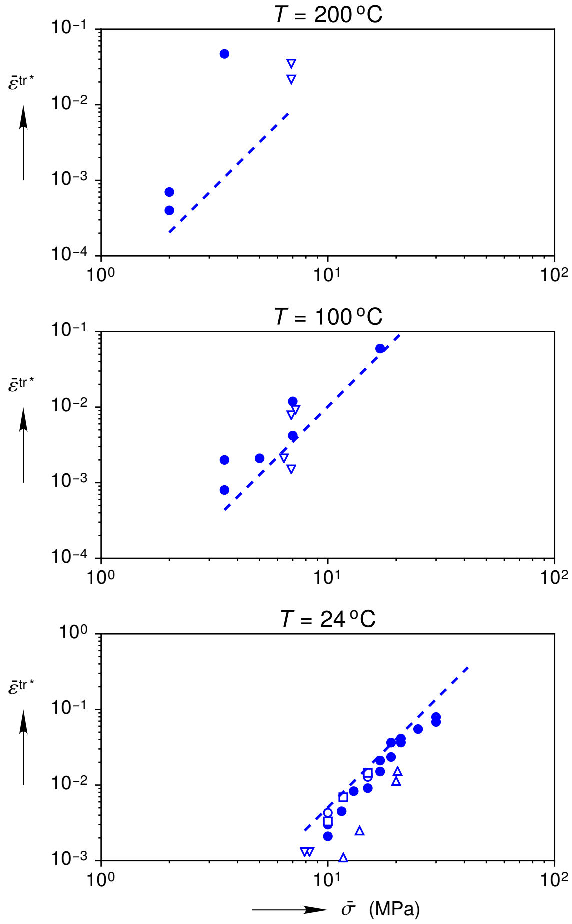

(a) Steady state rate

(c) Transient Limit

Figure 4.6: Legacy clean salt MD model calibration compared against clean salt creep measurements separated into various catagories. All experimental data points were were copied verbatim from Table 4-1 in *Mellegard and Pfeifle* (1993)

drift cores may become more significant at low equivalent stresses.

Creep tests on argillaceous borehole cores were not available in 1989, which is why *Munson et al.* (1989) felt justified placing the transient strain limit well above the argillaceous salt experimental data in Fig. 1.12c. New tests on borehole cores have not been performed since then, but a few tests were performed on argillaceous drift cores since 1989. Fig. 4.7 compares the legacy argillaceous salt calibration against all the legacy argillaceous salt experiments. Notably, *Mellegard and Pfeifle* (1993) performed five room temperature tests on argillaceous salt specimens and two of them produced $\bar{\varepsilon}^{\mathrm{tr}*}$ values that agree with the legacy argillaceous salt calibration. The room temperature plot in Fig. 4.7b makes the argillaceous $K_0 = 2.470 \times 10^{-6}$ value less speculative than the data that was available in 1989 (see Fig. 1.12c).

4.1.6 Sliding at clay seams

Morgan et al. (1986) found that reducing the coefficient of friction from $\eta = 0.4$ to 0 doubled the horizontal closure prediction of the south drift. This result is useful to get a sense of the sensitivity, but the clay seams are most likely not frictionless. *Munson et al.* (1989), in contrast, treated η as a free parameter and set it to 0.2. This report also used $\eta = 0.2$, except when the clay seams were eliminated to comply with the Joint Project III setup (see Fig. A.43a). If clay seams are not allowed to slide, the horizontal and vertical closures decrease by 19.4 % and 27.0 %, respecitvely, at $t = 1,354$ days. Clearly, the clay seam behavior is too important to be simplified to Coulomb friction with η a free parameter. A laboratory program to test clay seams in direct shear could provide the data to develop a proper model for the seams (see *Minkley and Mühlbauer* (2007) for an example), and an underground *in-situ* test could help calibrate and/or validate such a model.

4.1.7 Anhydrite strength

Similar to *Argüello and Holland* (2015); *Argüello* (2015), it was found here that including the anhydrite layers instead of treating them as salt decreased horizontal and vertical closures by about 20 % at $t = 1,354$ days. *Morgan and Krieg* (1984) selected the Drucker-Prager model parameters based on measurements of the yield and ultimate strength of anhydrite in *Teufel* (1981); *Senseny et al.* (1983). The Joint Project III partners, however, selected a Mohr-Coulomb model with lower strengths. The *Morgan and Krieg* (1984) parameters, in their opinion, were too strong compared to values usually employed in the German salt community. In a simulation without any clay seams, the weaker Mohr-Coulomb model increased the horizontal and vertical room closure by 15 % and 19 % compared to the legacy anhydrite model, at $t = 1,354$ days (see Fig. A.43a). Thus, the room closure is sensitive to the range of possible model parameters for the anhydrite model. A critical eye should assess the existing anhydrite calibration in *Morgan and Krieg* (1984) and any new experimental data in the literature. Analogous to the clay seams, a laboratory program may be necessary to characterize the anhydrite mechanical behavior properly.

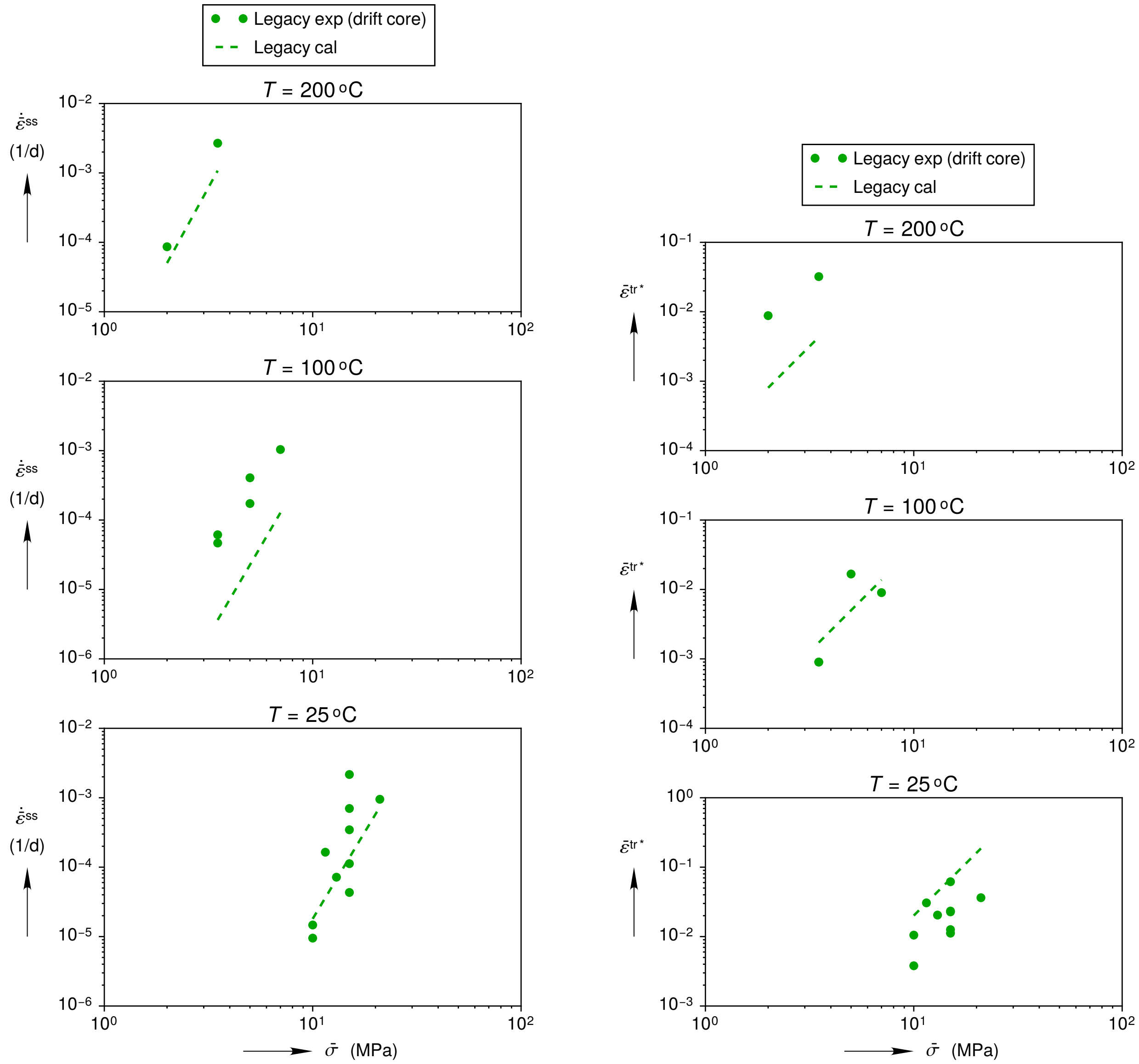

(a) Steady State Rate (b) Transient Limit

Figure 4.7: Legacy argillaceous salt MD model calibration compared against argillaceous salt creep measurements separated into various catagories. All experimental data points were were copied verbatim from Table 4-2 in *Mellegard and Pfeifle* (1993)

Chapter 5

Conclusion

This report details Sandia's participation in Joint Project III and Joint Project WEIMOS over the past year. The Joint Projects are U.S. / German collaborations, which seek to improve thermo-mechanical simulations of salt repositories through enhancing rock salt constitutive models and general simulation techniques. Participants calibrate their rock salt constitutive models against laboratory experiments, and then benchmark their models against underground experiments, such as Room D.

Room D was an isothermal drift in the Waste Isolation Pilot Plant (WIPP), where careful measurements recorded the horizontal and vertical closure between 1984 and 1991. Initial finite element simulations of Room D under predicted the vertical closure by 4.5×, prompting *Munson et al.* (1989) to liberally change the salt constitutive model, the constitutive model parameters, the stratigraphy, and the clay seam coefficient of friction. The changes resolved the discrepancies between simulations and measurements, but *Munson et al.* (1989) candidly acknowledged substantial uncertainties in specific model parameters.

Adjusting the model to match underground experiments is acceptable for engineering analyses, in the current author's opinion, especially if one can capture other underground experiments without further model adjustments. For example, it appears the modifications in *Munson et al.* (1989) enabled relatively successful comparisons with six other closure experiments at WIPP (*Munson*, 1997). The Joint Project participants, however, attempt to predict the evolution of the underground based on laboratory experiments *alone*. This approach requires a deeper scientific basis, but it improves confidence in model predictions and will be necessary for the next-generation repository, particularly if it is in a new location.

The push towards laboratory-based model predictions was begun by updating the legacy simulations of Room D. *Argüello and Holland* (2015) previously showed that the anhydrite layers reduce the vertical closure predictions by about 20 %. A follow-up study, however, had trouble achieving mesh convergence (*Argüello*, 2015). Here, the numerical issues were resolved after a significant effort and mesh convergence was demonstrated. The numerical changes essentially reversed the effect of the anhydrite layers, causing the simulations to agree with the measurements.

New clean salt and argillaceous salt cores were extracted from drifts at the WIPP and sent to Germany in 2013. The Joint Project partners generously performed a battery of triaxial creep tests, strength tests, petro-physical tests, and permeability tests. They, surprisingly, found virtually no difference between the clean and argillaceous salt creep behavior. Upon analyzing the data herein, the same conclusion was reached. The creep tests were also used to create two new Munson-Dawson constitutive model calibrations. The simulations using the two calibrations both under predicted vertical closure of Room D by about 3.1×. The majority of the difference occurred in the first 50 days, because the simulations failed to capture the large transient strain jump following the excavation of Room D.

Several potential causes for the differences between the predictions and the measurements are being considered. The current list includes

1. Creep behavior at low equivalent stresses
2. Extent of the simulation area
3. 1983 reference stratigraphy versus Munson 1989 stratigraphy
4. Creep behavior of clean salt versus argillaceous salt
5. Lost transient strains
6. Sliding at clay seams
7. Anhydrite strength

The Joint Project partners have already begun to tackle the first issue by planning more low equivalent stress creep tests to help reduce uncertainties in that regime. In the mean time, the Munson-Dawson model needs to be modified to capture low equivalent stress creep. Once the modified Munson-Dawson model is recalibrated, the second issue can be addressed by simply changing the size of the finite element model. The remaining issues will likely require varying levels of modeling, field, and experimental support, but there is reason to be optimistic about the potential for progress.

References

Argüello, J. G., Summary of FY15 results of benchmark modeling activities, *Tech. Rep. SAND2015-6273*, Sandia National Laboratories, Albuquerque, NM, USA; Livermore, CA, USA, 2015.

Argüello, J. G., and J. F. Holland, Two problems to benchmark numerical codes for use in potential HLW salt repositories, in *Mechanical Behavior of Salt VIII*, edited by L. Roberts, K. Mellegard, and F. D. Hansen, pp. 361–371, 2015.

Argüello, J. G., and J. S. Rath, Revisiting the 1980's WIPP Room D and B in-situ experiments: Performing thermo-mechanical simulations of rock salt using a state-of-the-art code suite, in *47th US Rock Mechanics/Geomechanics Symposium*, American Rock Mechanics Association, 2013.

Bérest, P., P. A. Blum, J. P. Charpentier, H. Gharbi, and F. Valès, Very slow creep tests on rock samples, *International Journal of Rock Mechanics and Mining Sciences*, *42*(4), 569–576, 2005.

Bérest, P., J. F. Béraud, H. Gharbi, B. Brouard, and K. DeVries, A very slow creep test on an Avery Island salt sample, *Rock Mechanics and Rock Engineering*, *48*(6), 2591–2602, 2015.

Brannon, R. M., T. J. Fuller, A. F. Fossum, and O. E. Strack, Kayenta: theory and user's guide, *Tech. Rep. SAND2015-0803*, Sandia National Laboratories, Albuquerque, NM, USA; Livermore, CA, USA, 2015.

Butcher, B. M., A summary of the sources of input parameter values for the waste isolation pilot plant final porosity surface calculations, *Tech. Rep. SAND97-0796*, Sandia National Laboratories, Albuquerque, NM, USA; Livermore, CA, USA, 1997.

Callahan, G. D., Crushed salt constitutive model, *Tech. Rep. SAND98-2680*, Sandia National Laboratories, Albuquerque, NM, USA; Livermore, CA, USA, 1999.

Callahan, G. D., A. F. Fossum, and D. K. Svalsta, *Documentation of SPECTROM-32: A Finite Element Thermomechanical Stress Analysis Program*, RE/SPEC, Rapid City, SD, 1986.

Carrasco, R., Cutting head radius for Room B and Room D corners, Personal Communication, 2015.

CUBIT Team, *CUBIT mesh generation environment. Users manual.*, Sandia National Laboratories, Albuquerque, NM, USA; Livermore, CA, USA, 15.0 ed., 2015.

Deal, D. E., et al., Brine sampling and evaluation program: 1988 report, *Tech. Rep. DOE-WIPP-89-015*, Westinghouse Electric Corp., Carlsbad, NM, USA. Waste Isolation Div., 1989.

Düsterloh, U., K. Herchen, K. Lux, K. Salzer, R. M. Gunther, W. Minkley, A. Hampel, J. G. Argüello Jr, and F. D. Hansen, Joint Project III on the comparison of constitutive models for the thermomechanical behavior of rock salt. III. Extensive laboratory test program with argillaceous salt from WIPP and comparison of test results, in *Mechanical Behavior of Salt VIII*, edited by L. Roberts, K. D. Mellegard, and F. D. Hansen, 2015.

Günther, R.-M., K. Salzer, T. Popp, C. Lüdeling, et al., Steady state-creep of rock salt-improved approaches for lab determination and modeling to describe transient, stationary and accelerated creep, dilatancy and healing, in *48th US Rock Mechanics/Geomechanics Symposium*, American Rock Mechanics Association, 2014.

Hansen, F. D., Substructures of undeformed WIPP and ERDA 9 salt, Memorandum, 1988.

Hansen, F. D., Micromechanics of isochoric salt deformation, in *48th US Rock Mechanics/Geomechanics Symposium*, American Rock Mechanics Association, 2014.

Hansen, F. D., and K. D. Mellegard, Creep behavior of bedded salt from southeastern new mexico at elevated temperature, *Tech. Rep. SAND79-7030*, Sandia National Laboratories, Albuquerque, NM, USA; Livermore, CA, USA, 1977.

Hansen, F. D., D. E. Munson, and A. F. Fossum, Substructures of salt from the WIPP site, Poster, American Geophysical Union Fall Conference, 1988a.

Hansen, F. D., P. E. Senseny, T. W. Pfeifle, and T. J. Vogt, Influence of impurities on the creep of salt from the Palo Duro Basin, in *The 29th US Symposium on Rock Mechanics (USRMS)*, American Rock Mechanics Association, 1988b.

Herrick, C., Room B and Room D corner radii estimate, Personal Communication, 2015.

Hindmarsh, A. C., ODEPACK, a systematized collection of ODE solvers, *IMACS transactions on scientific computation*, *1*, 55–64, 1983.

Krieg, R. D., Reference stratigraphy and rock properties for the waste isolation pilot plant (WIPP) project, *Tech. Rep. SAND83-1908*, Sandia National Laboratories, Albuquerque, NM, USA; Livermore, CA, USA, 1984.

Mellegard, K., and D. E. Munson, Laboratory creep and mechanical tests on salt data report (1975-1996), *Tech. Rep. SAND96-2765*, Sandia National Laboratories, Albuquerque, NM, USA; Livermore, CA, USA, 1997.

Mellegard, K. D., and T. W. Pfeifle, Creep tests on clean and argillaceous salt from the waste isolation pilot plant, *Tech. Rep. SAND92-7291*, Sandia National Laboratories, Albuquerque, NM, USA; Livermore, CA, USA, 1993.

Minkley, W., and J. Mühlbauer, Constitutive models to describe the mechanical behavior of salt rocks and the imbedded weakness planes, in *6th Conference on The Mechanical Behavior of Salt-SALTMECH6, Hannover, Germany*, pp. 22–25, 2007.

Morgan, H. S., and R. D. Krieg, Updated Drucker-Prager constants for anhydrite and polyhalite, Memorandum, 1984.

Morgan, H. S., and C. M. Stone, Pretest reference calculation for the overtest for simulated defense high level waste (WIPP Room B in situ experiment), *Tech. Rep. SAND85-0213*, Sandia National Laboratories, Albuquerque, NM, USA; Livermore, CA, USA, 1985.

Morgan, H. S., C. M. Stone, and R. D. Krieg, Use of field data to evaluate and improve drift response models for the waste isolation pilot plant (WIPP), in *The 26th US Symposium on Rock Mechanics (USRMS)*, American Rock Mechanics Association, 1985.

Morgan, H. S., C. M. Stone, and R. D. Krieg, An evaluation of WIPP structural modeling capabilities based on comparisons with south drift data, *Tech. Rep. SAND85-0323*, Sandia National Laboratories, Albuquerque, NM, USA; Livermore, CA, USA, 1986.

Morgan, H. S., M. Wallner, and D. Munson, Results of an international parallel calculations exercise comparing creep responses predicted with three computer codes for two excavations in rock salt, *Tech. Rep. SAND87-2125*, Sandia National Laboratories, Albuquerque, NM, USA; Livermore, CA, USA, 1987.

Munson, D. E., Constitutive model of creep in rock salt applied to underground room closure, *International Journal of Rock Mechanics and Mining Sciences*, *34*(2), 233–247, 1997.

Munson, D. E., and P. Dawson, Constitutive model for the low temperature creep of salt (with application to WIPP), *Tech. Rep. SAND79-1853*, Sandia National Laboratories, Albuquerque, NM, USA; Livermore, CA, USA, 1979.

Munson, D. E., and P. Dawson, Transient creep model for salt during stress loading and unloading, *Tech. Rep. SAND82-0962*, Sandia National Laboratories, Albuquerque, NM, USA; Livermore, CA, USA, 1982.

Munson, D. E., and A. F. Fossum, Comparison between predicted and measured south drift closures at the wipp using a transient creep model for salt, in *The 27th US Symposium on Rock Mechanics (USRMS)*, American Rock Mechanics Association, 1986.

Munson, D. E., T. Torres, and D. Blankenship, Early results from the thermal/structural in situ test series at the WIPP, in *The 27th US Symposium on Rock Mechanics (USRMS)*, American Rock Mechanics Association, 1986.

Munson, D. E., R. Matalucci, D. Hoag, and D. Blankenship, Construction of the thermal/structural interactions in situ tests at the waste isolation pilot plant (WIPP), *Tech. Rep. SAND87-2685*, Sandia National Laboratories, Albuquerque, NM, USA; Livermore, CA, USA, 1987a.

Munson, D. E., T. M. Torres, and R. L. Jones, Pseudostrain representation of multipass excavations in salt, in *The 28th US Symposium on Rock Mechanics (USRMS)*, American Rock Mechanics Association, 1987b.

Munson, D. E., R. Jones, D. Hoag, and J. Ball, Mining development test (Room D): In situ data report (March 1984-May 1988): Waste isolation pilot plant (WIPP) thermal/structural interactions program, *Tech. Rep. SAND88-1460*, Sandia National Laboratories, Albuquerque, NM, USA; Livermore, CA, USA, 1988.

Munson, D. E., A. F. Fossum, and P. E. Senseny, Advances in resolution of discrepancies between predicted and measured in situ WIPP room closures, *Tech. Rep. SAND88-2948*, Sandia National Laboratories, Albuquerque, NM, USA; Livermore, CA, USA, 1989.

Munson, D. E., K. L. DeVries, and G. D. Callahan, Comparison of calculations and in situ results for a large, heated, test room at the waste isolation pilot plant (WIPP), *Tech. Rep. SAND89-2268*, Sandia National Laboratories, 1990a.

Munson, D. E., R. Jones, J. Ball, R. Clancy, D. Hoag, and S. Petney, Overtest for simulated defense high-level waste (Room B): In situ data report (May 1984-February 1988). Waste isolation pilot plant (WIPP) thermal/structural interactions program., *Tech. Rep. SAND89-2671*, Sandia National Laboratories, Albuquerque, NM, USA; Livermore, CA, USA, 1990b.

Munson, D. E., R. Jones, C. Northrop-Salazar, and S. Woerner, Multipass mining sequence room closures: in situ data report. Waste isolation pilot plant (WIPP) thermal/structural interactions program, *Tech. Rep. SAND87-2687*, Sandia National Laboratories, Albuquerque, NM, USA; Livermore, CA, USA, 1992.

Nelder, J. A., and R. Mead, A simplex method for function minimization, *The computer journal*, *7*(4), 308–313, 1965.

Powers, D., Geology of cores from Q room alcove for the DRZ test program, *Tech. rep.*, Consulting Geologist, 2001.

Powers, D., Reference stratigraphy applied to rock mechanics studies for the waste isolation pilot plant: a review-may 2016, Personal Communication, 2016.

Rath, J. S., and J. G. Argüello, Revisiting historical numerical analyses of the waste isolation pilot plant (WIPP) Room B and D in-situ experiments regarding thermal and structural response, *Tech. Rep. SAND2012-7525*, Sandia National Laboratories, Albuquerque, NM, USA; Livermore, CA, USA, 2012.

Reedlunn, B., Quasi-static simulation of the Cattaneo-Mindlin problem in plane strain, Memorandum, 2013.

Rudnicki, J. W., and J. Rice, Conditions for the localization of deformation in pressure-sensitive dilatant materials, *Journal of the Mechanics and Physics of Solids*, *23*(6), 371–394, 1975.

Salzer, K., et al., Joint Project III on the comparison of constitutive models for the thermo-mechanical behavior of rock salt. III. Extensive laboratory test program with argillaceous salt from WIPP and comparison of test results, in *Mechanical Behavior of Salt VIII*, edited by L. Roberts, K. D. Mellegard, and F. D. Hansen, 2015.

Schuhen, M., Origin of 2013 cores, Personal Communication, 2016a.

Schuhen, M., Origin of "old" cores sent to the Technical University of Clausthal, Personal Communication, 2016b.

Senseny, P. E., Triaxial compression creep tests on salt from the waste isolation pilot plant, *Tech. Rep. SAND85-7261*, Sandia National Laboratories, Albuquerque, NM, USA; Livermore, CA, USA, 1986.

Senseny, P. E., Creep of salt from the ERDA-9 borehole and the WIPP workings, *Tech. Rep. SAND89-7098*, Sandia National Laboratories, Albuquerque, NM, USA; Livermore, CA, USA, 1990.

Senseny, P. E., A. F. Fossum, and T. W. Pfeifle, Non-associative constitutive laws for low porosity rocks, *International Journal for Numerical and Analytical Methods in Geomechanics*, *7*(1), 101–115, 1983.

Sierra/Solid Mechanics, *Sierra/solid mechanics user's guide.*, Sandia National Laboratories, Albuquerque, NM, USA; Livermore, CA, USA, 4.40 ed., 2016.

Stone, C. M., Final disposal room structural response calculations, *Tech. Rep. SAND97-0795*, Sandia National Laboratories, Albuquerque, NM, USA; Livermore, CA, USA, 1997a.

Stone, C. M., Santos: A two-dimensional finite element program for the quasistatic, large deformation, inelastic response of solids, *Tech. Rep. SAND90-0543*, Sandia National Laboratories, Albuquerque, NM, USA; Livermore, CA, USA, 1997b.

Teufel, L. W., Mechanical properties of anhydrite and polyhalite in quasi-static triaxial compression, *Tech. Rep. SAND81-0858*, Sandia National Laboratories, Albuquerque, NM, USA; Livermore, CA, USA, 1981.

Wawersik, W. R., and D. W. Hannum, Interim summary of Sandia creep experiments on rock salt from the WIPP study area, *Tech. Rep. SAND79-0115*, Sandia National Laboratories, Albuquerque, NM, USA; Livermore, CA, USA, 1979.

Appendix A

Appendix

A.1 Anhydrite and Polyhalite Material Models

The anhydrite and polyhalite are modeled with a hypoelastic, perfectly plastic, Drucker-Prager model. The elastic behavior is linear elastic (Eqs. (1.2) and (1.3)), the thermal behavior is linear (Eq. (1.4)), and the strain rate is decomposed as

$$\dot{\boldsymbol{\varepsilon}} = \dot{\boldsymbol{\varepsilon}}^{\mathrm{e}} + \dot{\boldsymbol{\varepsilon}}^{\mathrm{th}} + \dot{\boldsymbol{\varepsilon}}^{\mathrm{p}}, \tag{A.1}$$

where $\dot{\boldsymbol{\varepsilon}}^{\mathrm{p}}$ represents the plastic strain rate. Define the first invariant of the stress as I_1 and the second invariant of the deviatoric stress as J_2. The Drucker-Prager yield function g can be expressed in terms of the material constants a and C as

$$g = \sqrt{J_2} - a\, I_1 - C. \tag{A.2}$$

Morgan and Krieg (1984) does not specify the plastic flow potential for the anhydrite or polyhalite models, but the only Drucker-Prager model in SANCHO was the "Soils and Crushable Foams Model", which used (and still uses) a von Mises flow potential. Thus, the non-associated flow rule is

$$\psi = \sqrt{3\, J_2} \tag{A.3}$$

$$\dot{\boldsymbol{\varepsilon}}^{\mathrm{p}} = \lambda \frac{\partial \psi}{\partial \boldsymbol{\sigma}}, \tag{A.4}$$

where λ is the consistency parameter. The anhydrite and polyhalite calibrations specified in *Morgan and Krieg* (1984) are listed in Table A.1 for reference, and the Sierra/Solid Mechanics input syntax can be found in Appendices A.2.4 and A.2.5.

The non-associated flow rule in Eq. (A.4) was used in all the legacy simulations, but the non-associated flow rule produced strain localizations here, as discussed in Section 2.2. The solution was to switch to an associated flow rule

$$\dot{\boldsymbol{\varepsilon}}^{\mathrm{p}} = \lambda \frac{\partial g}{\partial \boldsymbol{\sigma}} \tag{A.5}$$

for all the simulations after that point.

Also, note that the simulations to participate in Joint Project III were performed using a different material model for the anhydrite and polyhalite, as detailed in Appendix A.9.

Table A.1: Anhydrite and Polyhalite Calibrations.

Parameter	Units	Anhydrite	Polyhalite
μ	GPa	27.8	20.3
K	GPa	83.4	65.8
a	–	0.45	0.473
C	MPa	1.35	1.42
α	K^{-1}	20.0×10^{-6}	24.0×10^{-6}
ρ	kg/m^3	2300	2300

A.2 Simulation Files

A.2.1 Example Cubit Journal File

```
#Cubit v15.0, Linux
cubit.cmd('reset')
cubit.set_playback_paused_on_error(False)
error_old = cubit.get_error_count()
cubit.cmd('undo off')
import math
from collections import OrderedDict
import re

sim_ID = 's160511A'

#Define whether to model clay seams as slipping surfaces
clay_seam_slip = True
#Define whether to split each element into 4 elements
split_elements = False
#Define the clay seam slip definition
seam_slip_defn = 'SAND88-2948'
#Define whether to model the anhydrite near the room
anhydrite_at_room = True
#Define the factor to scale the simulation boundaries by
sim_scale_factor = 1.0

#Define the fine element size
#(The Germans used a mesh with 88 elements from the top to the bottom of the room, and
#96 elements from the left to the right of the room.  We will use their horizontal mesh
#density.)
H = 5.5/96
#Define the radius of the fine region
R_fine = 5.5 * 1.6
#Define the coarsening rate
coarsen_rate = 0.36

#Define the total simulation dimensions as defined in SAND88-2948 (elevations relative
#to the bottom of the halite in room)
top_elev = 52.87
```

```
bot_elev = -54.19
width = 100.0
thickness = H

#Define the room dimensions (elevations relative to the bottom of the halite in room)
room_top_elev = 4.42
room_bot_elev = -1.08
room_width = 5.5
room_fillet_radius = 18.0 * 25.4 / 1000.0 #0.00001
room_ctr = [0.0, (room_bot_elev + room_top_elev) / 2.0]

#Increase the simulation dimensions by a factor to see if we have modeled far enough
#away from the room
top_elev = top_elev + (sim_scale_factor - 1.0) * (top_elev - room_ctr[1])
bot_elev = bot_elev + (sim_scale_factor - 1.0) * (bot_elev - room_ctr[1])
width = width * sim_scale_factor

#Define stratigraphy
#
#(bot is the bottom of each layer, relative to the bottom of the halite in the room.
#Clay defines whether there is a sliding layer of clay at the bottom.)
#
#(These definitions come from:
#Munson, D. E. , 1997. "Constitutive Model of Creep in Rock Salt Applied to
#Underground Room Closure,"   International Journal fo Rock Mechanics, Min. Sci.
#Volume 34, Number 2, pp. 233-247. Elsevier Science Ltd.
#The same elevations appear in SAND88-2948. )
layers = OrderedDict( [\
    ('polyhalite_1', dict(bot = -54.19, clay = None)), \
    ('arg_halite_1', dict(bot = -49.99, clay = None)), \
    ('anhydrite_1', dict(bot = -30.60, clay = 'A')), \
    ('arg_halite_2', dict(bot = -26.21, clay = None)), \
    ('anhydrite_2', dict(bot = -16.41, clay = 'B')), \
    ('arg_halite_3', dict(bot = -16.33, clay = None)), \
    ('arg_halite_4', dict(bot = -11.37, clay = 'D')), \
    ('anhydrite_3', dict(bot = -8.63, clay = 'E')), \
    ('arg_halite_5', dict(bot = -7.77, clay = None)), \
    ('arg_halite_6', dict(bot = -3.72, clay = None)), \
    ('arg_halite_7', dict(bot = -2.90, clay = 'F')), \
    ('halite_1', dict(bot = 0.0, clay = 'G')), \
    ('anhydrite_4', dict(bot = 2.10, clay = 'H')), \
    ('halite_2', dict(bot = 2.31, clay = None)), \
    ('arg_halite_8', dict(bot = 4.27, clay = 'I')), \
    ('arg_halite_9', dict(bot = 6.71, clay = 'J')), \
    ('arg_halite_10', dict(bot = 7.77, clay = None)), \
    ('anhydrite_5', dict(bot = 9.16, clay = 'K')), \
    ('arg_halite_11', dict(bot = 9.35, clay = None)), \
    ('arg_halite_12', dict(bot = 10.67, clay = None)), \
    ('arg_halite_13', dict(bot = 13.58, clay = 'L')), \
    ('anhydrite_6', dict(bot = 28.3, clay = 'M')), \
    ('arg_halite_14', dict(bot = 31.86, clay = None)), \
    ('anhydrite_7', dict(bot = 49.38, clay = None))])

if not anhydrite_at_room:
```

```
    layers = OrderedDict( [\
        ('polyhalite_1', dict(bot = -54.19, clay = None)), \
        ('arg_halite_1', dict(bot = -49.99, clay = None)), \
        ('anhydrite_1', dict(bot = -30.60, clay = 'A')), \
        ('arg_halite_2', dict(bot = -26.21, clay = None)), \
        ('anhydrite_2', dict(bot = -16.41, clay = 'B')), \
        ('arg_halite_3', dict(bot = -16.33, clay = None)), \
        ('arg_halite_4', dict(bot = -11.37, clay = 'D')), \
        ('anhydrite_3', dict(bot = -8.63, clay = 'E')), \
        ('arg_halite_5', dict(bot = -7.77, clay = None)), \
        ('arg_halite_6', dict(bot = -3.72, clay = None)), \
        ('arg_halite_7', dict(bot = -2.90, clay = 'F')), \
        ('halite_1', dict(bot = 0.0, clay = 'G')), \
        ('halite_3', dict(bot = 2.10, clay = 'H')), \
        ('halite_2', dict(bot = 2.31, clay = None)), \
        ('arg_halite_8', dict(bot = 4.27, clay = 'I')), \
        ('arg_halite_9', dict(bot = 6.71, clay = 'J')), \
        ('arg_halite_10', dict(bot = 7.77, clay = None)), \
        ('anhydrite_5', dict(bot = 9.16, clay = 'K')), \
        ('arg_halite_11', dict(bot = 9.35, clay = None)), \
        ('arg_halite_12', dict(bot = 10.67, clay = None)), \
        ('arg_halite_13', dict(bot = 13.58, clay = 'L')), \
        ('anhydrite_6', dict(bot = 28.3, clay = 'M')), \
        ('arg_halite_14', dict(bot = 31.86, clay = None)), \
        ('anhydrite_7', dict(bot = 49.38, clay = None))])

if sim_scale_factor > 1.0:
    #Add argillaceous halite layers above and below the region simulated in SAND88-2948,
    #in order to test whether we have modeled far enough away from the room.
    layers = OrderedDict( [\
        ('arg_halite_0', dict(bot = bot_elev, clay = None)), \
        ('polyhalite_1', dict(bot = -54.19, clay = None)), \
        ('arg_halite_1', dict(bot = -49.99, clay = None)), \
        ('anhydrite_1', dict(bot = -30.60, clay = 'A')), \
        ('arg_halite_2', dict(bot = -26.21, clay = None)), \
        ('anhydrite_2', dict(bot = -16.41, clay = 'B')), \
        ('arg_halite_3', dict(bot = -16.33, clay = None)), \
        ('arg_halite_4', dict(bot = -11.37, clay = 'D')), \
        ('anhydrite_3', dict(bot = -8.63, clay = 'E')), \
        ('arg_halite_5', dict(bot = -7.77, clay = None)), \
        ('arg_halite_6', dict(bot = -3.72, clay = None)), \
        ('arg_halite_7', dict(bot = -2.90, clay = 'F')), \
        ('halite_1', dict(bot = 0.0, clay = 'G')), \
        ('anhydrite_4', dict(bot = 2.10, clay = 'H')), \
        ('halite_2', dict(bot = 2.31, clay = None)), \
        ('arg_halite_8', dict(bot = 4.27, clay = 'I')), \
        ('arg_halite_9', dict(bot = 6.71, clay = 'J')), \
        ('arg_halite_10', dict(bot = 7.77, clay = None)), \
        ('anhydrite_5', dict(bot = 9.16, clay = 'K')), \
        ('arg_halite_11', dict(bot = 9.35, clay = None)), \
        ('arg_halite_12', dict(bot = 10.67, clay = None)), \
        ('arg_halite_13', dict(bot = 13.58, clay = 'L')), \
        ('anhydrite_6', dict(bot = 28.3, clay = 'M')), \
        ('arg_halite_14', dict(bot = 31.86, clay = None)), \
```

```
        ('anhydrite_7', dict(bot = 49.38, clay = None)), \
        ('arg_halite_15', dict(bot = 52.87, clay = None))])

if seam_slip_defn == 'SAND88-2948':
    #In SAND2012-7525 and SAND88-2948 the clay seams are labeled A through M, yet they
     ↪  only
    #make D through L (the nine nearest the room) active.  Thus, we turn off the clay
     ↪  seams
    #at -30.60 m, -16.41 m, 28.30 m.
    no_clay_elevs = [-30.6, -16.41, 28.3]
    for no_clay_elev in no_clay_elevs:
        for key in layers.keys():
            if no_clay_elev == layers[key]['bot']:
                layers[key]['clay'] = None

#Switch all clay seams to non-slipping interfaces, if desired.
if not clay_seam_slip:
    for key in layers.keys():
        layers[key]['clay'] = None

#Go through and populate the top elevation keys
layers[layers.keys()[-1]]['top'] = top_elev
prev_key = layers.keys()[-1]
for key in reversed(layers.keys()[:-1]):
    layers[key]['top'] = layers[prev_key]['bot']
    prev_key = key

#Generate the block
cubit.cmd('rotate -90 about X')
cubit.cmd('brick x %r y %r z %r' %(width/2.0, thickness, top_elev - bot_elev))
cubit.cmd('move volume 1 x %r y %r z %r' \
    %(width/4.0, thickness / 2.0, (top_elev - bot_elev)/2.0 + bot_elev))

#Cut out the room
cubit.cmd('create curve location 0 0 %r location %r 0 %r' \
    %(room_top_elev, room_width/2.0 - room_fillet_radius, room_top_elev))
cubit.cmd('create curve location %r 0 %r location %r 0 %r' \
    %(room_width/2.0, room_top_elev - room_fillet_radius, room_width/2.0, \
    room_bot_elev + room_fillet_radius))
cubit.cmd('create curve location %r 0 %r location 0 0 %r' \
    %(room_width/2.0 - room_fillet_radius, room_bot_elev, room_bot_elev))
cubit.cmd('create curve location 0 0 %r location 0 0 %r' %(room_bot_elev, room_top_elev))
cubit.cmd('create curve arc vertex 11 10 radius %r normal 0 -1 0' %(room_fillet_radius))
cubit.cmd('create curve arc vertex 13 12 radius %r normal 0 -1 0' %(room_fillet_radius))
cubit.cmd('create surface curve 13 14 15 16 17 18')
cubit.cmd('sweep surface 7 direction 0 1 0 distance %r' %(thickness))
cubit.cmd('chop volume 1 with volume 2')
cubit.cmd('delete volume 3')

#Slice the block at the layers
for key in layers.keys():
    if layers[key]['bot'] > bot_elev and layers[key]['bot'] < top_elev:
        if layers[key]['clay']:
            cubit.cmd('webcut volume all with plane zplane offset %r noimprint nomerge' \
```

```
                %(layers[key]['bot']))
        else:
            cubit.cmd('webcut volume all with plane zplane offset %r imprint merge' \
                %(layers[key]['bot']))

#Add a slice at the mid height of the room, so that it is easy to extract variables along
#a line.
cubit.cmd('webcut volume all with plane zplane offset %r imprint merge' \
    %((room_top_elev + room_bot_elev)/2.0))

#Cut volumes around room to assist with meshing
cubit.cmd('webcut volume all with cylinder radius ' + str(R_fine) \
    + ' axis y center ' + str(room_ctr[0]) + ' 0 ' + str(room_ctr[1]))

#Imprint and merge the layers (we will add the clay seams later)
cubit.cmd('imprint all')
cubit.cmd('merge all')

#Group each layer's volumes together
for key in layers.keys():
    layers[key]['volumes'] = cubit.parse_cubit_list('volume', \
        "with z_coord >= " + str(layers[key]['bot']) \
        + " and with z_coord <= " + str(layers[key]['top']))

#Specify the mesh

#Define some functions to help with meshing.
tol = 0.0001
def _curve_vertex_coordinates(curve_ID, ctr):
    #Order vertices based on their distance from the room
    vertex_IDs = cubit.get_relatives('curve', curve_ID, 'vertex')
    vertex_dist = []
    for vertex_ID in vertex_IDs:
        vertex = cubit.vertex(vertex_ID)
        vertex_dist.append(math.sqrt((vertex.coordinates()[0]-ctr[0])**2.0 \
            + (vertex.coordinates()[2]-ctr[1])**2.0))
    vertex_IDs = [vertex_IDs[vertex_dist.index(min(vertex_dist))], \
        vertex_IDs[vertex_dist.index(max(vertex_dist))]]
    #Get the vertex coordinates
    vertex_pos = []
    for vertex_ID in vertex_IDs:
        vertex = cubit.vertex(vertex_ID)
        vertex_pos.append(vertex.coordinates())
    return(vertex_IDs, vertex_pos)

def set_size_based_on_dist(curve_IDs, H_0, ctr, coarsen_rate, R_fine):
    for curve_ID in curve_IDs:
        [vertex_IDs, vertex_pos] = _curve_vertex_coordinates(curve_ID, ctr)
        [H_1, H_2] = _calc_size_based_on_dist(H_0, ctr, coarsen_rate, vertex_pos, R_fine)
        cubit.cmd('curve ' + str(curve_ID) + ' scheme bias fine size ' + str(H_1) \
            + ' coarse size ' + str(H_2) + ' start vertex ' + str(vertex_IDs[0]))
        cubit.cmd('curve ' + str(curve_ID) + ' interval soft')

def  _calc_size_based_on_dist(H_0, ctr, coarsen_rate, vertex_pos, R_fine):
```

```
    #Set to H_0 inside R_fine, otherwise, calculate the element sizes based on
    #X and Z distances from 'ctr'
    dist = math.sqrt((vertex_pos[0][0] - ctr[0])**2.0 + (vertex_pos[0][2] - ctr[1])**2.0)
    if dist<R_fine:
        H_1 = H_0
    else:
        H_1 = H_0 * (1.0 + (dist-R_fine) * coarsen_rate)
    dist = math.sqrt((vertex_pos[1][0] - ctr[0])**2.0 + (vertex_pos[1][2] - ctr[1])**2.0)
    if dist<R_fine:
        H_2 = H_0
    else:
        H_2 = H_0 * (1.0 + (dist-R_fine) * coarsen_rate)
    return(H_1, H_2)

#Mesh the front surfaces
curves = cubit.parse_cubit_list('curve', 'with y_coord <= ' + str(tol))
set_size_based_on_dist(curves, H, room_ctr, coarsen_rate, R_fine)
front_surf = cubit.parse_cubit_list('surface', 'with y_coord <= ' + str(tol))
front_surf_str = str(front_surf)[1:-1]
cubit.cmd('surface ' + front_surf_str + ' scheme pave')
cubit.cmd('mesh surface ' + front_surf_str)

#Perform a uniform refinement if requested
if split_elements:
    front_surf = cubit.parse_cubit_list('surface', 'with y_coord <= 0')
    cubit.cmd('volume all scale x 1 y 0.5 z 1')
    thickness = thickness * 0.5
    cubit.cmd('refine surface ' + str(front_surf)[1:-1] + ' numsplit 1')

#Sweep the mesh through the thickness
cubit.cmd('volume all scheme sweep vector 0 1 0')
#Set 'redistribute nodes on' so to preserve the bias during the sweep. (This does the
#same thing as the 'propagate bias' parameter in the sweep-source-target command)
cubit.cmd('volume all redistribute nodes on')

#Mesh thru the thickness
cubit.cmd('volume all interval 1')
cubit.cmd('mesh volume all')

#Find which volumes pertain to which materials
keys = layers.keys()
material_names = []
vol_IDs = []
material_dict = dict()
for key in keys:
    match = re.match(r'(\w+)(_\d+)', key)
    material_names.append(match.group(1))
    vol_IDs.append(layers[key]['volumes'])
#Initialize the dictionary with just the unique materials
unique_material_names = set(material_names)
for unique_material_name in unique_material_names:
    material_dict[unique_material_name] = []
#Populate the dictionary
for material_name, vol_list in zip(material_names, vol_IDs):
```

```
    material_dict[material_name].extend(vol_list)

#Only add in the slip lines after the rest of the mesh has been generated
#This way, the mesh will be identical, regardless of whether you have the slip lines
#on or off.
i = 1000
j = 0
for key in layers.keys()[1:]:
    if layers[key]['clay'] is not None:
        merged_surfaces = cubit.parse_cubit_list('surface', \
            'with z_coord >= ' + str(layers[key]['bot']-tol) \
            + ' and with z_coord <= ' + str(layers[key]['bot']+tol))
        cubit.cmd('unmerge surface ' + str(merged_surfaces)[1:-1])
        #(Note: you cannot assume that the previously merged surfaces all
        #remain on the top or the bottom of the clay seam.  Cubit can randomly
        #chose which surfaces remain on the top and which are on the bottom.
        #Instead we explicitly specify that the master surfaces must be in the
        #volumes above the clay seam.)
        master_surfaces = cubit.parse_cubit_list('surface', \
            'in volume ' + str(layers[key]['volumes'])[1:-1] \
            + ' with z_coord >= ' + str(layers[key]['bot']-tol) \
            + ' and with z_coord <= ' + str(layers[key]['bot']+tol))
        #Get the slave surfaces by subtracting the master surfaces from all the
        #surfaces at the clay seam
        surfaces = cubit.parse_cubit_list('surface', \
            'with z_coord >= ' + str(layers[key]['bot']-tol) \
            + ' and with z_coord <= ' + str(layers[key]['bot']+tol))
        slave_surfaces = list(set(surfaces) - set(master_surfaces))
        j = j + 1
        i = i + 1
        cubit.cmd('sideset ' + str(i) + ' surface ' + str(master_surfaces)[1:-1])
        cubit.cmd('sideset ' + str(i) + ' name ' \
            + '\'SS_clay_' +  layers[key]['clay'] + '_master\'')
        i = i + 1
        cubit.cmd('sideset ' + str(i) + ' surface ' + str(slave_surfaces)[1:-1])
        cubit.cmd('sideset ' + str(i) + ' name ' \
            + '\'SS_clay_' +  layers[key]['clay'] + '_slave\'')

#Create the blocks
for i, key in enumerate(material_dict.keys()):
    cubit.cmd('Block ' + str(i+1) + ' volume ' + str(material_dict[key])[1:-1])
    cubit.cmd('Block ' + str(i+1) + ' name \'B_' + key + '\'')

#Create the nodesets and sidesets
#Plane strain surfaces
front_surf = cubit.parse_cubit_list('surface', 'with y_coord <= 0')
cubit.cmd('nodeset 1 surface ' + str(front_surf)[1:-1])
cubit.cmd('nodeset 1 name \'NS_front_surf\'')
back_surf = cubit.parse_cubit_list('surface', 'with y_coord >= ' + str(thickness-tol))
cubit.cmd('nodeset 2 surface ' + str(back_surf)[1:-1])
cubit.cmd('nodeset 2 name \'NS_back_surf\'')
#Left and right surfaces
left_surf = cubit.parse_cubit_list('surface', "with x_coord <= 0")
cubit.cmd('nodeset 3 surface ' + str(left_surf)[1:-1])
```

```
cubit.cmd('nodeset 3 name \'NS_left_surf\'')
cubit.cmd('sideset 3 surface ' + str(left_surf)[1:-1])
cubit.cmd('sideset 3 name \'SS_left_surf\'')
right_surf = cubit.parse_cubit_list('surface', 'with x_coord >= ' + str(width/2.0 - tol))
cubit.cmd('nodeset 4 surface ' + str(right_surf)[1:-1])
cubit.cmd('nodeset 4 name \'NS_right_surf\'')
cubit.cmd('sideset 4 surface ' + str(right_surf)[1:-1])
cubit.cmd('sideset 4 name \'SS_right_surf\'')
#Top and bottom surfaces
bot_surf = cubit.parse_cubit_list('surface', 'with z_coord <= ' + str(bot_elev + tol))
cubit.cmd('nodeset 5 surface ' + str(bot_surf)[1:-1])
cubit.cmd('nodeset 5 name \'NS_bot_surf\'')
cubit.cmd('sideset 5 surface ' + str(bot_surf)[1:-1])
cubit.cmd('sideset 5 name \'SS_bot_surf\'')
top_surf = cubit.parse_cubit_list('surface', 'with z_coord >= ' + str(top_elev - tol))
cubit.cmd('nodeset 6 surface ' + str(top_surf)[1:-1])
cubit.cmd('nodeset 6 name \'NS_top_surf\'')
cubit.cmd('sideset 6 surface ' + str(top_surf)[1:-1])
cubit.cmd('sideset 6 name \'SS_top_surf\'')
#Top right, fixed, anhydrite surface
top_anhydrite_right_surf = cubit.parse_cubit_list('surface', \
    'with z_coord >= ' + str(49.38 - tol) + ' and with x_coord >= ' + str(width/2.0-tol))
cubit.cmd('nodeset 7 surface ' + str(top_anhydrite_right_surf)[1:-1])
cubit.cmd('nodeset 7 name \'NS_top_anhydrite_right_surf\'')
#Interior room surfaces
roof_surf = cubit.parse_cubit_list('surface', \
    'with z_coord <= ' + str(room_top_elev + tol) \
    + ' and with z_coord >= ' + str(room_top_elev-tol) \
    + ' and with x_coord <= ' + str(room_width/2.0 + tol))
floor_surf = cubit.parse_cubit_list('surface', \
    'with z_coord <= ' + str(room_bot_elev + tol) \
    + ' and with z_coord >= ' + str(room_bot_elev-tol) \
    + ' and with x_coord <= ' + str(room_width/2.0 + tol))
wall_surf = cubit.parse_cubit_list('surface', \
    'with z_coord <= ' + str(room_top_elev + tol) \
    + ' and with z_coord >= ' + str(room_bot_elev-tol) \
    + ' and with x_coord <= ' + str(room_width/2.0 + tol) \
    + ' and with x_coord >= ' + str(room_width/2.0 - room_fillet_radius))
room_surf = []
room_surf.extend(roof_surf)
room_surf.extend(floor_surf)
room_surf.extend(wall_surf)
cubit.cmd('sideset 7 surface ' + str(room_surf)[1:-1])
cubit.cmd('sideset 7 name \'SS_room_surf\'')
#Room nodesets for history traces
roof_vertex = cubit.parse_cubit_list('vertex', \
    'with y_coord <= 0 \
    and with x_coord >= ' + str(0 - tol) \
    + ' and with x_coord <= ' + str(0 + tol) \
    + ' and with z_coord >= ' + str(room_top_elev - tol) \
    + ' and with z_coord <= ' + str(room_top_elev + tol))
cubit.cmd('nodeset 8 vertex ' + str(roof_vertex)[1:-1])
cubit.cmd('nodeset 8 name \'NS_roof_ctr\'')
floor_vertex = cubit.parse_cubit_list('vertex', \
```

```
    'with y_coord <= 0 \
    and with x_coord >= ' + str(0 - tol) \
    + ' and with x_coord <= ' + str(0 + tol) \
    + ' and with z_coord >= ' + str(room_bot_elev - tol) \
    + ' and with z_coord <= ' + str(room_bot_elev + tol))
cubit.cmd('nodeset 9 vertex ' + str(floor_vertex)[1:-1])
cubit.cmd('nodeset 9 name \'NS_floor_ctr\'')
wall_vertex = cubit.parse_cubit_list('vertex', \
    'with y_coord <= 0 \
    and with x_coord >= ' + str(room_width/2.0 - tol) \
    + ' and with x_coord <= ' + str(room_width/2.0 + tol) \
    + ' and with z_coord >= ' + str(room_ctr[1] - tol) \
    + ' and with z_coord <= ' + str(room_ctr[1] + tol))
cubit.cmd('nodeset 10 vertex ' + str(wall_vertex)[1:-1])
cubit.cmd('nodeset 10 name \'NS_wall_ctr\'')

#Export the Mesh
import os
pwd = os.getcwd()
export_path = pwd + '/' + sim_ID + '/' + sim_ID + '.g'
print export_path
cubit.cmd('export Genesis \'%s\' overwrite' % export_path)

#Print the pressures at the top and bottom surfaces
p1 = -15.97e6
p2 = -13.57e6
z1 = -54.19
z2 = 52.87
p = lambda z: (p2 - p1) / (z2 - z1) * (z - z1) + p1
print 'At z = ' + str(bot_elev) + ' p = ' + str(p(bot_elev))
print 'At z = ' + str(top_elev) + ' p = ' + str(p(top_elev))

#Print the error count
error_new = cubit.get_error_count()
print 'Cubit error count = %r' %(error_new - error_old)
```

A.2.2 Sierra/SM Input Syntax For Legacy Clean Salt Material Model

```
begin property specification for material halite

    density = 2300.0

    begin parameters for model implicit_wipp_crushed_salt

        #Intact salt parameters
        #(These parameters came from the Clean Salt values in Table 2 and Table 3 of
         ↪  SAND97-0795)
        bulk modulus  = 20.7e9 # Pa  compute bulk modulus from E=31e+09 Pa and nu = 0.25
        shear modulus = 12.4e9  # Pa
        a1      = 8.386e22 # 1/sec
```

```
        q1/R    = 12580.5 # K = 25000 cal / mol / 1.9872035 cal / (mol K)
        n1      = 5.5
        b1      = 6.086e6 # 1/sec
        a2      = 9.672e12 # 1/sec
        q2/R    = 5032.2 # K = 10000 cal/mol / 1.9872035 cal/(mol*K)
        n2      = 5.0
        b2      = 3.034e-2 # 1/sec
        sig0    = 20570000.0 # Pa
        qlc     = 5335.0
        m       = 3.0
        k0      = 6.275e5
        c       = 0.009198 # 1/K
        alpha   = -17.37
        beta    = -7.738
        deltalc = 0.58

        #Crushed salt parameters
        SH0            = 12.4e9
        SH1            = 0.0
        BK0            = 20.7e9 # Pa  compute bulk modulus from E=31e+09 Pa and nu = 0.25
        BK1            = 0.0
        MU             = 12.4e9   # same as SH0 (shear modulus)
        INI_DENSITY    = 2299.99    # initial density set close to intact density for
         ↪  modeling intact salt with this model
        INT_DENSITY    = 2300.
        KA0            = 0.0
        KA1            = 1.005
        N              = 1.331
        DT             = 1.0
        ET0            = 0.0
        ET1            = 3.9387
        NF             = 3.5122
        A              = 0.3147
        P              = 1.6332
        NS             = 0.5576
        QS/R           = 1077.46
        R1             = 1.04136e-12
        R3             = 15.128
        R4             = 0.1678
        W              = 0.0   # water content set to zero turns off pressure solution
         ↪  for crushed salt
        amult          = 0.95
        GRAINSZ        = 0.001
        ANGLE          = 0.1
        EPSTOL         = 0.01
        #       EPSTOL         = 1.0
        TSCALE         = 0.
    end parameters for model implicit_wipp_crushed_salt

end property specification for material halite
```

A.2.3 Sierra/SM Input Syntax For Legacy Argillaceous Salt Material Model

```
begin property specification for material arg_halite

    density = 2300.0

    begin parameters for model implicit_wipp_crushed_salt

        #Intact salt parameters
        #(These parameters came from the Argillaceous Salt values in Table 2 and Table 3
         ↪  of SAND97-0795)
        bulk modulus  = 20.7e9 # Pa  compute bulk modulus from E=31e+09 Pa and nu = 0.25
        shear modulus = 12.4e9  # Pa
        a1      = 1.407e23 # 1/sec
        q1/R    = 12580.5 # K = 25000 cal/mol / 1.9872035 cal/(mol*K)
        n1      = 5.5
        b1      = 8.998e6 # 1/sec
        a2      = 1.314e13
        q2/R    = 5032.2 # K = 10000 cal/mol / 1.9872035 cal/(mol*K)
        n2      = 5.0
        b2      = 4.289e-2 # 1/sec
        sig0    = 20570000.0 # Pa
        qlc     = 5335.0
        m       = 3.0
        k0      = 2.470e6
        c       = 0.009198 # 1/K
        alpha   = -14.96
        beta    = -7.738
        deltalc = 0.58

        #Crushed salt parameters
        SH0            = 12.4e9
        SH1            = 0.0
        BK0            = 20.7e9 # Pa  compute bulk modulus from E=31e+09 Pa and nu = 0.25
        BK1            = 0.0
        MU             = 12.4e9   # same as SH0 (shear modulus)
        INI_DENSITY    = 2299.99    # initial density set close to intact density for
         ↪  modeling intact salt with this model
        INT_DENSITY    = 2300.
        KA0            = 0.0
        KA1            = 1.005
        N              = 1.331
        DT             = 1.0
        ET0            = 0.0
        ET1            = 3.9387
        NF             = 3.5122
        A              = 0.3147
        P              = 1.6332
        NS             = 0.5576
        QS/R           = 1077.46
        R1             = 1.04136e-12
        R3             = 15.128
```

```
        R4             = 0.1678
        W              = 0.0   # water content set to zero turns off pressure solution
         ↪  for crushed salt
        amult          = 0.95
        GRAINSZ        = 0.001
        ANGLE          = 0.1
        EPSTOL         = 0.01
        #      EPSTOL         = 1.0
        TSCALE         = 0.
    end parameters for model implicit_wipp_crushed_salt

end property specification for material arg_halite
```

A.2.4 Sierra/SM Input Syntax For Legacy Anhydrite Material Model

```
begin definition for function anhydrite_pressure_volstrain_function
    type is piecewise linear
    ordinate is volumetric_strain
    abscissa is pressure
    begin values
        -1  -8.344444444e+10 # -83.44444444 GPa
        0  0
        1  8.344444444e+10 # 83.44444444 GPa = bulk modulus = E / (3*(1-2*nu)), where E =
         ↪  75.1 GPa and nu = 0.35
    end values
end definition for function anhydrite_pressure_volstrain_function

begin property specification for material anhydrite

    #These parameters came from SAND97-0796, Pages A-40 through A-41, Section 2.5.2

    #The yield function for this model is
    #phi = sqrt(3*J_2) - (a0 + a1 * p + a2 * p^2)
    #This model has a Drucker-Prager yield surface if a2 = 0
    #The Drucker-Prager yield function is often written as (compression is negative)
    #phi = sqrt(J_2) + a * I_1 - C
    #Thus, we can write a0 and a1 in terms of a and C

    density = 2300.0
    begin parameters for model soil_foam
        poissons ratio  = 0.35
        youngs modulus  = 7.51e10 # Pa
        a0              = 2338268.59 # Pa = sqrt(3) * C, where C = 1.35 MPa
        a1              = 2.33826859 # = 3 * sqrt(3) * a, where a = 0.45
        a2              = 0.0
        pressure cutoff = -1000000.0 # Pa
        pressure function = anhydrite_pressure_volstrain_function
    end parameters for model soil_foam

end property specification for material anhydrite
```

A.2.5 Sierra/SM Input Syntax For Legacy Polyhalite Material Model

```
begin definition for function polyhalite_pressure_volstrain_function
    type is piecewise linear
    ordinate is volumetric_strain
    abscissa is pressure
    begin values
        -1  -6.583333333e+10 # -65.83333333 GPa
        0  0
        1  6.583333333e+10 # 65.83333333 GPa = bulk modulus = E / (3*(1-2*nu)), where E =
         ↪  55.3 GPa and nu = 0.36
    end values
end definition for function polyhalite_pressure_volstrain_function

begin property specification for material polyhalite

    #These parameters came from SAND97-0796, Pages A-40 through A-41, Section 2.5.2

    #The yield function for this model is
    #phi = sqrt(3*J_2) - (a0 + a1 * p + a2 * p^2)
    #This model has a Drucker-Prager yield surface if a2 = 0
    #The Drucker-Prager yield function is often written as (compression is negative)
    #phi = sqrt(J_2) + a * I_1 - C
    #Thus, we can write a0 and a1 in terms of a and C

    density = 2300.0
    begin parameters for model soil_foam
        poissons ratio  = 0.36
        youngs modulus  = 5.53e+10 # Pa
        a0              = 2459512.147 # Pa = sqrt(3) * C, where C = 1.42 MPa
        a1              = 2.457780096 # unitless = 3 * sqrt(3) * a, where a = 0.473
        a2              = 0.0
        pressure cutoff = -1000000.0 # Pa
        pressure function = polyhalite_pressure_volstrain_function
    end parameters for model soil_foam
end property specification for material polyhalite
```

A.2.6 Example Sierra/SM Input File

```
begin sierra  WIPP Isothermal Room D

  title Adagio Simulation of WIPP Room D Closure - MD Model

  define direction y with vector 0.0 1.0 0.0
  define direction x with vector 1.0 0.0 0.0
  define direction z with vector 0.0 0.0 1.0
  define direction negative_z with vector 0.0  0.0 -1.0
  define point origin with coordinates 0.0 0.0 0.0

  #---------- Functions ---------
```

```
begin definition for function function_constant
  type is piecewise linear
  begin values
      -1.0e16  -1.0
      1.0e16   1.0
  end values
end definition for function function_constant

begin definition for function temperature
      type is piecewise linear
      #SAND88-2948 used 300 K
      begin values
          -1.0e16  300.0
          1.0e16   300.0
      end values
end definition for function temperature

begin definition for function fluid_density_ramp
    type is piecewise linear
    begin values
        -0.01    2300 #kg/m^3 = density for the proper lithostatic pressure at room at
         ↪  t=-0.01
        0.0     0.0 #kg/m^3 = density for zero applied pressure at room at t=0
    end values
end definition for function fluid_density_ramp

#---------- Materials ----------

  begin property specification for material halite

      density = 2300.0

      begin parameters for model implicit_wipp_crushed_salt

          #Intact salt parameters
          #(These parameters came from recalibrating the Clean Salt values in Table 2
           ↪  and
          #Table 3 of SAND97-0795 against the IfG experiments from Joint Project III.
           ↪  The
          #IfG experiments were fit to each individual experiment using method B. Then
           ↪  a
          #global fit was found using the experiments with T <= 60C and stress_eq > 7.0
           ↪  MPa.
          #The recovery rate variable was not extracted from the experiments, so it was
           ↪  left
          #at 0.58.)
          bulk modulus  = 20.7e9 # Pa  compute bulk modulus from E=31e+09 Pa and nu =
           ↪  0.25
          shear modulus = 12.4e9  # Pa
          a1      = 8.386e22 # 1/sec
          q1/R    = 12580.5 # K = 25000 cal / mol / 1.9872035 cal / (mol K)
          n1      = 5.5
          b1      = 6.086e6 # 1/sec
```

```
        a2      = 1.074e+14 # 1/sec
        q2/R    = 5.177e+03 # K
        n2      = 5.3528
        b2      = 3.034e-2 # 1/sec
        sig0    = 20570000.0 # Pa
        qlc     = 5335.0
        m       = 4.0406
        k0      = 3.918e+08
        c       = 1.093e-02 # 1/K
        alpha   = 3.367
        beta    = -0.6838
        deltalc = 0.58

        #Crushed salt parameters
        SH0            = 12.4e9
        SH1            = 0.0
        BK0            = 20.7e9 # Pa  compute bulk modulus from E=31e+09 Pa and nu =
         ↪  0.25
        BK1            = 0.0
        MU             = 12.4e9   # same as SH0 (shear modulus)
        #Set initial density close to intact density for modeling intact salt with
         ↪  this model
        INI_DENSITY    = 2299.99
        INT_DENSITY    = 2300.
        KA0            = 0.0
        KA1            = 1.005
        N              = 1.331
        DT             = 1.0
        ET0            = 0.0
        ET1            = 3.9387
        NF             = 3.5122
        A              = 0.3147
        P              = 1.6332
        NS             = 0.5576
        QS/R           = 1077.46
        R1             = 1.04136e-12
        R3             = 15.128
        R4             = 0.1678
        #Water content set to zero turns off pressure solution redeposition for
         ↪  crushed salt
        W              = 0.0
        amult          = 0.95
        GRAINSZ        = 0.001
        ANGLE          = 0.1
        EPSTOL         = 0.01
        TSCALE         = 0.
    end parameters for model implicit_wipp_crushed_salt

end property specification for material halite

begin property specification for material anhydrite
    density = 2300.0 # kg / m^3
    #Sierra/SM needs to have elastic parameters defined with these names, so we
     ↪  repeat
```

```
    #the values in the "begin parameters ..." block.
    bulk modulus = 83.4444444e9 # Pa = bulk modulus
    shear modulus = 27814814814 # Pa = shear modulus

    #These Drucker-Prager parameters came from SAND97-0795, Table 6, except it does
     ↪  not
    #mention a dilation angle.  They almost certainly used the soil and foam model,
     ↪  which
    #has a dilatation angle of 0 degrees.  Here, we have switched to associated flow.
    #The Drucker-Prager yield function is often written as phi = sqrt(J_2) + a * I_1
     ↪  - C
    #B0 = bulk modulus = 83.4444444e9 Pa
    #G0 = shear modulus = 27814814814 Pa
    #C = 1.35
    #a = 0.45
    #alpha = dilatation angle = 24.227745 deg = atan(0.45)

    #Reduce Kayenta to Drucker-Prager
    begin parameters for model kayenta
        B0 = 83.4444444e9   # Pa = bulk modulus
        G0 = 27814814814    # Pa = shear modulus
        J3TYPE = 1 # Sets the dependence on J_3.  J3TYPE = 1 is a von Mises
         ↪  dependence.
        A1 = 1350000 # Pa
        A2 = 0.0
        A3 = 0.0
        A4 = 0.45
        RK = 1.0
        P0 = -1.0e99        # Put the compression cap at virtually infinity
        P1 = 0.0            # No cap
        P2 = 0.0            # No cap
        P3 = 0.0            # Zero porosity
        CR = 0.001          # Minimize the size of the curved part of the cap
        HC = 0.0            # Disable kinematic hardening
        RN = 0.0            # Disable kinematic hardening
    end parameters for model kayenta
end property specification for material anhydrite

begin definition for function polyhalite_pressure_volstrain_function
    type is piecewise linear
    ordinate is volumetric_strain
    abscissa is pressure
    #E = 55.3 GPa and nu = 0.36
    begin values
        -1  -6.583333333e+10 # -65.833 GPa
        0  0
        1  6.583333333e+10 # 65.833 GPa = bulk modulus = E / (3*(1-2*nu))
    end values
end definition for function polyhalite_pressure_volstrain_function

begin property specification for material polyhalite

    #These parameters came from SAND97-0796, Pages A-40 through A-41, Section 2.5.2
```

```
      #The yield function for this model is
      #phi = sqrt(3*J_2) - (a0 + a1 * p + a2 * p^2)
      #This model has a Drucker-Prager yield surface if a2 = 0
      #The Drucker-Prager yield function is often written as
      #phi = sqrt(J_2) + a * I_1 - C
      #Thus, we can write a0 and a1 in terms of a and C

      density = 2300.0
      begin parameters for model soil_foam
          poissons ratio  = 0.36
          youngs modulus  = 5.53e+10 # Pa
          a0              = 2459512.147 # Pa = sqrt(3) * C, where C = 1.42 MPa
          a1              = 2.457780096 # unitless = 3 * sqrt(3) * a, where a = 0.473
          a2              = 0.0
          pressure cutoff = -1000000.0 # Pa
          pressure function = polyhalite_pressure_volstrain_function
      end parameters for model soil_foam
  end property specification for material polyhalite

begin solid section solid_1
  formulation = selective_deviatoric
  deviatoric parameter = 1.0
  strain incrementation = strongly_objective
end solid section solid_1

#---------- Finite Element Model -----------

begin finite element model room
  Database name = %B.g
  Database type = exodusII

 begin parameters for block b_halite
   material halite
   solid mechanics use model implicit_wipp_crushed_salt
   section = solid_1
 end parameters for block b_halite

 begin parameters for block b_arg_halite
   material halite
   solid mechanics use model implicit_wipp_crushed_salt
   section = solid_1
 end parameters for block b_arg_halite

 begin parameters for block b_anhydrite
   material anhydrite
   solid mechanics use model kayenta
   section = solid_1
 end parameters for block b_anhydrite

 begin parameters for block b_polyhalite
   material polyhalite
   solid mechanics use model soil_foam
   section = solid_1
 end parameters for block b_polyhalite
```

```
end finite element model room

begin adagio procedure The_Procedure

  #---------- Time Step Control ----------

  begin time control

    begin time stepping block p0
      start time = -1.0e-2
      begin parameters for adagio region AdagioRegion
        time increment = 1.0e-6
      end parameters for adagio region AdagioRegion
    end time stepping block p0


    begin time stepping block p1
      start time = 0.0
      begin parameters for adagio region AdagioRegion
        time increment = 1e-2
      end parameters for adagio region AdagioRegion
    end time stepping block p1

    termination time = 116985600.0 #s = 1354 days

  end time control

  begin adagio region AdagioRegion

    use finite element model room

    begin adaptive time stepping time
       method = material
       cutback factor = 0.9
       growth factor  = 1.02
       maximum multiplier = 1e14
       minimum multiplier = 1.e-4
       maximum failure cutbacks = 10
    end adaptive time stepping time

    #--------- Boundary Conditions ---------

    begin gravity
      include all blocks
      gravitational constant = 9.79  # SAND88-2948 used 9.79 m/s^2
      direction = negative_z
      function = function_constant
    end gravity

    begin prescribed temperature
      include all blocks
      function = temperature
```

```
  scale factor = 1.0
end prescribed temperature

begin pressure
  surface = SS_top_surf
  function = function_constant
  scale factor = 13.57E+06
end pressure

begin fixed displacement
  node set = NS_bot_surf
  components = z
end fixed displacement

begin fixed displacement
  node set = NS_left_surf
  components = x
end fixed displacement

begin fixed displacement
  node set = NS_right_surf
  components = x
end fixed displacement

begin fixed displacement
  node set = NS_back_surf
  components = y
end fixed displacement

begin fixed displacement
  node set = NS_front_surf
  components = y
end fixed displacement

begin fluid pressure
  surface = SS_room_surf
  active periods = p0
  #Specify which direction corresponds to the depth of fluid.
  fluid surface normal = z
  #The depth function is defined relative to the reference point.
  #See the figure in the fluid pressure section of the Sierra/SM manual for more
   ↪  info.
  reference point = origin
  #Set the fluid height, relative to the reference point,
  #to give the proper lithostatic pressure at room
  #p1 = -15.97e6 Pa
  #p2 = -13.57e6 Pa
  #z1 = -54.19 m
  #z2 = 52.87 m
  #slope = (p2-p1)/(z2-z1)
  #p = slope*(z-z1)+p1
  #z0 = depth = elevation of fluid surface
  #depth = -p1 / slope + z1
  depth = 658.2050833333333 #m = height
```

```
        #Specify the function to ramp the fluid density down by time = 0
        density function = fluid_density_ramp
        gravitational constant = 9.79
      end fluid_pressure

#       --------- CONTACT MODEL --------------

    begin contact definition slipping_clay_seams

        enforcement = al
        contact surface clay_D_master contains SS_clay_D_master
        contact surface clay_D_slave contains SS_clay_D_slave
        contact surface clay_E_master contains SS_clay_E_master
        contact surface clay_E_slave contains SS_clay_E_slave
        contact surface clay_F_master contains SS_clay_F_master
        contact surface clay_F_slave contains SS_clay_F_slave
        contact surface clay_G_master contains SS_clay_G_master
        contact surface clay_G_slave contains SS_clay_G_slave
        contact surface clay_H_master contains SS_clay_H_master
        contact surface clay_H_slave contains SS_clay_H_slave
        contact surface clay_I_master contains SS_clay_I_master
        contact surface clay_I_slave contains SS_clay_I_slave
        contact surface clay_J_master contains SS_clay_J_master
        contact surface clay_J_slave contains SS_clay_J_slave
        contact surface clay_K_master contains SS_clay_K_master
        contact surface clay_K_slave contains SS_clay_K_slave
        contact surface clay_L_master contains SS_clay_L_master
        contact surface clay_L_slave contains SS_clay_L_slave

        begin constant friction model just_slide_frict
          friction coefficient = 0.20
        end

        begin interaction clay_D
          master = clay_D_master
          slave = clay_D_slave
          friction model = just_slide_frict
        end interaction

        begin interaction clay_E
          master = clay_E_master
          slave = clay_E_slave
          friction model = just_slide_frict
        end interaction

        begin interaction clay_F
          master = clay_F_master
          slave = clay_F_slave
          friction model = just_slide_frict
        end interaction

        begin interaction clay_G
          master = clay_G_master
          slave = clay_G_slave
```

```
    friction model = just_slide_frict
  end interaction

  begin interaction clay_H
    master = clay_H_master
    slave = clay_H_slave
    friction model = just_slide_frict
  end interaction

  begin interaction clay_I
    master = clay_I_master
    slave = clay_I_slave
    friction model = just_slide_frict
  end interaction

  begin interaction clay_J
    master = clay_J_master
    slave = clay_J_slave
    friction model = just_slide_frict
  end interaction

  begin interaction clay_K
    master = clay_K_master
    slave = clay_K_slave
    friction model = just_slide_frict
  end interaction

  begin interaction clay_L
    master = clay_L_master
    slave = clay_L_slave
    friction model = just_slide_frict
  end interaction

end contact definition slipping_clay_seams

#--------- Initial Conditions ---------

begin initial condition
  include all blocks
  #It is important to initialize unrotated_stress and not stress, because
  #stress is just an output that gets calculated as needed, while
  #unrotated_stress gets stored and used by the constitutive models.
  #As of November 2015, initializing stress does nothing.
  initialize variable name = unrotated_stress
  variable type = element
  subroutine real parameter: top = 52.87
  subroutine real parameter: bot = -54.19
  subroutine real parameter: p1 = -13.57e6
  subroutine real parameter: po = -15.97e6
  subroutine real parameter: kvert_xx = 1.0
  subroutine real parameter: kvert_yy = 1.0
  subroutine real parameter: kvert_zz = 1.0
  subroutine real parameter: kvert_xy = 0.0
  subroutine real parameter: kvert_yz = 0.0
```

```
  subroutine real parameter: kvert_zx = 0.0
  subroutine string parameter: dir = Z
  element block subroutine = geo_is
 end initial condition

#--------- User Output Variable Definitions ----------

begin user output
  compute element el_avg_stress as average of element cauchy_stress
  compute element el_avg_mean_stress as average of element hydrostatic_stress
  compute element el_avg_prin_stress as average of element principal_stresses
  compute element el_avg_von_mises as average of element von_mises
  compute element el_avg_vol_strain as average of element evol
  compute element el_avg_eqcs as average of element eqcs
  compute element el_avg_eqcs_ss_rate1 as average of element eqcsrate_s1
  compute element el_avg_eqcs_ss_rate2 as average of element eqcsrate_s2
  compute element el_avg_eqcs_ss_rate3 as average of element eqcsrate_s3
  compute element el_avg_tr_eqcs as average of element zeta
  compute element el_avg_tr_eqcs_lim as average of element etstar
  compute element el_avg_log_strain as average of element unrotated_log_strain
end user output

begin user output
  node set = NS_roof_ctr
  compute global roof_disp as average of nodal displacement
end

begin user output
  node set = NS_floor_ctr
  compute global floor_disp as average of nodal displacement
end

begin user output
  node set = NS_wall_ctr
  compute global wall_disp as average of nodal displacement
end

#--------- Results Output ---------

begin results output output_1
  database name = %B-r.e
  database type = exodusII
  at time -1.0e-2 increment = 2e-3
  at time 0.0 increment = 1.0e-2
  at time 1.0e-2 increment = 86400.0 #every 1 days
  at time 864000.0 increment = 864000.0 #every 10 days
  at time 8640000.0 increment = 8640000.0 #every 100 days
  at time 31536000.0 increment = 31536000.0 #every 365 days
  nodal variables = displacement as disp
  nodal variables = residual as resid
  nodal variables = reaction
  element variables = el_avg_stress
  element variables = el_avg_mean_stress
  element variables = el_avg_prin_stress
```

```
  element variables = el_avg_von_mises
  element variables = el_avg_vol_strain
  element variables = el_avg_eqcs
  element variables = el_avg_tr_eqcs
  element variables = el_avg_tr_eqcs_lim
  element variables = el_avg_eqcs_ss_rate1
  element variables = el_avg_eqcs_ss_rate2
  element variables = el_avg_eqcs_ss_rate3
  element variables = el_avg_log_strain
  global variables = total_iter as itotal
end results output output_1

#--------- History Output ---------

begin history output output_2
  database name = %B-h.e
  database type = exodusII
  at time -0.1 increment = 5e-2
  at step 0 increment = 1
  at time 1e-2 increment = 292464.0 #s = 1354 days / 400 pts
  global time
  global roof_disp
  element el_avg_prin_stress nearest location 0 0 4.42 as roof_el_avg_prin_stress
  element el_avg_von_mises nearest location 0 0 4.42 as roof_el_avg_von_mises
  element el_avg_vol_strain nearest location 0 0 4.42 as roof_el_avg_vol_strain
  element el_avg_eqcs nearest location 0 0 4.42 as roof_el_avg_eqcs
  element el_avg_eqcs_ss_rate1 nearest location 0 0 4.42 as
   ↪  roof_el_avg_eqcs_ss_rate1
  element el_avg_eqcs_ss_rate2 nearest location 0 0 4.42 as
   ↪  roof_el_avg_eqcs_ss_rate2
  element el_avg_eqcs_ss_rate3 nearest location 0 0 4.42 as
   ↪  roof_el_avg_eqcs_ss_rate3
  element el_avg_tr_eqcs nearest location 0 0 4.42 as roof_el_avg_tr_eqcs
  element el_avg_tr_eqcs_lim nearest location 0 0 4.42 as roof_el_avg_tr_eqcs_lim
  global floor_disp
  element el_avg_prin_stress nearest location 0 0 -1.08 as floor_el_avg_prin_stress
  element el_avg_von_mises nearest location 0 0 -1.08 as floor_el_avg_von_mises
  element el_avg_vol_strain nearest location 0 0 -1.08 as floor_el_avg_vol_strain
  element el_avg_eqcs nearest location 0 0 -1.08 as floor_el_avg_eqcs
  element el_avg_eqcs_ss_rate1 nearest location 0 0 -1.08 as
   ↪  floor_el_avg_eqcs_ss_rate1
  element el_avg_eqcs_ss_rate2 nearest location 0 0 -1.08 as
   ↪  floor_el_avg_eqcs_ss_rate2
  element el_avg_eqcs_ss_rate3 nearest location 0 0 -1.08 as
   ↪  floor_el_avg_eqcs_ss_rate3
  element el_avg_tr_eqcs nearest location 0 0 -1.08 as floor_el_avg_tr_eqcs
  element el_avg_tr_eqcs_lim nearest location 0 0 -1.08 as floor_el_avg_tr_eqcs_lim
  global wall_disp
  element el_avg_prin_stress nearest location 2.75 0 1.6699999 as
   ↪  wall_el_avg_prin_stress
  element el_avg_von_mises nearest location 2.75 0 1.6699999 as
   ↪  wall_el_avg_von_mises
  element el_avg_vol_strain nearest location 2.75 0 1.6699999 as
   ↪  wall_el_avg_vol_strain
```

```
  element el_avg_eqcs nearest location 2.75 0 1.6699999 as wall_el_avg_eqcs
  element el_avg_eqcs_ss_rate1 nearest location 2.75 0 1.6699999 as
   ↪  wall_el_avg_eqcs_ss_rate1
  element el_avg_eqcs_ss_rate2 nearest location 2.75 0 1.6699999 as
   ↪  wall_el_avg_eqcs_ss_rate2
  element el_avg_eqcs_ss_rate3 nearest location 2.75 0 1.6699999 as
   ↪  wall_el_avg_eqcs_ss_rate3
  element el_avg_tr_eqcs nearest location 2.75 0 1.6699999 as wall_el_avg_tr_eqcs
  element el_avg_tr_eqcs_lim nearest location 2.75 0 1.6699999 as
   ↪  wall_el_avg_tr_eqcs_lim
end history output output_2

#--------- Restart ---------

  begin restart data restart_1
      database name = %B.rsout
      at time 0.0 increment = 86400.0 #every 1 days
      at time 864000.0 increment = 864000.0 #every 10 days
      at time 8640000.0 increment = 8640000.0 #every 100 days
      at time 31536000.0 increment = 31536000.0 #every 365 days
  end restart data restart_1

#--------- Solver ---------

Begin solver

begin loadstep predictor
  type = scale_factor
  scale factor = 0.0
end loadstep predictor

  begin control contact
    level = 1
    target relative residual = 1e-5
    acceptable relative residual = 1e-5
    target residual = 1.0e-5
    acceptable residual = 1.0e-5
    maximum iterations = 100
  end control contact

   begin cg
    target relative residual = 1.0e-6
    acceptable relative residual = 1.0e-6
    target residual = 1.0e-6
    acceptable residual = 1.0e-6
    maximum iterations = 5000
    iteration print = 100
    line search secant 1.0e-4
    begin full tangent preconditioner
      conditioning = no_check
      small number of iterations = 15
      nodal preconditioner method = probe
      iteration update = 100
    end
```

```
        end cg

      end solver

    end adagio region AdagioRegion

  end adagio procedure The_Procedure

end sierra WIPP Isothermal Room D
```

A.3 Axial Compliance Correction

An issue with the compliance of the load stack was identified in Section 3.3. The axial strain drop $\Delta\varepsilon_{zz}(t_1)$ due to the axial stress drop of $\Delta\sigma_{zz}(t_1) = -2$ MPa at $t = t_1 \approx 50$ days is larger than the expected in the low equivalent stress tests. To investigate, the effective axial stiffness E^{eff} was calculated as

$$E^{\text{eff}} = \frac{\Delta\sigma_{zz}(t_1)}{\Delta\varepsilon_{zz}(t_1)} \tag{A.6}$$

for all the IfG tests. The E^{eff} values are listed for each test in Table A.2. (Many TUC tests did not include an axial stress drop, so E^{eff} was set to E for those tests.) Fig. A.1 contains E^{eff} plotted against the first non-zero equivalent stress for each IfG experiment. As expected, E^{eff} is less than E for the low equivalent stress tests. The effective axial stiffness varies more at high equivalent stress tests probably because $\Delta\varepsilon_{zz}$ is too small and noisy for a reliable measurement when the load frame is set up to measure large values of ε_{zz}. Fortunately, the elastic strain is less than 10 % of $\bar{\varepsilon}^{\text{tr}}$ for $\bar{\sigma} \geq 12$ MPa, so the uncertainty in E^{eff} for the high equivalent stress tests is inconsequential.

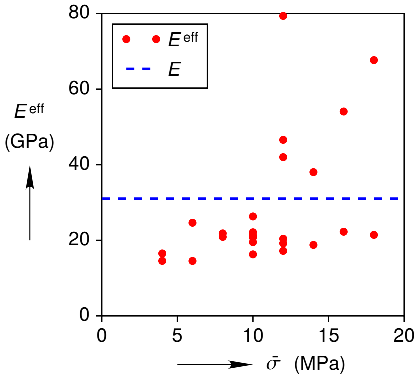

Figure A.1: Effective modulus plotted against the first non-zero equivalent stress for each IfG test. The effective modulus is also compared against the accepted Young's modulus for WIPP salt.

The values of E^{eff} were used during the analysis of the experiments. To calculate $\bar{\varepsilon}^{\text{tr}}(t)$,

E was replaced with E^{eff} in Eq. (1.23), resulting in

$$\bar{\varepsilon}^{\mathrm{tr}}(t) - \bar{\varepsilon}^{\mathrm{tr}}(t_i^-) = \left[\varepsilon_{zz}(t) - \varepsilon_{zz}(t_i^-)\right] - \frac{\Delta\bar{\sigma}(t_i)}{E^{\mathrm{eff}}} - \dot{\bar{\varepsilon}}^{\mathrm{ss}}\, t. \tag{A.7}$$

Also, when the M-D model was fit or compared to the individual triaxial creep experiments, B was replaced with $B^{\mathrm{eff}} = E^{\mathrm{eff}}/(3\,(1-2\,\nu))$ and μ with $\mu^{\mathrm{eff}} = E^{\mathrm{eff}}/(2\,(1+\nu))$ in Eqs. (1.2) and (1.3), to obtain

$$\dot{\boldsymbol{\sigma}} = \boldsymbol{\mathcal{C}}^{\mathrm{eff}} : \dot{\boldsymbol{\varepsilon}}^{\mathrm{e}} \tag{A.8}$$

$$\boldsymbol{\mathcal{C}}^{\mathrm{eff}} = (B^{\mathrm{eff}} - 2/3\,\mu^{\mathrm{eff}})\,\boldsymbol{I}\otimes\boldsymbol{I} + 2\,\mu^{\mathrm{eff}}\,\boldsymbol{\mathcal{I}}. \tag{A.9}$$

The equations for the steady-state strain rate (Eqs. (1.9) to (1.11)) and the transient strain limit (Eq. (1.12)) also contain the shear modulus μ, but it just normalizes $\bar{\sigma}$, so μ was left untouched in those equations.

A.4 Fits of IfG Triaxial Creep Tests on 2013 Cores

Nearly all the IfG creep tests listed in *Salzer et al.* (2015); *Düsterloh et al.* (2015) were analyzed herein. The IfG tests on 2013 clean salt cores are listed in Table 2 of *Salzer et al.* (2015) and the IfG tests on 2013 argillaceous salt cores are listed in rows 1 through 24 of Table 2 of *Düsterloh et al.* (2015). C_IfG_TCC3 was ignored because it had different specimen dimensions than the other IfG specimens. C_IfG_TCC1 was a good surrogate for C_IfG_TCC3 since it was tested under the same conditions.

Fitting method A and method B successfully fit the majority of the IfG triaxial creep tests. Fig. A.2 through Fig. A.25 show the analysis of each test. Taking Fig. A.2 as an example, Fig. A.2a shows method A's direct measurement of $\dot{\bar{\varepsilon}}^{\mathrm{ss}}$ and $\bar{\varepsilon}^{\mathrm{tr}*}$. Fig. A.2b displays method A's κ_{h} fit and method B's fit of $\dot{\bar{\varepsilon}}^{\mathrm{ss}}$, $\bar{\varepsilon}^{\mathrm{tr}*}$, and κ_{h} together. Fig. A.2c compares simulations of the test using calibration 1A and 1B against the experimental measurements. Table A.2 displays the test temperature T, the equivalent stress $\bar{\sigma}$, the effective axial stiffness E^{eff}, the weighting factor w, and the results of fitting method A and method B for each test.

Unfortunately, both fitting methods had trouble extracting from test C_IfG_TCC16 and A_IfG_TCC11. The $\bar{\varepsilon}^{\mathrm{tr}}$ curve in C_IfG_TCC16 has a strange local maximum shortly after t_0, and it even becomes negative after t_1 (see Fig. A.19). The $\bar{\varepsilon}^{\mathrm{tr}}$ curve in A_IfG_TCC11 is better behaved, but still problematic. The differential stress was dropped from 10 MPa to 8 MPa between hardening and recovery, while $\bar{\varepsilon}^{\mathrm{tr}*}$ dropped from 0.18 % strain to 0.036 % strain. That drop in $\bar{\varepsilon}^{\mathrm{tr}*}$ would require an exponent of $m = 7.2$ in Eq. (1.12). It is highly unlikely that the stress dependence is that steep, because m is typically near 3. It is more likely that C_IfG_TCC16 and A_IfG_TCC11 specimens were previously deformed ($\bar{\varepsilon}^{\mathrm{tr}}(t_0^-) \neq 0$), which caused $\bar{\varepsilon}^{\mathrm{tr}*}$ to be under measured during hardening. A low value of $\bar{\varepsilon}^{\mathrm{tr}}(t_1^-)$ then caused $\bar{\varepsilon}^{\mathrm{tr}*}$ to be very under measured. For these reasons, the values of $\bar{\varepsilon}^{\mathrm{tr}*}$ and κ_{h} from C_IfG_TCC16 and A_IfG_TCC11 were discarded. The $\dot{\bar{\varepsilon}}^{\mathrm{ss}}$ measurements from fitting method A were retained, however, because the steady-state strain rate is invariant to $\bar{\varepsilon}^{\mathrm{tr}}(t_0^-)$.

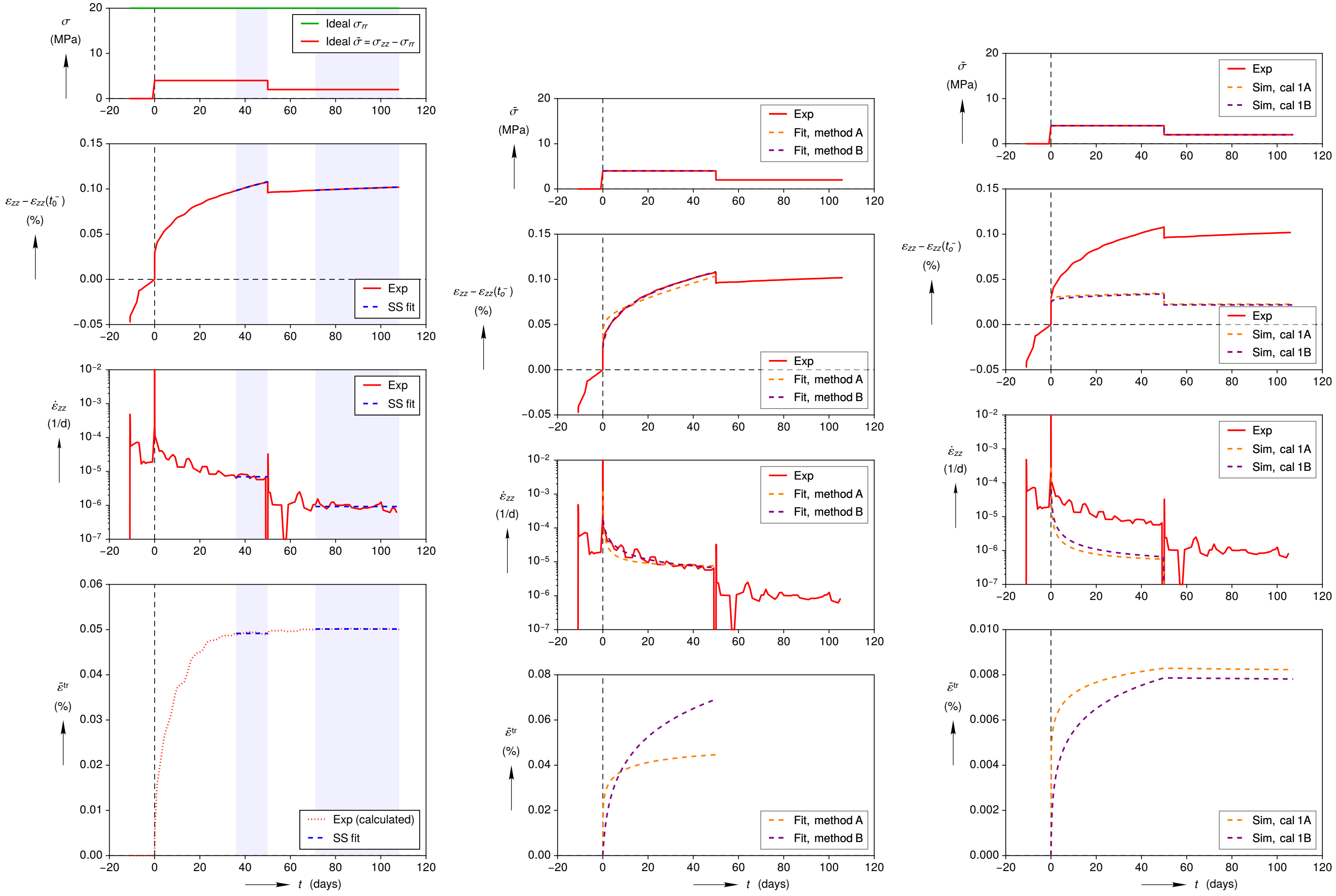

(a) Measurements (b) Individual fits (c) Global calibrations

Figure A.2: Experiment A_IfG_TCC1 at $T = 60$ °C

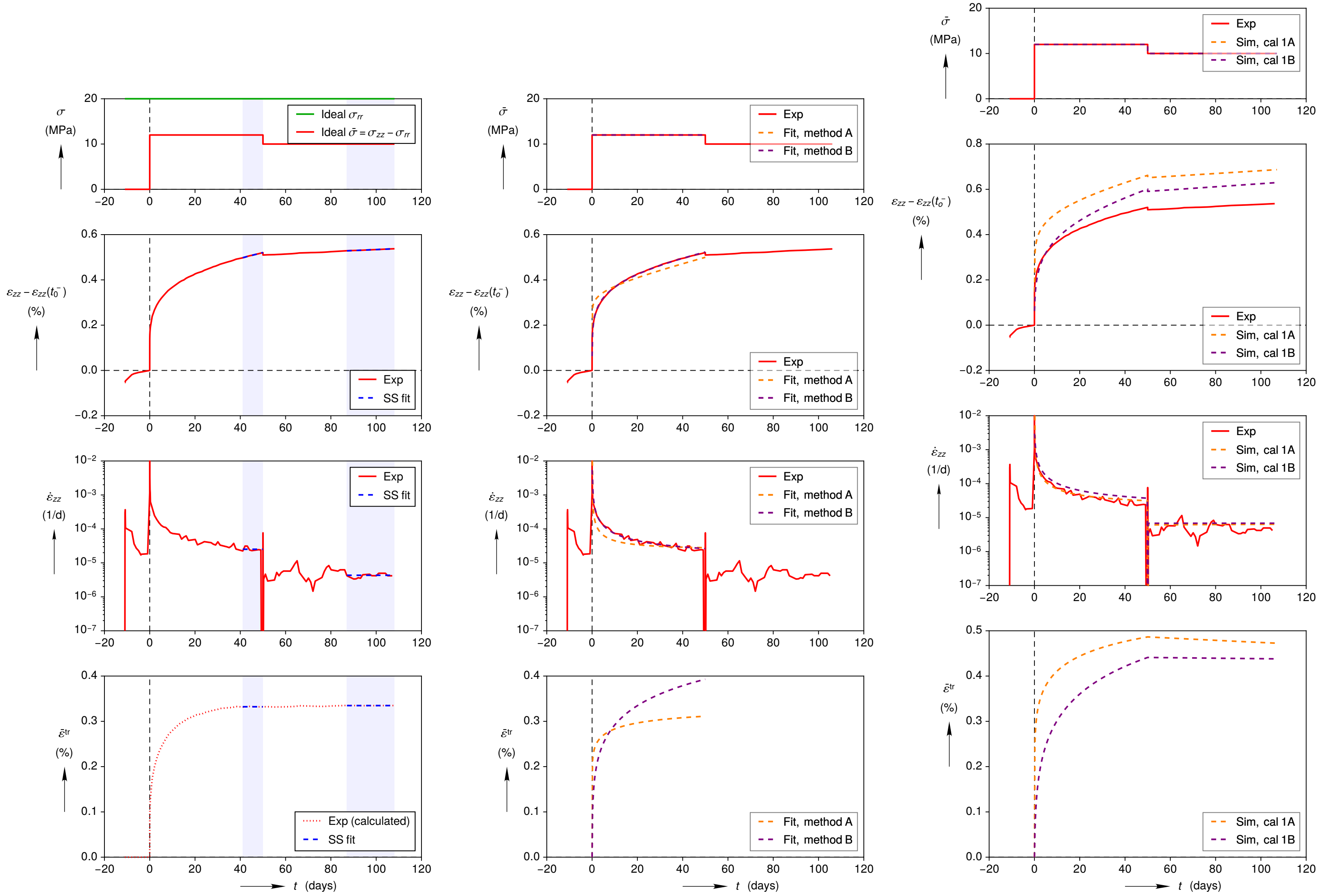

(a) Measurements (b) Individual fits (c) Global calibrations

Figure A.3: Experiment A_IfG_TCC10 at $T = 25$ °C

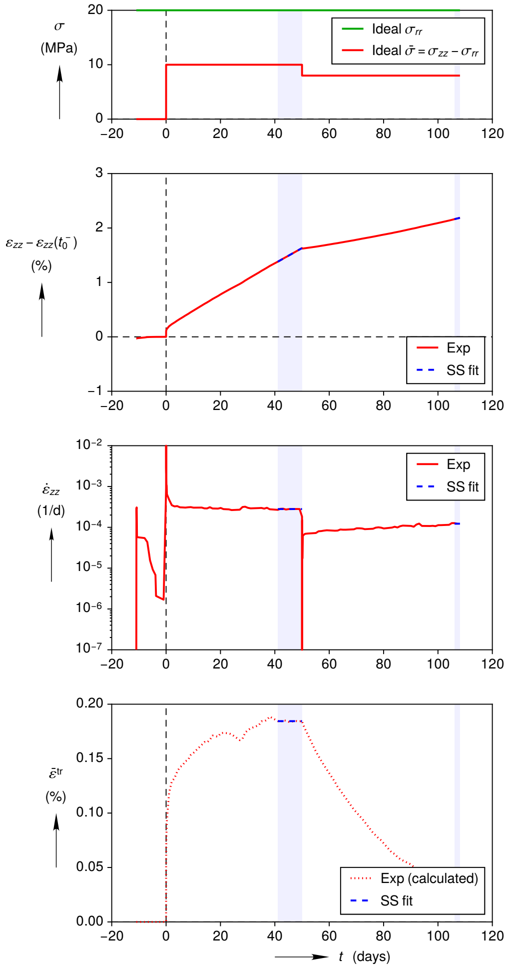

(a) Measurements

Figure A.4: Experiment A_IfG_TCC11 at $T = 80$ °C

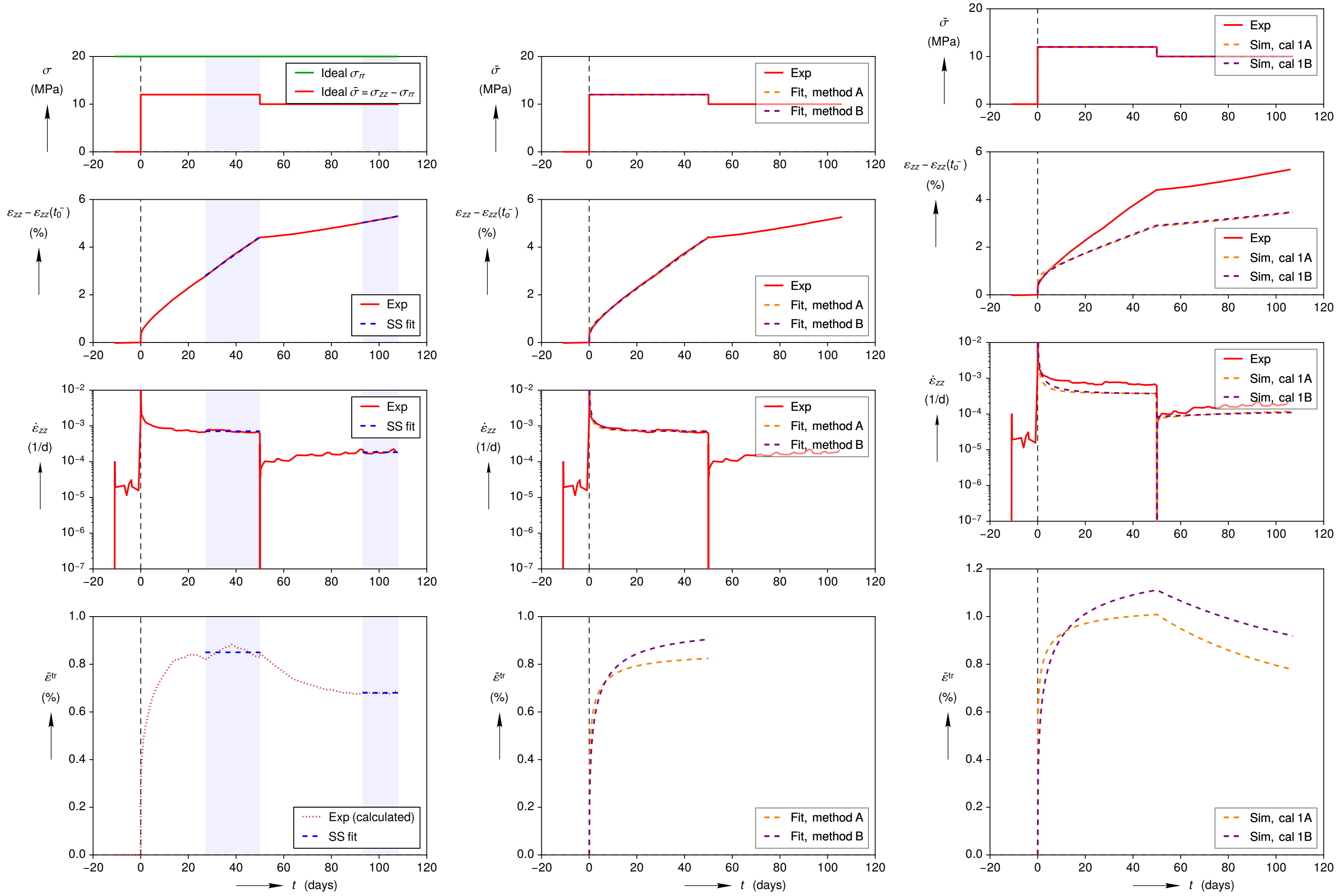

(a) Measurements

(b) Individual fits

(c) Global calibrations

Figure A.5: Experiment A_IfG_TCC12 at $T = 80$ °C

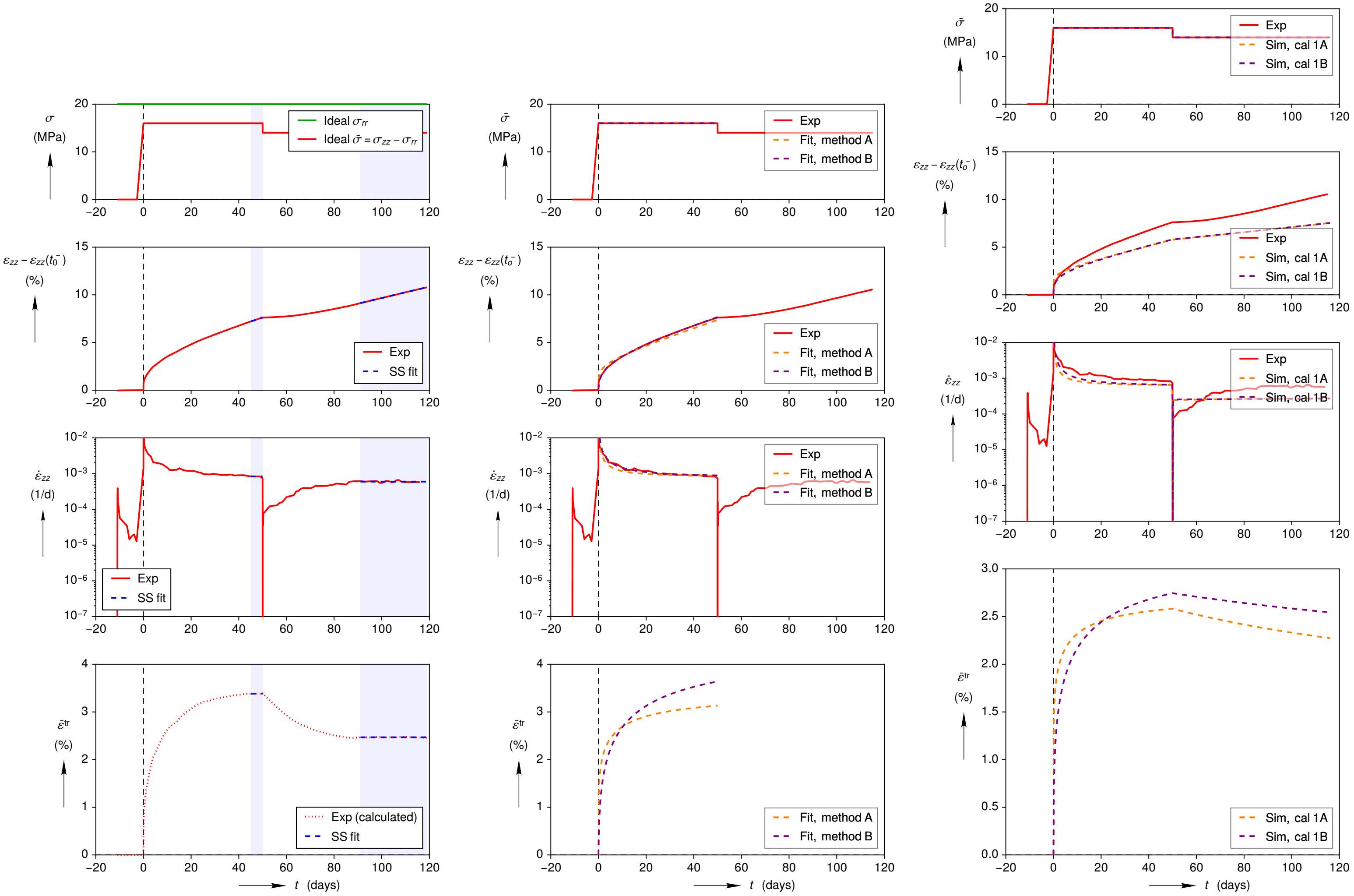

(a) Measurements (b) Individual fits (c) Global calibrations

Figure A.6: Experiment A_IfG_TCC13 at $T = 60$ °C

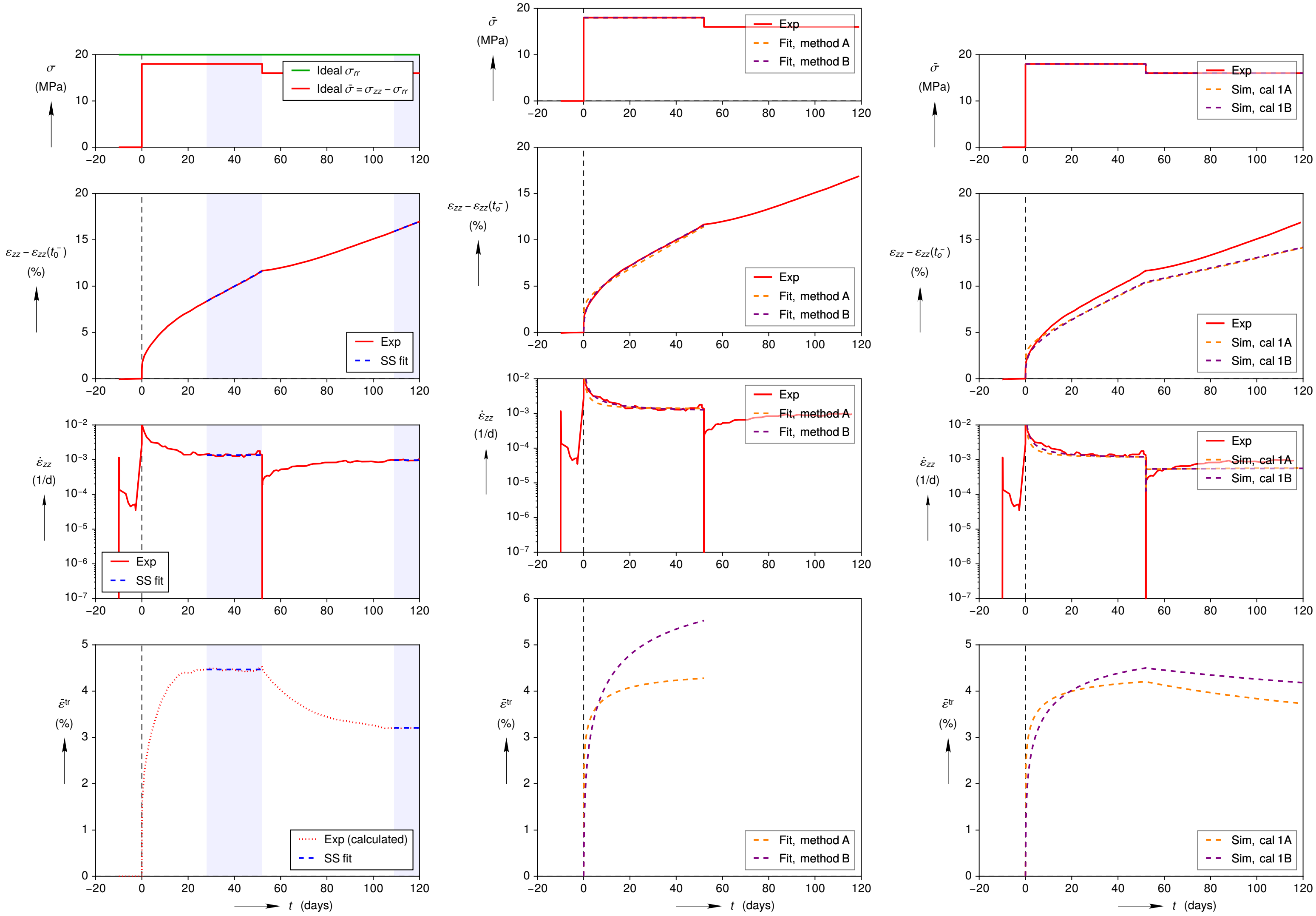

(a) Measurements (b) Individual fits (c) Global calibrations

Figure A.7: Experiment A_IfG_TCC14 at $T = 60$ °C

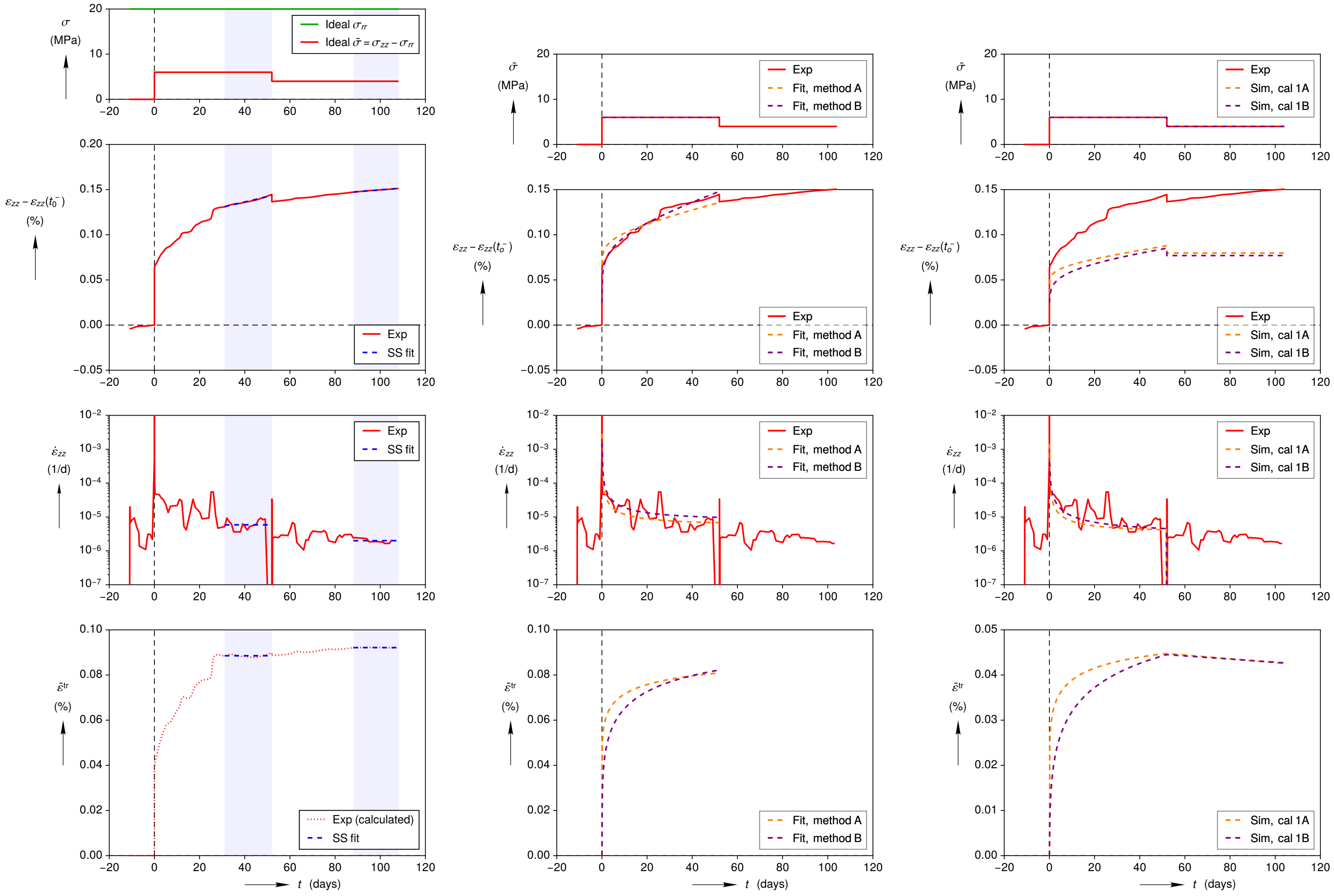

(a) Measurements (b) Individual fits (c) Global calibrations

Figure A.8: Experiment A_IfG_TCC2 at $T = 60$ °C

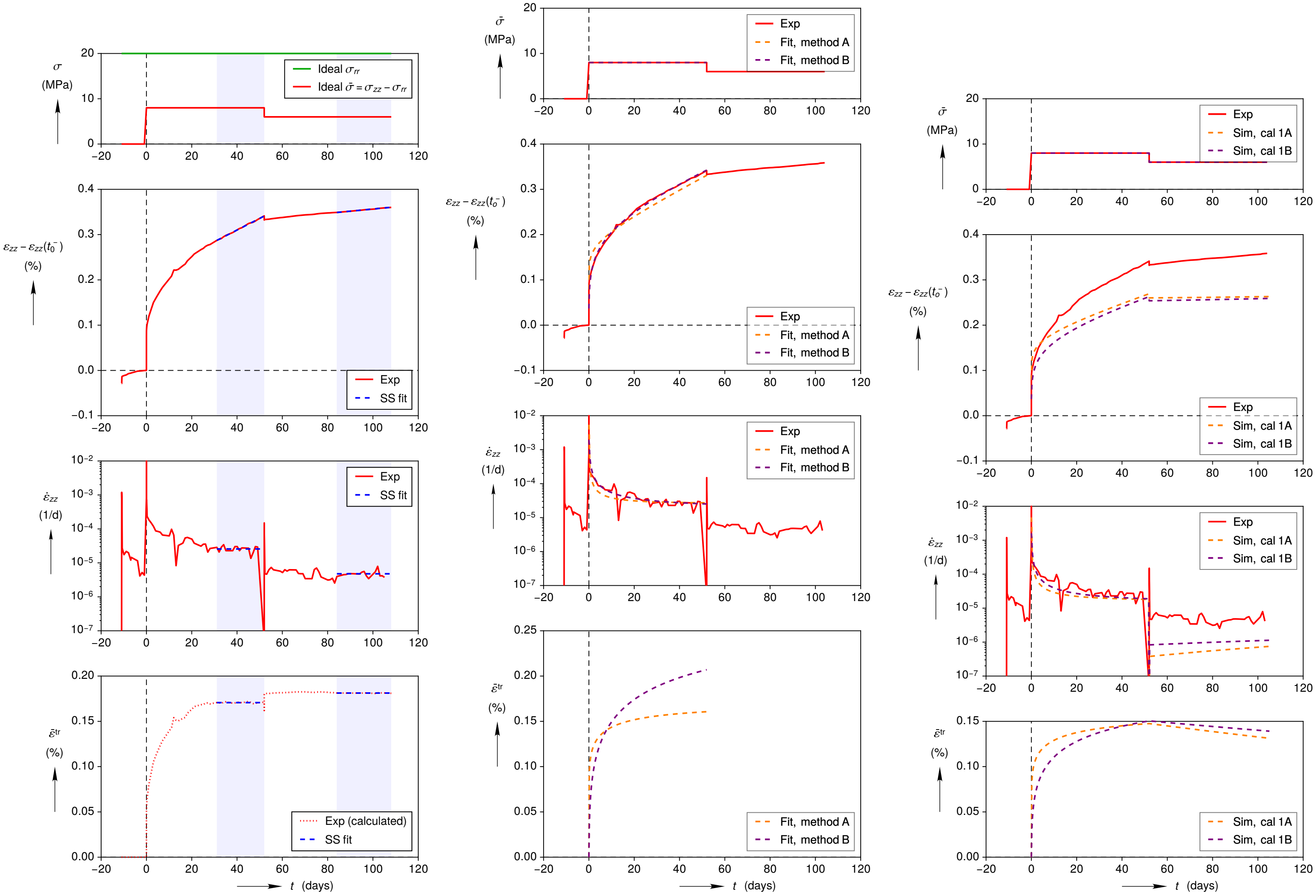

(a) Measurements (b) Individual fits (c) Global calibrations

Figure A.9: Experiment A_IfG_TCC3 at $T = 60$ °C

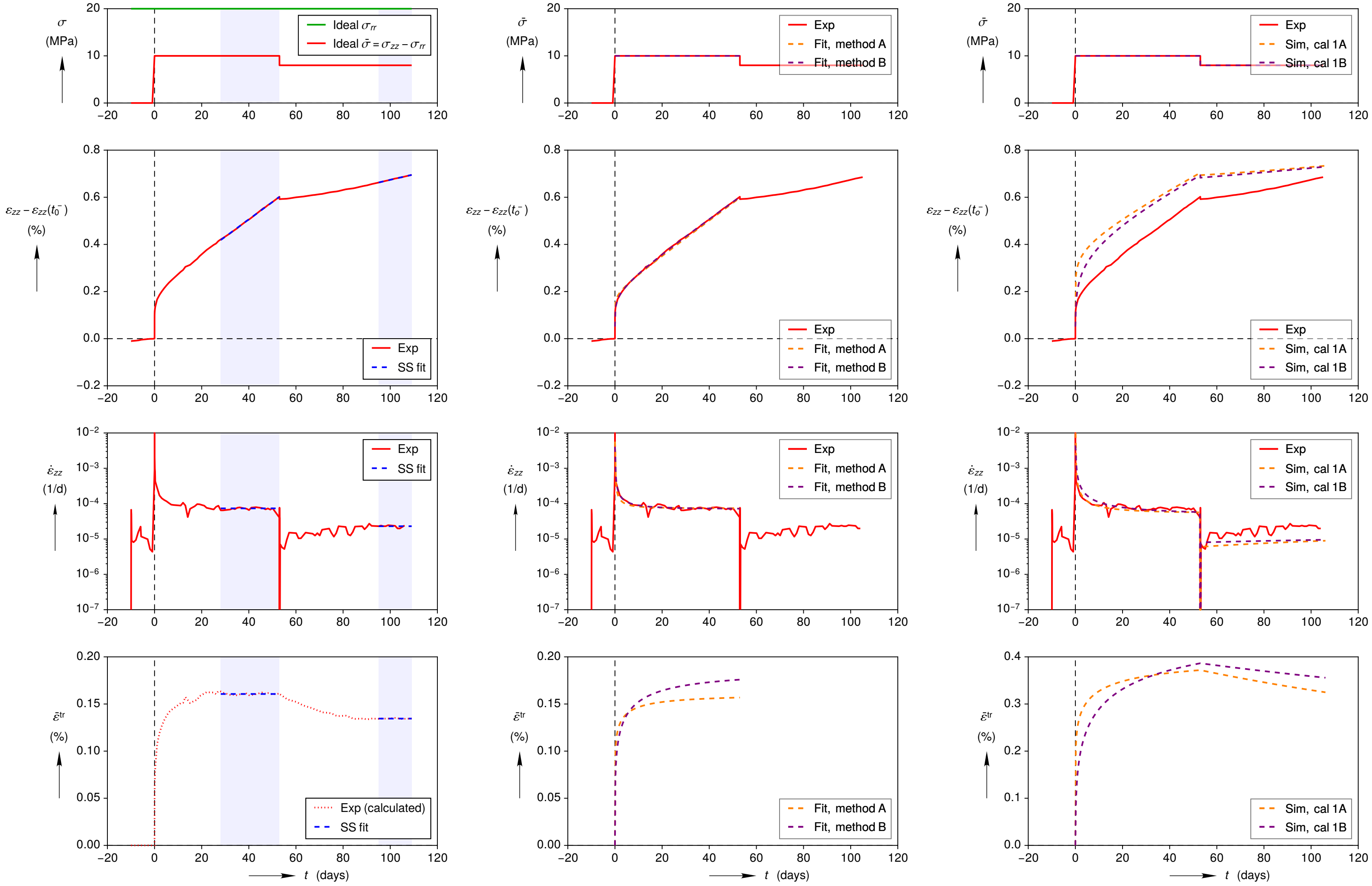

(a) Measurements (b) Individual fits (c) Global calibrations

Figure A.10: Experiment A_IfG_TCC4 at $T = 60$ °C

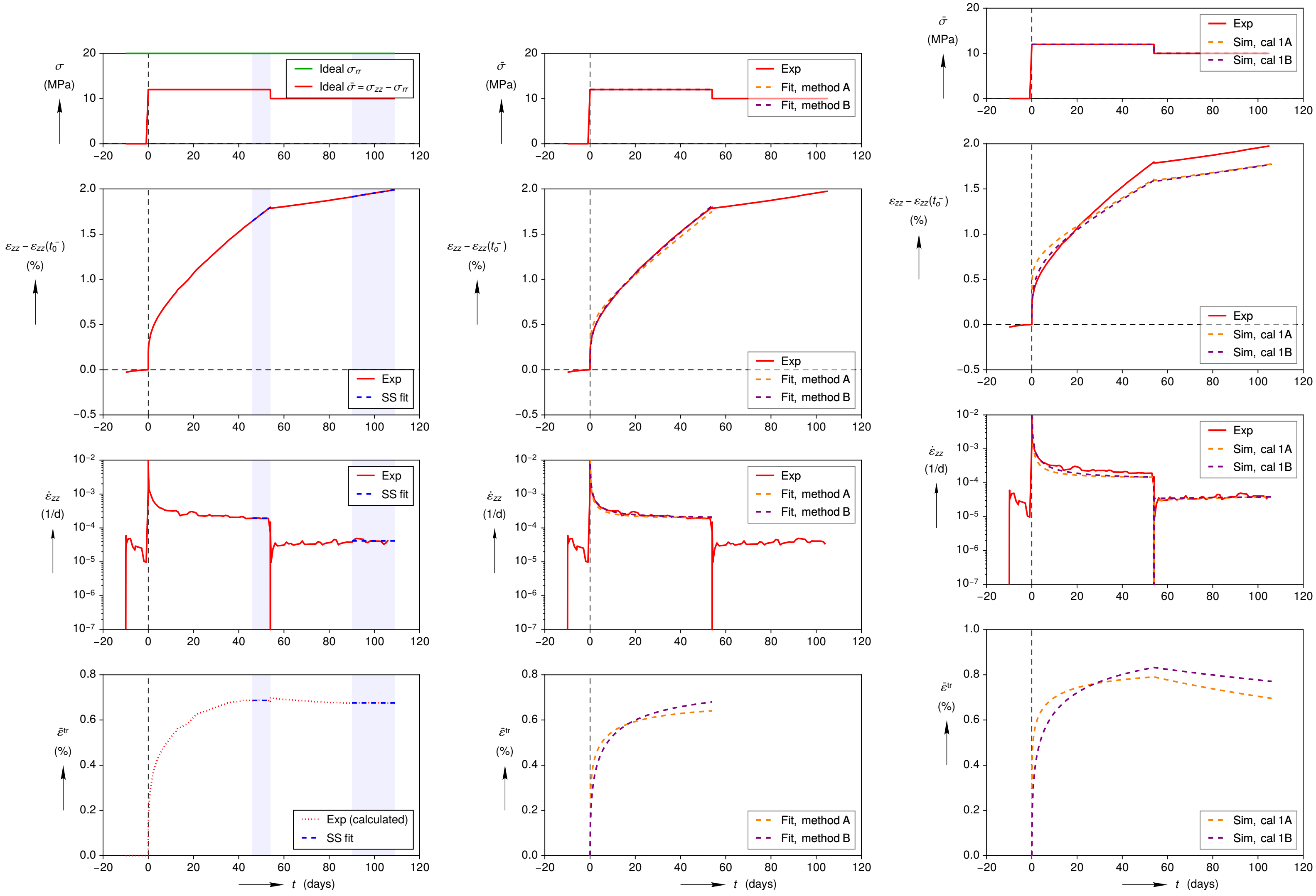

(a) Measurements

(b) Individual fits

(c) Global calibrations

Figure A.11: Experiment A_IfG_TCC5 at $T = 60$ °C

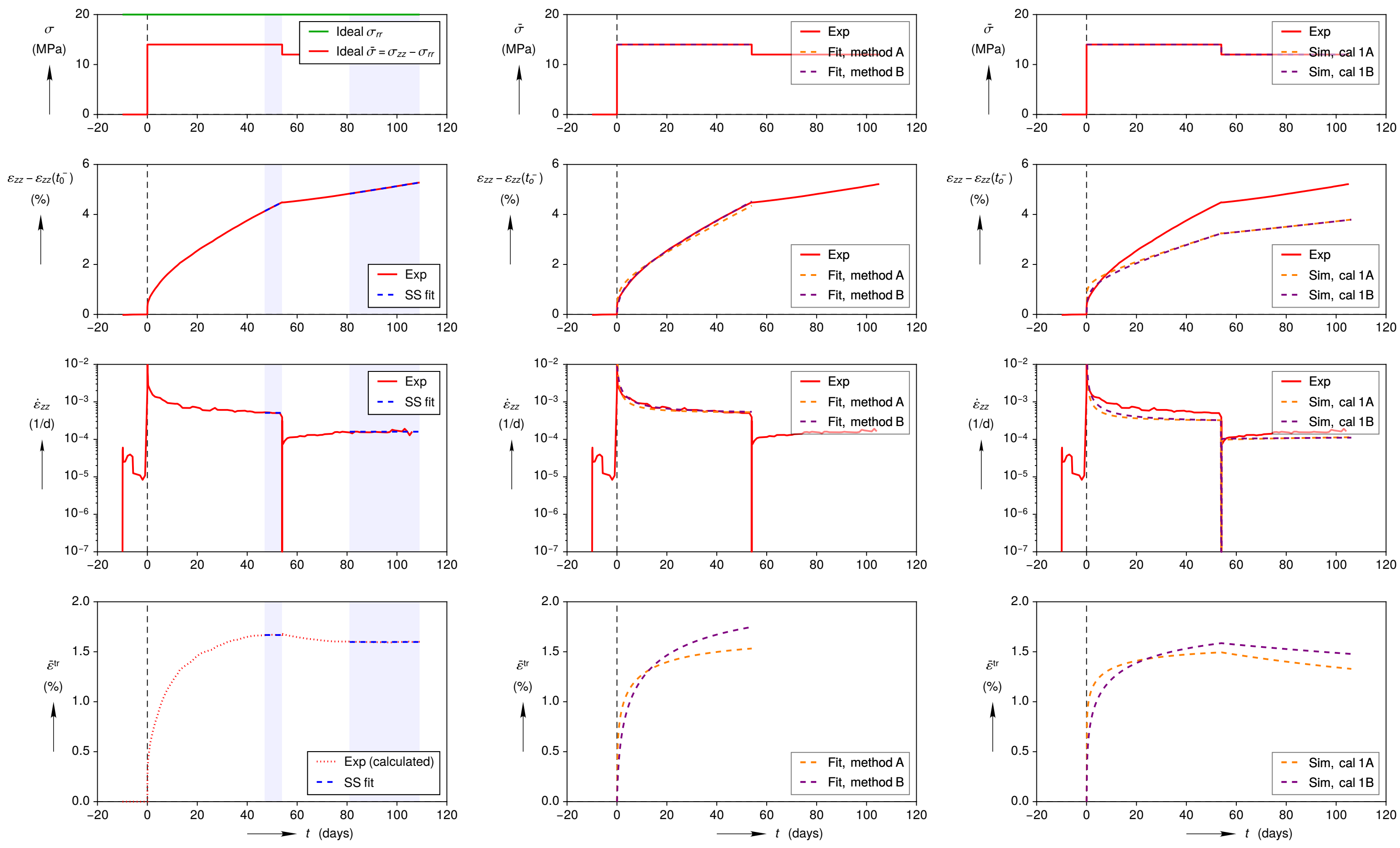

(a) Measurements (b) Individual fits (c) Global calibrations

Figure A.12: Experiment A_IfG_TCC6 at $T = 60$ °C

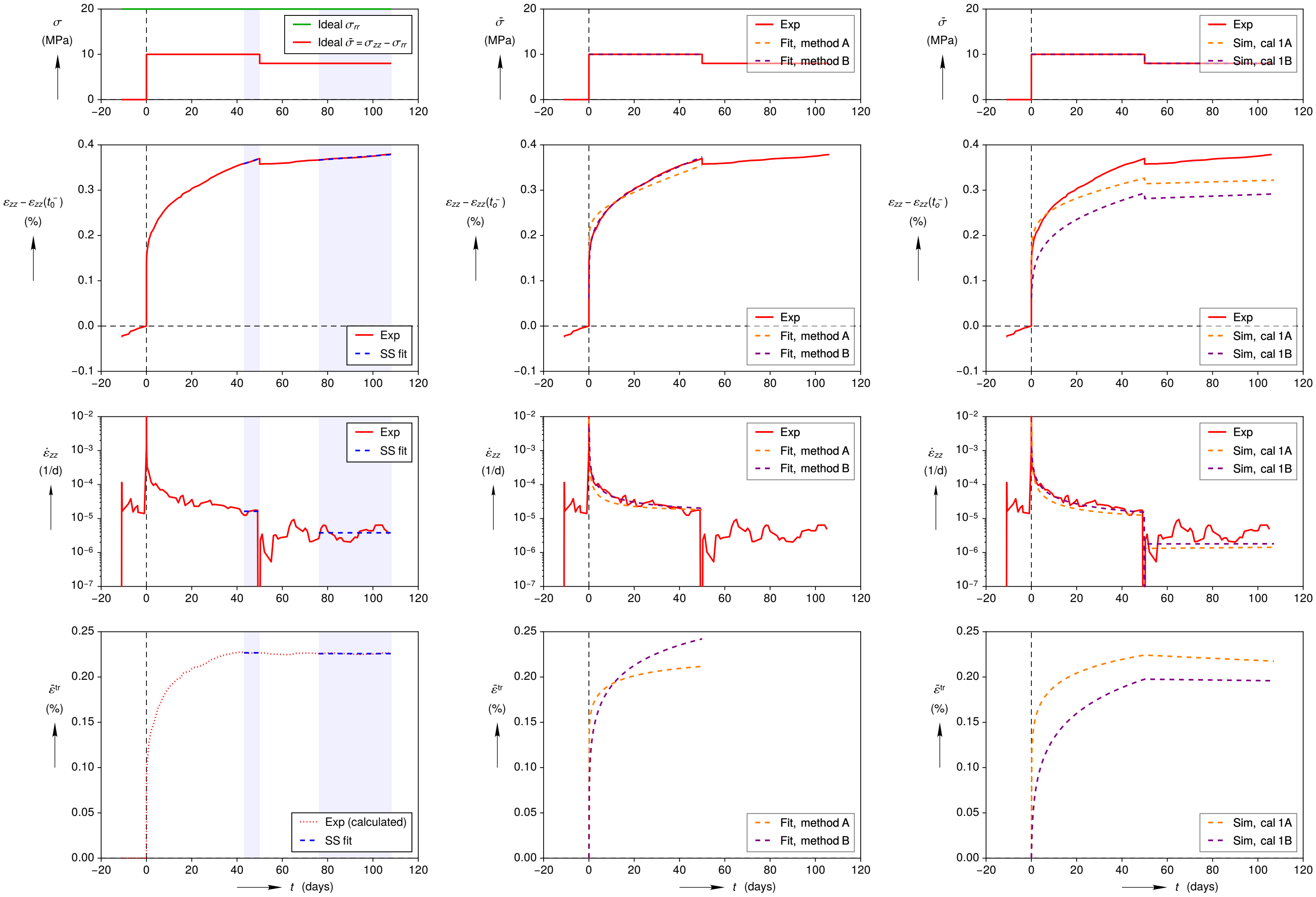

(a) Measurements (b) Individual fits (c) Global calibrations

Figure A.13: Experiment A_IfG_TCC9 at $T = 24$ °C

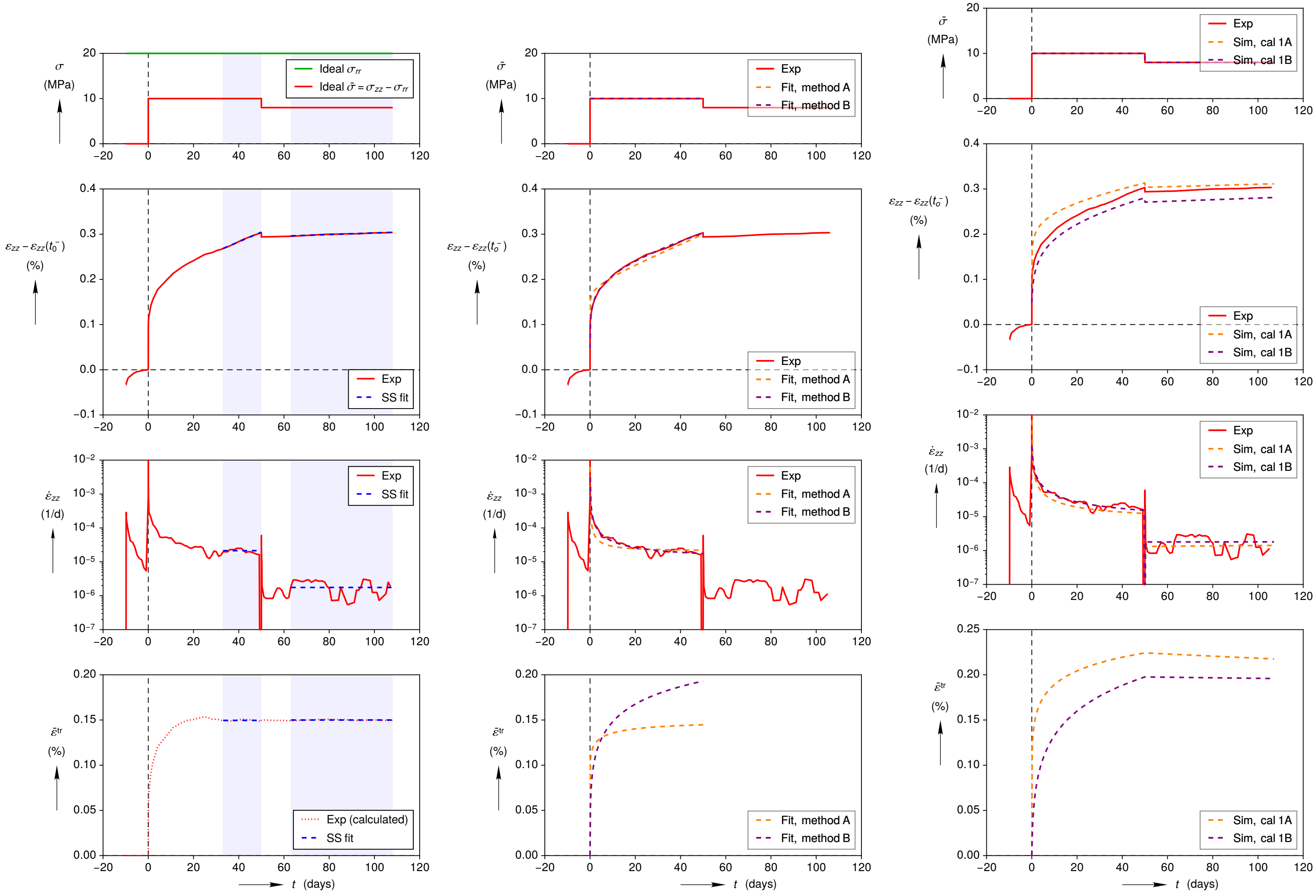

(a) Measurements

(b) Individual fits

(c) Global calibrations

Figure A.14: Experiment C_IfG_TCC1 at $T = 24$ °C

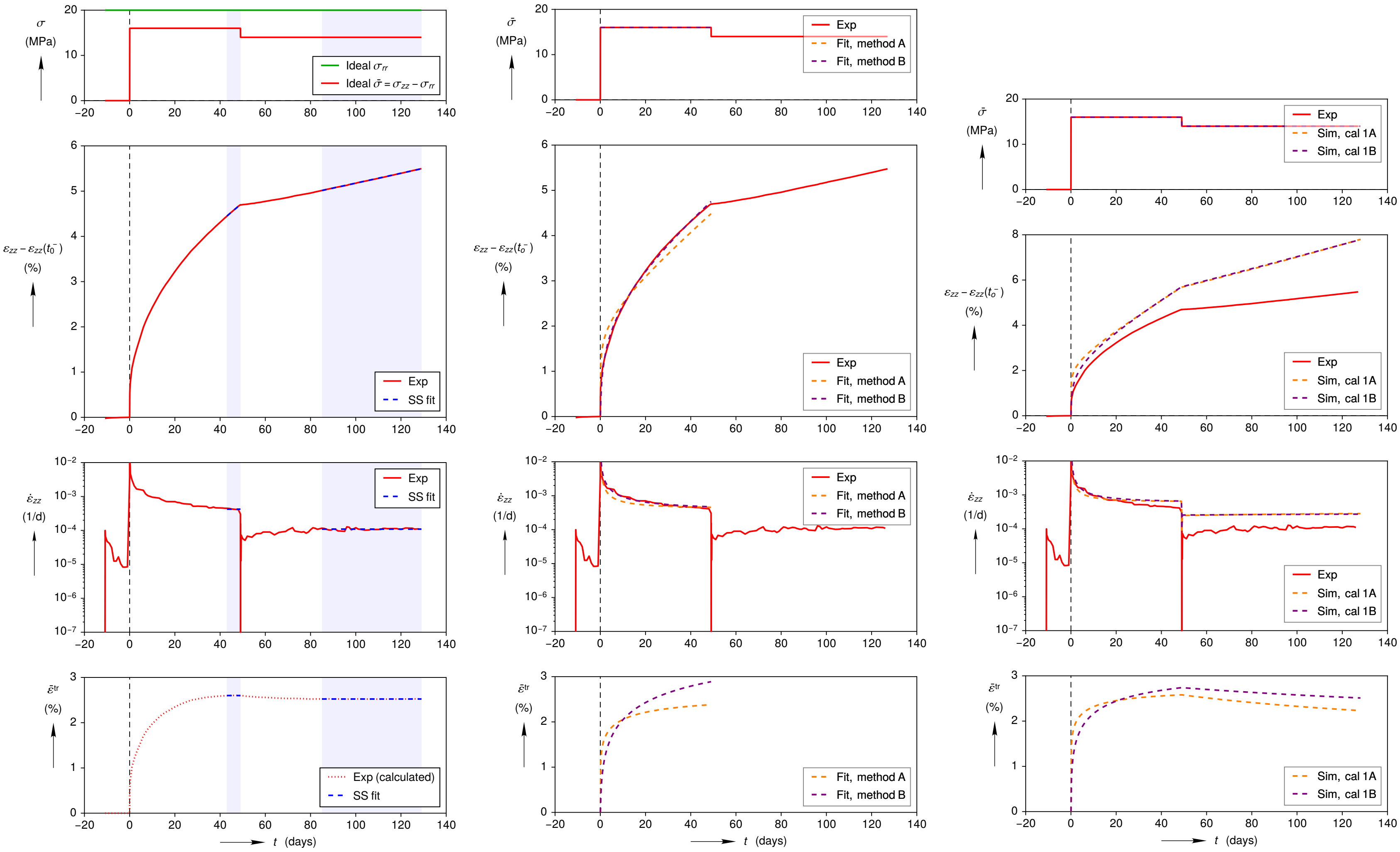

(a) Measurements

(b) Individual fits

(c) Global calibrations

Figure A.15: Experiment C_IfG_TCC11 at $T = 60$ °C

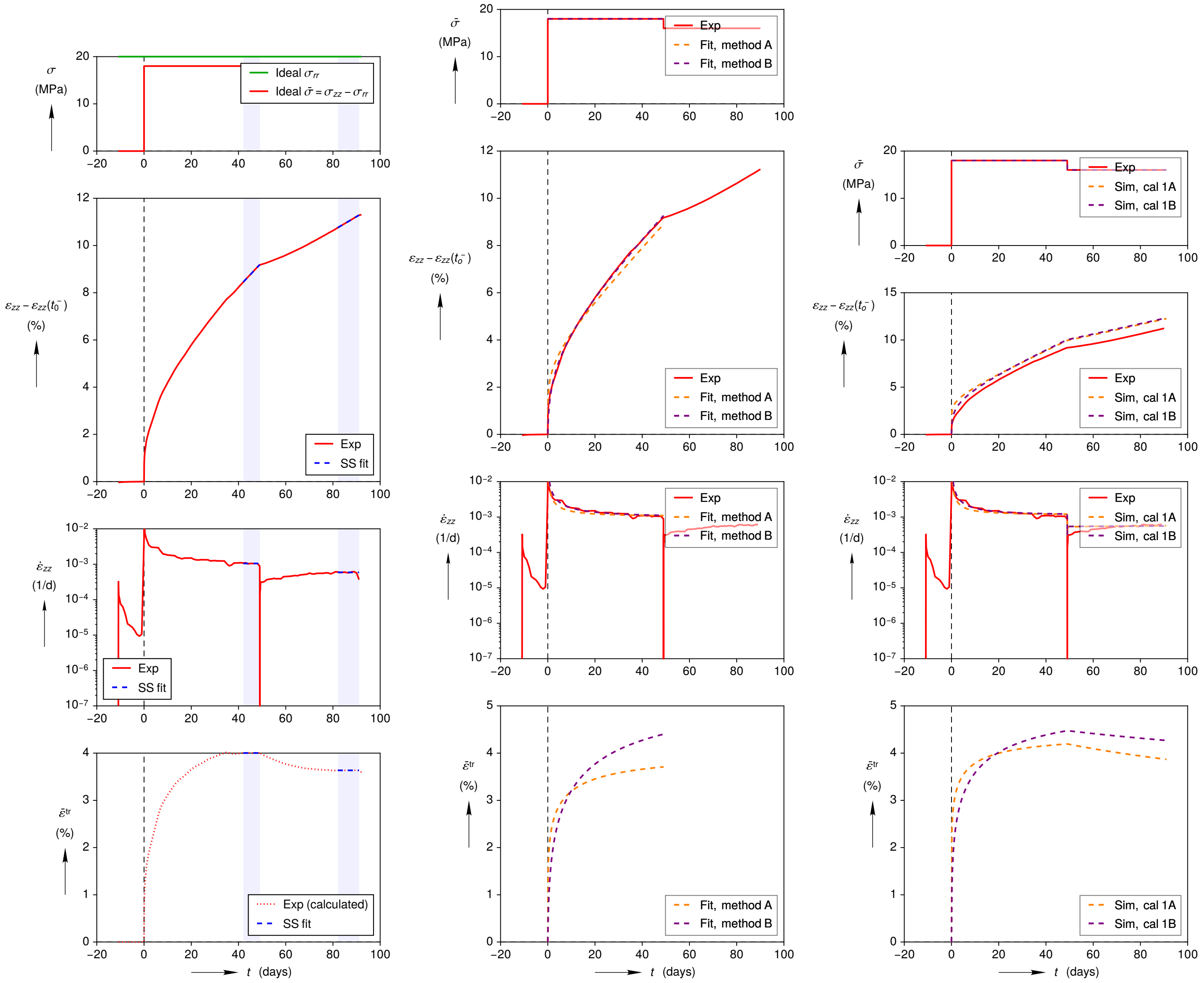

(a) Measurements (b) Individual fits (c) Global calibrations

Figure A.16: Experiment C_IfG_TCC12 at $T = 60$ °C

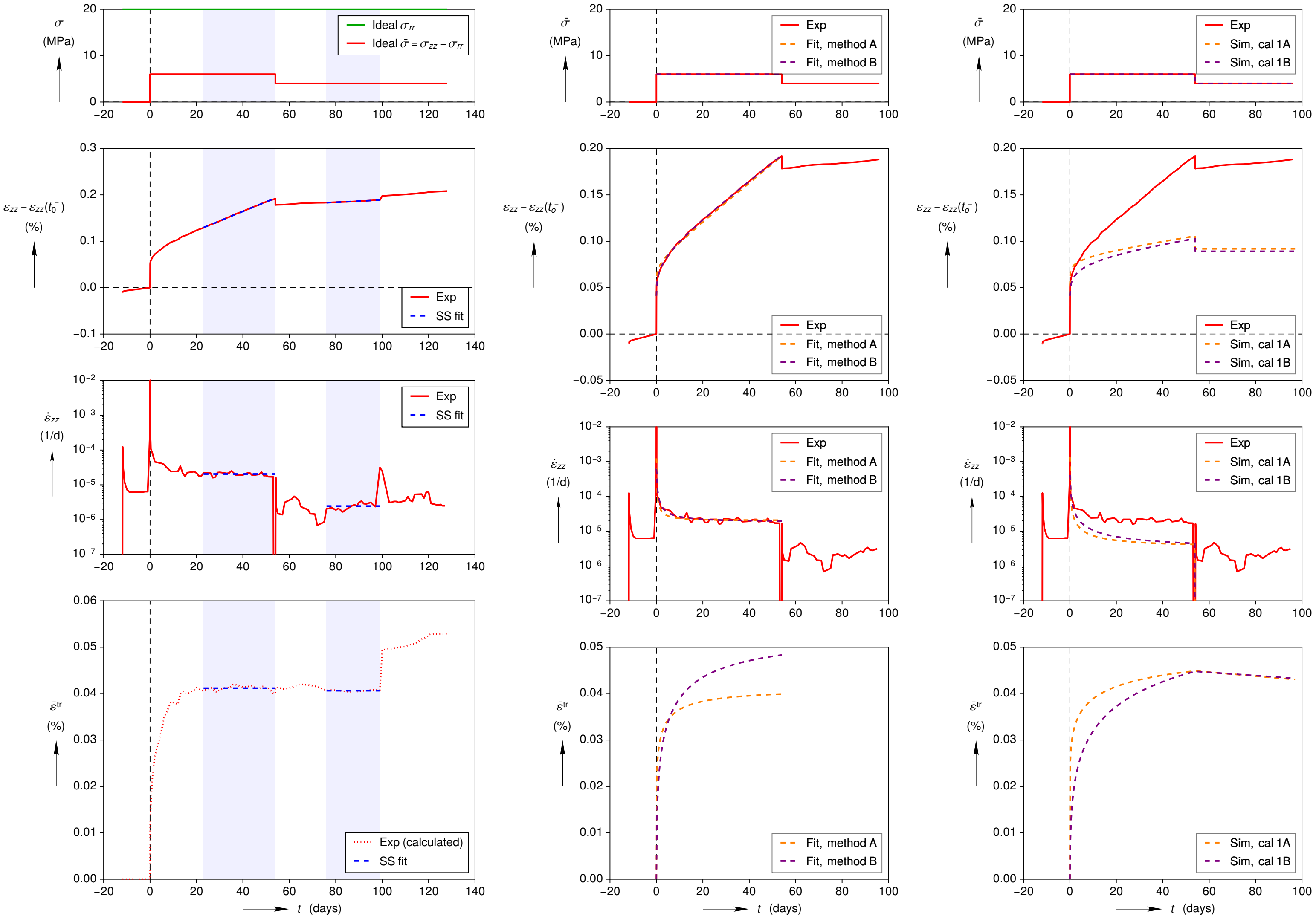

(a) Measurements (b) Individual fits (c) Global calibrations

Figure A.17: Experiment C_IfG_TCC13 at $T = 60$ °C

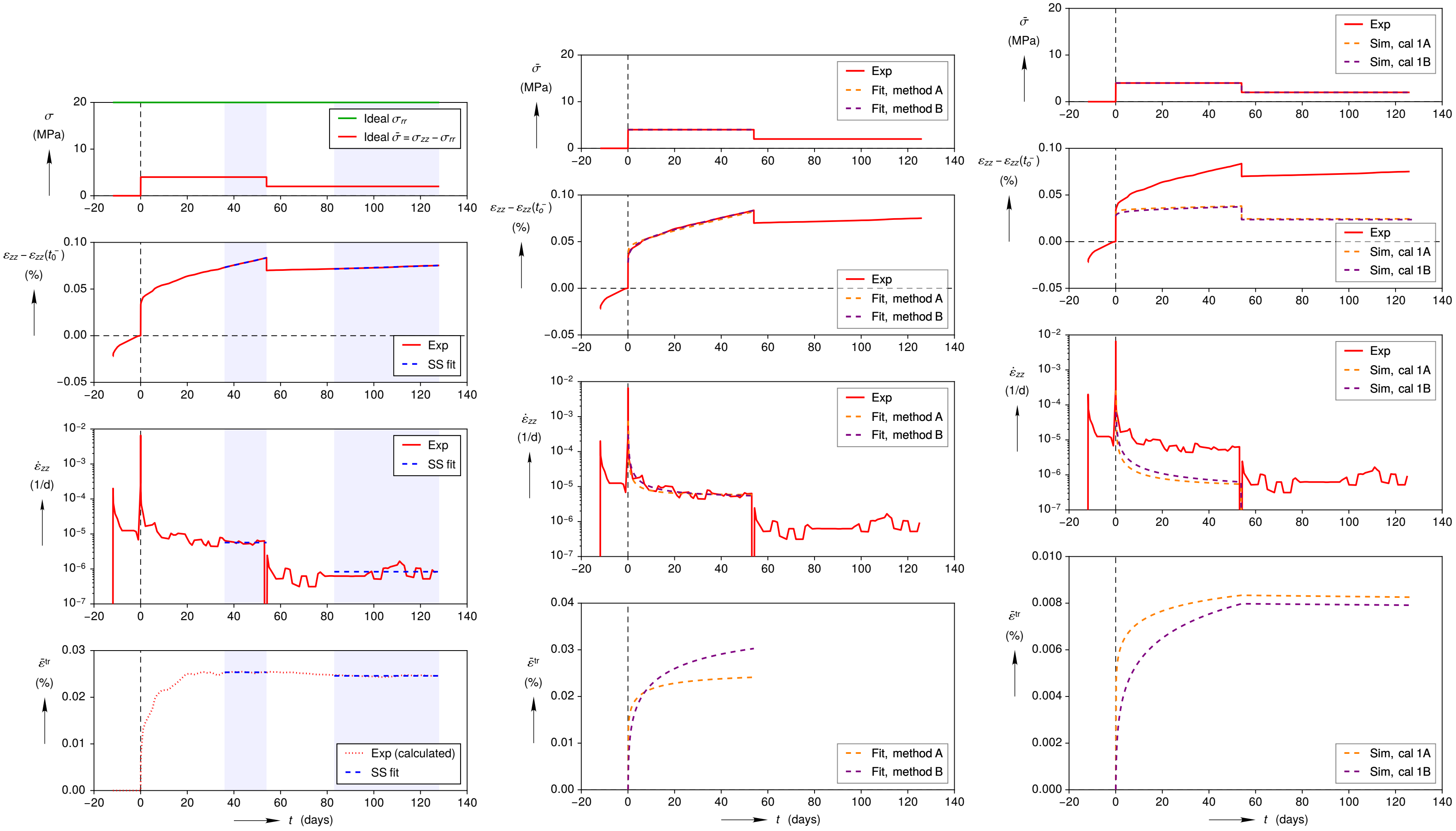

(a) Measurements (b) Individual fits (c) Global calibrations

Figure A.18: Experiment C_IfG_TCC15 at $T = 60$ °C

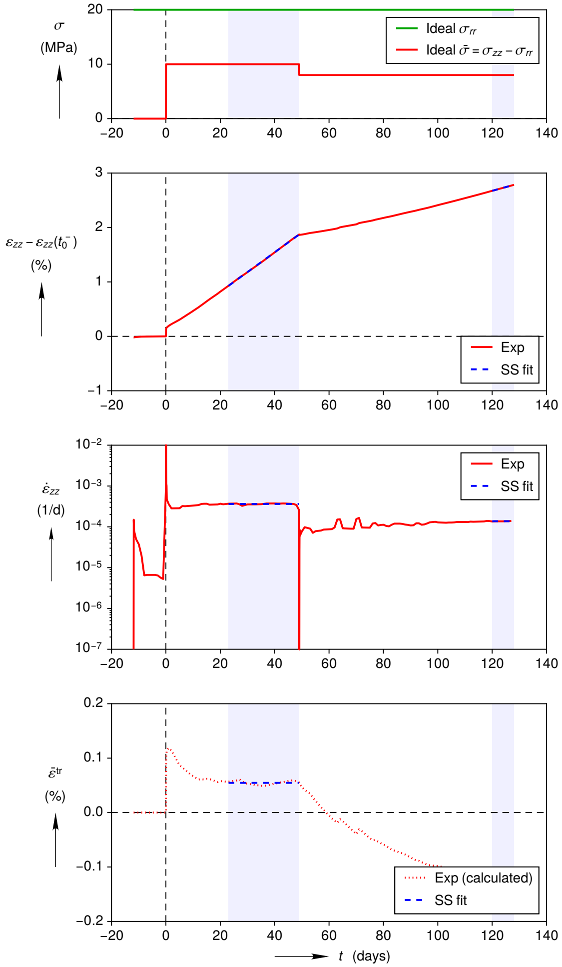

(a) Measurements

Figure A.19: Experiment C_IfG_TCC16 at $T = 80$ °C

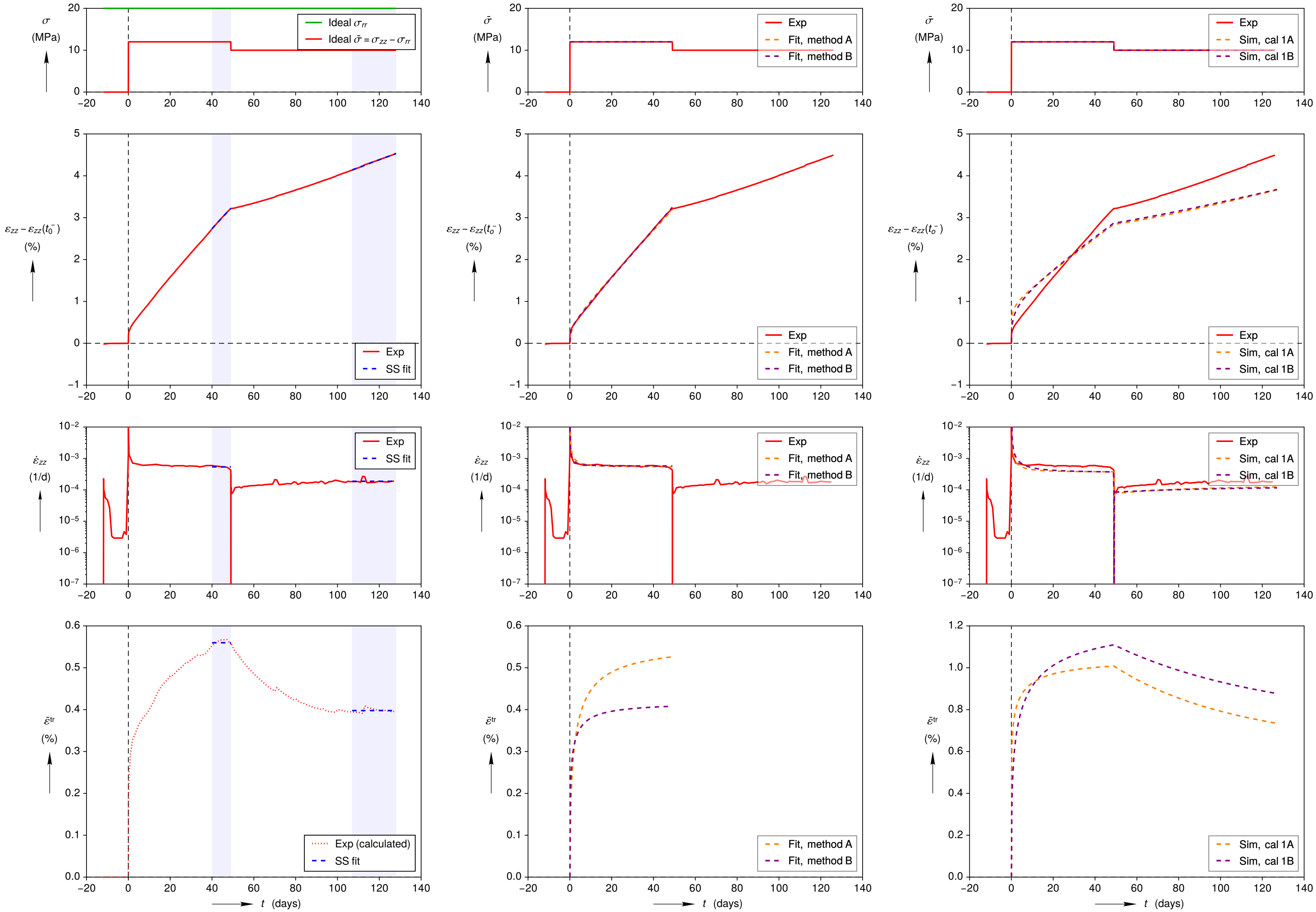

(a) Measurements

(b) Individual fits

(c) Global calibrations

Figure A.20: Experiment C_IfG_TCC19 at $T = 80$ °C

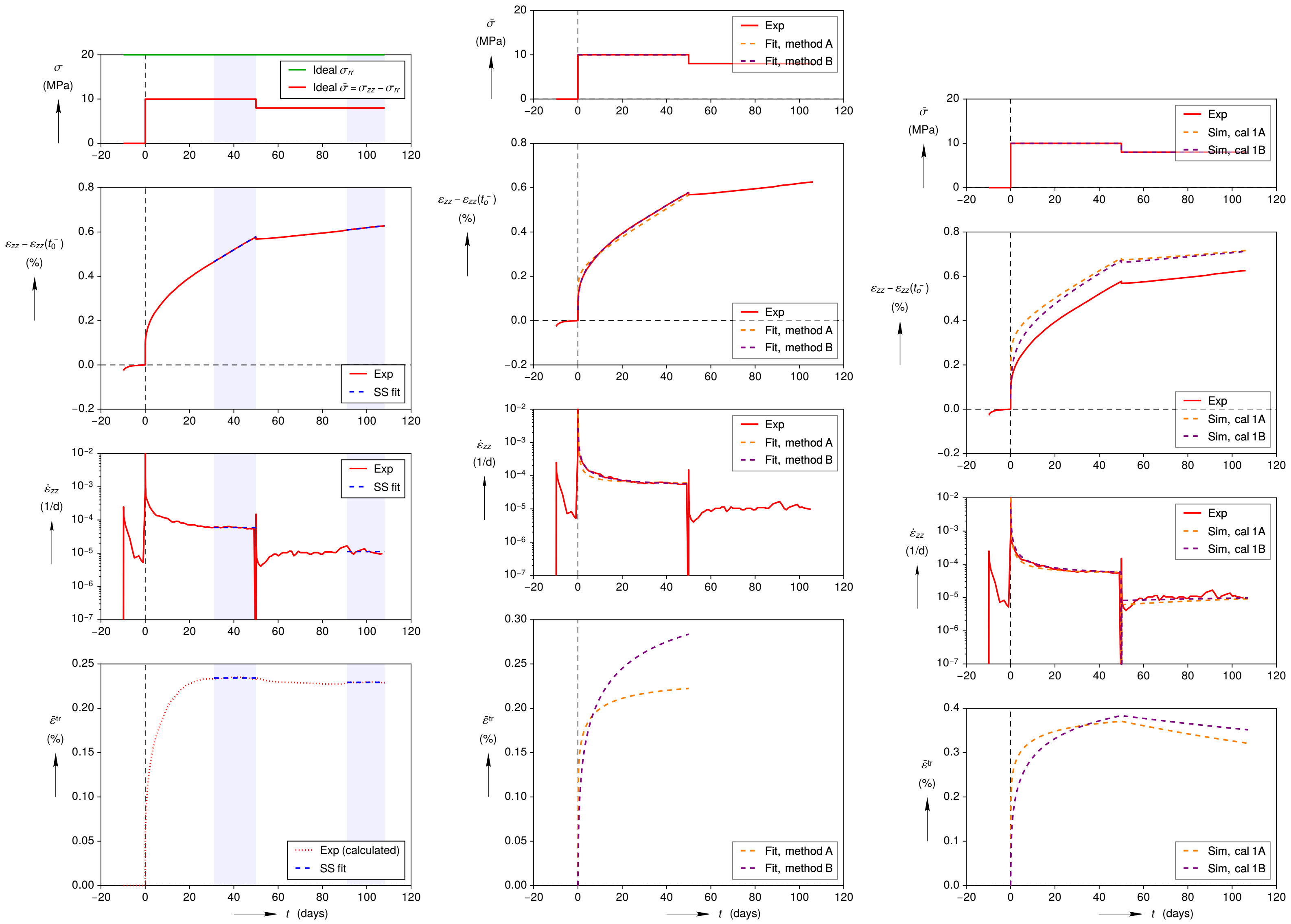

(a) Measurements (b) Individual fits (c) Global calibrations

Figure A.21: Experiment C_IfG_TCC2 at $T = 60$ °C

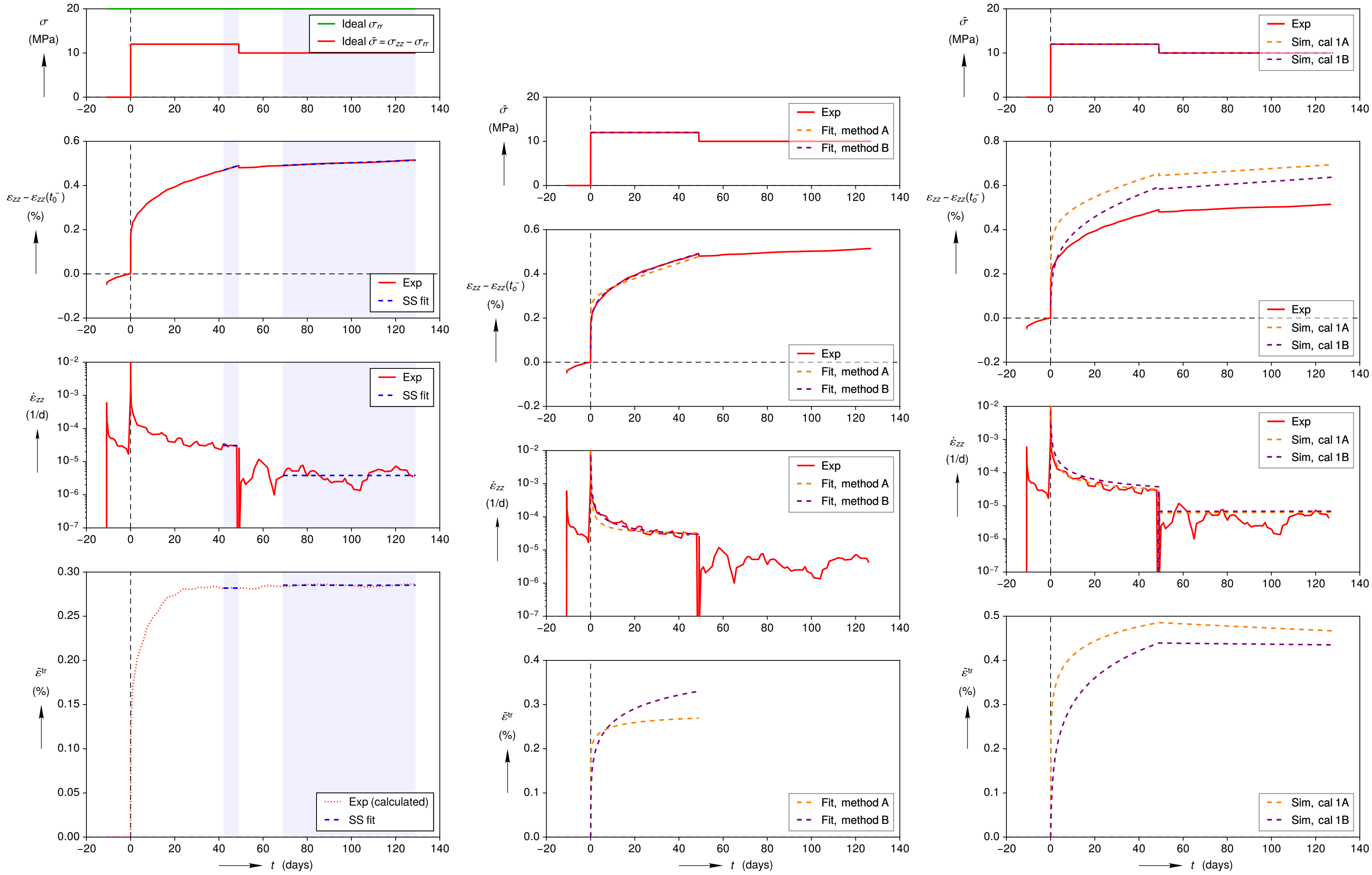

(a) Measurements (b) Individual fits (c) Global calibrations

Figure A.22: Experiment C_IfG_TCC5 at $T = 25$ °C

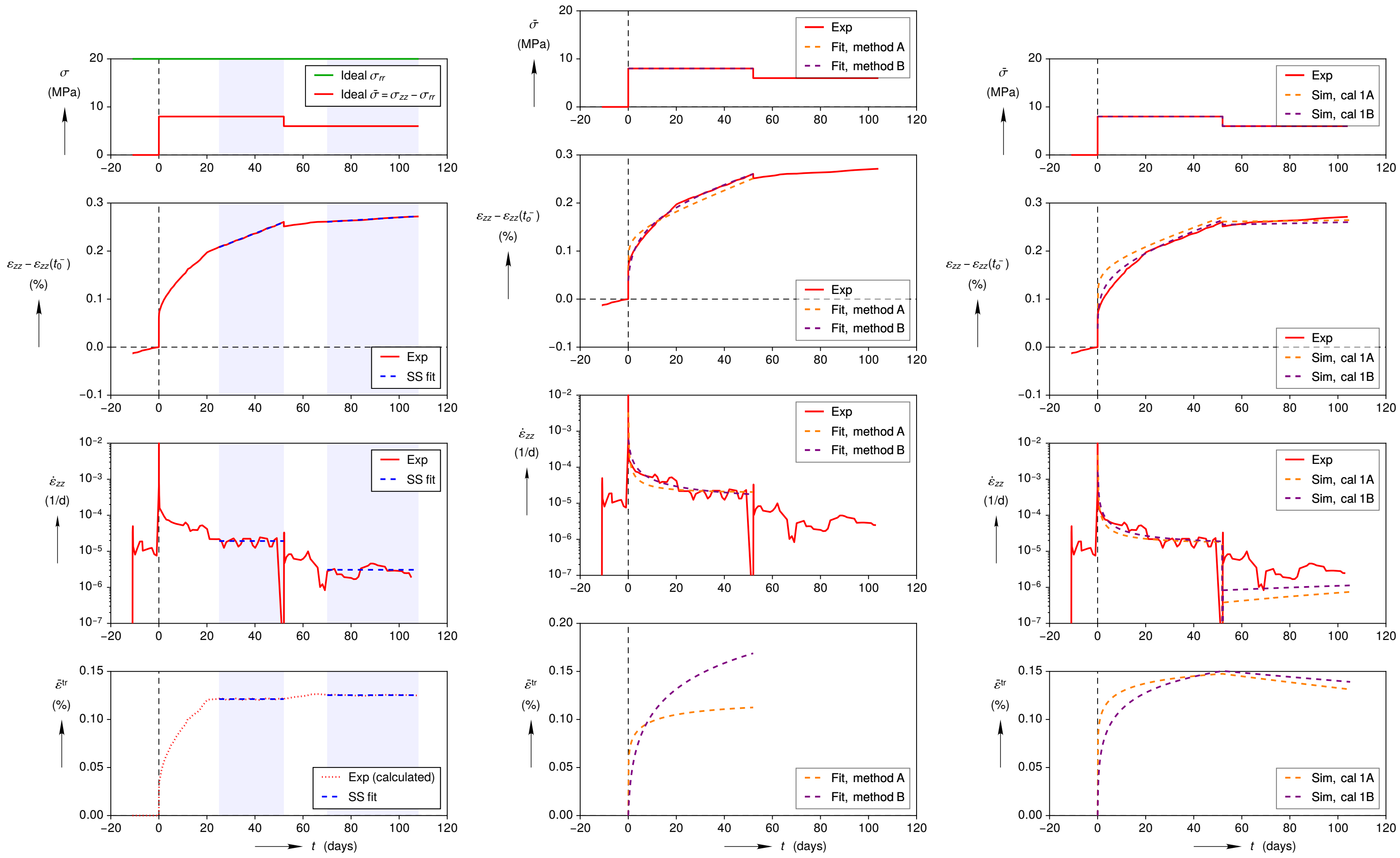

(a) Measurements (b) Individual fits (c) Global calibrations

Figure A.23: Experiment C_IfG_TCC6 at $T = 60$ °C

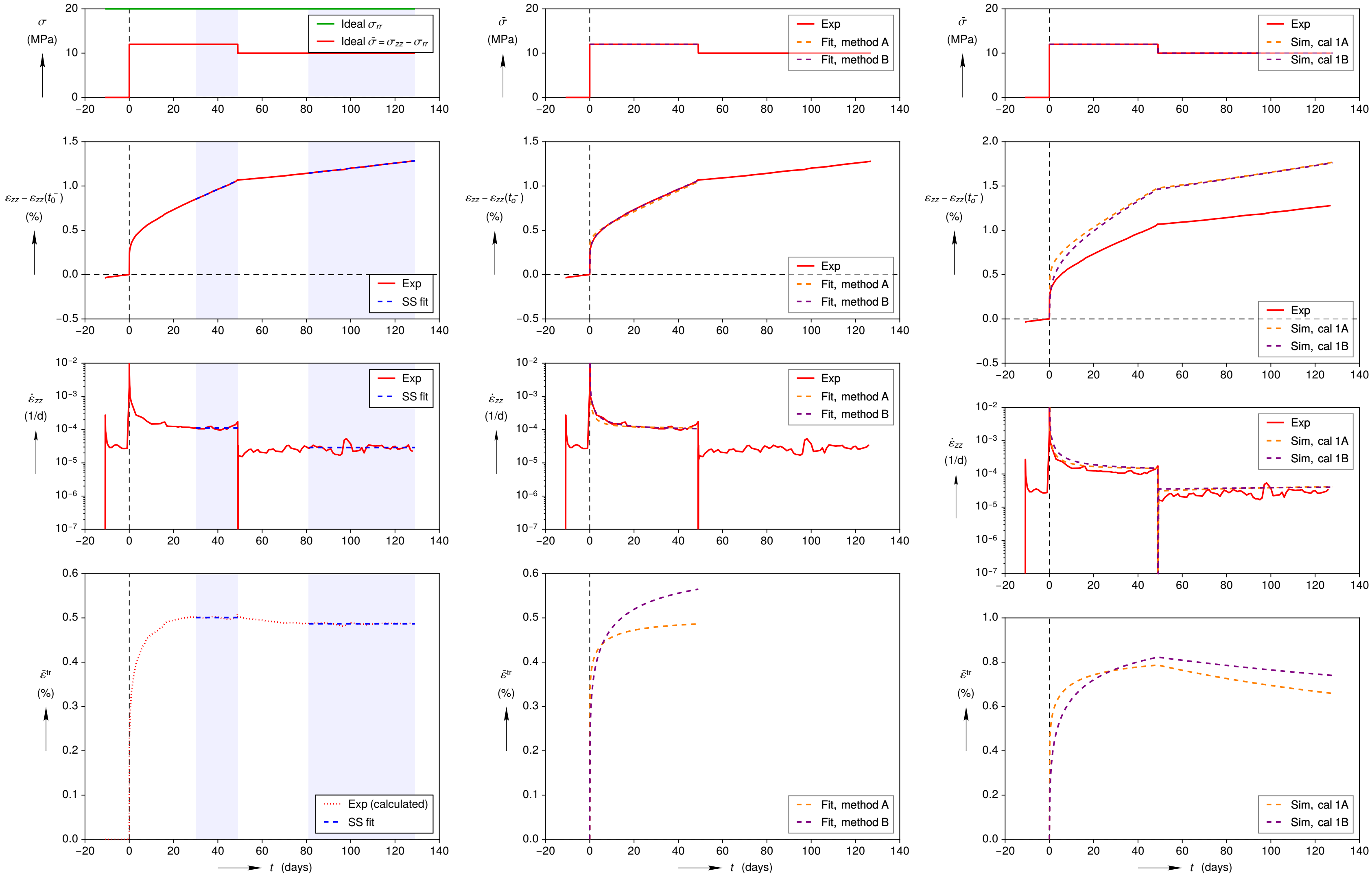

(a) Measurements (b) Individual fits (c) Global calibrations

Figure A.24: Experiment C_IfG_TCC7 at $T = 60$ °C

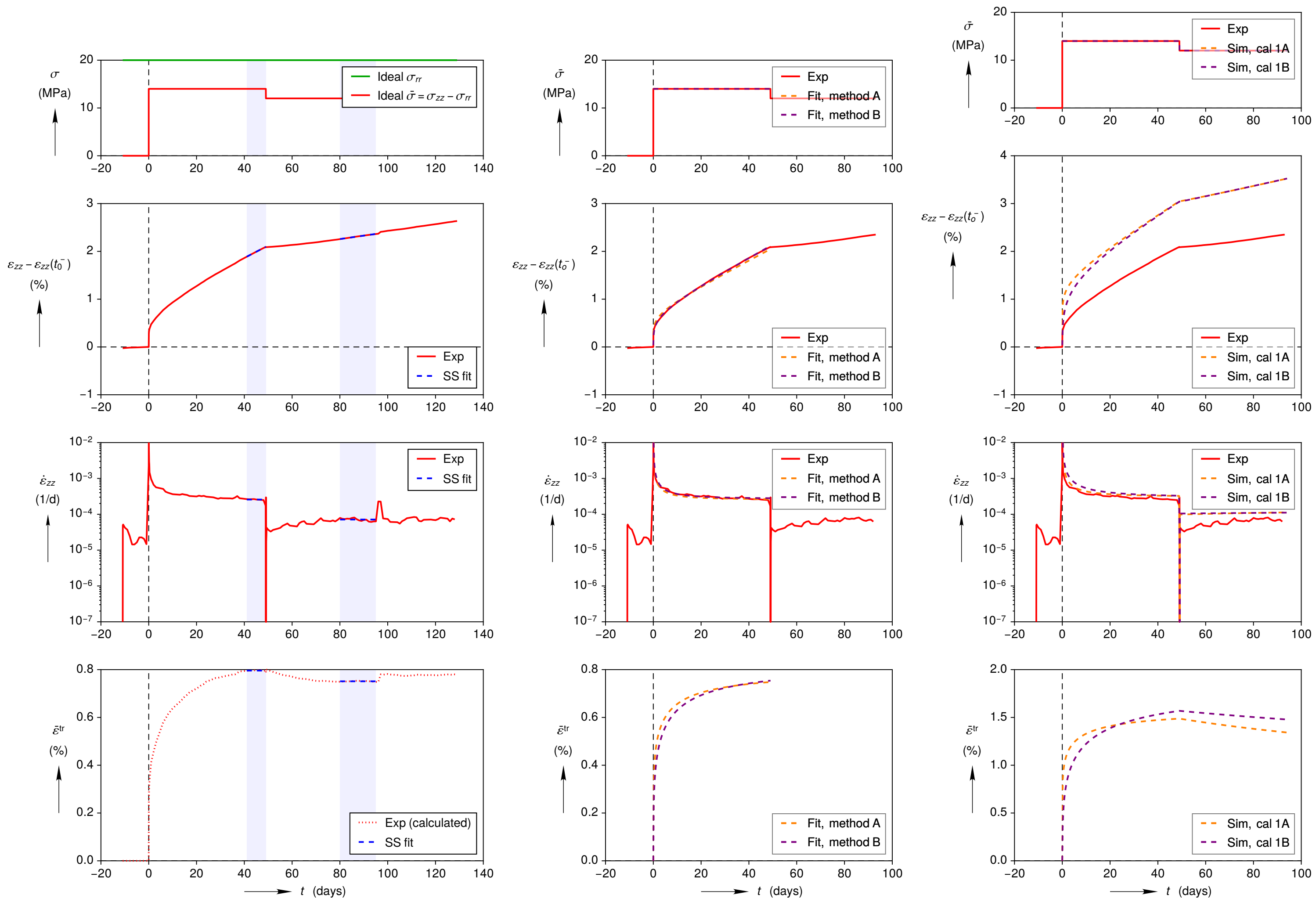

(a) Measurements (b) Individual fits (c) Global calibrations

Figure A.25: Experiment C_IfG_TCC9 at $T = 60$ °C

Table A.2: IfG creep test results on 2013 cores

					Method A			Method B		
Exp ID	T (°C)	E^{eff} (GPa)	$\bar{\sigma}$ (MPa)	w (−)	$\dot{\bar{\varepsilon}}^{\mathrm{ss}}$ (1/days)	$\bar{\varepsilon}^{\mathrm{tr}*}$ (%)	κ_{h} (−)	$\dot{\bar{\varepsilon}}^{\mathrm{ss}}$ (1/days)	$\bar{\varepsilon}^{\mathrm{tr}*}$ (%)	κ_{h} (−)
C_IfG_TCC1	24	20.78	10.0	1.0	2.135e-05	0.1496	33.49	1.225e-05	0.2483	7.265
			8.0	1.0	1.754e-06	0.15	–	1.754e-06	0.15	–
C_IfG_TCC2	60	21.23	10.0	1.0	5.952e-05	0.2341	12.36	4.959e-05	0.343	4.67
			8.0	1.0	1.120e-05	0.2293	–	1.120e-05	0.2293	–
C_IfG_TCC5	25	20.42	12.0	0.8	3.062e-05	0.2819	30.48	2.113e-05	0.4158	8.051
			10.0	1.0	3.825e-06	0.2851	–	3.825e-06	0.2851	–
C_IfG_TCC7	60	79.37	12.0	1.0	1.117e-04	0.5008	26.23	9.818e-05	0.6267	8.767
			10.0	1.0	2.900e-05	0.4868	–	2.900e-05	0.4868	–
C_IfG_TCC6	60	20.90	8.0	1.0	1.931e-05	0.1212	11.91	1.025e-05	0.264	4.203
			6.0	1.0	3.069e-06	0.1253	–	3.069e-06	0.1253	–
C_IfG_TCC9	60	38.04	14.0	0.8	2.575e-04	0.7961	8.286	2.698e-04	0.8235	5.609
			12.0	1.0	7.127e-05	0.7512	–	7.127e-05	0.7512	–
C_IfG_TCC15	60	14.55	4.0	1.0	5.677e-06	0.02535	13.39	4.763e-06	0.03629	5.007
			2.0	1.0	8.333e-07	0.02458	–	8.333e-07	0.02458	–
C_IfG_TCC16	80	26.31	10.0	1.0	3.632e-04	–	–	3.632e-04	–	–
			8.0	1.0	1.372e-04	–	–	1.372e-04	–	–
C_IfG_TCC11	60	54.07	16.0	0.6	4.234e-04	2.6	10.22	3.745e-04	3.753	4.362
			14.0	1.0	1.093e-04	2.524	–	1.093e-04	2.524	–
C_IfG_TCC13	60	14.54	6.0	1.0	2.049e-05	0.04116	10.7	1.907e-05	0.05305	4.476
			4.0	0.8	2.451e-06	0.04063	–	2.451e-06	0.04063	–
C_IfG_TCC12	60	67.68	18.0	0.9	1.053e-03	4.003	7.928	9.867e-04	5.355	3.788
			16.0	0.9	5.894e-04	3.635	–	5.894e-04	3.635	–
C_IfG_TCC19	80	46.58	12.0	1.0	5.386e-04	0.5598	3.071	5.749e-04	0.4178	5.91
			10.0	1.0	1.874e-04	0.3978	–	1.874e-04	0.3978	–
A_IfG_TCC6	60	18.78	14.0	0.8	5.087e-04	1.667	5.75	4.999e-04	2.093	3.112
			12.0	1.0	1.598e-04	1.598	–	1.598e-04	1.598	–
A_IfG_TCC5	60	17.20	12.0	1.0	1.930e-04	0.6867	7.647	1.975e-04	0.7679	4.477
			10.0	1.0	4.136e-05	0.6758	–	4.136e-05	0.6758	–
A_IfG_TCC4	60	19.52	10.0	1.0	7.359e-05	0.1606	15.47	7.064e-05	0.1867	6.989
			8.0	1.0	2.301e-05	0.1345	–	2.301e-05	0.1345	–
A_IfG_TCC3	60	21.83	8.0	1.0	2.569e-05	0.1707	15.76	1.899e-05	0.2691	5.313
			6.0	1.0	4.763e-06	0.1812	–	4.763e-06	0.1812	–
A_IfG_TCC2	60	24.64	6.0	0.8	5.863e-06	0.08854	19.56	7.972e-06	0.09796	7.675
			4.0	1.0	1.998e-06	0.09214	–	1.998e-06	0.09214	–
A_IfG_TCC1	60	16.52	4.0	0.6	6.949e-06	0.04916	10.16	3.026e-06	0.1235	4.121
			2.0	1.0	9.224e-07	0.05014	–	9.224e-07	0.05014	–
A_IfG_TCC9	24	16.28	10.0	0.6	1.633e-05	0.2267	26.08	1.398e-05	0.3062	8.321
			8.0	1.0	3.797e-06	0.2258	–	3.797e-06	0.2258	–

Table A.2: IfG creep test results on 2013 cores

					Method A			Method B		
Exp ID	T (°C)	E^{eff} (GPa)	$\bar{\sigma}$ (MPa)	w (−)	$\dot{\bar{\varepsilon}}^{\mathrm{ss}}$ (1/days)	$\bar{\varepsilon}^{\mathrm{tr}*}$ (%)	κ_{h} (−)	$\dot{\bar{\varepsilon}}^{\mathrm{ss}}$ (1/days)	$\bar{\varepsilon}^{\mathrm{tr}*}$ (%)	κ_{h} (−)
A_IfG_TCC14	60	21.43	18.0	1.0	1.358e-03	4.468	12.25	1.145e-03	6.52	4.52
			16.0	1.0	9.685e-04	3.205	–	9.685e-04	3.205	–
A_IfG_TCC13	60	22.26	16.0	0.8	8.329e-04	3.383	8.102	7.916e-04	4.387	4.004
			14.0	1.0	5.959e-04	2.468	–	5.959e-04	2.468	–
A_IfG_TCC12	80	42.00	12.0	1.0	7.106e-04	0.85	7.021	7.016e-04	0.9606	4.012
			10.0	1.0	1.834e-04	0.6802	–	1.834e-04	0.6802	–
A_IfG_TCC11	80	22.12	10.0	1.0	2.802e-04	–	–	2.802e-04	–	–
			8.0	0.6	1.227e-04	–	–	1.227e-04	–	–
A_IfG_TCC10	25	19.20	12.0	0.6	2.518e-05	0.3322	26.55	1.351e-05	0.5627	7.313
			10.0	1.0	4.316e-06	0.3348	–	4.316e-06	0.3348	–

A.5 Fits of the TUC Triaxial Creep Tests on 2001 Cores

Most TUC creep tests were performed on old cores drilled in the years 2000 to 2001 from the Room Q alcove, according to the *Deal et al.* (1989) stratigraphy in Fig. 3.1a. Further details on the 2001 core drilling can be found in *Powers* (2001). After storing these 4 inch diameter, 9 inch long cores for more than a decade, they were sent to Germany in November 2012 (*Schuhen*, 2016b). The TUC tests on argillaceous cores are listed in rows 25 through 38 of Table 2 in *Düsterloh et al.* (2015). A_TUC_TCC20 is the only other 2001 core test performed by the TUC, to the current author's knowledge. It is not listed in Table 2 of *Düsterloh et al.* (2015), and it was tested at $\bar{\sigma} = 10$ MPa, with no confining pressure ($\sigma_{rr} = 0$). All other creep tests used $\sigma_{rr} = 20$ MPa, so A_TUC_TCC20 is ignored herein. The TUC tests on clean cores are not listed in *Salzer et al.* (2015). This is probably because *Salzer et al.* (2015) was written principally by the IfG instead of the TUC.

The TUC tests in this section and in Appendix A.6 were quite similar to the IfG, but a few differences should be mentioned. The TUC included the measured stress histories with every test instead of just the nominal values. These stress histories, along with idealized stress histories, are included in the figure for each TUC experiment. The TUC applied hydrostatic pressure for one day instead of ten and did not record data during this time. The TUC sometimes applied three or four equivalent stress levels, instead of two. The first two equivalent stresses were below the dilatancy strength and used to characterize the creep response. The third and fourth were above the dilatancy strength and used to characterize the damage induced creep response. Only the first two levels are considered herein. As mentioned in Appendix A.3, some TUC tests did not include an axial stress drop, so E^{eff} was simply set to E.

Fitting the TUC 2001 core tests was problematic. Fig. A.26 through Fig. A.34 show the analysis of the tests. A_TUC_TCC11 (see Fig. A.26) exhibited similar behavior to C_IfG_TCC16 (see Appendix A.4 for a discussion), so its values of $\bar{\varepsilon}^{\text{tr}^*}$ and κ_{h} were discarded. Method A failed to fit κ_{h} in all tests, except A_TUC_TCC2. Method B even failed to fit C_TUC_TCC6 and C_TUC_TCC8, probably because they have ε_{zz} vs. t curves that rapidly increase and level off. When method B failed to fit an experiment, the method A's values for $\dot{\bar{\varepsilon}}^{\text{ss}}$ and $\bar{\varepsilon}^{\text{tr}^*}$ were assumed for method B. Table A.3 displays the test temperature T, the equivalent stress $\bar{\sigma}$, the effective axial stiffness E^{eff}, the weighting factor w, and the results of fitting method A and method B for each test.

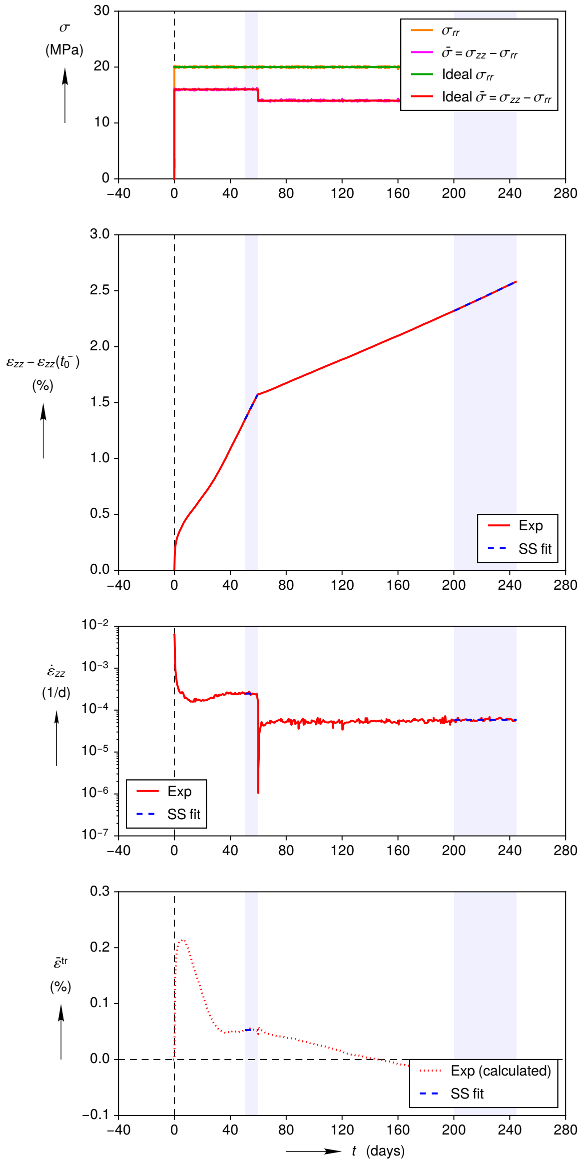

(a) Measurements

Figure A.26: Experiment A_TUC_TCC11 at $T = 27$ °C

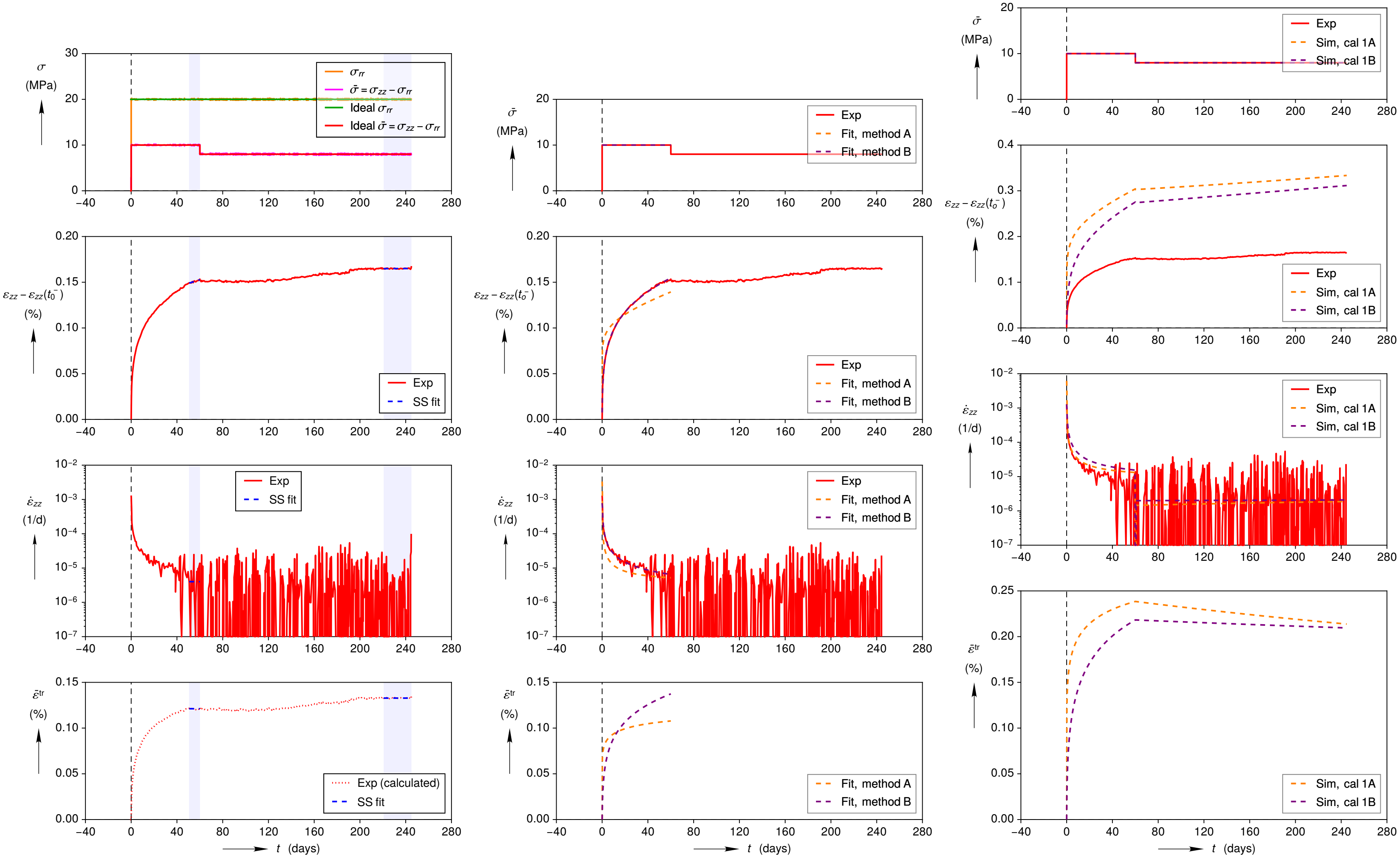

(a) Measurements (b) Individual fits (c) Global calibrations

Figure A.27: Experiment A_TUC_TCC2 at $T = 27$ °C

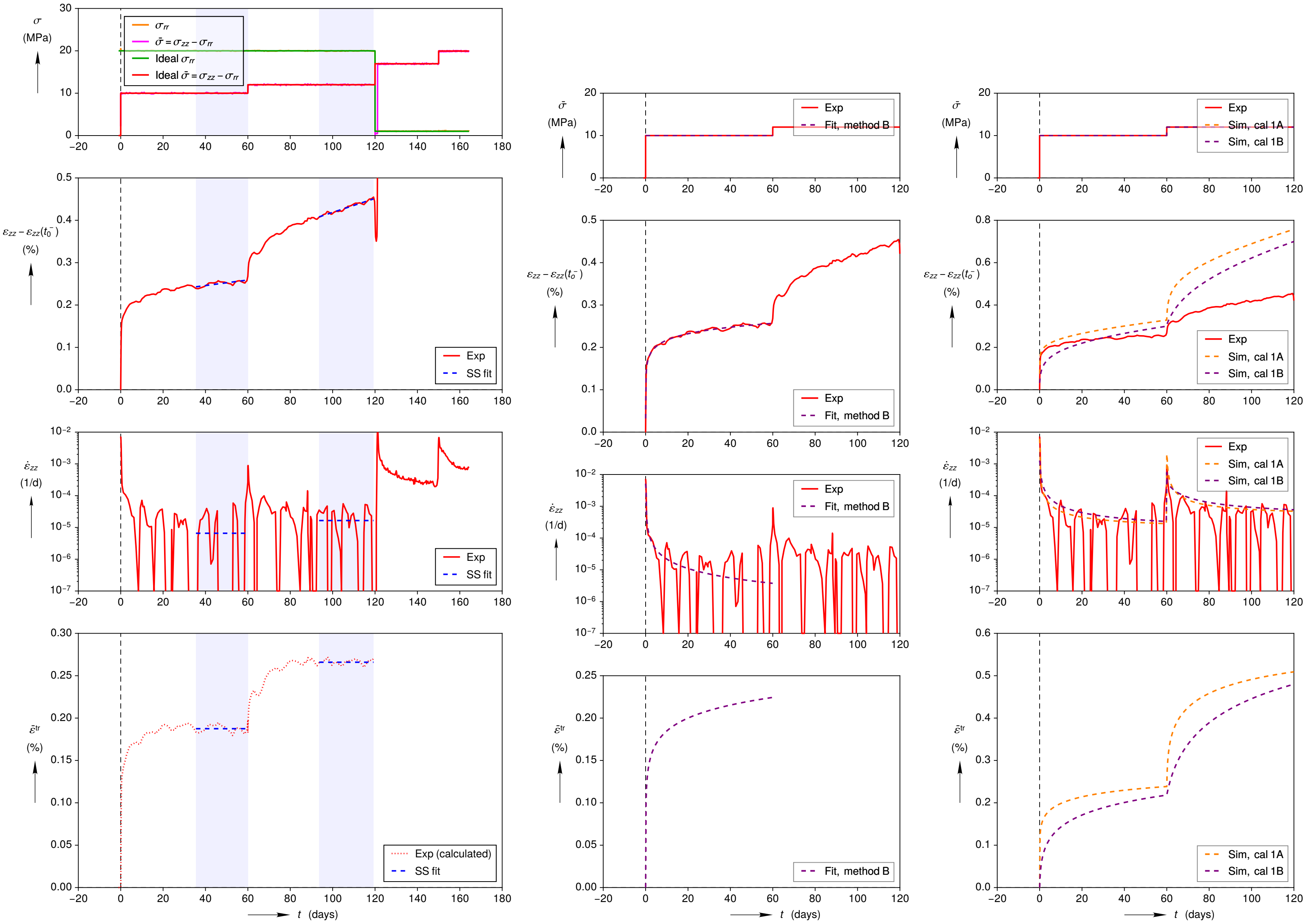

(a) Measurements (b) Individual fit (c) Global calibrations

Figure A.28: Experiment A_TUC_TCC3 at $T = 27$ °C

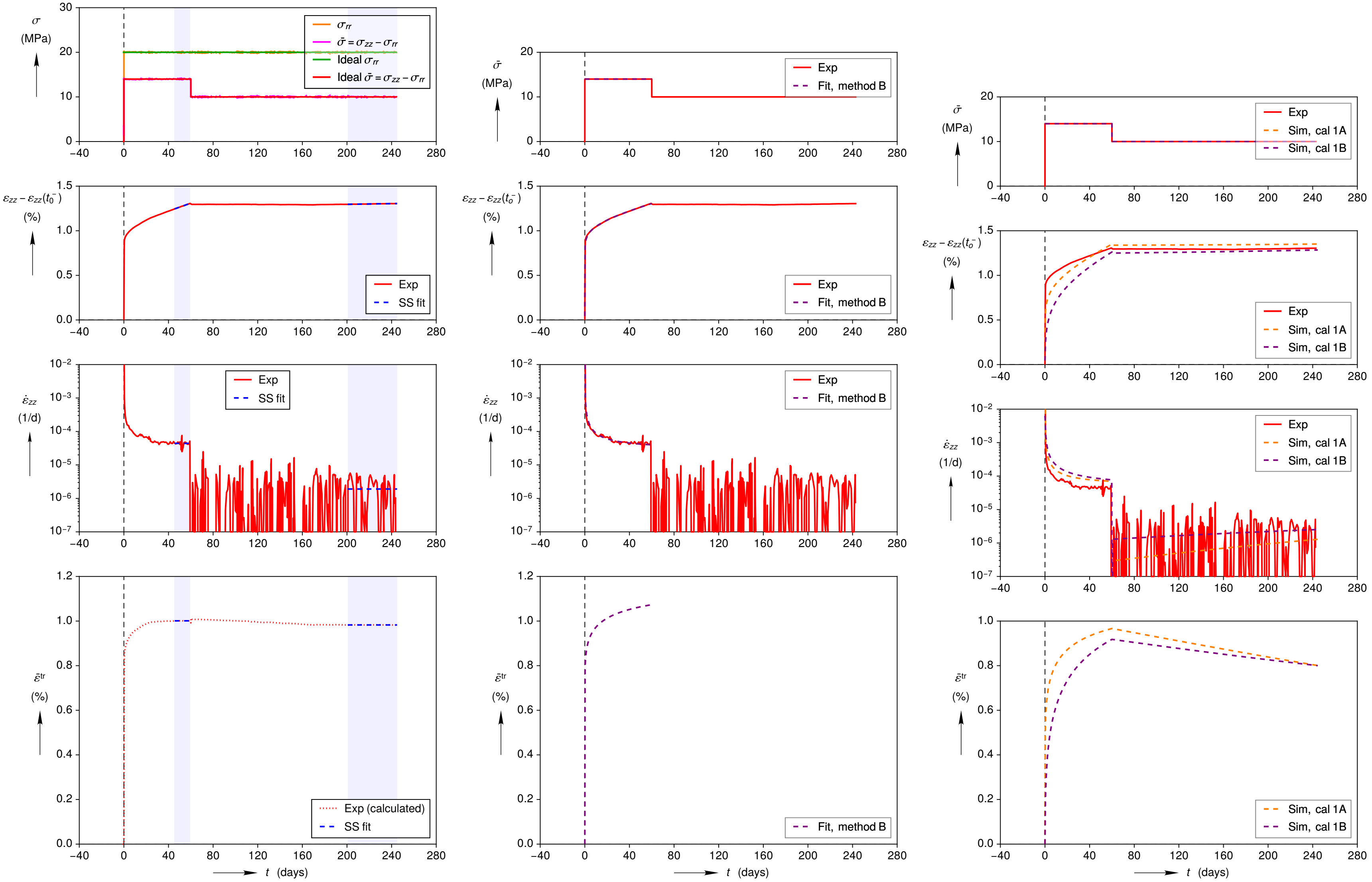

(a) Measurements (b) Individual fit (c) Global calibrations

Figure A.29: Experiment A_TUC_TCC4 at $T = 27$ °C

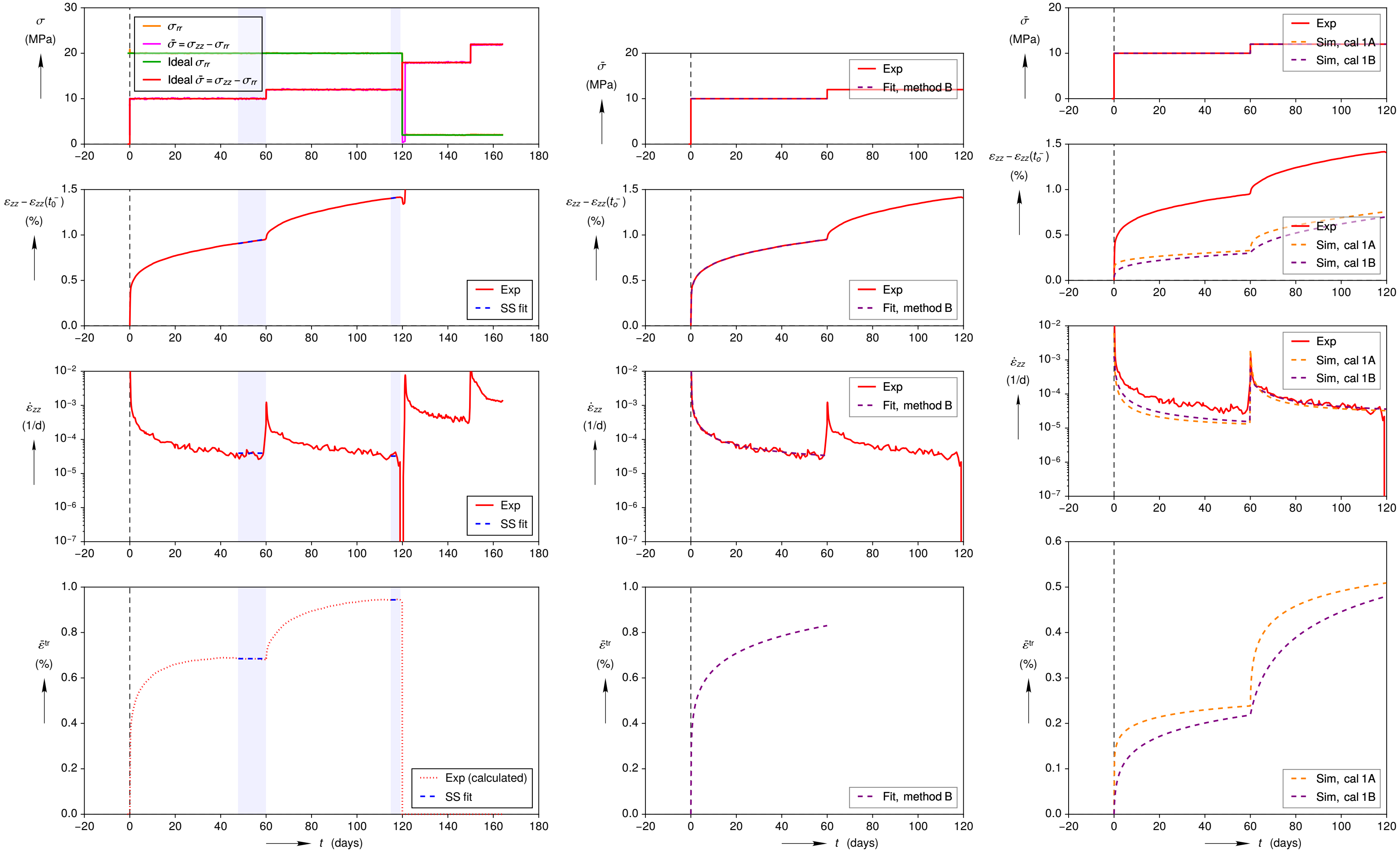

(a) Measurements (b) Individual fit (c) Global calibrations

Figure A.30: Experiment A_TUC_TCC9 at $T = 27$ °C

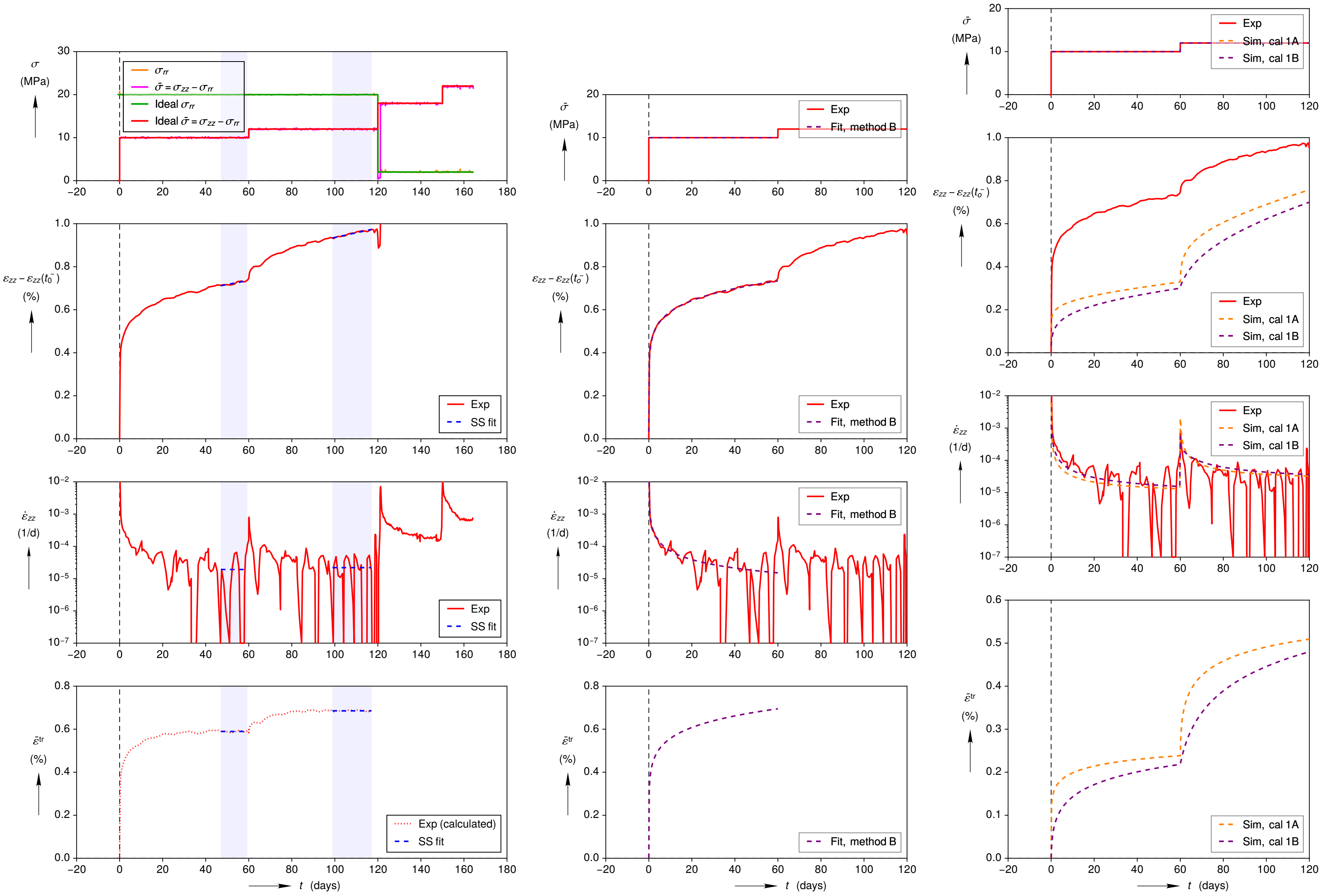

(a) Measurements

(b) Individual fit

(c) Global calibrations

Figure A.31: Experiment C_TUC_TCC12 at $T = 27$ °C

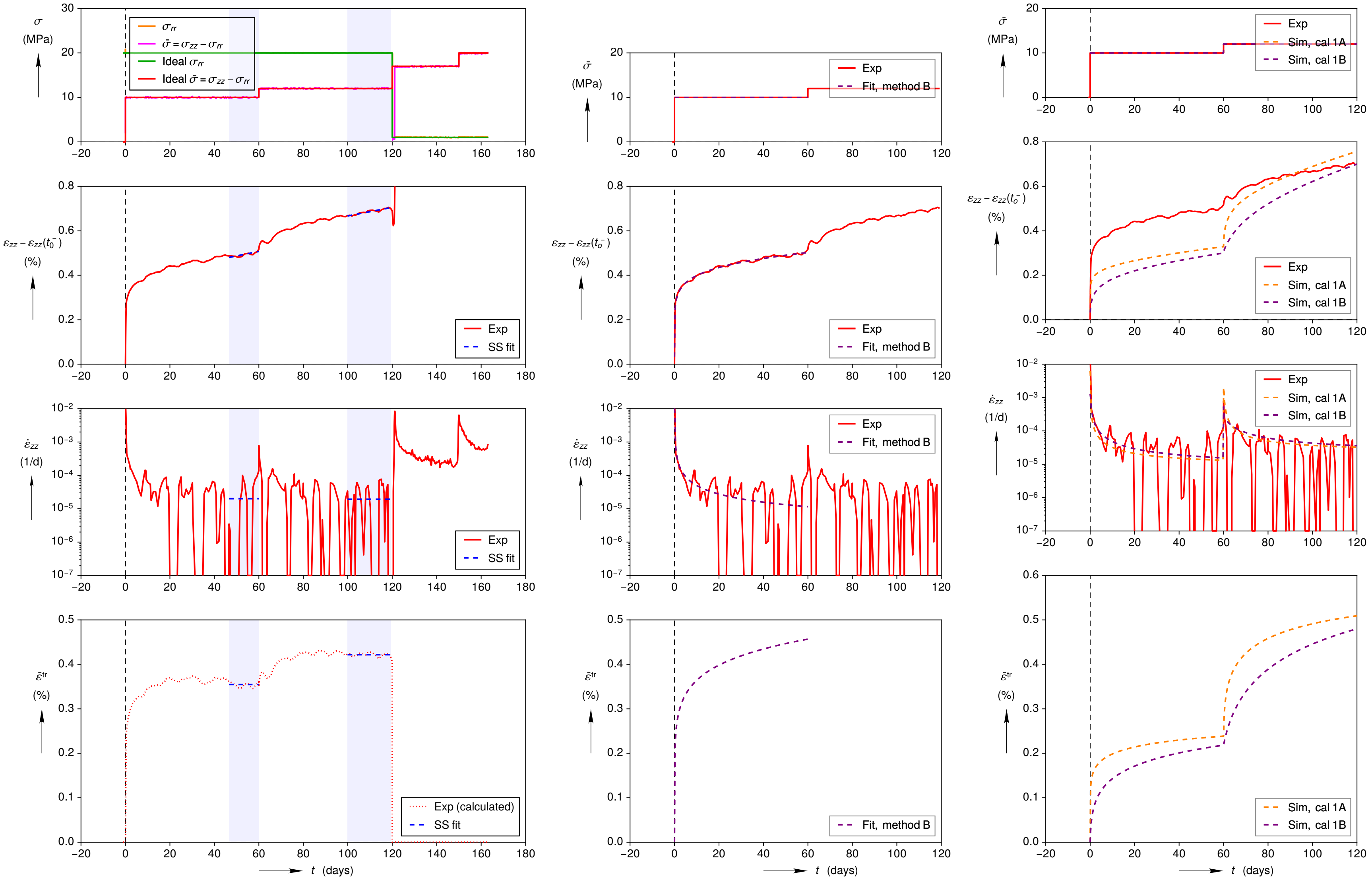

(a) Measurements

(b) Individual fit

(c) Global calibrations

Figure A.32: Experiment C_TUC_TCC19 at $T = 27$ °C

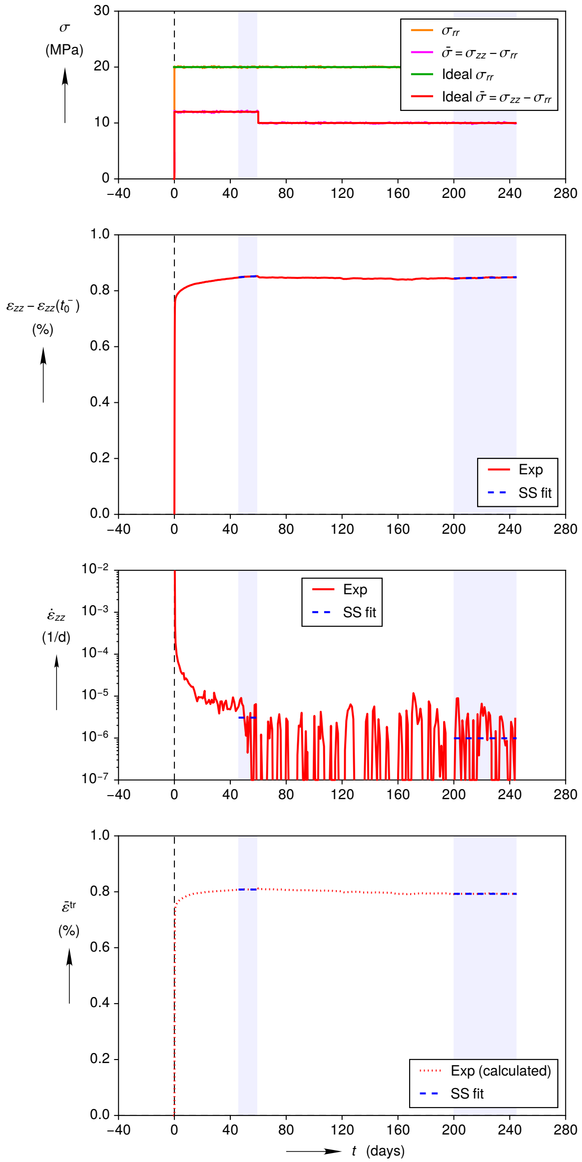

(a) Measurements

Figure A.33: Experiment C_TUC_TCC6 at $T = 27$ °C

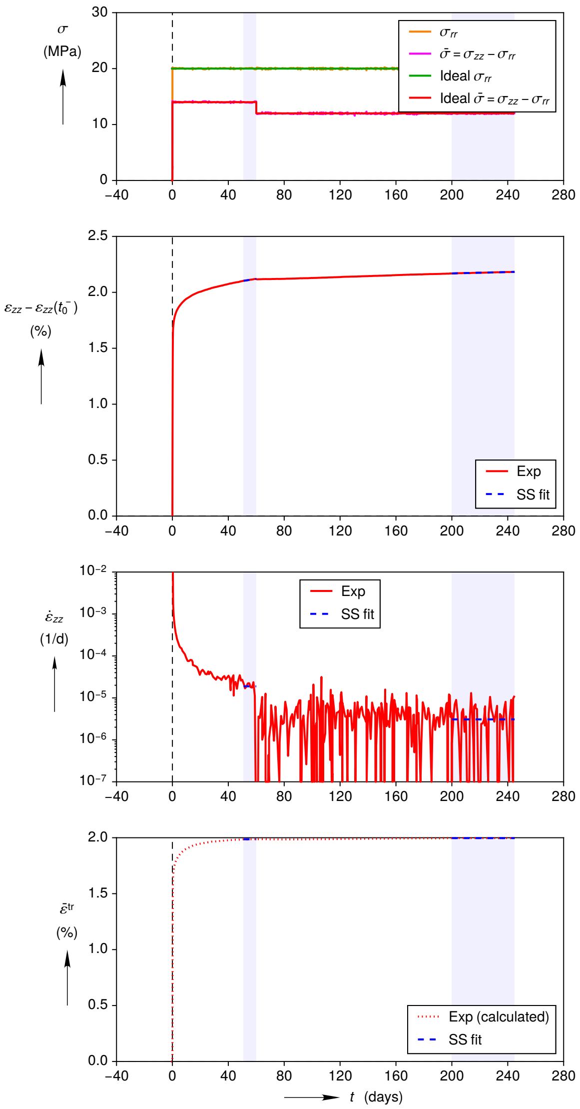

(a) Measurements

Figure A.34: Experiment C_TUC_TCC8 at $T = 27$ °C

Table A.3: TUC creep test analysis results on 2001 cores

					Method A			Method B		
Exp ID	T (°C)	E^{eff} (GPa)	$\bar{\sigma}$ (MPa)	w (–)	$\dot{\bar{\varepsilon}}^{\mathrm{ss}}$ (1/days)	$\bar{\varepsilon}^{\mathrm{tr}*}$ (%)	κ_{h} (–)	$\dot{\bar{\varepsilon}}^{\mathrm{ss}}$ (1/days)	$\bar{\varepsilon}^{\mathrm{tr}*}$ (%)	κ_{h} (–)
C_TUC_TCC6	27	46.15	12.0	1.0	3.068e-06	0.8081	–	3.068e-06	0.8081	–
			10.0	1.0	9.876e-07	0.7928	–	9.876e-07	0.7928	–
A_TUC_TCC11	27	35.34	16.0	0.3	2.474e-04	–	–	2.474e-04	–	–
			14.0	1.0	5.877e-05	–	–	5.877e-05	–	–
C_TUC_TCC12	27	31.00	10.0	1.0	1.915e-05	0.5893	–	1.152e-06	1.209	14.24
			12.0	1.0	2.190e-05	0.6854	–	2.190e-05	0.6854	–
C_TUC_TCC19	27	31.00	10.0	1.0	2.003e-05	0.3547	–	2.199e-06	0.7055	13.32
			12.0	1.0	1.921e-05	0.4217	–	1.921e-05	0.4217	–
C_TUC_TCC8	27	66.45	14.0	1.0	1.889e-05	1.986	–	1.889e-05	1.986	–
			12.0	1.0	3.075e-06	1.997	–	3.075e-06	1.997	–
A_TUC_TCC9	27	31.00	10.0	1.0	3.952e-05	0.6849	–	1.484e-05	1.163	10.03
			12.0	0.8	3.240e-05	0.9439	–	3.240e-05	0.9439	–
A_TUC_TCC4	27	32.44	14.0	1.0	4.415e-05	1.001	–	3.148e-05	1.165	38.07
			10.0	1.0	1.905e-06	0.9825	–	1.905e-06	0.9825	–
A_TUC_TCC3	27	31.00	10.0	1.0	6.561e-06	0.1875	–	1.381e-15	1.223	32.59
			12.0	1.0	1.649e-05	0.2659	–	1.649e-05	0.2659	–
A_TUC_TCC2	27	133.20	10.0	0.5	4.010e-06	0.1212	21.31	1.637e-06	0.2533	6.592
			8.0	0.3	8.529e-08	0.1328	–	8.529e-08	0.1328	–

A.6 Fits of TUC Triaxial Creep Tests on 2013 Cores

The only TUC creep tests on 2013 cores were A_TUC_TCC41, A_TUC_TCC42, and C_TUC_TCC94. A_TUC_TCC41 and A_TUC_TCC42 are probably rows 39 through 41 and rows 42 through 45, respectively, in Table 2 of *Düsterloh et al.* (2015)[1]. These two tests were rejected by some of the Joint Project III partners because of disturbances to the creep curves. The tests are included in Figs. A.35 and A.36 for completeness, but they were not used to calibrate the Munson-Dawson model for the reasons discussed in Appendix A.7. The third test (C_TUC_TCC94) was a creep failure test performed close to the dilatancy boundary

---

[1] Table 2 of *Düsterloh et al.* (2015) does not explicitly call out the experiment names, so one must match up a group of stresses and temperatures to list of consecutive rows. Rows 39 and 40 match the stresses and temperatures in the first two stages of A_TUC_TCC41, but row 41 does not match A_TUC_TCC41's final stage. Rows 42 and 43 match the stresses and temperatures in the first two stages of A_TUC_TCC42, but rows 44 and 45 do not match A_TUC_TCC42's final stages. Given that all other TUC tests on argillaceous cores correspond to rows 25 through 38 in Table 2, the stresses in rows 41, 44, and 45 are probably just typographical errors or planned test inputs that were changed at a later time.

($\bar{\sigma} = 42.5$ MPa, and $\sigma_{rr} = 5$ MPa), so it was neglected here. See Appendix A.5 for a brief summary of important differences between the IfG and TUC creep tests.

Fig. A.35 and Fig. A.36 show the analysis of the tests. Fitting method B successfully fit both creep tests, but method A failed to fit κ_{h} probably because of the disturbances in the first stage of each test. Table A.4 displays the test temperature T, the equivalent stress $\bar{\sigma}$, the effective axial stiffness E^{eff}, the weighting factor w, and the results of fitting method A and method B for each test.

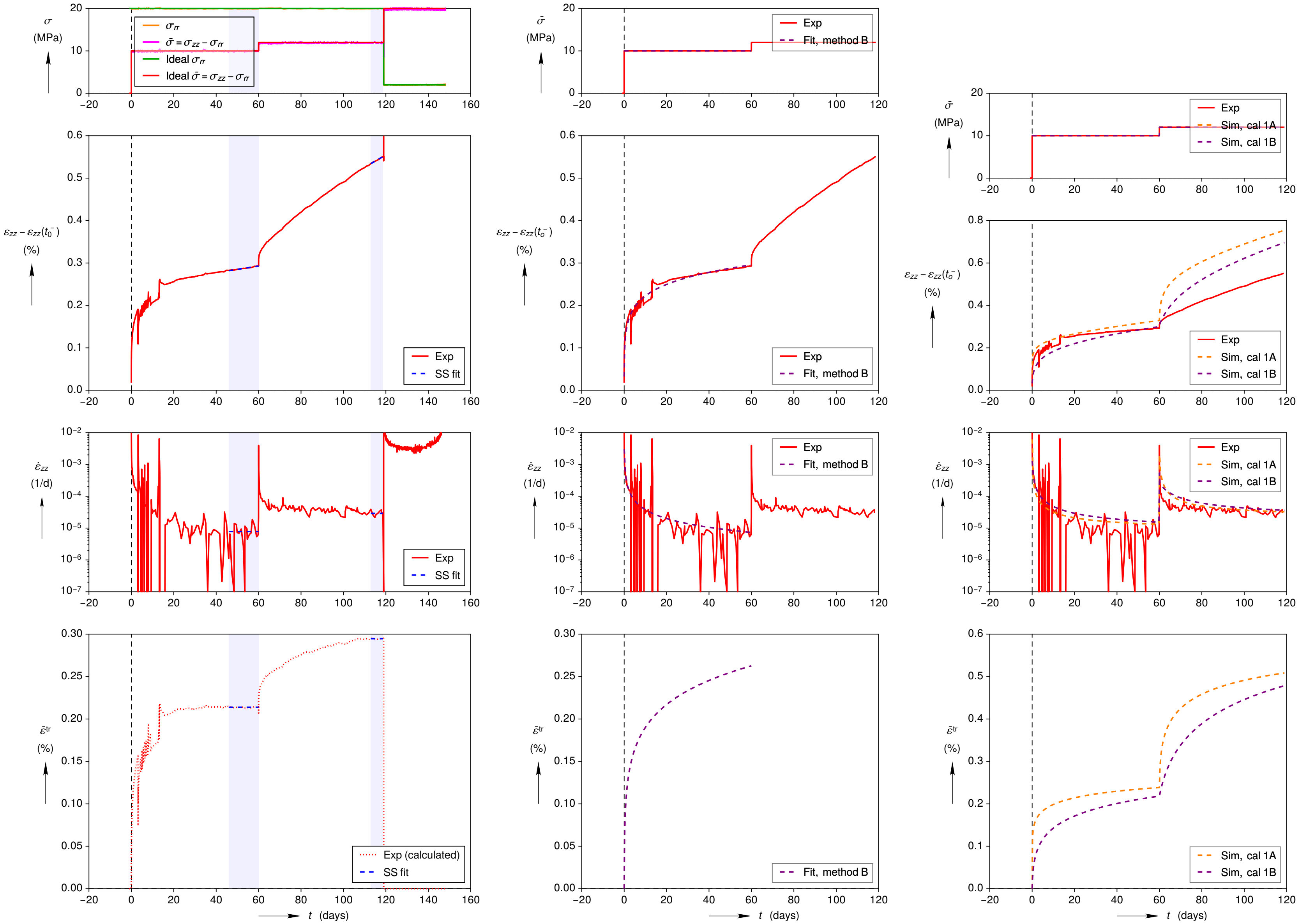

(a) Measurements (b) Individual fit (c) Global calibrations

Figure A.35: Experiment A_TUC_TCC41 at $T = 27$ °C

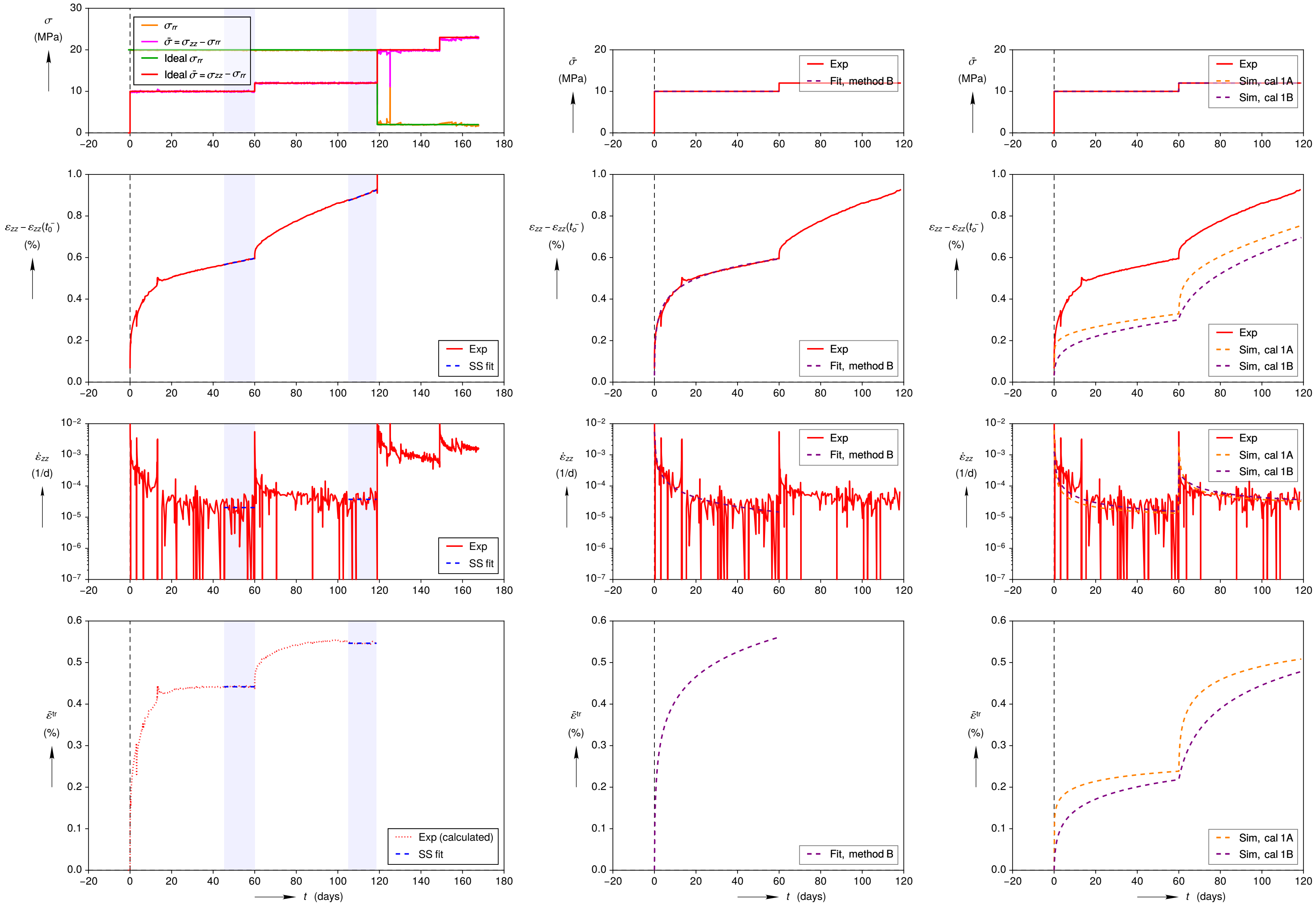

(a) Measurements (b) Individual fit (c) Global calibrations

Figure A.36: Experiment A_TUC_TCC42 at T = 27 °C

Table A.4: TUC creep test results on 2013 cores

Exp ID	T (°C)	E^{eff} (GPa)	$\bar{\sigma}$ (MPa)	w (−)	Method A $\dot{\bar{\varepsilon}}^{\mathrm{ss}}$ (1/days)	 $\bar{\varepsilon}^{\mathrm{tr}*}$ (%)	 κ_{h} (−)	Method B $\dot{\bar{\varepsilon}}^{\mathrm{ss}}$ (1/days)	 $\bar{\varepsilon}^{\mathrm{tr}*}$ (%)	 κ_{h} (−)
A_TUC_TCC41	27	31.00	10.0	0.2	7.777e-06	0.2138	–	8.034e-08	0.6933	11.69
			12.0	0.8	2.898e-05	0.2947	–	2.898e-05	0.2947	–
A_TUC_TCC42	27	31.00	10.0	0.4	2.030e-05	0.4418	–	6.294e-15	4.439	28.26
			12.0	1.0	3.730e-05	0.5465	–	3.730e-05	0.5465	–

A.7 Triaxial Creep Tests Compared

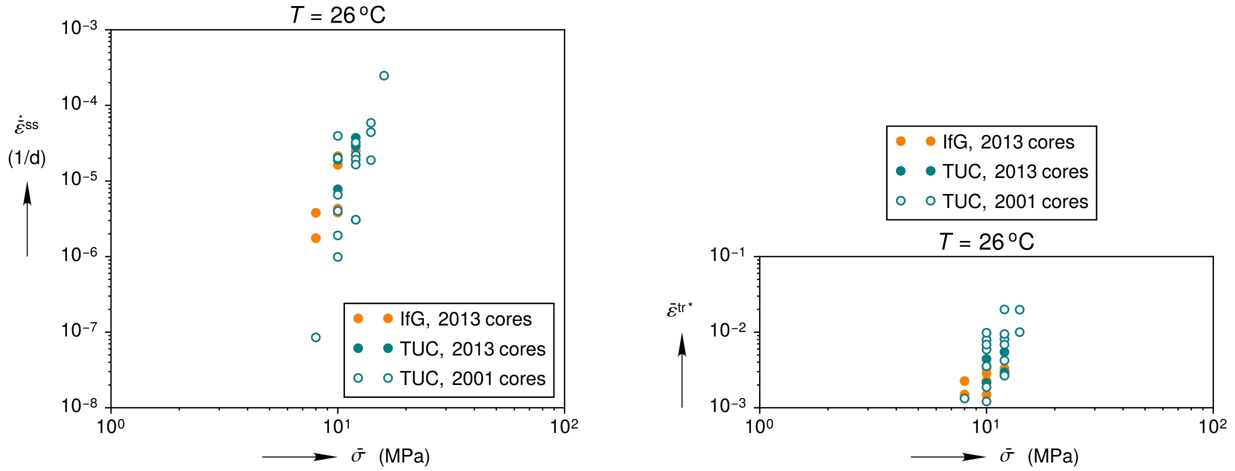

(a) Steady State Rate

(b) Transient Limit

Figure A.37: Steady state equivalent creep strain rates and transient equivalent creep strain limits compared for 2001 and 2013 cores. All data points were obtained using fitting method A.

Fitting method A is better suited for comparing experiments to experiments than method B, as mentioned in Section 3.3, so we'll first compare the method A results from the 2001 and 2013 cores. The IfG and TUC both measured similar values of $\dot{\bar{\varepsilon}}^{\mathrm{ss}}$ and $\bar{\varepsilon}^{\mathrm{tr}*}$ on 2013 cores in Fig. A.37. The 2001 cores, however, generally exhibit lower $\dot{\bar{\varepsilon}}^{\mathrm{ss}}$ values and higher $\bar{\varepsilon}^{\mathrm{tr}*}$ values than 2013 cores. In addition, the 2001 core measurements have more scatter than the 2013 core measurements. It is not possible to compare the κ_{h} values from the two core types, because the κ_{h} optimization step for method A failed to converge for all but one 2001 core test, despite repeated attempts.

Fitting method B was used to facilitate a comparison between the κ_{h} values for the two

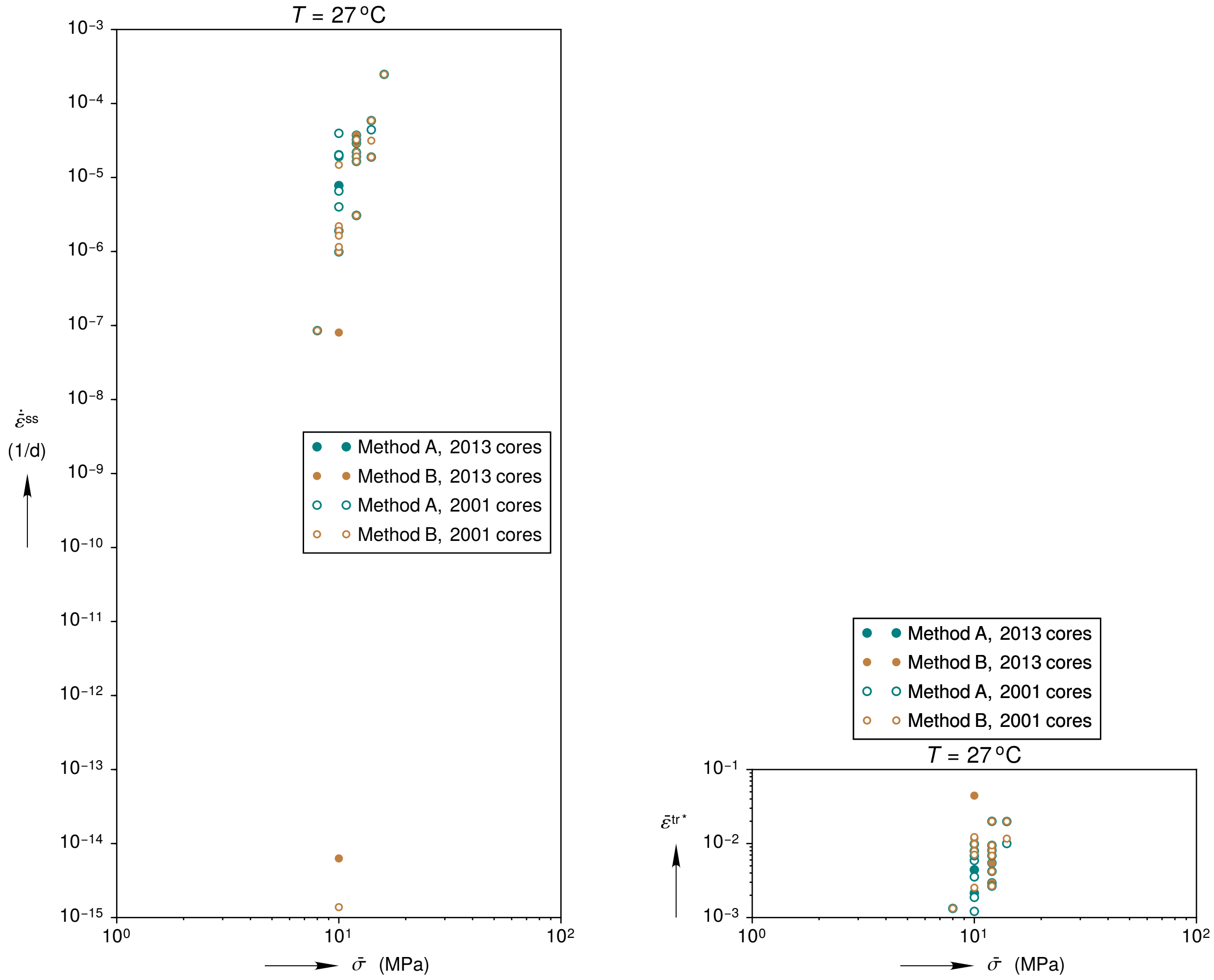

(a) Steady State Rate

(b) Transient Limit

Figure A.38: A comparison of experiment fitting methods for the TUC experiments.

core types. A comparison of the TUC $\dot{\bar{\varepsilon}}^{\mathrm{ss}}$ and $\bar{\varepsilon}^{\mathrm{tr}*}$ values from the two fitting methods is shown in Fig. A.38. The $\dot{\bar{\varepsilon}}^{\mathrm{ss}}$ values are lower and the $\bar{\varepsilon}^{\mathrm{tr}*}$ values are higher for method B. The two lowest steady-state strain rates show why it is important to be cautious with method B. Note, nonetheless, that method B did not produce any strange results for the IfG experiments on 2013 cores, as shown in Fig. 3.6.

Method B produced significantly different values of κ_{h} for the IfG and TUC experiments. As depicted in Fig. A.39, nearly all κ_{h} values were higher in the TUC experiments. This difference means the ε_{zz} vs t curve would jump upwards and level off more quickly in the TUC experiments.

A number of differences have been identified between the IfG experiments on 2013 cores and the TUC experiments.

1. The TUC specimens only experienced 24 hours of hydrostatic consolidation instead of

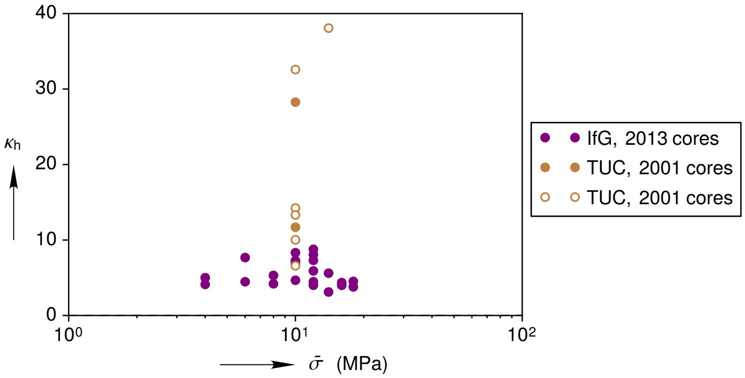

Figure A.39: Transient rate variables compared for the 2001 and 2013 cores. All data points were obtained using fitting method B.

10 days.

2. Many TUC experiments did not include a load drop off to pick off the effective axial stiffness E^{eff}, forcing the use of E instead.
3. Method A was unable to fit κ_h on all but one TUC experiment.
4. The $\dot{\bar{\varepsilon}}^{\text{ss}}$ and $\bar{\varepsilon}^{\text{tr}*}$ values from the two fitting methods do not agree for the TUC experiments.
5. The method B values of κ_h differ substantially between the IfG and the TUC experiments.

For these reasons, the TUC tests were discarded, and the M-D model was fit against only the IfG experiments on the 2013 cores.

A.8 Munson-Dawson Calibration 1A

The M-D model was recalibrated twice in this report. Calibration 1A, shown here, was created using $\dot{\bar{\varepsilon}}^{\text{ss}}$, $\bar{\varepsilon}^{\text{tr}*}$, and κ_h values extracted from the IfG experiments using fitting method A. Calibration 1B, discussed in Section 3.4, was created using $\dot{\bar{\varepsilon}}^{\text{ss}}$, $\bar{\varepsilon}^{\text{tr}*}$, and κ_h values extracted from the IfG experiments using fitting method B. Besides the methods used to collect $\dot{\bar{\varepsilon}}^{\text{ss}}$, $\bar{\varepsilon}^{\text{tr}*}$, and κ_h, both calibrations followed identical procedures to select values for the parameters A_2, Q_2, n_2, K_0, c, m, α_h, and β_h. On the whole, the two calibrations are similar, so the calibration 1A plots that correspond to the calibration 1B plots in Section 3.4 are displayed in Figs. A.40 to A.42 without further description.

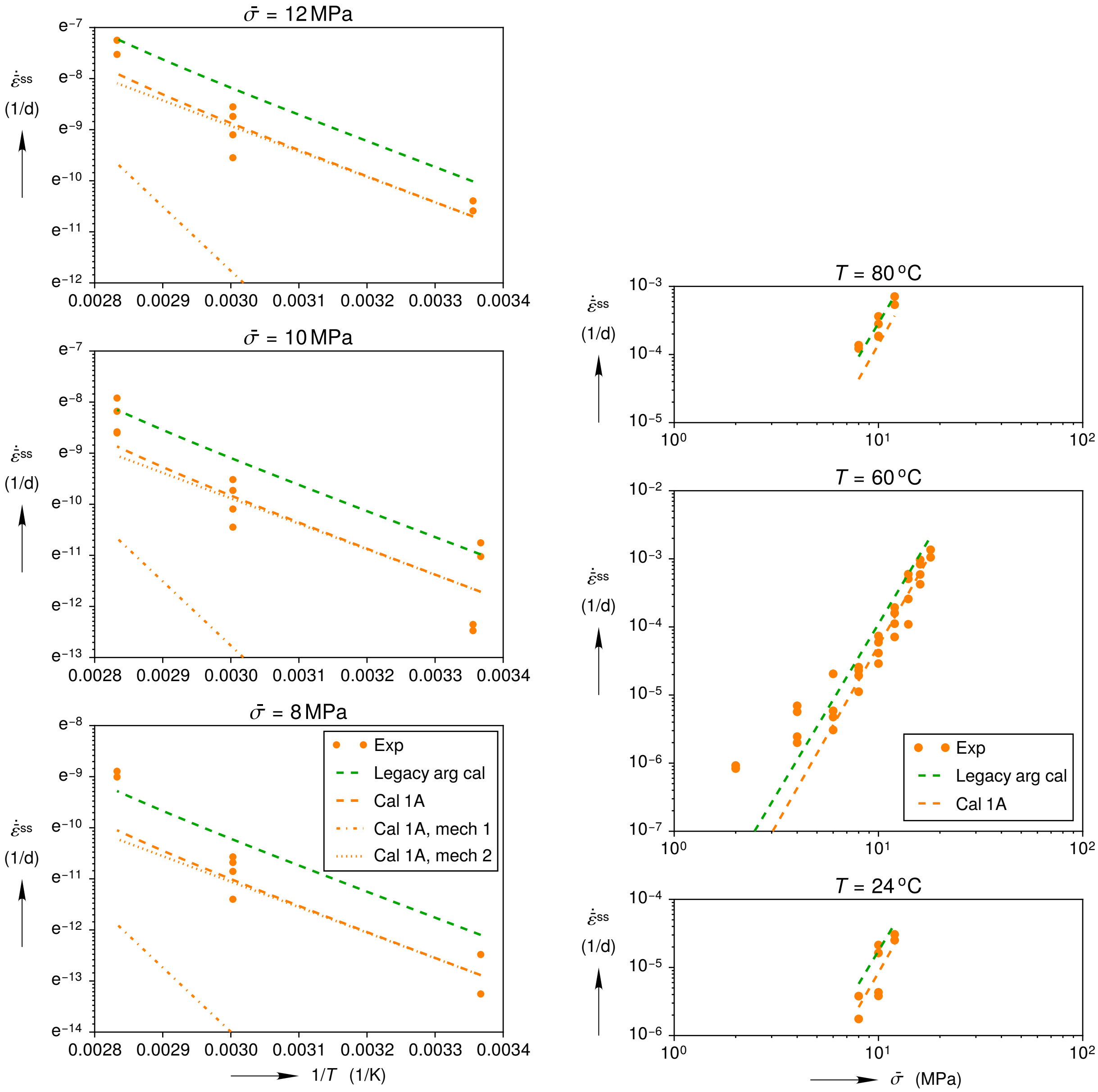

(a) Temperature Dependence (b) Stress Dependence

Figure A.40: Calibration 1A equivalent creep strain steady state rate compared against experiments. Experimental data points were obtained using fitting method A.

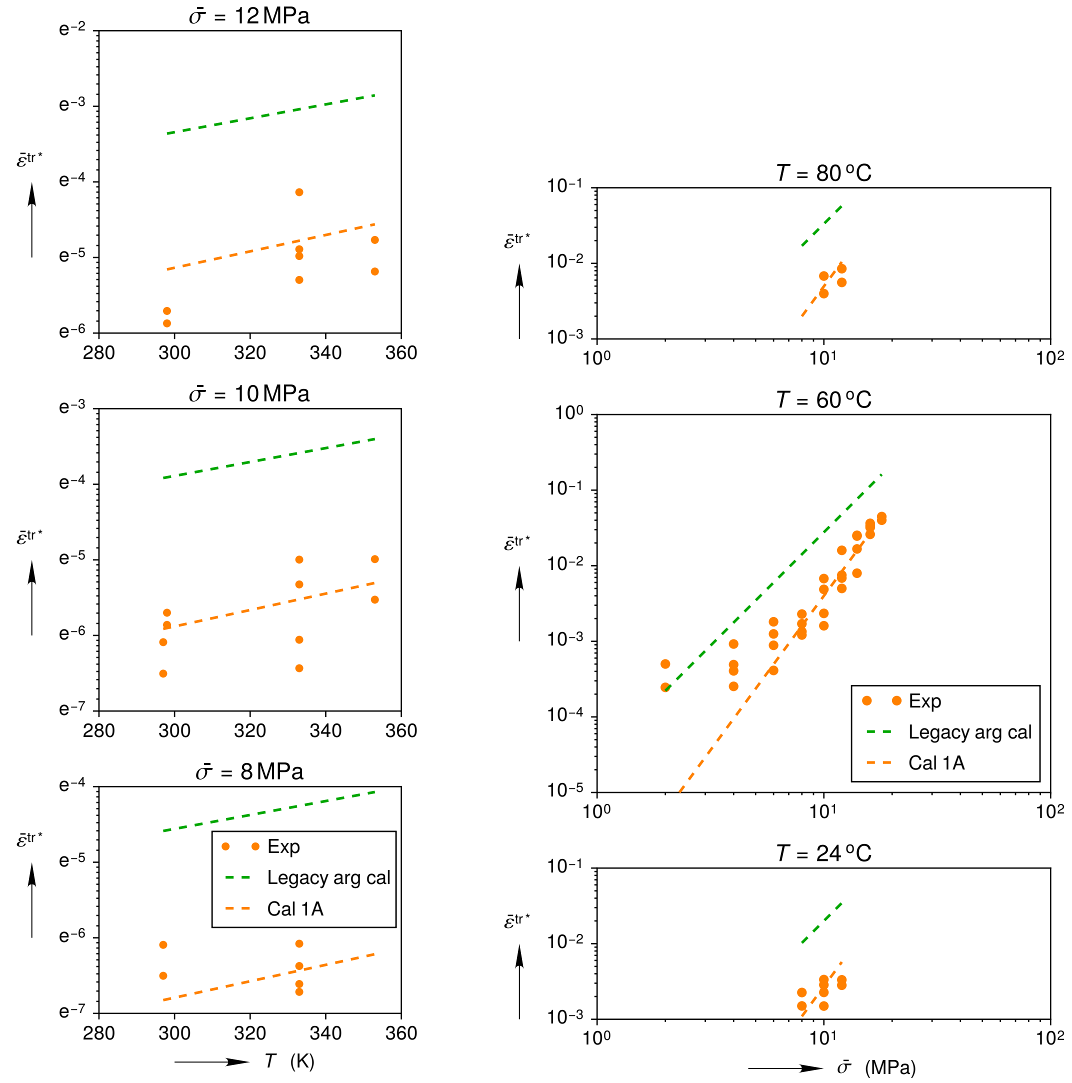

(a) Temperature Dependence

(b) Stress Dependence

Figure A.41: Calibration 1A equivalent creep strain transient limit compared against experiments. Experimental data points were obtained using fitting method A.

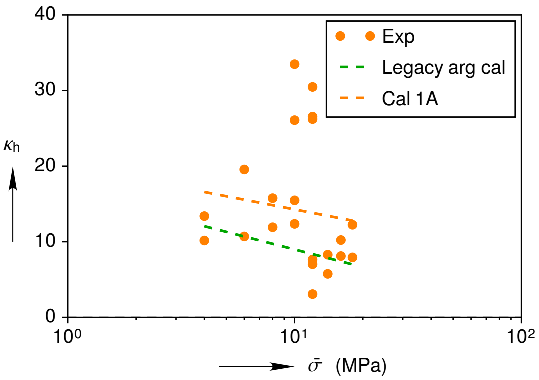

Figure A.42: Calibration 1A hardening rate variable compared against experiments. Experimental data points were obtained using fitting method A.

A.9 Joint Project III Simulations

Joint Project III partners made three different modeling choices when they simulated the closure of Room D. To participate in the benchmarking process, the simulations discussed in Chapter 4 were modified to meet the Joint Project III conditions. These simulations are documented here rather than in the main body of the report to avoid potentially confusing the reader.

The three Joint Project III changes were:

1. The clay seams were not allowed to slide.
2. The anhydrite was modeled using an elastic, perfectly-plastic, Mohr-Coulomb model instead of an elastic, perfectly plastic, Drucker-Prager model.
3. The polyhalite was modeling using an elastic, plastic, power law creep model instead of an elastic, perfectly plastic, Drucker-Prager model.

These changes were implemented in the Sierra/Solid Mechanics simulations in the following manner:

1. Prohibiting sliding at the clay seams was done by simply merging the nodes on either side of the seams. Thus, the Joint Project III simulations in this section used the same fine mesh shown in Fig. 2.7b.
2. Sierra/Solid Mechanics does not have a simple Mohr-Coulomb model. Instead, Kayenta was reduced to a Mohr-Coulomb model according to Appendix B.4.8 in *Brannon et al.* (2015). The Joint Project III parameter set, and their Kayenta equivalents are listed in Appendix A.9.1.
3. Sierra/Solid Mechanics does have a power law creep model. The Joint Project III parameter set is listed in Appendix A.9.2.

Interestingly, the Mohr-Coulomb model included a non-associated flow potential with a dilatation angle of 0°, yet the strain localizations exhibited by the Drucker-Prager model with a von Mises flow potential in Fig. 2.5c were not observed. That being said, when the clay seams were allowed to slide with the Mohr-Coulomb non-associated flow model, Sierra/Solid Mechanics conjugate gradient solver had a very hard time converging at $t = 6$ s. Sierra/Solid Mechanics will output the unconverged solution to help the analyst debug any issues. The unconverged strain fields did exhibit strain localizations similar to those in Fig. 2.5c. Out of curiosity, the flow rule was switched to an associated flow rule and the simulation was able to run well past $t = 6$ s before it was stopped. The particular Mohr-Coulomb model parameter set appears to be less susceptible to the material instability that plagues non-associated flow rule models, but not immune.

Although two Munson-Dawson model calibrations were documented in this report, only the simulation results from calibration 1B were submitted for the Joint Project III benchmarking exercise. Calibration 1B was chosen because fitting method B seems better suited for calibrating constitutive models, provided method B is performed with care. (See Section 3.3 for further discussion.) Regardless, the two calibrations predict similar room closures (see Fig. 4.1), so the decision was not very influential.

A.9.1 Sierra/SM Input Syntax for the Joint Project III Anhydrite Model

```
begin property specification for material anhydrite
    density = 2300.0 # kg / m^3
    #Sierra/SM needs to have elastic parameters defined with these names, so we repeat
    #the values in the "begin parameters ..." block.
    bulk modulus = 40.0e9 # Pa = bulk modulus
    shear modulus = 24.0e9 # Pa = shear modulus

    #The Joint Partners used FLAC3D's Mohr-Coulomb model.
    #These Mohr-Coulomb parameters came from Ralf-Michael Gunther, who chose them based
    #on experience.  He wanted the strength to represent an anhydrite with microcracks,
    #since anhydrite is typically not found intact in the underground.
    #B0 = bulk modulus = 40.0e9 Pa
    #G0 = shear modulus = 24.0e9 Pa
    #S0 = cohesion strength = 2.0e6 Pa
    #phi = friction angle = 30 degrees
    #alpha = dilatation angle = 0 degrees

    #As of January 2016, we do not have a Mohr-Coulomb model in Sierra/SM.  We can,
    #however, reduce Kayenta to Mohr-Coulomb by using the instructions in Appendix B.4.8
    #of SAND2015-0803.
    begin parameters for model kayenta
        B0 = 40.0e9    # Pa = bulk modulus
        G0 = 24.0e9    # Pa = shear modulus
        J3TYPE = 3     # Sets the dependence on J_3.  J3TYPE = 3 is a Mohr-Coulomb
         ↪  dependence.
        A1 = 2.4e6     # Pa = 2 * sqrt(3) / (3 - sin(phi)) * S0 * cos(phi)
        A2 = 0.0
        A3 = 0.0
        A4 = 0.2309401 # = 2 * sqrt(3) / (3 - sin(phi)) * sin(phi) / 3
        RK = 0.7142857 # = (3 - sin(phi)) / (3 + sin(phi))
        A2PF = 0.0
        A4PF = 1.0e-11 # = 2 * sqrt(3) / (3 - sin(alpha)) * sin(alpha) / 3
        RKPF = 1.0     # = (3 - sin(alpha)) / (3 + sin(alpha))
        P0 = -1.0e99   # Put the cap at virtually infinity
        P1 = 0.0       # No cap
        P2 = 0.0       # No cap
        P3 = 0.0       # Zero porosity
        CR = 0.001     # Minimize the size of the curved part of the cap
        CRPF = 0.001   # Prevent cap influence on shear response
        HC = 0.0       # Disable kinematic hardening
```

```
        RN = 0.0        # Disable kinematic hardening
    end parameters for model kayenta
end property specification for material anhydrite
```

A.9.2 Sierra/SM Input Syntax for the Joint Project III Polyhalite Model

```
begin property specification for material polyhalite
    density = 2300.0  # kg / m^3
    #These parameters came from Ralf-Michael Gunther, who chose them based on experience.
    #The Joint Partners used FLAC3D's two component power law model, but they only used
    #the first component, so it can be captured by the power_law_creep model in
     ↪  Sierra/SM.
    #The parameters are identical, so no conversion is necessary between the two models.
    begin parameters for model power_law_creep
        bulk modulus = 19.0e9 # Pa
        shear modulus = 12.0e9 # Pa
        creep constant = 5.20833333e-40 # 1/(Pa^4*s)
        creep exponent = 4.0 # Unitless
        #Set to thermal constant to zero to mimic FLAC3D's two component power law,
        #which does not have temperature dependence.
        thermal constant = 0.0 # Kelvin = Q/R
    end parameters for model power_law_creep
end property specification for material polyhalite
```

A.9.3 Joint Project III Simulation Results

The impact of the three Joint Project III changes are displayed in Fig. A.43a for simulations using the full stratigraphy. Both the legacy calibration and calibration 1B exhibit less room closure when the clay seams are removed. Changing the material models for the anhydrite and polyhalite, by contrast, increased the room closure predictions. This increase was expected because the anhydrite strength was purposely lowered by the Joint Project III partners. In their estimation, the Drucker-Prager parameters specified in *Morgan and Krieg* (1984) were too strong compared to values typically used in the German salt community.

The sensitivity to different stratigraphies and M-D model calibrations are depicted in Fig. A.43b. Note that the stratigraphy in the legacy calibration, all salt, simulation differs from the stratigraphy used in the legacy recreated, all salt, simulation in Fig. 2.2. *Munson et al.* (1989) did not state whether they modeled the anhydrite and polyhalite as clean salt or argillaceous salt, so *Argüello and Holland* (2015); *Argüello* (2015) chose to model those layers as clean salt. The Joint Project III partners chose to model the anhydrite/polyhalite with whichever salt type sandwiched the anhydrite/polyhalite layer for the all salt simulations. Generally, though, the legacy calibration simulations have the same ordering of the clean salt, all salt, and full stratigraphy predictions as observed in Fig. 2.2, despite a number of differences between the simulations.

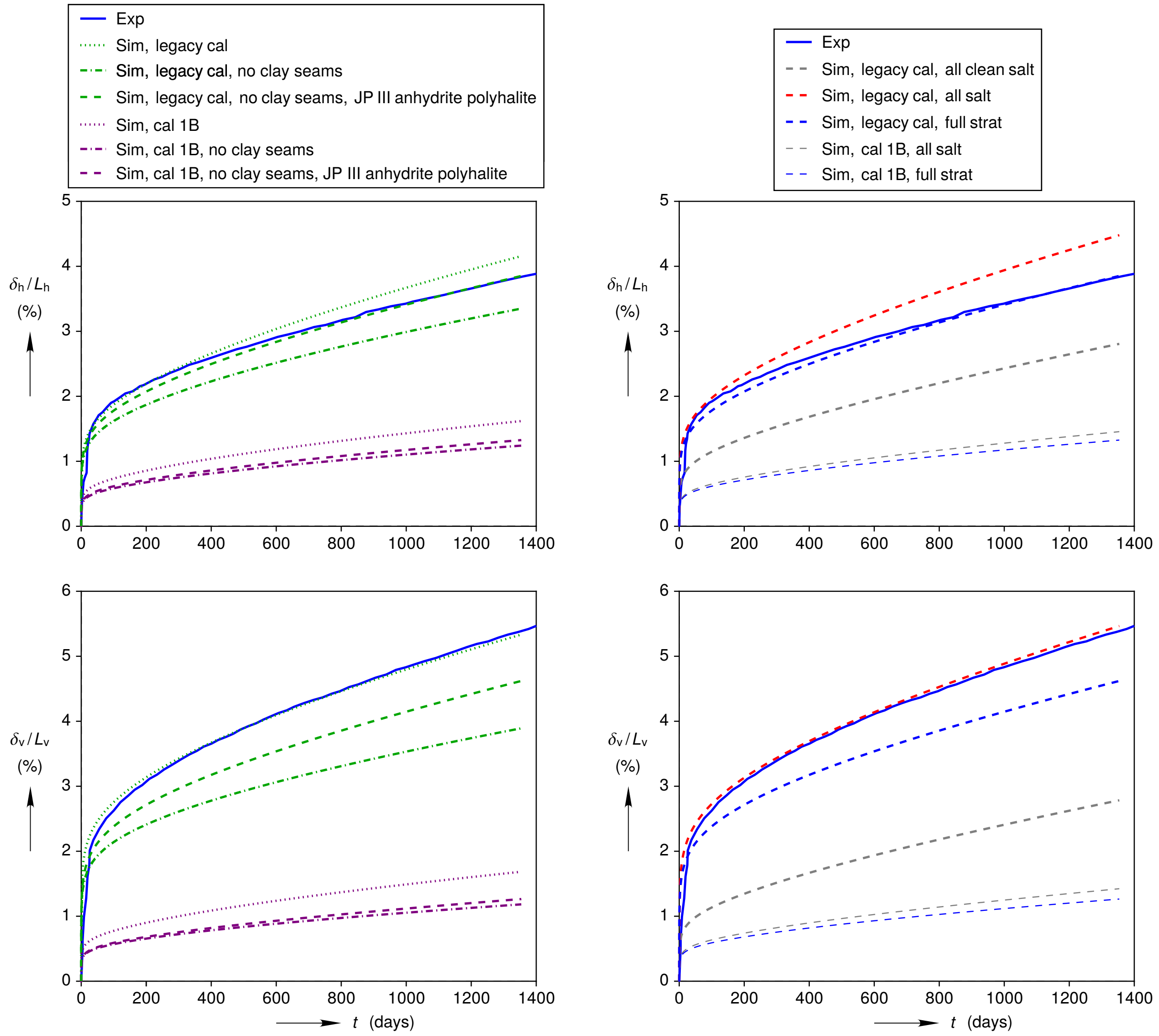

(a) Full stratigraphy, switch to Joint Project III setup

(b) Joint Project III setup, comparison between different calibrations and stratigraphies

Figure A.43: Full stratigraphy simulations converted to the Joint Project III setup. The legacy calibration is then compared against calibration 1B for various stratigraphies using the Joint Project III setup.

DISTRIBUTION:

1 J. Guadalupe Argüello
8328 S. Sandoval Ct. N.E.
Albuquerque, NM 87122

1 Andreas Hampel
Grünberger Straße 56
55129 Mainz
Germany

2 Leibniz Universität Hannover
Institut für Geotechnik
Abteilung Unterirdisches Bauen
Attn: Kurt Staudtmeister, Savas Yildirim
Welfengarten 1a
30167 Hannover
Germany

2 Technische Universität Braunschweig
Institut für Grundbau und Bodenmechanik
Attn: Joachim Stahlmann, Andreas Gährken
Beethovenstraße 51b
38106 Braunschweig
Germany

2 Institut für Gebirgsmechanik GmbH
Attn: Klaus Salzer, Ralf-Michael Gunther, Christoph Lüdeling
Friederikenstraße 60
4279 Leipzig
Germany

4 Technische Universität Clausthal
Institut für Aufbereitung, Deponietechnik und Geomechanik
Attn: Karl-Heinz Lux, Ralf Wolters, Kai Herschen, Uwe Düsterloh
Erzstraße 20
38678 Clausthal-Zellerfeld
Germany

4 RESPEC
Attn: Kirby Mellegard, Kerry DeVries, Leo Van Sambeek, Stuart Buchholz
3824 Jet Drive
Rapid City, SD 57703

2 Southwest Research Institute
Center for Nuclear Waste Regulatory Analyses
Attn: Goodluck Ofoegbu, Biswajit Dasgupta
6220 Culebra Rd.
P.O. Drawer 28510
San Antonio, TX 78228

1 Dennis Powers
170 Hemley Rd.
Anthony, TX 79821

1 Lawrence Berkeley National Laboratory Nuclear Energy and Waste Program
Attn: Jens Birkholzer
One Cyclotron Road, Room 308, Mail Stop 74R316C
Berkeley, CA 94720

2 US Department of Energy
Attn: Prasad Nair, Tim Gunter
DOE-NE
232 Energy Way
North Las Vegas, NV 89030

1 US Nuclear Regulatory Commission
Office of Nuclear Material Safety and Safeguards
Attn: Jin-Ping Gwo
11545 Rockville Pike
Rockville, MD 20852

1	MS 0346	J. Holland, 1556
1	MS 0735	E. Webb, 6910
1	MS 0747	R. MacKinnon, 6224
1	MS 0747	K. Kuhlman, 6224
1	MS 0751	S. Sobolik, 6912
1	MS 0751	B. Park, 6912
1	MS 0751	F. Hansen, 6930
1	MS 0840	J. Bean, 1554
1	MS 0840	J. Bishop, 1554
1	MS 0840	E. Fang, 1554
1	MS 0840	J. Pott, 1555
1	MS 0840	J. Rath, 1555
1	MS 1033	S. Bauer, 6914
1	MS 1033	S. Broome, 6914
1	MS 1395	P. Shoemaker, 6930

1	MS 1395	C. Herrick, 6931
1	MS 1395	C. Leigh, 6932
1	MS 1395	M. Schuhen, 6932
1	MS 0899	Technical Library, 9536 (electronic copy)

Sandia National Laboratories